EXCLUSIVE ρ^0 PRODUCTION
MEASURED WITH THE HERMES RECOIL DETECTOR

Inaugural-Disertation

zur Erlangung des Doktorgrades der Naturwissenschaften

der Justus-Liebig-Universität Gießen

des Fachbereich 07

(Mathematik und Informatik, Physik, Geographie)

vorgelegt von

Roberto Francisco Pérez Benito

aus Paris, France

«Men are haunted by the vastness

of eternity

And so we ask ourselves...

...will our actions echo

across the centuries?

Will strangers hear our names

long after we're gone...

...and wonder who we were...

...how bravely we fought...

... how fiercely we loved?»

«If they ever tell my story, let them say

I walked with Giants.

Men rise and fall like the winter wheat

but these names will never die.

Let them say I lived in the time of Hector

tamer of horses.

Let them say

I lived in the time of Achilles.»

Odysseus

Troy (2004), based on Homer's - "The Iliad"

Zusammenfassung

Das Hermes Experiment (HERa Measurement of Spin) am Desy wurde entwickelt um die Spinstruktur der Nukleonen in semiinklusiver tiefinelastischer Streuung zu studieren. Die detaillierte Untersuchung der internen Struktur der Nukleonen ergab, dass der Beitrag des intrinsischen Spins zum Gesamtspin des Nukleons nur ca. 30% beträgt. Um die fundamentalen Strukturen des Nukleons zu verstehen wurde ein neuer Formalismus, genannt General Parton Distributions (GPDs), entwickelt, der die innere Struktur des Nukleons beschreibt. Zugang zu diesen GPDs gewährt die Messung von harten exklusiven Reaktionen und Prozessen, die in GPD-Funktionen ausgedrückt werden. Die akkumulierten Hermes Daten ermöglichen Zugriff auf die GPDs in verschiedenen Kombinationen von Strahlladung und Target Helizitätsasymmetrien.

Um die Exklusivität der Messung zu verbessern und um die Auflösung der kinematischen Variablen zur Untersuchung der harten exklusiven Prozesse zu erhöhen, die Zugriff auf die GPDs gewähren und die Möglichkeit der Berechnung des orbitalen Drehimpulses eröffnen, wurde im Januar 2006 der Rückstoß-Detektor installiert, der das interne Gas-Target des Hermes Experiments umschließt.

Der Rückstoß-Detektor besteht aus drei Komponenten: Einem Silizium-Zähler innerhalb der Streukammer, einem Detektor aus szintillierenden Fasern und einem Photon-Detektor. Alle drei Detektoren wurden innerhalb des Solenoid des Magneten platziert, der ein Magnetfeld von 1T Stärke bereitstellt. Der Rückstoß-Detektor verbessert, zum einen durch das direkte Messen des Impulses und der Pfadrichtung des zurück gestoßenen Teilchens und zum anderen durch Ausschluss des nichtexklusiven Hintergrundes, die Selektion der exklusiven Ereignisse. Der Detektor war hierbei ein ausgezeichnetes neues Werkzeug, um Energiemessungen und Positionsmessungen für geladene Teilchen in einem Impulsbereich von 0.1 GeV/c bis 1.4 GeV/c zu kombinieren. Der Rückstoßdetektor war bis zur Einstellung des Hera-Betriebes im Juli 2007 voll funktionsfähig und nahm kontinuierlich Daten.

In dieser Arbeit berichten wir über die Performance des Rückstoßdetektors und im Speziellen über die des Detektors aus szintillierenden Fasern, der an der Justus-Liebig-Universität Gießen gebaut wurde. Diese Arbeit behandelt unter anderem die interne Ausrichtung, das mapping, den Lichtleitertest, die Datenqualitätsanalyse und das online Überwachungssystem. Die Effizienz des szintillierenden Faser Detektor wird in dieser Arbeit bestimmt. Eine erste Analyse der exklusiven ρ^0 aus den letzten Daten (07c2) wurde durchgeführt und die verbesserte Auswahl der exklusiven Ereignisse mit dem Rückstoßdetektor wurde demonstriert.

Abstract

The HERMES experiment (HERa MEasurement of Spin) at DESY was designed to study the spin structure of the nucleon in semi-inclusive deep inelastic scattering. The internal structure of the nucleon has been investigated in detail and it has been measured that the intrinsic quark spin contribution is only about 30% of the total spin of the nucleon. A formalism to describe the internal structure of the nucleon called Generalised Patron Distributions (GPDs) was developed recently to understand the fundamental structure of the nucleon. These GPDs can be accessed by the measurement of hard exclusive reactions and hard exclusive processes that can be understood in terms of GPDs. The accumulated HERMES data offer access to GPDs in different combinations of beam charge and beam and target helicity asymmetries.

To improve exclusivity and to enhance the resolution of kinematic variables to study hard exclusive processes which provide access to the GPDs and hence to the orbital angular momentum of the quarks, in January 2006 a Recoil Detector was installed that surrounded the internal gas target of the HERMES experiment.

The HERMES Recoil Detector consisted of three components: a silicon strip detector inside the vacuum, a scintillating fiber tracker and the photon detector. All three detectors were located inside a solenoidal magnet which provided a 1T longitudinal magnetic field. The Recoil Detector improves the selection of exclusive events by a direct measurement of the momentum and track position of the recoiling particle as well as by rejecting non-exclusive background. This detector was an ideal novel tool to combine energy and position measurements for charged particles in a momentum range of 0.1 to 1.4 GeV/c. The Recoil Detector was fully commissioned and operating. Data was taken continuously until the final HERA shutdown in July of 2007.

In this thesis we report on the performance of the Recoil Detector and more specificly about the scintillating fiber tracker which was built in the Justus-Liebig Universität Giessen. Alignment run, mapping, light guide test, gain monitoring system, pedestal stability, data quality, online monitoring and efficiency are reparted in this thesis for the scintillating fiber tracker (SFT). A preliminary analysis of exclusive ρ^0 of the latest data 07c2 was carried out to show the improvement of the selection of exclusive events with the Recoil Detector.

Contents

Chapter 1

Introduction

To understand and describe our universe and the nature of matter, people started a long time ago to think about the structure of material objects. Around 460 B.C., a Greek philosopher, Democritus, developed the idea of atoms. He asked this question: If you break a piece of matter in half, and then break it in half again, how many breaks will you have to make before you can break it no further? Democritus thought that it ended at some point, a smallest possible bit of matter. He called these basic matter particles, atoms. Unfortunately, the atomic ideas of Democritus had no lasting effects on other Greek philosophers, including Aristotle. For more than 2000 years nobody did anything to continue the explorations that the Greeks had started into the nature of matter.

Not until the early 1800's did people begin again to ask about the structure of matter. One of the first answers was the discovery of the structure of atoms, composed of electrons and a nucleus, which consists of protons and neutrons. The indication that the nucleons and other strongly interacting particle (hadrons), are not elementary structure lead us to formulate a more sophisticated theory. The first to refer to the elementary constituents of a hadrons as quarks was M. Gell-Mann [1] and, G. Zweig [2] in 1964.

Particle	Flavour			electric charge (Q/e)
Lepton	e	μ	τ	-1
	ν_e	ν_μ	ν_τ	0
quarks	u	c	t	$+\frac{2}{3}$
	d	s	b	$-\frac{1}{3}$

Table 1.1: The leptons form a family of elementary particles with three known flavours: electron, muon and tau. [3]

In the '70s, the *Standard Model*, a model to describe the particles and their interaction was developed. The fundamental constituents of the matter are six quarks and six leptons, together with their antiparticles (see Table 1.1). Four fundamental interactions, or fields govern the aspects of physics. The *electromagnetic* interaction, described by Quantum Electrodynamics (QED) theory, binds together atoms and molecules, governs the chemistry and solid state physics. A *photon* exchange mediates the electromagnetic interaction.

The *weak* interaction characterizes rare processes, as the nuclear β-decay. These interactions are mediated by the $W^{\pm}$ and Z^0 boson. The *strong* interaction, described by Quantum Chromodynamics (QCD) theory, is responsible for binding the quarks in particles. This force is mediated by the gluons (see Table 1.2). There is one force not included in the *Standard Model*: the *Gravitational* interaction. On the scale of the universe this is the dominant force, but is the weakest on the atomic scale. The *graviton* is the mediator of the gravitational force.

Interaction	Mediator	Spin/parity	Strength	Theory
Strong	gluon g	1^-	10	Chromodynamics
Electromagnetic	photon γ	1^-	10^{-2}	Electrodynamics
Weak	$W^{\pm}, Z^0$	$1^-,1^+$	10^{-13}	Flavourdynamics
Gravitational	graviton G	2^+	10^{-42}	Geometrodynamics

Table 1.2: The fundamental interactions [4].

Even though the standard model predictions are very well tested and verified, this model is probably not complete and many experiments are investigating its limitations. In 1987, the European Muon Collaboration (EMC) [5], investigated, the nucleon spin budget, naively taking a relativistic quark model where three quarks as partons of the nucleon carry the spin of the nucleon. These measurements from EMC and later E143 [6] indicated that the intrinsic contribution by the quarks are much lower than expected. The result significantly deviated from the prediction of Ellis-Jaffe sum rule [5]. Assuming $SU3$ symmetry, the EMC data imply that only 12% of the nucleon spin is carried by quarks. Later the E143 experiment measures this contribution to be $a_0^{inv} = 0.33 \pm 0.66$, and in the parton model interpretation the contribution of the individual quark is:$\Delta u = 0.84 \pm 0.02$, $\Delta d = -0.42 \pm 0.02$, and $\Delta s = -0.09 \pm 0.02$ [6]. Because of this surprising result often cited as "spin crisis", a new series of experiments was proposed which could test the validity of EMC measurement with increased accuracy, and to search for answers to thes question. To have a complete picture of the nucleon spin, also the spin contributions from the gluons and the orbital angular momentum of the partons in the nucleon should be taken into account according to the expression:

$$\frac{1}{2}\hbar = S_z = \frac{1}{2}\Delta\Sigma + \Delta G + \Delta L, \qquad (1.1)$$

where $\Delta\Sigma = \Delta u + \Delta d + \Delta s$ refers to the sum of the spin contributions from sea and valence quarks and ΔG is the gluon spin contribution and ΔL is the gluon and quarks orbital angular momentum. An experimental access to the orbital angular momentum is possibly through measurements of Generalized Parton Distributions (GPDs) [7, 8]. These describe correlation of tranverse spatial distributions, known from Form Factor (FFs) very precisely, and of longitudinal momentum distributions as described by Parton Distribution Functions (PDFs).

The HERMES (HERa MEasurement of Spin) experiment [9, 10] was designed to study the spin structure of the nucleon by measuring inclusive and semi-inclusive deep inelastic scattering processes [11]. A precise measurement of the spin polarised structure function g_1 has been obtained at HERMES [12, 13] and spin

asymmetries in different semi-inclusive processes have been measured, to be able to separate the spin contribution from the each quark flavour [14]. The neutron spin structure function g_1^n was extracted by combining proton and deuteron data. For the flavor-singlet axial charge a_0 HERMES obtaned im a leading-twist NNLO analysis a value of $0.330 \pm 0.011(theo.) \pm 0.025(exp.) \pm 0.028(evol.)$ [15].

In addition, a deeper understanding of the quark and gluon structure of the nucleon can be accessed through exclusive processes. One of the cleanest processes to approach GPDs, is Deeply Virtual Comptom Scattering (DVCS). Another exclusive process that is described by GPDs is the exclusive vector meson production, which is of special interest to this thesis. The exclusive, diffractive production of ρ^0 vector mesons from positron scattering reactions on hydrogen and deuteron has already been studied by HERMES before [16].

To improve the exclusivity in the HERMES measurement and increase the resolution of the kinematics variables, in January 2006 a Recoil Detector was installed that surrounded the internal gas target. The Hermes Recoil Detector was the lastest planned upgrade of the Hermes experiment. The Recoil detector consists of a Silicon Strip Detector, a Scintillating Fiber Tracker and the Photon Detector [17, 18].

In this thesis I report on the performance of the Recoil Detector and more specifically about the scintillating fiber tracker which was built at the Justus Liebig Universität Giessen. Alignment run, mapping, light guide test, gain monitoring system, pedestal stability, data quality, online monitoring and efficiency of the scintillating fiber tracker (SFT) are subject of this thesis. A preliminary analysis of exclusive ρ^0 production in the latest data $07c2$ was carried out to show the improvement of the selection of exclusive events and the benefit to the ρ^0 analysis due to the Recoil Detector.

2.1   The HERA Synchrotron

The HERA storage ring provided a polarized lepton and proton beam for the four experiment operating at DESY; H1, ZEUS, HERA-B and HERMES [19]. In the east hall of the storage ring, HERMES was a fixed target experiment using lepton beams which were either electrons or positrons at $27,6$GeV/c. The collider experiments H1 (north) and ZEUS (south) were investigating nucleon structure functions by means of deep inelastic scattering over a wide kinematic region. They were using the 820 to 920GeV/c proton beam in the opposite direction to the lepton beam, in collider mode. The goal of the HERA-B experiment was to study CP-violation in B-meson production in proton-nuclei collisions, see figure 2.1 for schematic view.
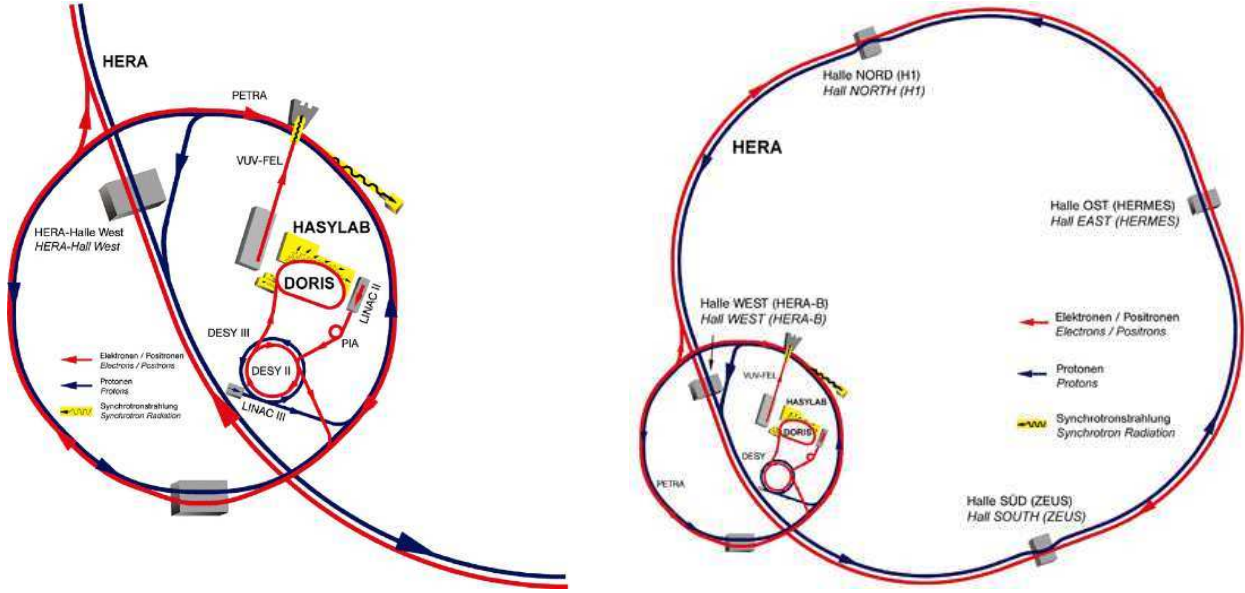
Figure 2.2: Schematic view of the HERA accelerator facility and its chain of pre-accelerators, indicated on the left half of the figure.

The $6336m$ circumference HERA storage ring consists of two concentric rings shown in figure 2.2. The HERA electron beam has a time structure of 189 bunches which have a length of $27ps$ and were separated by $96ns$ and ordered in three trains of bunches. The peak beam current at injection was up to $50mA$ which decays nearly exponentially. The average lifetime, which can be derived from the decay constant, was around $13hours$, shown in Fig 2.3.

HERA PROPERTIES

CIRCUMFERENCE	C_H	6335.83 m		
REVOLUTION FREQUENCY	f_0	47.317 kHz		
NUMBER OF BUCKETS	N_b	220		
NUMBER OF COLLIDING BUNCHES	N_{cbun}	174		
		HERA-e	**HERA-p**	
ENERGY	E_e	27.5 GeV	E_p	920 GeV
TOTAL CURRENT	I_e	50 mA	I_p	90 mA
NUMBER OF BUNCHES		189		180
SINGLE BUNCH CURRENT	I_{be}	211 μA	I_{bp}	500 μA
BUNCH POPULATION	N_e	$2.79 \cdot 10^{10}$	N_p	$6.59 \cdot 10^{10}$
BUNCH LENGTH (RMS)	σ_{ez}	10.3 mm	σ_{pz}	191 mm
BUNCH TIME LENGTH	$\sigma_{et} = \sigma_{ez}/c$	34.3 ps	$\sigma_{pt} = \sigma_{pz}/c$	637 ps
PEACK CURRENT	$\frac{N_e \cdot q}{\sqrt{2\pi} \cdot \sigma_t}$	52 A	$\frac{N_p \cdot q}{\sqrt{2\pi} \cdot \sigma_t}$	6.6 A

Table 2.1: Some properties of the HERA taken from Reference [20].
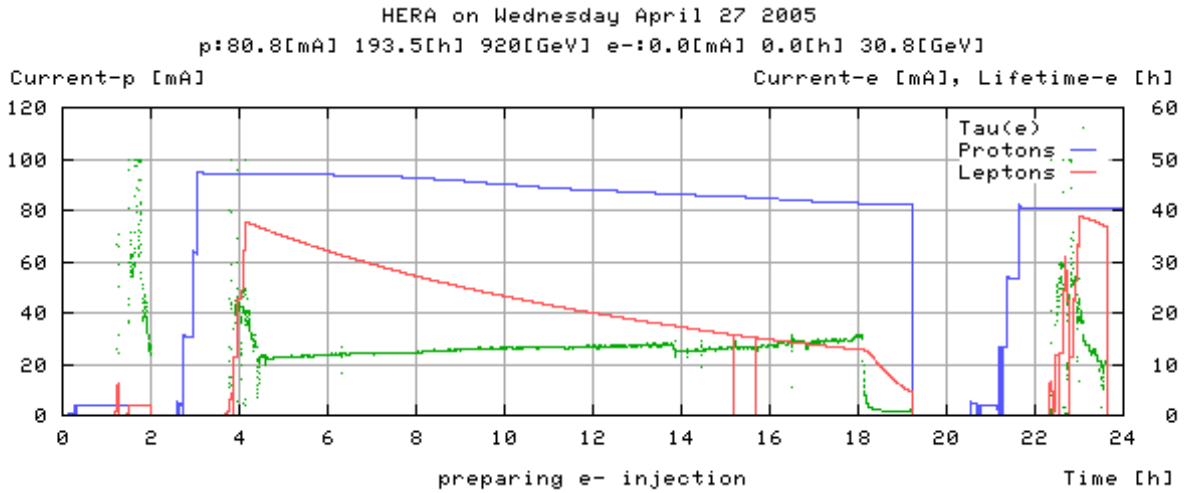
Figure 2.3: Typical beam history of the electron and proton beam in HERA. The upper curve (blue) corresponds to the proton beam current with the scale indicated on the left. The curve in the middle (red) is the electron beam current. The lower curve shows the electron beam life time, the scale for the latter two are depicted on the right. At ~18:00 the lifetime dropped from about 15 hours to 2 hours due to the injection of high density gas in the HERMES target cell.

In an high-energy flat storage ring, electron beams can become polarized antiparallel to the guide field by the emission of synchrotron radiation (SR), named due to the Sokolov-Ternov effect [21, 23].This is due to a small difference between the spin flip rates up-to-down and vice versa, shown in figure 2.4. Only a very small fraction of the synchrotron radiation power causes spin flip, so that the polarization process tends to be slow on the time scale of other dynamical phenomena of storage rings.

Figure 2.4: The HERA ring showing the positions of the spin rotators and the four experiments. HERA consists of two concentric storage rings. The green circle shows the proton ring while the blue circle show the lepton ring.

The effect accumulates over successive circulations of the electron beam and SR emission of electrons in arcs, and leads to a large overall polarization, see figure 2.5 for one fill. The polarization P is defined as:

$$P = \frac{N\downarrow - N\uparrow}{N\downarrow + N\uparrow}, \tag{2.1}$$

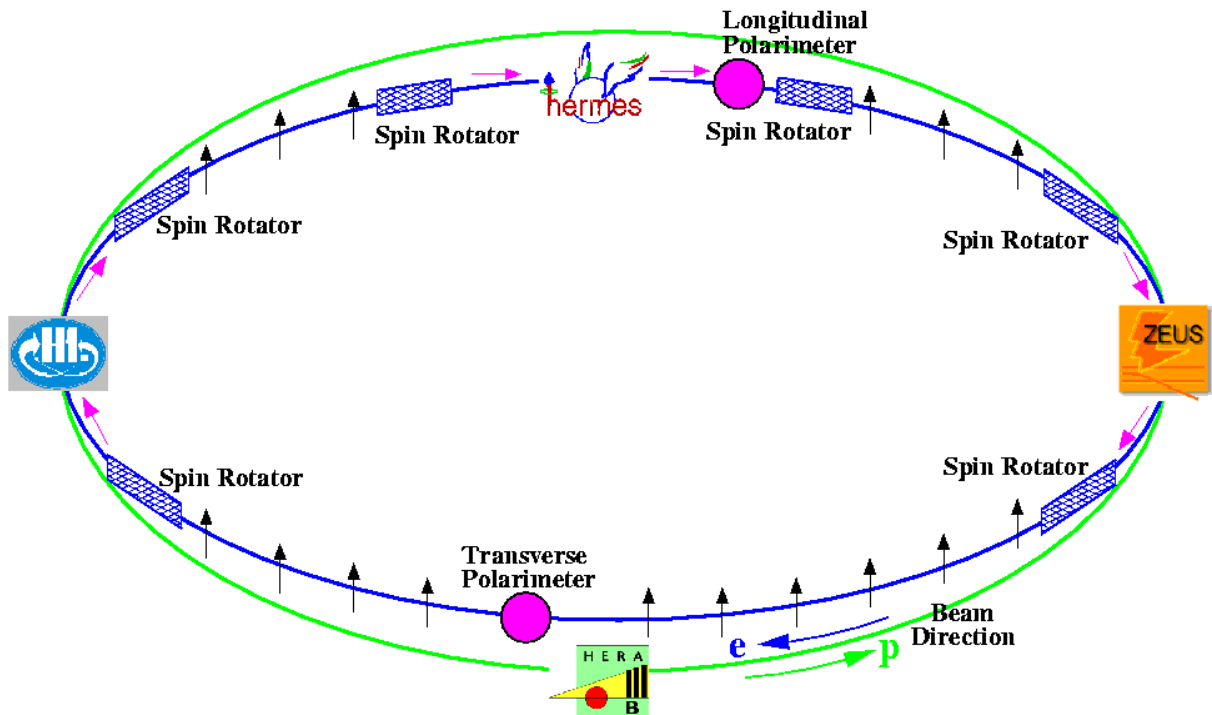where $N\downarrow$ ($N\uparrow$) denotes the number of leptons with their spins aligned parallel (antiparallel) to the vertical field supplied by the bending magnets. The rise in polarization shown in figure 2.5 has an exponential time dependence.
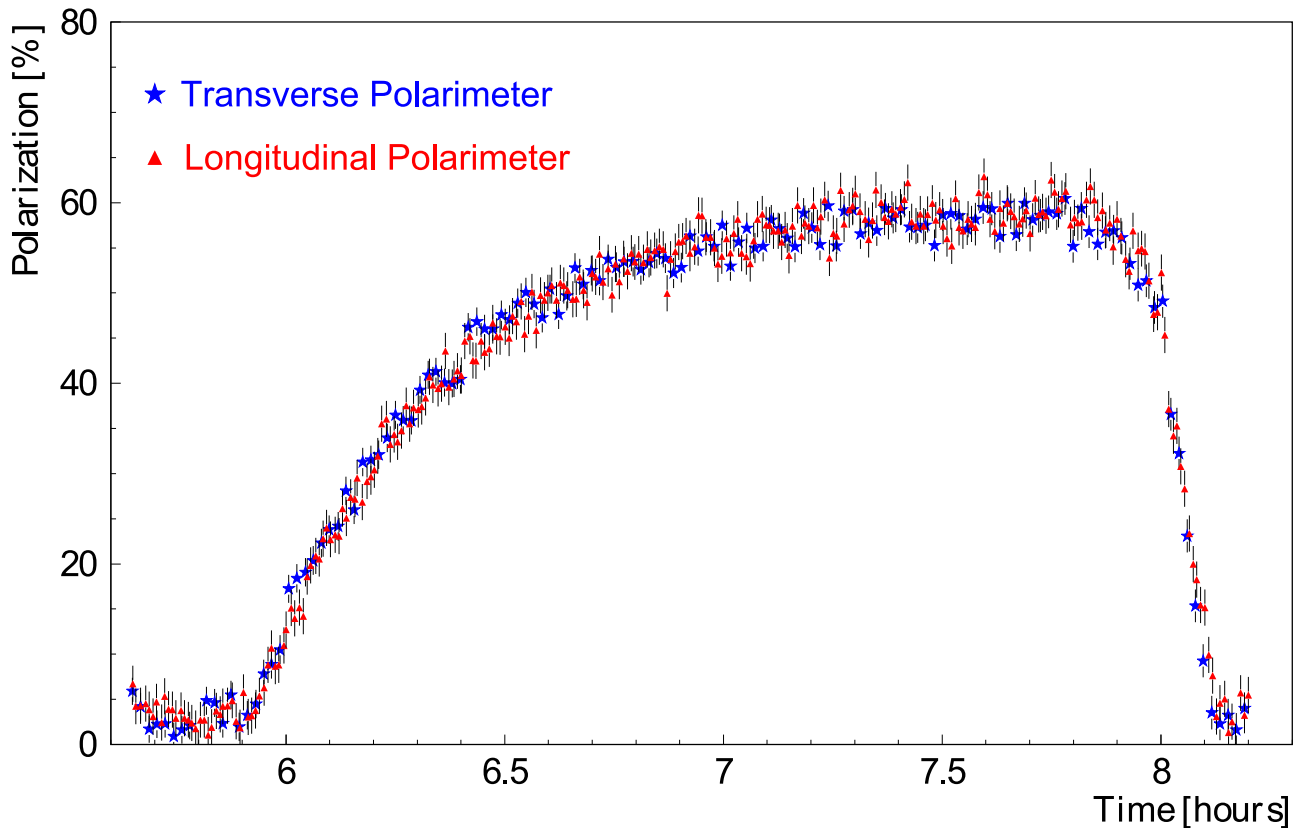
Figure 2.5: The HERA lepton beam self polarization due to an asymmetry in synchrotron radiation described by Sokolov-Ternov effect [23].

Under ideal conditions the polarization rise time at HERA was $\approx 40 minutes$ and the theoretical limit of the equilibrium polarization was 92.4% [23]. The magnetic field inhomogeneities give a rise to depolarization effects which impose a limit on the polarization values. The effective polarization rise time for HERA requires combined depolarization effects with the Sokolov-Ternov effect. In runs during 1992, utilizing special orbit corrections, polarization values close to 60% have been achieved.

In order to measure the polarization of the HERA beam, two polarimeters, using the Compton backscattering process, shown in figure 2.4 were installed, one for the transversal polarization [22] behind the HERA-B experiment in the West Hall and a second for the longitudinal polarization [24] after the HERMES experiment in the East Hall.

2.2 The HERMES Spectrometer

The HERMES experiment was used to study in a complete and precise way the spin structure of the nucleon. It has measured spin dependent deep inelastic scattering from the proton and neutron using the longitudinally polarized electron beam of HERA storage ring, and Hydrogen, Deuteron and Helium targets.
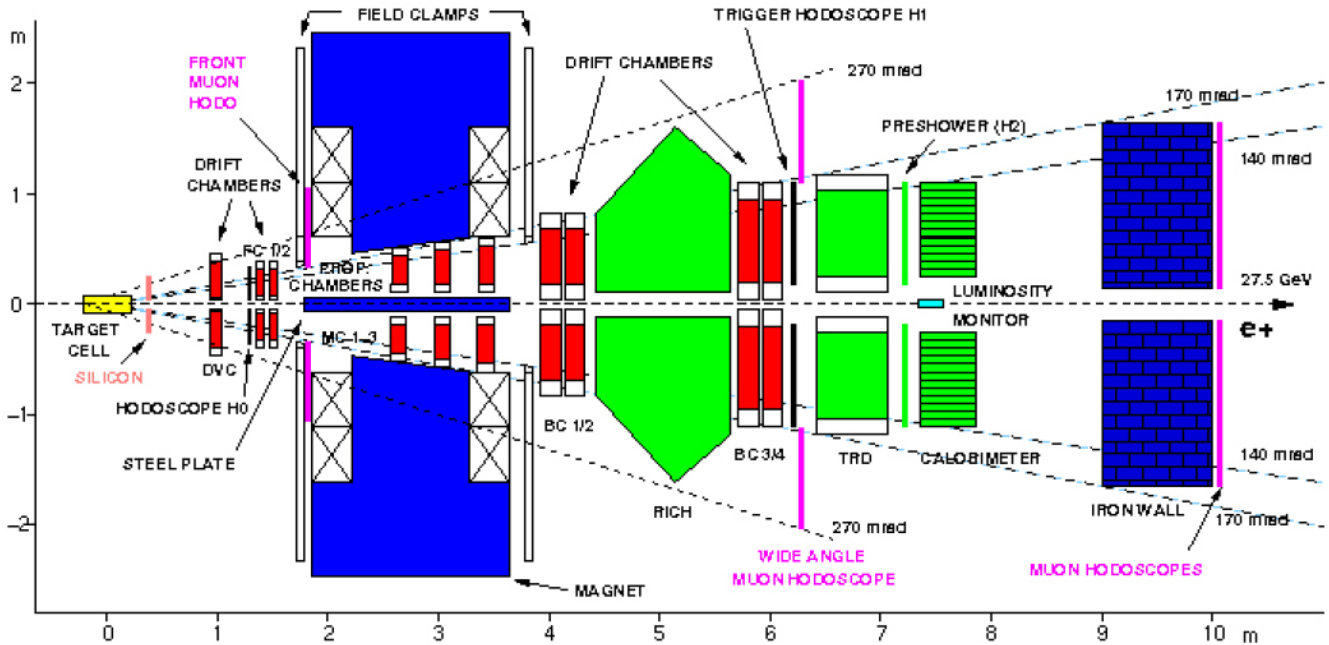
Figure 2.6: Schematic of the HERMES spectrometer. The PID detectors are shown in green, the tracking system are colored in red, the luminosity monitor is shown in light blue and the acceptance of the spectrometer is indicated by dashed lines

A schematic side view of the HERMES spectrometer is shown in figure 2.6. It was a forward angle spectrometer consisting of two identical parts, one above and one below the HERA lepton (and proton) beam line. Both beams were shielded against the HERMES spectrometer magnetic field, and passed through the central plane of the spectrometer separated by $72cm$ horizontally. The HERMES coordinate system uses lepton beam direction to define the z axis, the x axis is horizontal and pointing outside the HERA ring and the y axis vertically upwards.

The two half spectrometers consist of a set of tracking detectors; Drift-Vertex Chamber (DVC), drift Chamber or front chamber (FC) in the forward region of the magnet, proportional chambers (MC) in the magnet and other drift chambers or Back Chambers (BC) in the backward region of the magnet. The proportional chambers in the magnet help to match the track deflection due to the magnetic field of $1.3Tm$ integrated field strength.

The acceptance of scattering particle in the spectrometer was vertically from 40 to $140mrad$ and horizontally to $\pm 170mrad$ [25].

2.3   The HERMES Target system

The HERMES experiment was using an innovative technique for the polarized target, the internal gas target to the HERA storage ring. This technique permits background free measurement from highly polarized nucleons and the possibility to change the type of gas at any time.

The experiment was running with a polarized or unpolarized gas target. The lighter gases H_2, D_2 and ^3He were polarized and heavier gases ^4He, ^{14}N, ^{20}Ne, ^{84}Kr and common isotopes of Xe were unpolarized [26]. A low density target at 44% dosing valve opening with the Recoil detector up to $4.9 \cdot 10^{14} nucleons/cm^2$ was employed in order to avoid significant losses in the beam current.
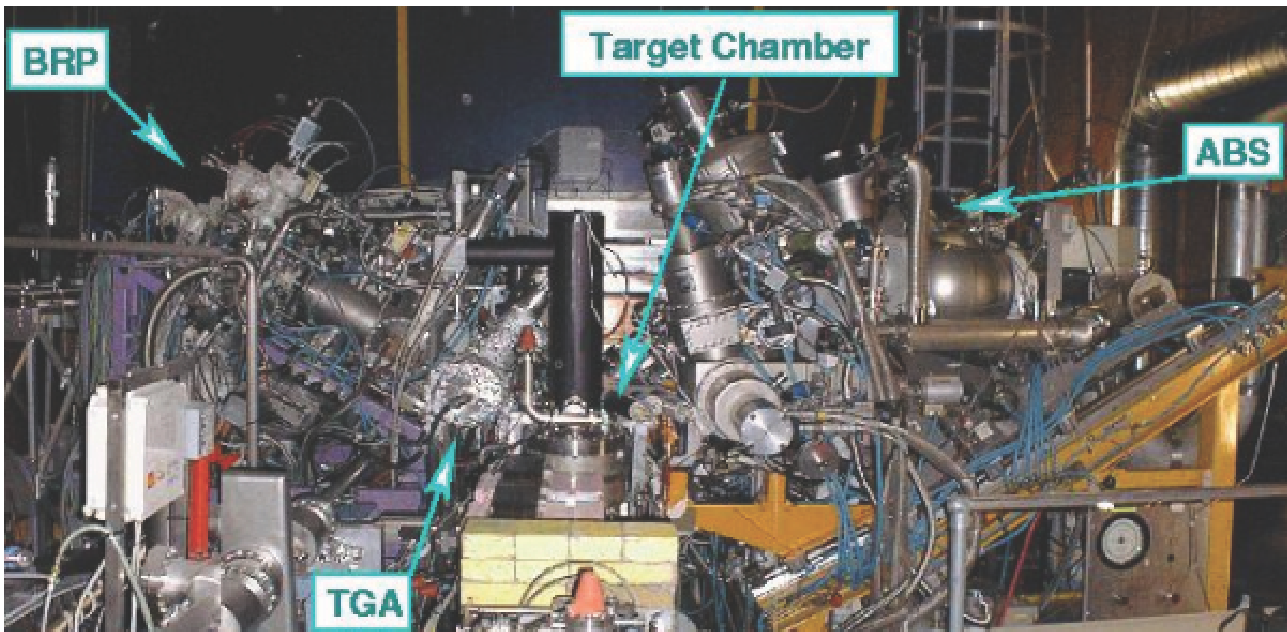
Figure 2.7: Equipment of the polarized gas target [27]. The target gas was dissociated and polarized in the ABS (Atomic Beam Source) [28] before entering into the storage cell. The TGA (Target Gas Analyzer)[29] and the BRP (Breit-Rabi-Polarimeter) [30] were used to analyze the cleanliness of the gas and measure the polarization.

For polarized operations, the atomic beam source (ABS) separates the spins of dissociated molecular H_2 with the Stern-Gerlach method and injects the resulting polarized states into the beam vacuum [28] of the target cell with a pressure of about $10^{-7} mbar$. The target storage cell was an elliptical form, made of ultra-pure aluminum with a uniform thickness of $75 \mu m$ at a length of $40 cm$. The mix of atomic versus molecular states remaining in the target was monitored by the target gas analyzer (TGA), and the polarization measured by the Breit-Rabi polarimeter (BRP). A strong uniform magnetic field is provided over the target region by the target magnet to prevent beam-induced depolarization and keep spin orientation [31].

As the space in the target area was limited (see picture 2.7), for expanding significantly the physics program, the HERMES Collaboration chose to remove the apparatus of polarized gas target and installed the HERMES recoil detector. The recoil detector was taking data from the two last year of HERA running $2006 - 2007$.

2.4 Tracking detectors

The main task of the tracking system is to measure a full component of the track momentum for any registered particle and reconstruct the track information. The HERMES tracking detectors can be split into three regions along the beam line: the front, the magnet and the backward region, defined in respect to the spectrometer magnet.
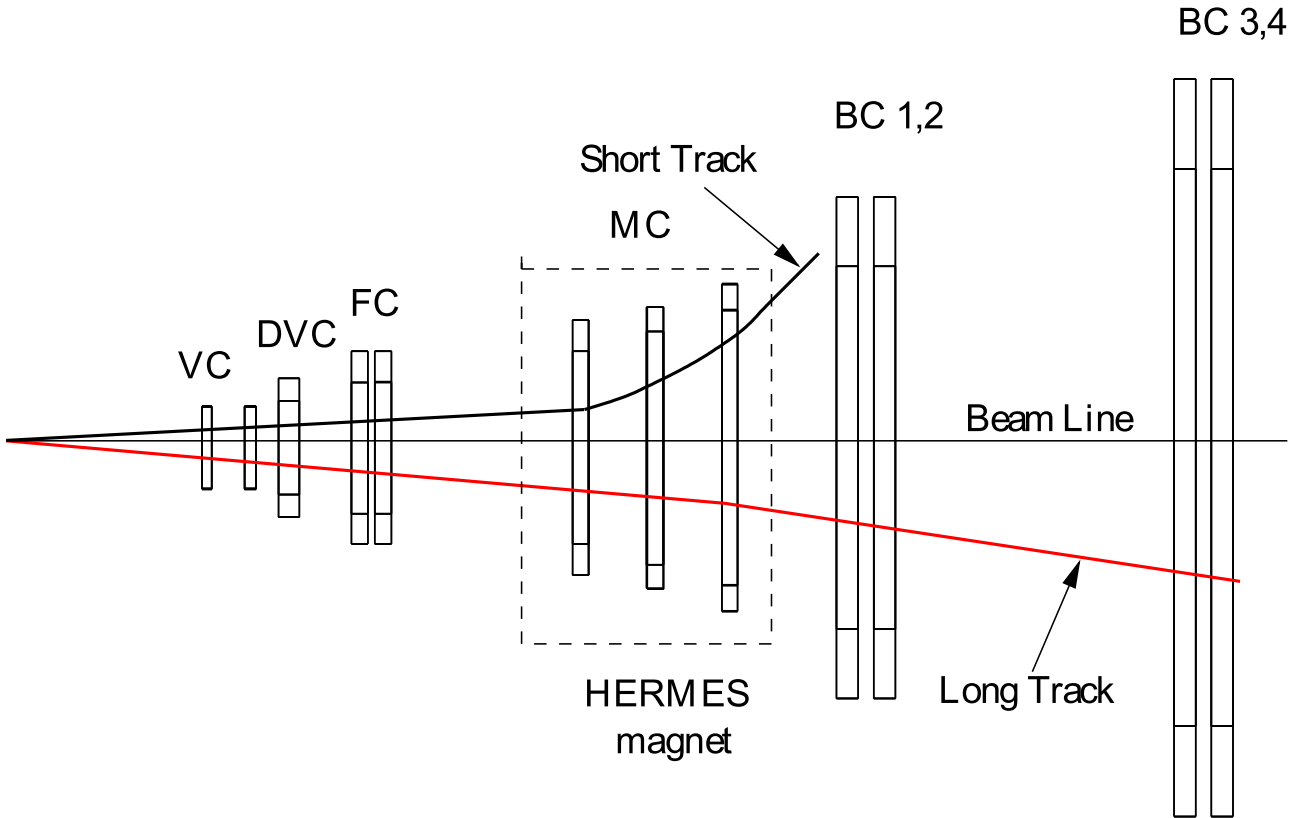
Figure 2.8: Schematic of HERMES spectrometer tracking system (top view). One long track crossing all the tracking chambers and one short track going out of the tracking system before BC1, deflected by the HERMES magnet out of the acceptance.

The front region contains the Vertex Chamber (VC), Drift Vertex Chamber (DVC) and the front Chambers (FC), and the magnet region contains the Magnet Chambers (MC) and the backward region contains the Back Chambers (BC), shown in figure 2.8. All tracking detectors were wire chambers, Multi-Wire Proportional Chambers (MWPCs) or Drift Chambers (DC). Each wire chamber module consists of several planes oriented in three directions: vertical and tilted $\pm 30^{o}$. All of these relied on the principle of charge ionization and amplification in a gas [32].

2.4.1 Vertex Chambers (VC)

The Vertex Chambers contained six micro strip gas chamber (MSGC) planes, grouped into two 'modules' VC1 and VC2. They was proposed to provide high-precision measurements of the scattering angle and the vertex position over the full acceptance of the experiment [25].
In 1998 the damaged Vertex Chambers were removed and in 2000 the Lambda Wheels was install in order to increase the acceptance for long-living particles which decay just outside of the target region [33, 34].

2.4.2   Drift Vertex Chambers (DVCs)

The Drift Vertex Chambers were installed in 1996. They helped to increase the redundancy of the tracking system in the front region, mainly to increase the efficiency for the detection of events from charmed particle decay. The 6 planes configuration XX',UU' and VV' with 1088 wires and a spacing of $6mm$ was giving a spacial resolution of $200\mu m$ per plane. The DVC acceptance extends vertically from $\pm35mrad$ to $\pm270mrad$, and covers $\pm200mrad$ horizontally.

2.4.3   Drift Chambers (FC and BC)

The drift chambers FC1/2 [35], BC1/2 and BC3/4 [36, 37] are of the conventional horizontal-drift type. Each layer of drift cells consists of a plane of alternating anode and cathode wires between a pair of cathode foils. The cathode wires and the foils are at negative high voltage with the anode wires at ground potential. The chambers are assembled as modules consisting of six such drift cell layer in three coordinate doublets (UU',XX' and VV'). The wires are vertical for X planes and at an angle of $\pm30^0$ to the vertical for the U and V plans, shown in Fig. 2.9 for the back drift chambers [25].
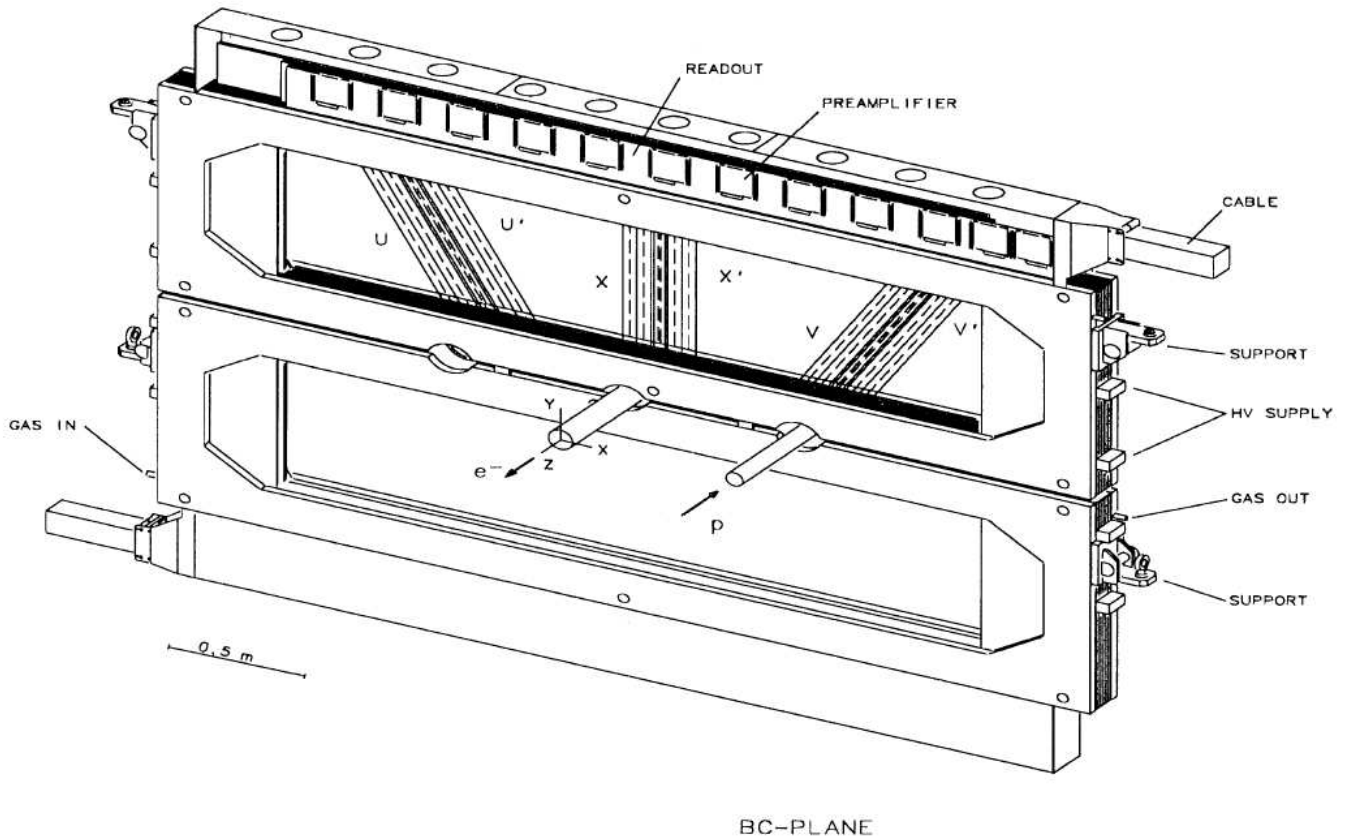
Figure 2.9: Schematic view of the large BC module

2.4.4   Multi-Wire Proportional Chambers (MWPCs)

In the Magnet Chambers (MC) were three sets of Multi-Wire Proportional Chambers installed in the gap of the spectrometer magnet, shown in Fig. 2.10. They were originally intended to help resolve multiple tracks in the event reconstruction in case of missing planes in the front region. Since low backgrounds have made unnecessary, their primary function was to determine the momentum of low energy particles that did not enter the back drift chamber after the spectrometer magnet.
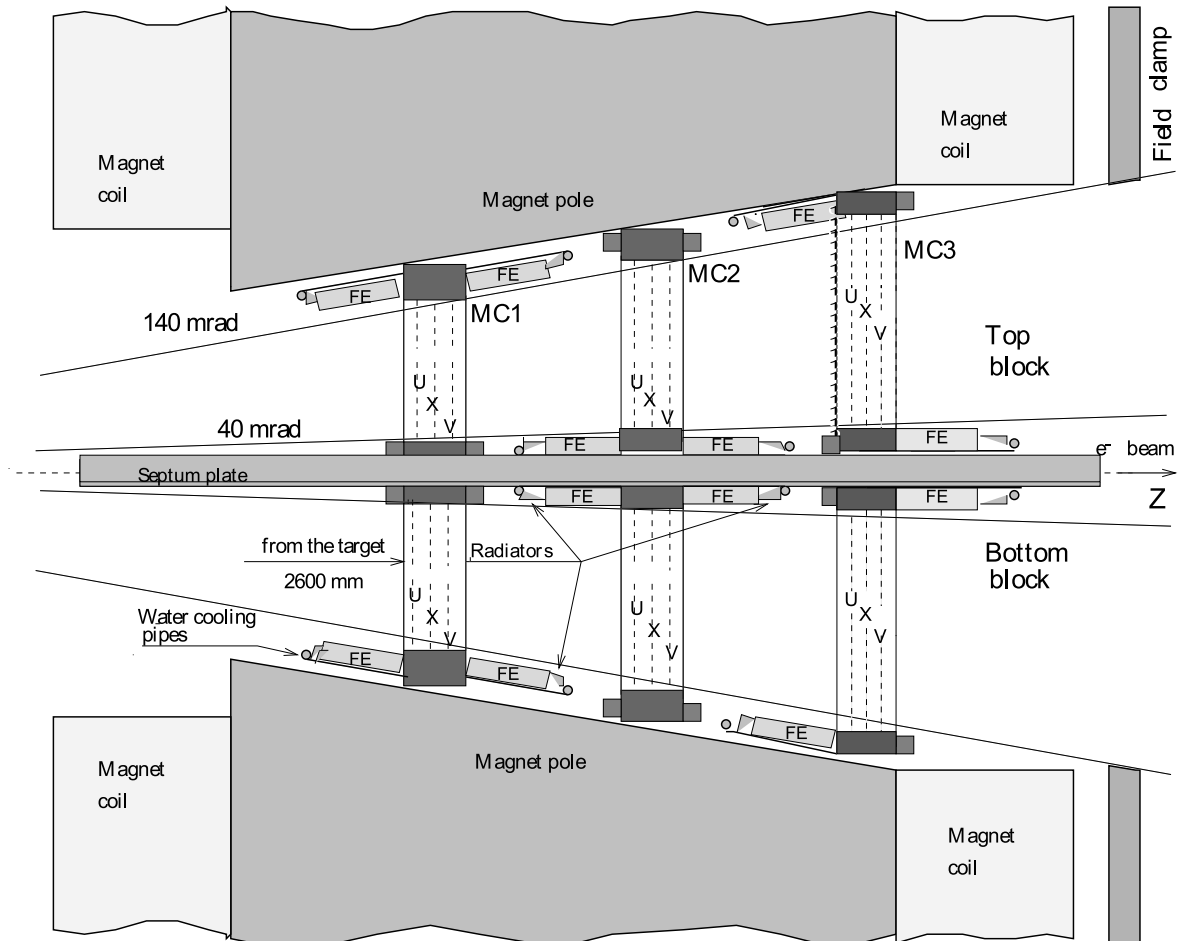
Figure 2.10: Side view of the MC set up inside the magnet. FE indicates front-end readout electronics location

The capability of allowing the reconstruction of short tracks makes the Magnet Chambers system of special importance in the study of semi-inclusive channels where low momentum particles are involved [38].

2.5   Alignment

The precise alignment of tracking detectors was important to obtain a good momentum resolution in an experiment with a magnetic spectrometer like HERMES. The detector needed to be aligned with a precision better than the intrinsic resolution of the detectors. The initial alignment during the detector installation was done using conventional optical techniques. The motion of the detectors due to temperature changes was not negligible compared with the detector resolution. Therefore, it was important to monitor continuously the relative position of the detectors before and after the switching on (off) of the spectrometer magnet.

For this purpose, a system was developed using a laser and Fresnel zone plates to align the detectors in two directions perpendicular to the beam axis. The $2cm$ laser beam was created by one He-Ne laser and a semi-transparent mirror. A Fresnel zone plate is shown in Fig 2.11(a). A typical pattern image is shown in Fig 2.11(b). The laser alignment system was used at HERMES since 1995, the measurement was performed about every $30min$ during the experiment. The relative position of the detectors were monitored with a precision of better than $\pm60\mu m$ (1σ) [39].

<div align="center">(a)</div>

<div align="center">(b)</div>
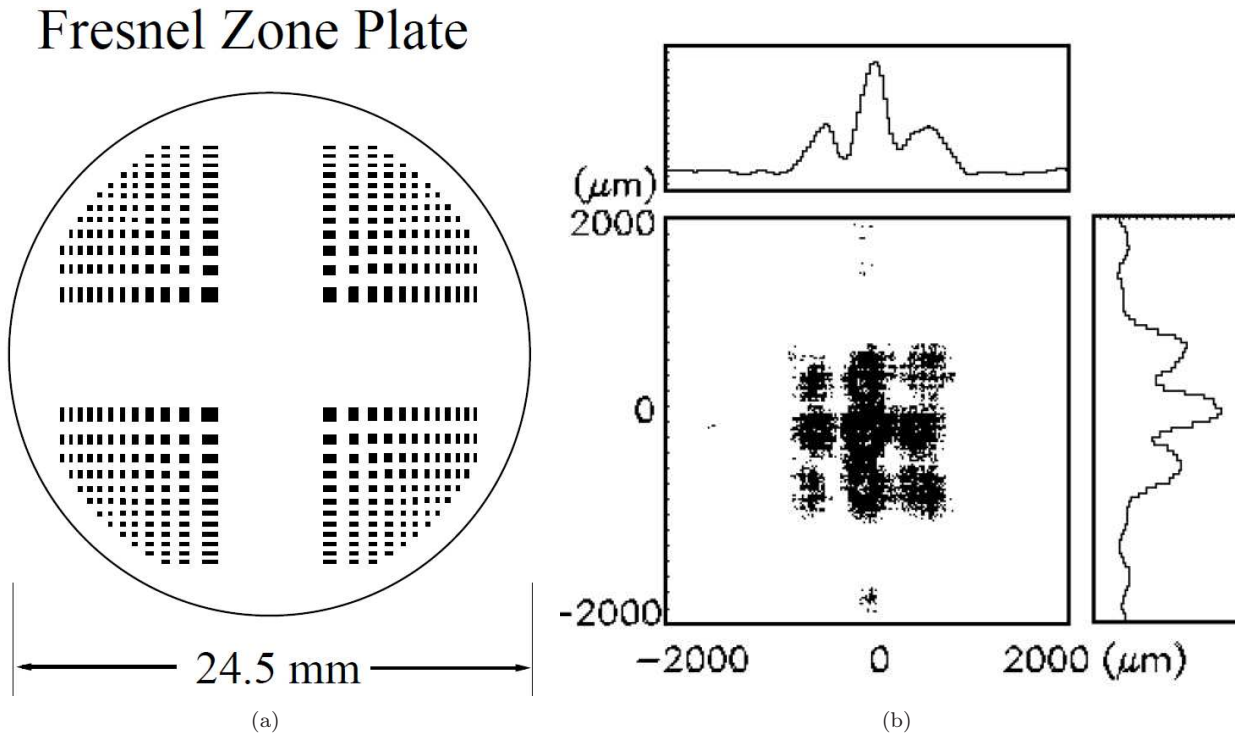
Figure 2.11: The block diagram of the control system of the moving mechanism of the Fresnel zone plates made of $13\mu m$ thick stainless steel with a diameter of $24.5mm$ (a). The two-dimensional Fresnel pattern image of BC1, and its projection to the horizontal and vertical axes (b)

After correction of the internal misalignments of the spectrometer, studies about the effects of the external misalignments of the spectrometer have been realized to estimate the influence in the asymmetry measurement. Some misalignment was introduced into Monte Carlo. The misalignment effects of the spectrometer and the beam on the extracted asymmetry amplitudes were really small [40].

2.6 Track Reconstruction

The main task of the reconstruction program was to identify particle tracks using the hits in the tracking detectors. The HERMES reconstruction program (HRC) [41] was made of two methods: the tree-search algorithm for fast track finding and a look-up table for fast momentum determination.

2.6.1 Treesearch and Track Finding

Treesearch is a pattern recognition algorithm that identifies straight lines in a picture. The algorithm was based on the use of a pattern database that contains all possible particle tracks for a given detector system and resolution.
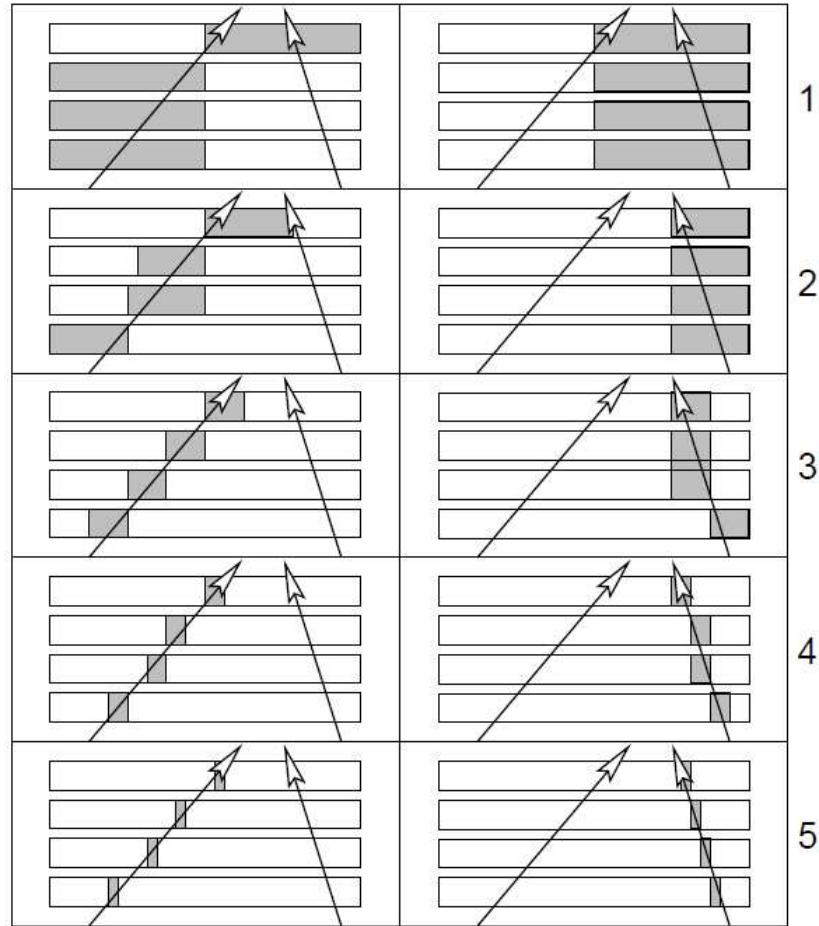
(a)
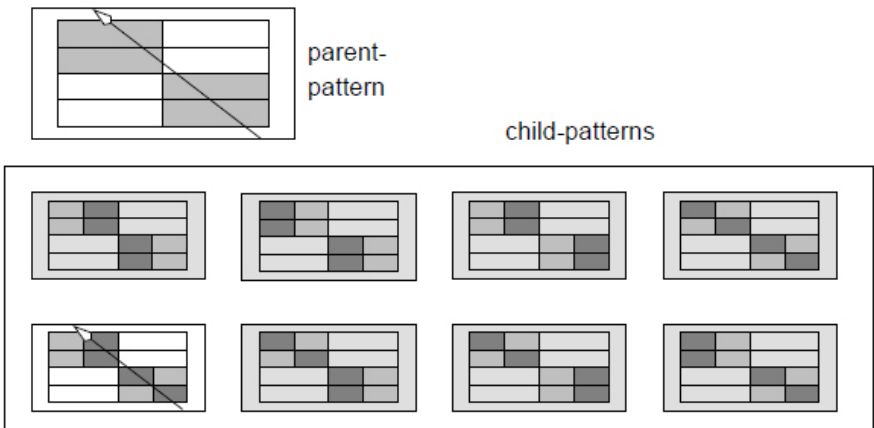
(b)

Figure 2.12: Treesearch for two tracks. The detector pattern was matched against the pattern database with increasing resolution. The algorithm looks at the hits of the tracking detectors. In every treeseach level the resolution was doubled until a resolution was reached that was optimal for track finding.

The basic idea of pattern recognition using the treesearch algorithm was to look at the whole hit pattern of the detectors as illustrated in Fig. 2.12(a). For each detected pattern of a given resolution, also referred to as a parent pattern, only a limited number of child patterns (at double resolution) exist that fit into the former Fig. 2.12(b). The track search algorithm is highly recursive. However, after about 14 iterations of the binary treesearch, the resolution of the detector was reached. The detector resolution was approximately 250 μm. This procedure was applied independently to the front and back regions, all combinations of front and back partial tracks were tested to see if they matched spacially. Those combinations that matched were combined to form a full track.

2.7 Particle identification detectors

A clean identification of the scattered positron is crucial for inclusive measurements in all DIS experiments due to the large hadronic backgrounds. Furthermore for semi-inclusive studies the discrimination between different species of hadrons is important. The HERMES Particle Identification Detectors (PID) system provides an excellent hadron-lepton separation with a hadron rejection factor estimated to be over 100 for 99% $e^{\pm}$ efficiency [25]. The PID system consists of several subsystems, the relevant one for ρ^0 analysis was the electromagnetic calorimeter, the Ring-Imaging Čerenkov, transition radiation detector (TRD) and the preshower supplied by the H_2 hodoscope.
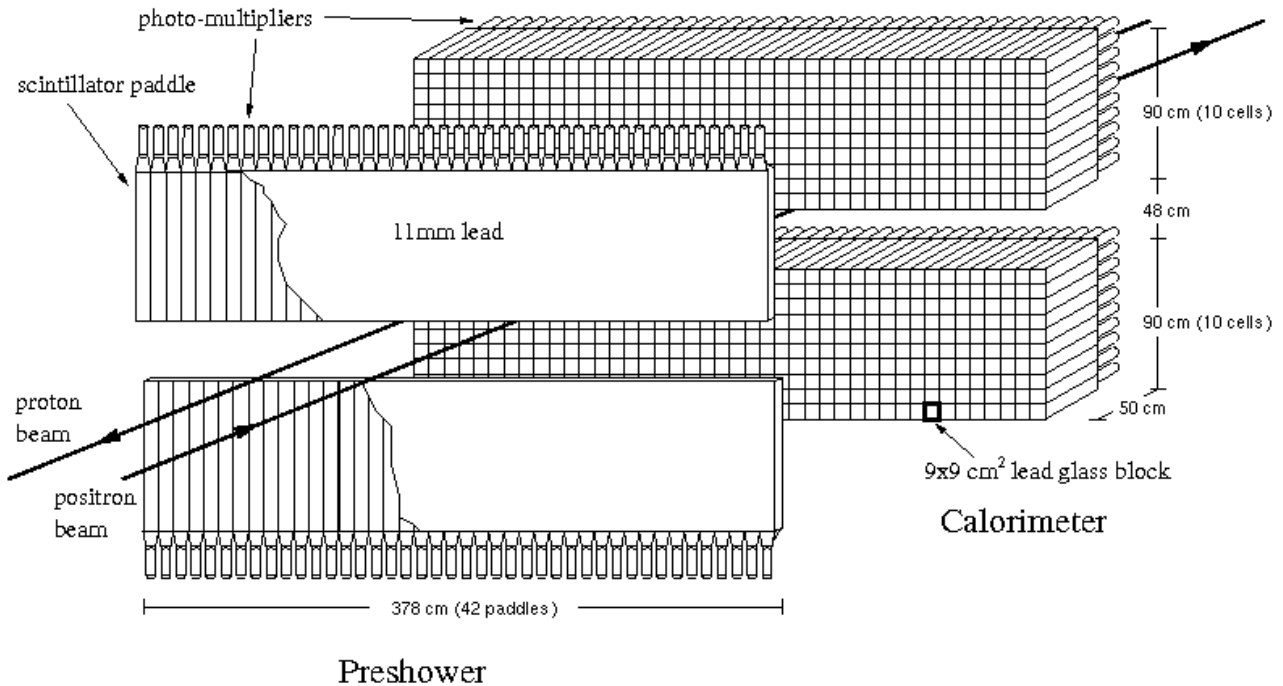

Figure 2.13: Schematic drawing of the Electromagnetic Calorimeter and Preshower Detector

2.7.1   Electromagnetic Calorimeter and Preshower Detector

Electromagnetic showers are created by the interactions of high energy electrons, positrons or photons with matter. For energies above $100MeV$ the dominating processes are bremsstrahlung for electrons/positrons and pair production for photons. These processes successively produce a cascade of particles until finally the low energy secondary particles lose their energy primarily by ionization [42].

The function of the electromagnetic calorimeter and the preshower detector was to provide a first level trigger for scattered beam leptons and to provide particle identification for the off-line analysis [43].

The preshower detector was a scintillating hodoscope with a $11mm$ thick cover of lead in front. The hodoscope (H_2) consist of 42 plastic scintillator paddles which are a size of $9.3{\times}91{\times}1cm^3$. To avoid acceptance gaps adjacent paddles overlap by $1.5mm$. The paddles were read out by photomultipliers at the top or bottom end. The calorimeter consists of 840 radiation-hard lead glass blocks, arranged in two $42{\times}10$ arrays, both above and below the beam line. Blocks measured $9{\times}9{\times}50cm^3$, with approximately 18 radiation lengths to ensures that the shower was almost completely contained in the calorimeter. A schematic diagram is shown in Fig 2.13.
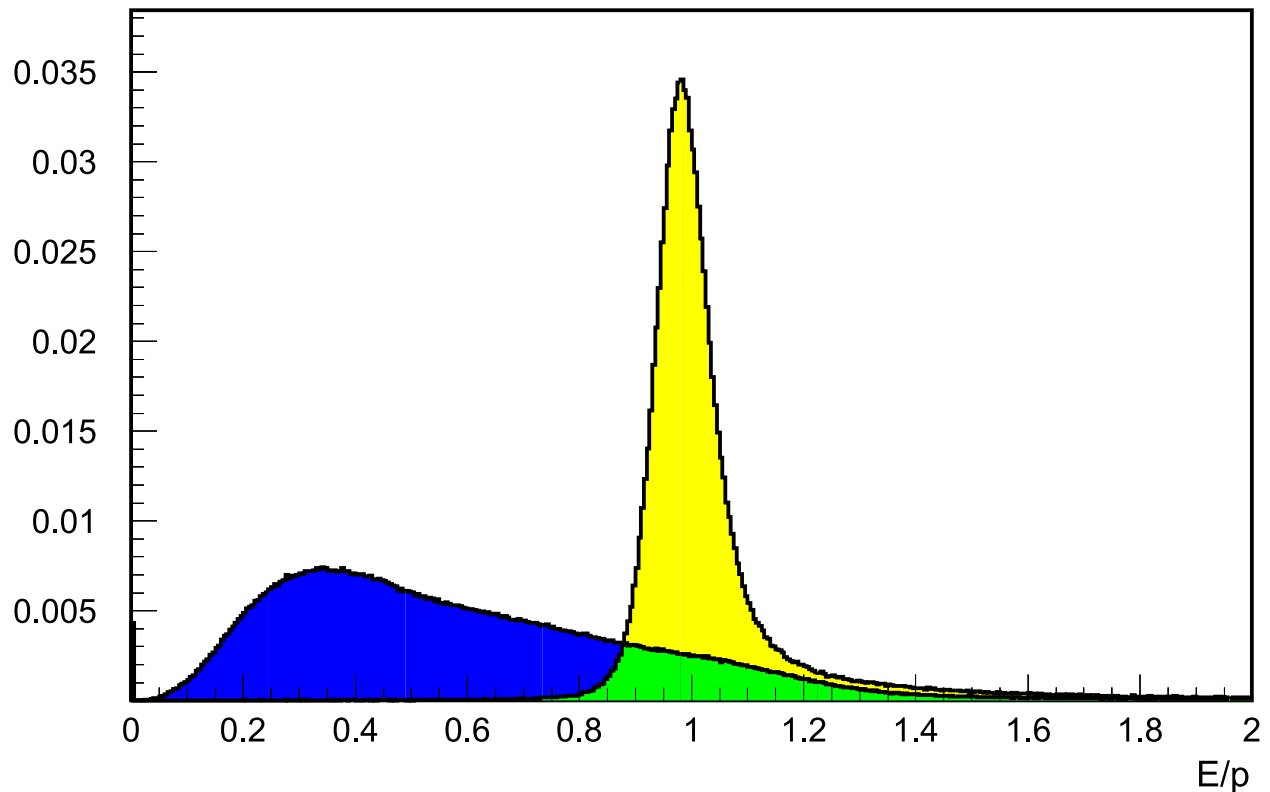
Figure 2.14: Energy response of the Calorimeter, normalized distribution of E_{cal}/p from HERMES data for hadrons in dark blue and electrons or positrons in yellow integrated over all momenta.

Based on energy deposition, as electromagnetic showers of electrons or positrons passed through the detector they radiated Čerenkov light. Since the electrons or positrons lose almost all of their energy and hadrons lose only a small fraction of their energy, the total deposited energy E_{calo} measured by the calorimeter was close to the momentum P of the lepton measured with the spectrometer. The ratio of $E_{calo}/p{\simeq}1$, see Fig. 2.14

2.7.2   Ring-Imaging Čerenkov Detector (RICH)

Čerenkov radiation is emitted by a charged particle when it enters a medium with a velocity higher than the velocity of light $\frac{c}{n}$ in that medium. The light is emitted as a cone with its characteristic opening angle θ_c given by:

$$cos\theta_c = \frac{1}{\beta n} \qquad\qquad (2.2)$$

where n is the refractive index of the material and $\beta = \frac{v}{c}$ is the ratio of the velocity v of the particle and the speed of light in vacuum c.

Hence no light is emitted if the particle velocity is less than a threshold velocity of

$$\beta_t = \frac{1}{n} \qquad\qquad (2.3)$$
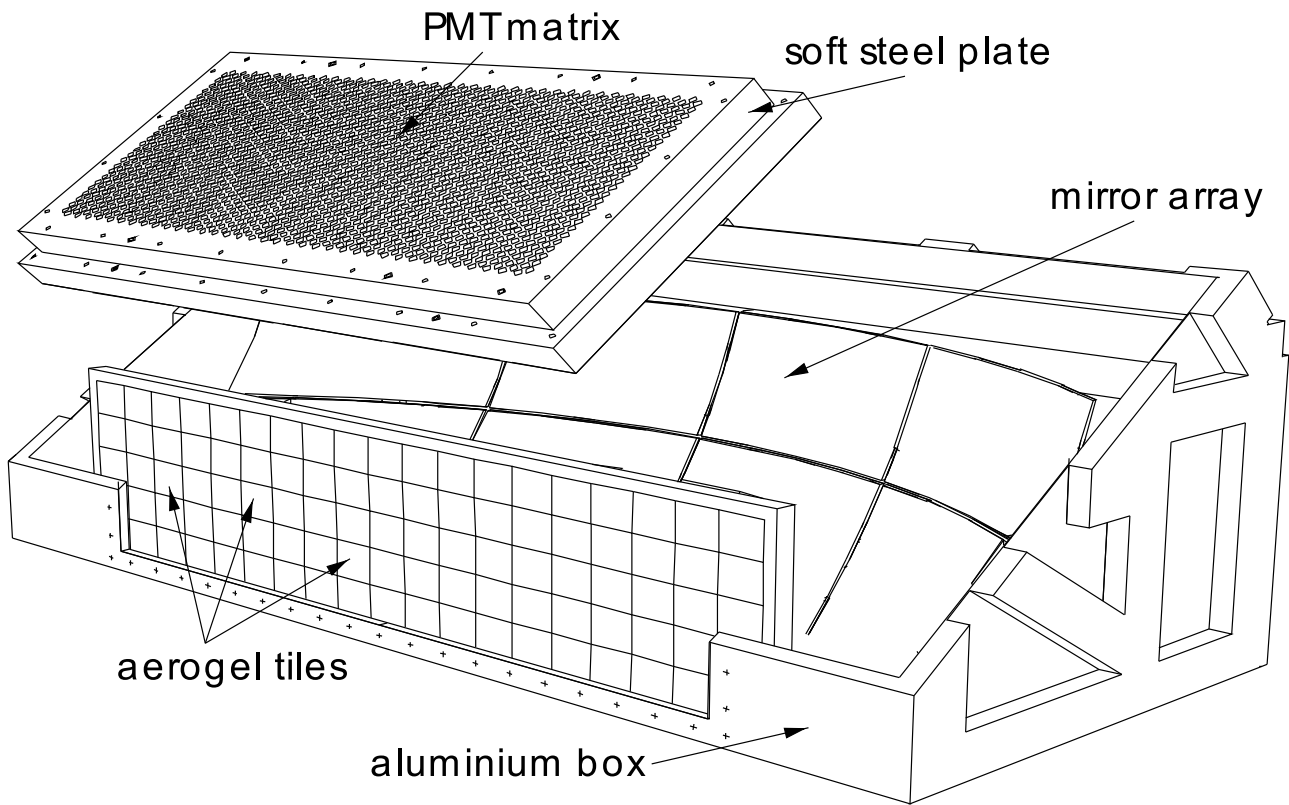
Figure 2.15: A perspective view of the upper half of the RICH detector schematically drawn.

About 95% of all hadrons detected in the HERMES experiment were found in the range of $1.0 - 15.0 GeV$. This defined which momentum range a clear PID should provide. To provide hadron identification over this full kinematic range, especially the low momentum region of the HERMES experiment, the gas threshold Čerenkov counters were replaced by the dual-radiator ring-imaging Čerenkov detectors incorporating for the first time aerogel (SiO_2) and C_4F_{10} gas as radiator materials [44].

The Geometry which was adopted for the Čerenkov radiators and ring imaging system consists of two symmetric RICH modules, which were positioned between the two rear tracking chamber BC1/2 and BC3/4. The schema of the upper half is shown in Fig. 2.15.

CHARACTERISTIC

		AEROGEL	C_4F_{10}
	n	1.0304	1.00137
	$\beta_t\gamma_t$	4.03	19.10
THRESHOLD MOMENTUM	π	0.6 GeV/c	2.7 GeV/c
	K	2.0 GeV/c	9.4 GeV/c
	p	3.8 GeV/c	17.9 GeV/c

Table 2.2: The Čerenkov light threshold for pions, kaons and protons. The index of refraction n is given at $633nm$, $\beta = 1/n$ is the threshold velocity and $\gamma_t = 1/\sqrt{1 - \beta_t^2}$ [45, 46]

The low momentum range determines the index of refraction necessary for the aerogel. A value of $n(\lambda = 633nm) = 1.03$ was chosen since it leads to a kaon threshold of $2GeV$. The Čerenkov angles produced by the combination of this aerogel and heavy gas (C_4F_{10}) for pions, kaons and protons are plotted as a function of particle momentum. The theoretical calculation are included with the real data in Fig. 2.16. The corresponding threshold momenta are listed in Table 2.2 [47, 48].
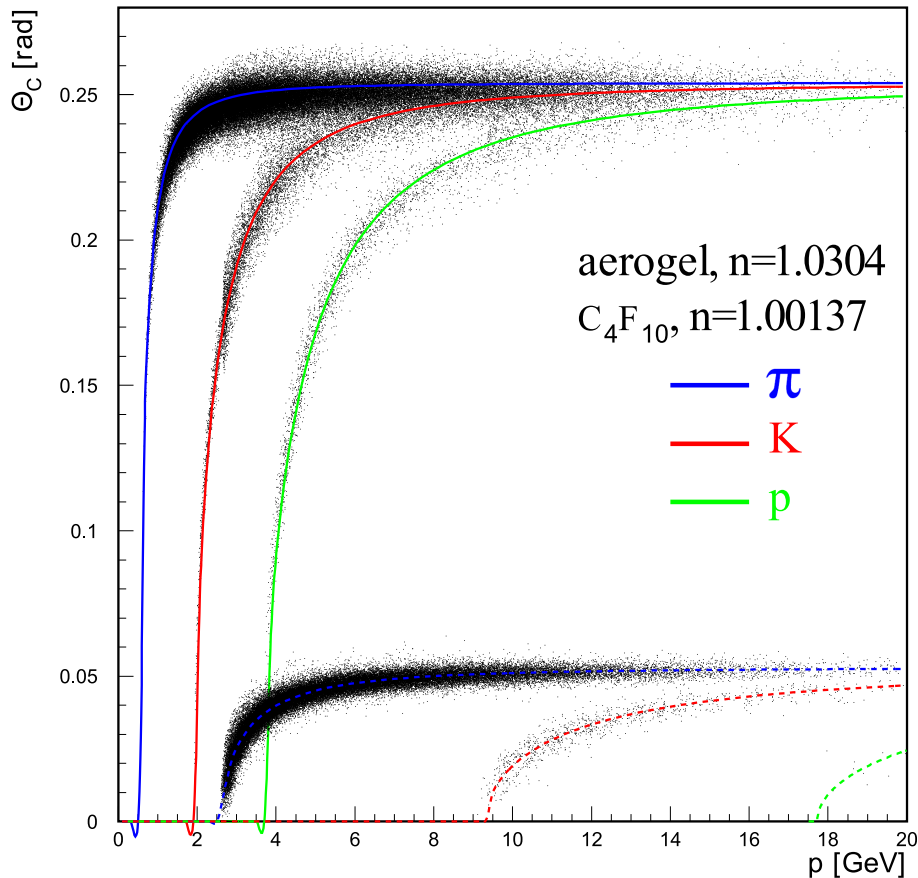
Figure 2.16: The angle of the Čerenkov cone versus the momentum for the major particle types are shown. The theoretical calculation are included with the real data [49].

The detected 'rings' were in fact not circular, but rather distorted ellipses, as the photon detector was not exactly in the mirror's focal plan. The aerogel rings were rather difficult to detect, since only a few photons were produced in the aerogel layer. It is clear that the RICH was a powerful PID instrument, though the reconstruction was not that simple. More information about the RICH PID can be found in Ref. [50, 51, 52, 53, 54, 55].

2.7.3   Transition Radiation Detector (TRD)

Transition radiation is emitted when charged particles with highly relativistic energies cross the boundary between two media with different dielectric constants. This can be explained by the required continuity of the Coulomb fields at the boundary. This gives rise to an additional field observed as the transition radiation. The total energy of the emitted radiation for a transition between a medium and vacuum,

$$E = \frac{2}{3} \, \alpha_{em} \, \omega_p \, \gamma \tag{2.4}$$

where $\alpha_{em} = 1/137$ is the electromagnetic fine structure constant, $\gamma = (1/\sqrt{1-\beta^2})$ is the Lorentz factor and ω_p is the plasma frequency of the medium [56].

The transition radiation is emitted in a cone around the particle trajectory with an opening angle of $\theta = 1/\gamma$. As the Lorentz factor γ for the hadrons are much lower due to the larger mass than for the leptons this allows a hadron lepton separation by energy deposition.
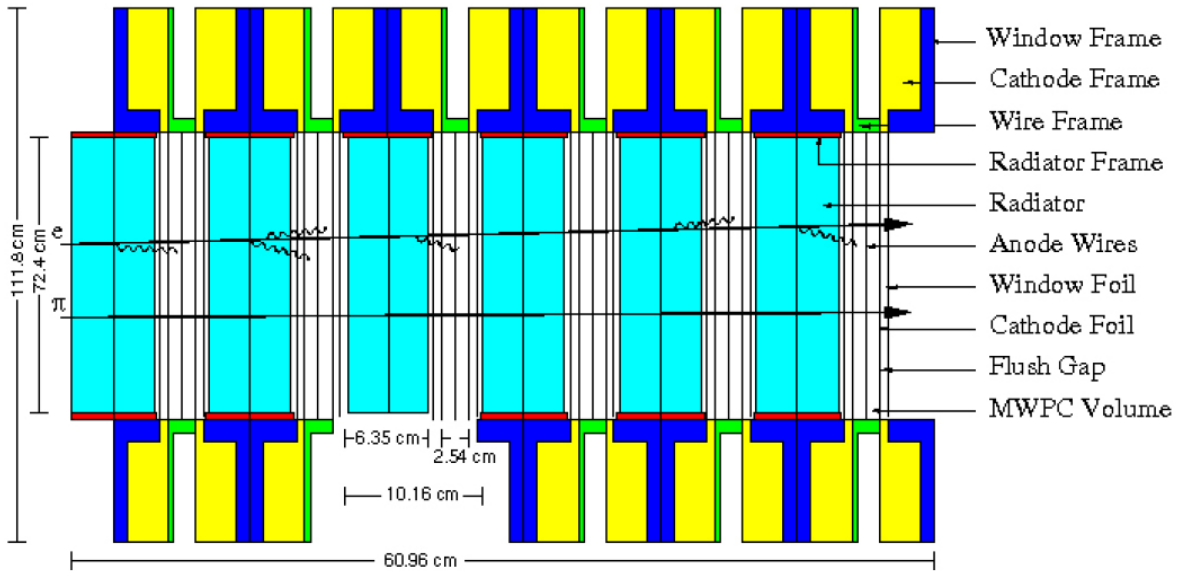
Figure 2.17: Schematic of the 6 modules of the HERMES TRD. Each module is made up out of a radiator and the proportional chamber. The upper half of the TRD setup is illustrated with a lepton and pion trajectory.

In order to obtain a sufficiently large lepton-hadron separation, the installation of a detector with a pion rejection factor of about 100 was required. Because of the limited available space the technique of transition radiation was chosen.

As the probability for the emission of transition radiation is small for a single boundary the HERMES TRD consists of a sequence of 6 modules each with a active area of $72.4 \times 325 cm^2$. Each of these consists of a fibre radiator and adjacent proportional wire chamber. The radiators were a two-dimensional matrix of fibers of $17 - 20 \mu m$ diameter in a material with a density of $0.059 g/cm^3$. They were $6.35 cm$ thick, which corresponds to an average of 267 dielectric layers. The proportional wire chamber was built out of 256 vertical wires of $75 \mu m$ gold coated $Be - Cu$ separated by $1.27 cm$. Both hadron and lepton produce a signal in the wire chambers due to ionization of the gas mixture of 90% X_e and 10% CH_4. The mixture was optimized to have energy deposited by the lepton approximately twice as large as the energy deposited by hadrons. The TRD is schematically drawn in Fig. 2.17 [57].

2.7.4 PID system performance

The lepton-hadron separation of the separate detectors was improved by combining the responses of the transition radiation detector, the Čerenkov detector, the preshower hodoscope and the electromagnetic calorimeter. Using the probability P^i determined from the measurement responses in each detector for a given particle i. The logarithm of the ratio of the probabilities P^l for leptons and P^h hadrons was calculated for each detector,

$$PID \ = \ log_{10} \frac{P^l}{P^h} \tag{2.5}$$

The following sums of the particle identification detectors were defined:

$$PID_3 \ = \ PID_{Calorimeter} \ + \ PID_{Preshower} \ + \ PID_{\check{C}erenkov} \tag{2.6}$$

$$PID_5 \ = \ PID_{Transition \ Radiation \ Detector} \tag{2.7}$$
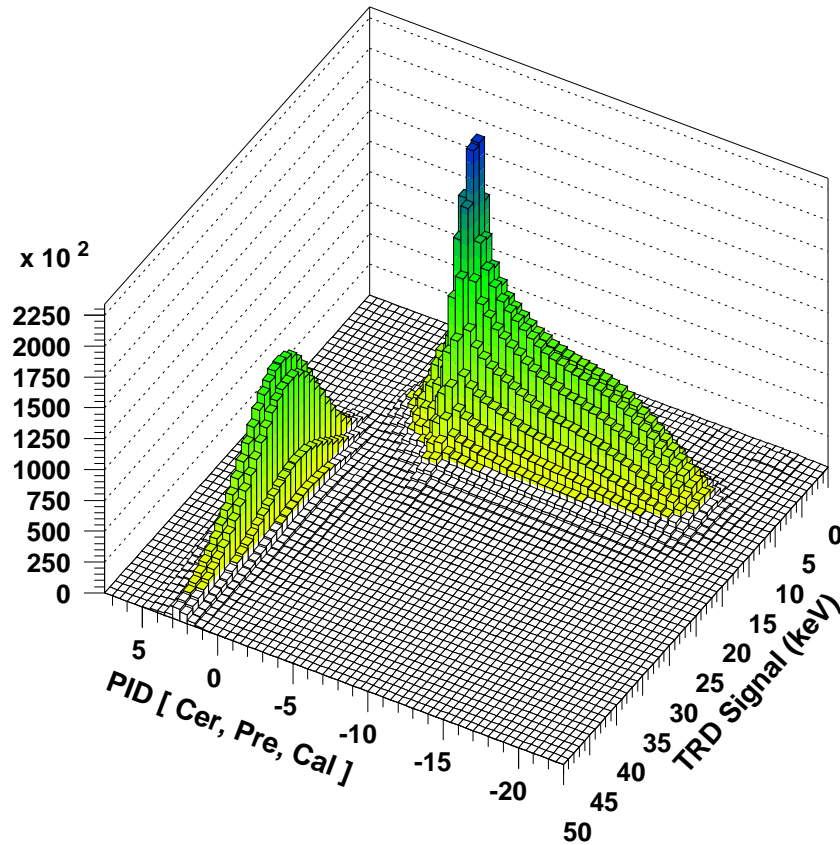
Figure 2.18: The performance of the PID system shows a clear separation between leptons and hadrons. The leptons are located left while the hadrons are on the right side

In Fig. 6.1 the variable PID_3 and PID_5 are shown for events collected by the spectrometer. The separation between leptons (left) and hadrons (right) is clearly visible. Usually, the $sum \ PID_3 \ + \ PID_5$ was required to be smaller than zero for the hadrons and larger than zero for the leptons.

2.8   Luminosity monitor

The Luminosity measurements are based on the observation of the coincident detection of electron-positron and photon pairs, or electron pairs, originated from the interaction of the beam positrons, or electrons, with the electrons of the target.
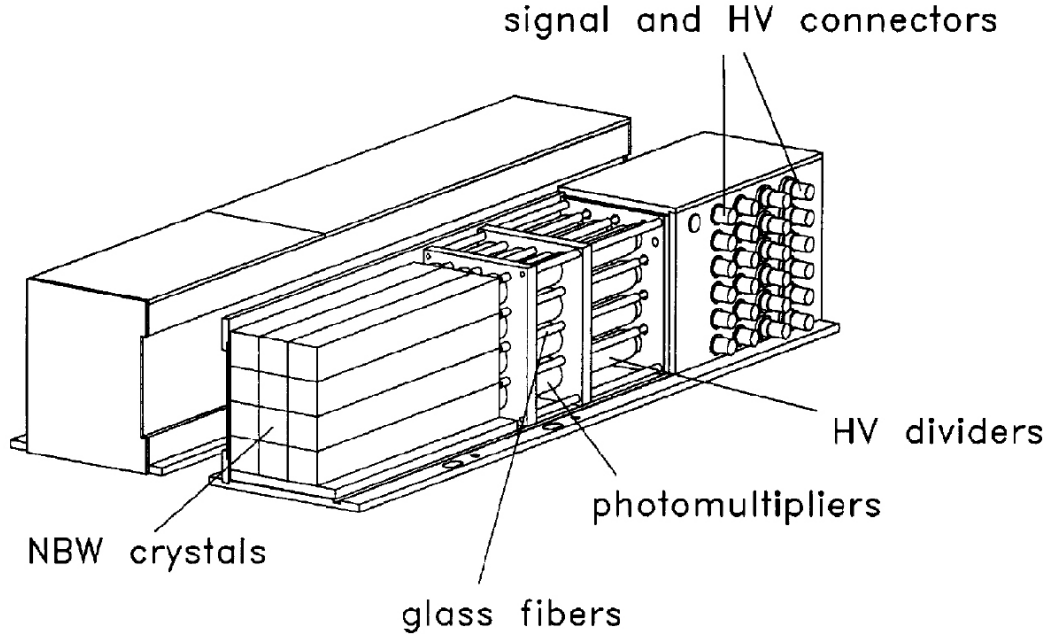
Figure 2.19: Schematic Overview of the luminosity detector.

A precise determination of the relative luminosity was necessary for the measurement of cross section asymmetries and the absolute luminosity was required for the measurement of absolute structure functions. Also of importance was the luminosity for the online monitoring of the HERMES experiment performance.

The cross sections of these processes are well known, using Quantum Electrodynamics (QED) the electron density in the target is the same as the nucleon density, then the luminosity can be extracted precisely by measuring the event rate R and the cross section of the process [58]

$$\mathcal{L} \; = \; \frac{R}{\sigma} \tag{2.8}$$

The total cross section σ is the integral of the differential cross section over the acceptance $\Delta\Omega$ of the luminosity monitor and taking into account the detector efficiency ϵ.

$$\sigma \; = \; \int_{\Delta\Omega} \epsilon \frac{d\sigma}{d\Omega} d\Omega \tag{2.9}$$

The Luminosity monitor (LUMI) consisted of two calorimeters, each containing 12 Čerenkov crystals with a size of $22\times22\times200 mm^3$ arranged in a 3×4 matrix, see Fig.2.19. The crystals were made of $NaBi(WO_4)_2$ which has a very high radiation hardness of about $7\times10^5 Gy$ [59].

2.9 The Gain Monitoring System

The Gain Monitoring System (GMS) was installed in the HERMES experiment to monitor various HERMES detectors which have photo-multipliers (PMT). The GMS provide light pulses of different intensities to the PMT's via optical fibers, as well as to an array of reference detectors (see Fig. 2.20).
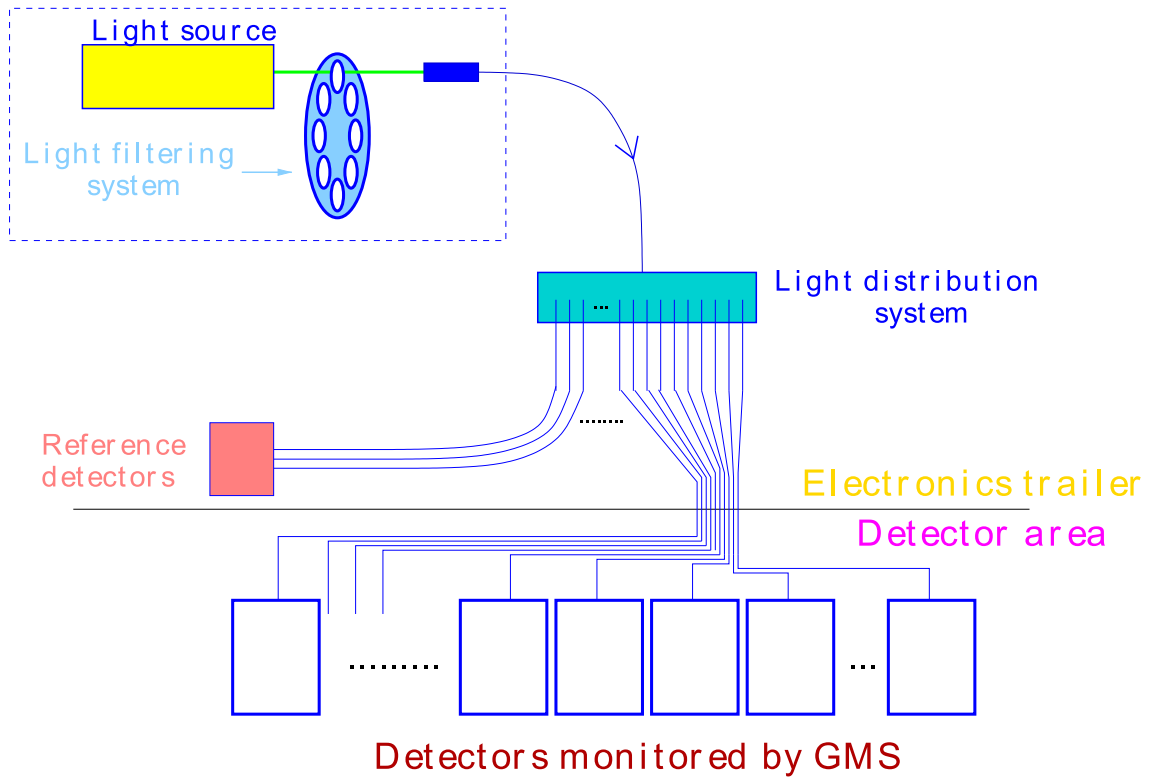
Figure 2.20: Schematic Overview of the GMS components.(Taken from [60])

The response of the detectors to these pulses was measured in the same way as for the signals. The Gain Monitoring System was used to provide the relative gain of the detectors and to check the detector response in real time. More information can be found in [60].

2.10 The HERMES Trigger

The readout of the detector signals was initiated by the trigger system. The HERMES spectrometer was equipped with a variety of first level trigger systems. The trigger set-up was optimized to select events with DIS electrons, the non-physics triggers were prescaled. This keeps the overall trigger rate low enough for the data acquisition.

The main physical trigger corresponding to the DIS electron or positron was fired when there was a hit in the three scintillator hodoscopes $H0$, $H1$ and $H2$ (see Fig. 2.6). Note that the top and bottom were treated separately, the hit in the $H0$ top can not form a coincidence with hits in $H1$ bottom etc. The minimum requirement was to establish that the calorimeter response was above the threshold. For this a signal above the minimum ionization energy deposited to suppress the maximum background events was required. Due to the spacial (and thus the timing) separation of the hodoscopes $H1$ and $H2$, it was not sufficient to discriminate between background or real events coming from the HERMES target. For normal

data taking, this threshold was 1.4 GeV and for high density was increased to 3.5 GeV. In addition to this important physical trigger were other triggers sensitive to produced hadrons, for detectors monitoring or for the calibration. See details in [25, 61, 62].

Chapter 3

Physics program of Hermes with the Recoil Detector

The internal structure of the nucleon was studied through *inclusive* and *semi-inclusive* scattering of high energy leptons in deeply inelastic scattering (DIS). *Unpolarized* DIS gave us evidence of the structure of the nucleon as a bound state of the quark and Alon's, *Polarized* DIS revealed that only a small fraction of the spin of the nucleon is carried by the intrinsic spin of the quarks [63, 64, 65].

The treatment of hard *exclusive* and *semi-exclusive* reactions has been introduced by the recently developed formalism of Generalized Parton Distributions (GPDs) to enlarge the knowledge of the internal structure of the nucleon. Under well defined kinematic conditions, the reaction amplitude factorize. This factorization provides a solid starting point to study GPDs in exclusive reactions [66, 67].
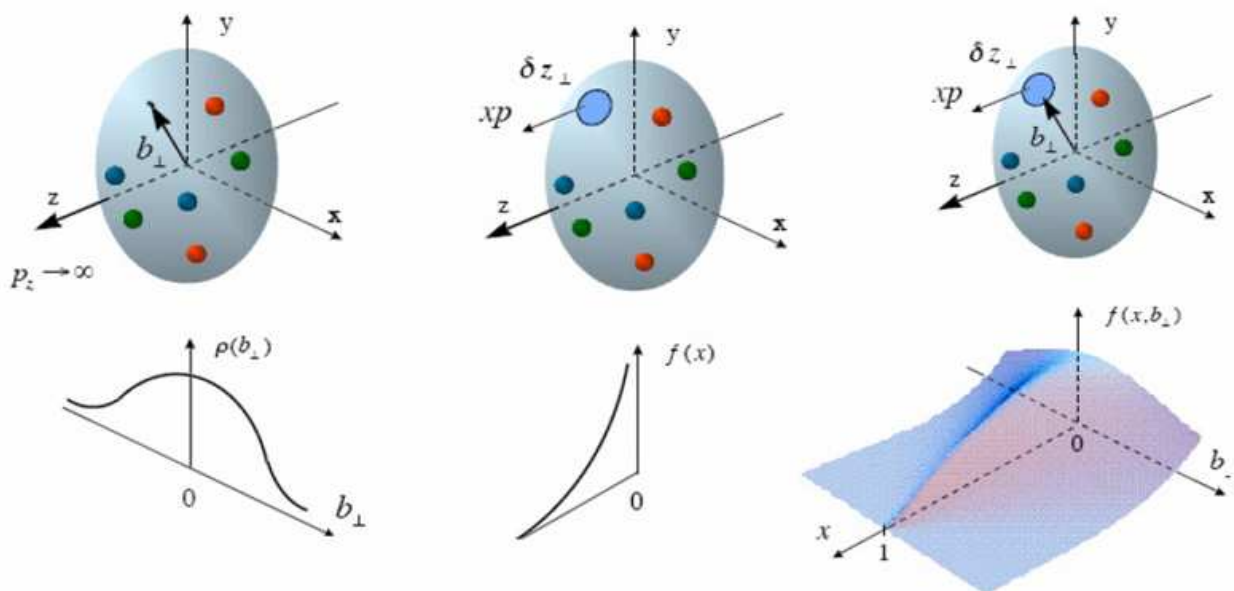

Figure 3.1: Probabilistic interpretation of form factors, parton densities and generalized parton distribution in the infinite momentum frame [64].

3.1 Generalized Parton Distributions

Generalized Parton Distributions (GPDs) [7, 63, 65] were developed a few years ago to combine transverse charge distribution information, named Form Factors, with longitudinal momentum distribution information called Parton Density Functions, for description of exclusive processes, see Fig. 3.1.

The usual parton distributions represent the probability to find a parton with specified longitudinal momentum fraction x in the fast moving hadron. They are expectation values of quark or gluon operators for a hadron state, describing forward kinematics and related to cross sections through the optical theorem. Generalized Parton Distributions are the natural extension to non-forward kinematics. They represent the interference of different wave functions, one with a parton having the longitudinal momentum fraction $x + \xi$ and one with a parton having longitudinal momentum fraction $x - \xi$. The variable ξ, also called *skewedness* parameter, is related to x_{Bj}, the momentum fraction of the nucleon carried by the struck quark.

GDPs depend on a third variable, in addition to the momentum fraction variables x and ξ, the Mandelstam invariant $-t = (p-p')^2$ which is related to the momentum transfer between two hadron states with momentum p and p' respectively, and are shown in Fig. 3.2.
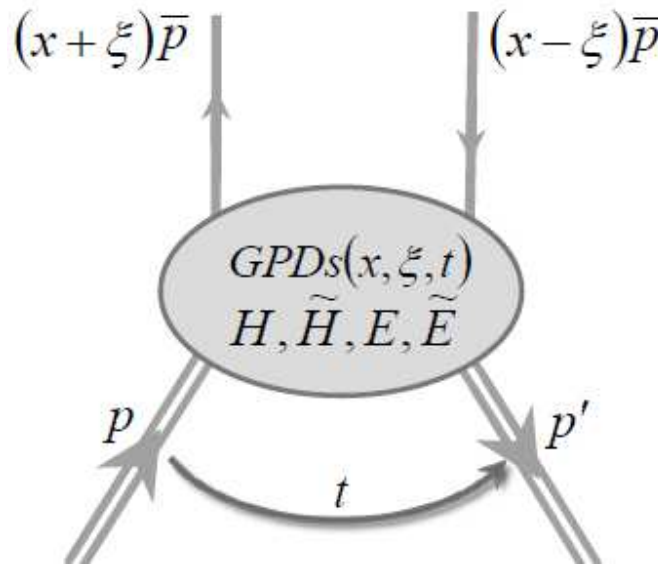
Figure 3.2: The GPD handbag diagram. Description of GPDs by momentum fraction variable x, the *skewedness* parameter ξ and the Mandelstam invariant $-t$ which is related to the momentum transfer between two hadron states with momentum p and p', respectively.

There are four different types of quark GPDs that contribute to the simplest hard exclusive process - Deeply Virtual Compton Scattering (DVCS), $ep \rightarrow ep\gamma$. The unpolarized distributions $H^q(x, \xi, t)$ and $E^q(x, \xi, t)$ and the polarized distributions $\widetilde{H}^q(x, \xi, t)$ and $\widetilde{E}^q(x, \xi, t)$. The GPDs H^q and $\widetilde{H}^q$ conserve nucleon helicity while E^q and $\widetilde{E}^q$ are associated with a helicity-flip of the nucleon. GPDs offer a unified description of form factors and parton densities. In the limit of $t \rightarrow 0$, $\xi \rightarrow 0$

$$H^q(x, 0, 0) = q(x), \quad \widetilde{H}^q(x, 0, 0) = \Delta q(x), \tag{3.1}$$

where $q(x)$ and $\Delta q(x)$ are the ordinary quark and quark helicity distributions. The variable x is defined in the range $(-1, +1)$ and negative values of it correspond to antiquark distributions in the following way:

$$q(-x) = -\overline{q}(x) =, \quad \Delta q(-x) = \Delta \overline{q}(x), \tag{3.2}$$

The first moments of the GPDs simplify to the flavour dependent form factors:

$$
\begin{aligned}
\int_{-1}^{1} dx\, H^q(x,\xi,t) &= F_1^q(t), &&\text{Dirac form factor} \\
\int_{-1}^{1} dx\, E^q(x,\xi,t) &= F_2^q(t), &&\text{Pauli form factor} \\
\int_{-1}^{1} dx\, \widetilde{H}^q(x,\xi,t) &= g_A^q(t), &&\text{Axial-vector form factor} \\
\int_{-1}^{1} dx\, \widetilde{E}^q(x,\xi,t) &= h_A^q(t), &&\text{Pseudo-scalar form factor}
\end{aligned}
\tag{3.3}
$$

where $F_1(t)$ and $F_2(t)$ are the Dirac and Pauli form factor and $g_A(t)$ and $h_A(t)$ are the axial-vector and pseudo-scalar form factors.

A strong motivation to study GPDs followed from the finding of Ji [8, 63], who discovered the relation between the second moment of the unpolarized GPDs H^a and E^a with a given flavor a, in the limit $t = 0$, to the spin structure of the nucleon and gave the gauge invariant quark total angular momentum

$$
\lim_{t\to 0} \frac{1}{2} \int_{-1}^{1} dx\; x[H^a(x,\xi,t) + E^a(x,\xi,t)] = J_q,
\tag{3.4}
$$

J_q, i.e. the sum of intrinsic and orbital angular momentum carried by quarks of flavor q in the nucleon. A determination of contributions J_q from all quark flavours gives the total quark angular momentum J_q which decomposes as

$$
\frac{1}{2} = J_q + J_g = \frac{1}{2}\Delta\Sigma + \Delta G + L_q + L_g,
\tag{3.5}
$$

where $\Delta\Sigma = \sum \Delta q(q = u, d, ...)$ is the fraction of the nucleon helicity carried by quarks and antiquarks, ΔG the contribution from the gluon spin to the nucleon spin, and $L_q(L_g)$ the contribution from orbital angular momentum of the quarks and antiquarks (gluons). The total angular momentum carried by quarks, $J_q = \frac{1}{2}\Delta q + L_q$, and by the gluons, $J_g = \Delta G + L_g$, in the nucleon may be accessed through GPDs [63].

As $\Delta\Sigma$ is measured through polarized inclusive and semi-inclusive DIS experiment [15], a measurement may be used to derive the contribution of the quark orbital momentum L_q to the nucleon spin, in principle, from the contribution of the total gluon momentum J_g.

$$
\frac{1}{2} = J_q + J_g,
\tag{3.6}
$$

It should be noted that this requires access to both unpolarized GPDs, H^q and E^q, and that it is necessary to be able to extrapolate to $t = 0$. This stresses the importance of measurements at low values of t.

3.2   Deeply Virtual Compton Scattering

Theoretically the simplest process to access GPDs is DVCS (deeply virtual Compton scattering). The DVCS process shown in Fig. 3.3 is a process in which a virtual photon γ^* interacts with a quark inside the hadronic target and produces a real photon γ living intact the hadronic target.
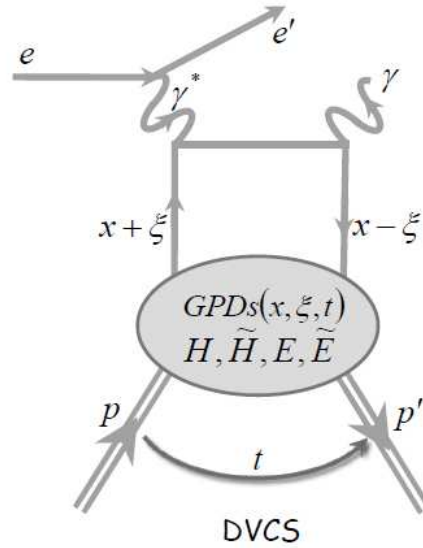
Figure 3.3: Feynman diagram of deeply virtual Compton scattering (non-forward Compton scattering). The shadow blob represents a generalized parton distribution.

The DVCS process combines the advantages of deep inelastic scattering (DIS) and the Compton scattering: the initial photon is off-shell, thus opening an additional dimensional parameter with respect to the real Compton scattering, because the virtuality can be 'tuned' (in the given kinematic limits).
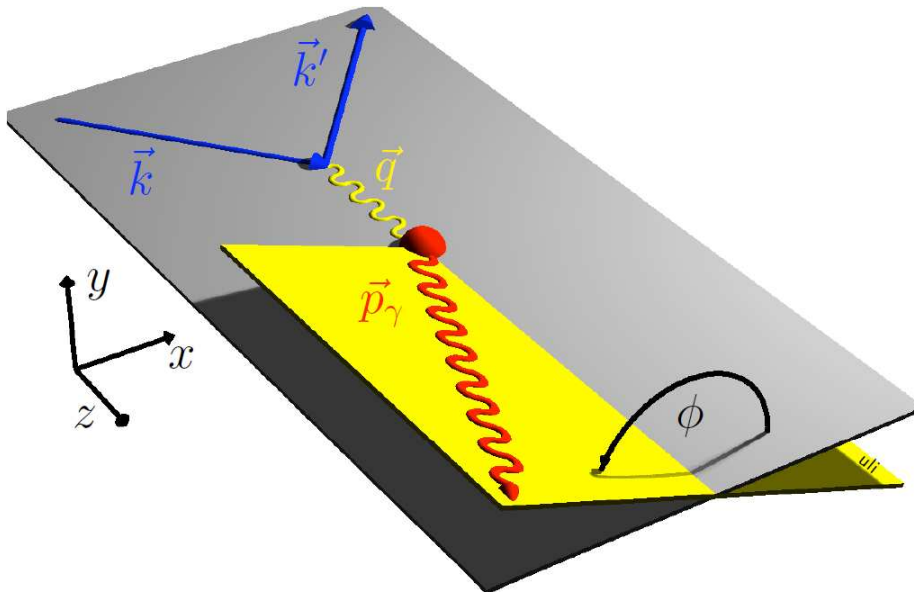
Figure 3.4: Diagram of DVCS kinematics. The scattering plane (grey) is defined by the incoming and the scattered electron momentum vectors $\vec{k}$ and $\vec{k'}$. The production plane (yellow) is given by the virtual and the real photon momentum $\vec{q}$ and $\vec{q'}$ ($\vec{p_\gamma}$). The angle between scattering and production plane defines the azimuthal angle ϕ, (drawn by U.Elschenbroich).
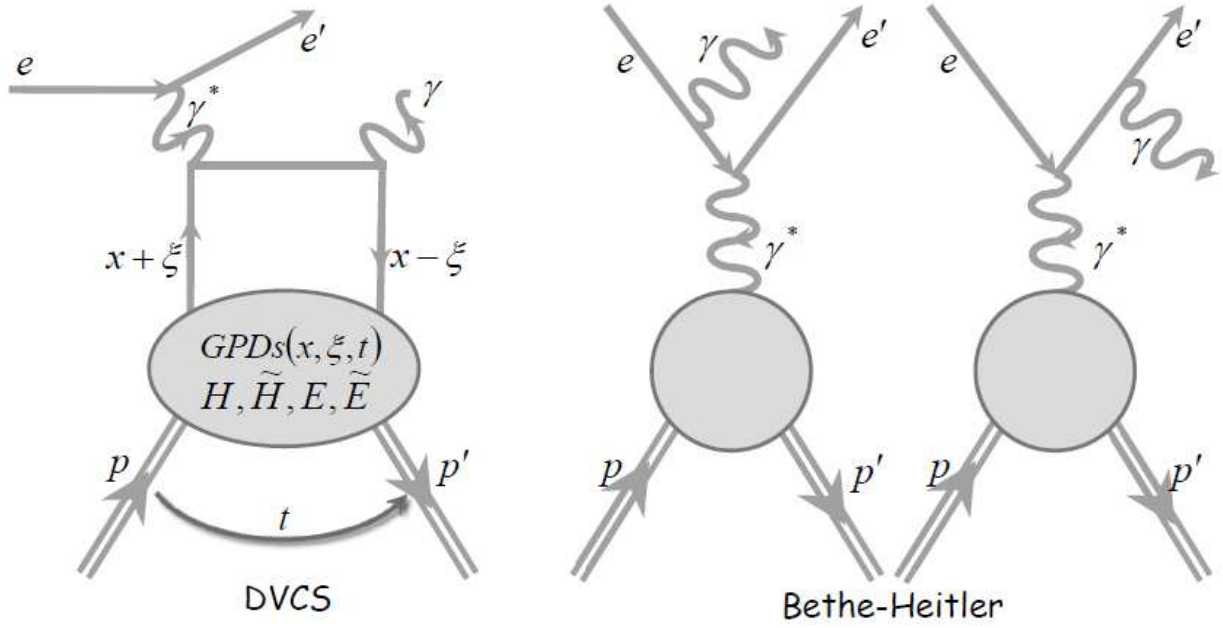
Figure 3.5: Feynman Graphs for DVCS (left panel) and Bethe-Heitler process (right panel). Both processes lead to the same final state.

In electron (or positron) scattering experiments there exists another process that leads to the same final state as DVCS, namely the Bethe-Heitler process (BH), in which the incoming or outgoing electron radiates a Bremsstrahlung photon in the Coulomb field of the proton (shown in Fig 3.5).

$$ep \; \rightarrow \; e'p'\gamma,$$

The amplitude of DVCS and BH are interfering, thus prohibiting the measurement of the pure DVCS process. The relative contributions of BH and DVCS to the total amplitude depend strongly on the lepton energy. At HERMES energies, the BH contribution is mostly dominant, except at large values of the Bjorken variable x_B and Q^2. This situation is used as an opportunity, since the interference of the two contributions offers a way to access both the real and the imaginary part of the DVCS amplitude. At higher energies, where the DVCS amplitude dominates over the BH amplitude, only the square of the DVCS amplitude can be accessed [77].

3.3   Hard Exclusive Meson Production

One of the Hard Exclusive Meson production which has special interest for this thesis is the exclusive ρ^0 production in lepton-nucleon scattering. This can be described by various theoretical models. Many of its basic features are reproduced by the *Vector Meson Dominance* (VMD) model.

Figure 3.6: Feynman Graph for Vector Meson process.

Exclusive electroproduction of the meson can provide new information about the structure of the nucleon because of its relation to gener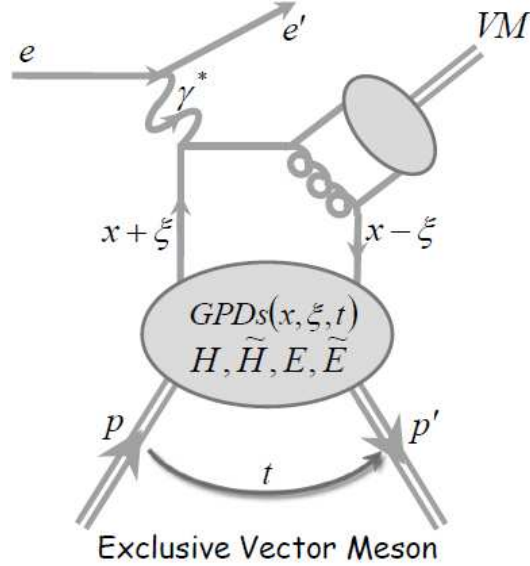alized parton distributions (GPDs) [7, 63]. At leading twist, meson production is described by four types of GPDs: $H^{q,g}$, $E^{q,g}$, $\widetilde{H}^{q,g}$ and $\widetilde{E}^{q,g}$, where q stands for a quark flavour and g for a gluon. The quantum numbers of the produced meson determine the sensitivity to the various GPDs. In particular, at leading twist, production of vector mesons is sensitive only to the GPDs H^q, E^q, H^g and E^g. In Fig 3.6 a representation of exclusive vector meson production is depicted.

3.3.1   Kinematics

The ρ^0 meson is an unstable particle with a very short lifetime and decays into two pions with the branching ratio of $99, 9\%$.

$$e(l)P(p) \;\rightarrow\; e'(l')P'(p')\rho^0(q') \;\rightarrow\; e'p'\pi^+\pi^-, \tag{3.7}$$

which is described in terms of the four-momenta of the incoming and outgoing electron (l, l') and proton (p, p'). HERMES is a fixed-target experiment, so that the target nucleon is at rest $(P = (M, 0))$ and the center of mass energy is defined by the lepton beam energy $E = 27.6 GeV$; $\sqrt{s} = 7.3 GeV$ where the lepton nucleon system center of mass is defined by

$$s = (l + p)^2 \stackrel{lab}{\approx} M^2 + 2ME \tag{3.8}$$

to a very good approximation, the lepton-nucleon interaction is mediated by the exchange of one neutral virtual boson, γ or Z^0. As s is much smaller than the Z^0 mass ($m_{z^0} \approx 91.2 \; GeV/c^2$), the week interaction can be neglected. This process is represented in Fig 3.7.
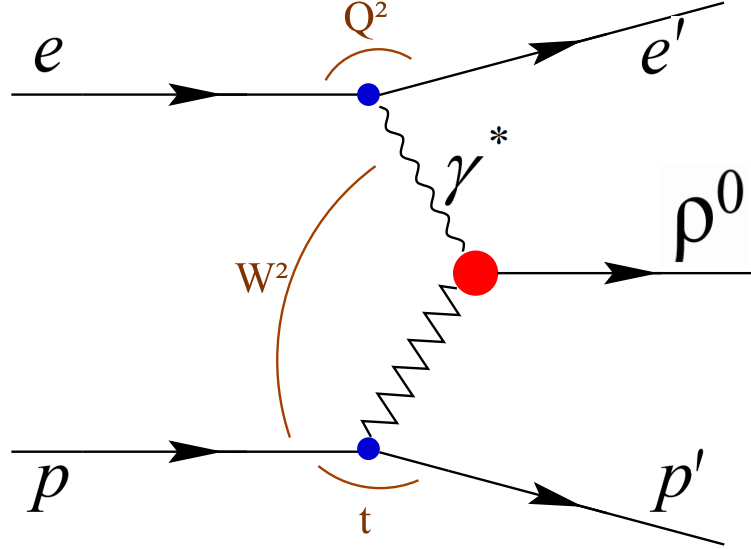
Figure 3.7: Schematic view of exclusive ρ^0 leptoproduction with t-channel exchange [81].

The measure of the spacial resolution q, can be used to calculate the squared invariant mass of the virtual photon and is defined by

$$Q^2 = -q^2 = -(l - l')^2 \overset{lab}{\approx} 4EE' \sin^2 \frac{\theta}{2}, \tag{3.9}$$

In the laboratory frame (lab) E and E' denote the initial and final electron energy and θ is the scattering angle of the electron. An important variable used to describe the kinematics is the Bjorken scaling variable x_B defined as

$$x_B \equiv \frac{Q^2}{2\,\mathbf{p}.\mathbf{q}} \overset{lab}{=} \frac{Q^2}{2\,M\nu} \tag{3.10}$$

interpreted in DIS as the momentum fraction of the nucleon carried by the struck quark. In the fixed target experiment with the target nucleon at rest, the energy transfer ν, given by

$$\nu = \frac{\mathbf{p}.\mathbf{q}}{M} \overset{lab}{=} E - E', \tag{3.11}$$

is the energy loss of the scattered electron. The squared center of mass energy W^2 of the photon-nucleon system is given by

$$W^2 = (q + p)^2 \overset{lab}{=} M^2 + 2M\nu - Q^2 = M^2 + Q^2 \frac{1 - x_B}{x_B}, \tag{3.12}$$

The variable y is the fractional energy transfer from the lepton to the nucleon $(0 < y < 1)$, given by

$$y = \frac{\mathbf{p}.\mathbf{q}}{\mathbf{p}.\mathbf{l}} \overset{lab}{=} \frac{\nu}{E}, \tag{3.13}$$

All variables described above (q^2, ν, W^2, x_B) are fully defined by the electron kinematics. The squared four momentum transfer to the target or the *Mandelstam* variable t can be calculated from the virtual photon to the produced meson by

$$t = (p - p')^2 = (q - q')^2 \overset{lab}{=} 2M(M - E_{p'}), \tag{3.14}$$

where $E_{p'}$ is the energy of the recoiling proton.

3.3.2   Exclusive Production of ρ^0 at HERMES

Electroproduction of the neutral vector mesons at intermediate energies is an important research topic of the HERMES Experiment. So far the production of ρ^0, Φ and ω [79, 80, 81] has been studied.

Theoretically, the interpretation of the exchanged neutral object depends on the values of W and Q^2 at which the process occurs. At low values of Q^2 the Vector Meson Dominance model can provide a phenomenological description of the world data by assuming Pomeron exchange between the virtual photon and the nucleon, where the former fluctuates into a vector meson. At higher values of W and moderate Q^2 pQCD-models based on two-gluon-exchange mechanisms are quite successful. However, they are not able to describe HERMES data at lower values of W. This is especially seen for the light vector meson ρ^0. Therefore a GPD based approach appears promising in interpreting the HERMES data.
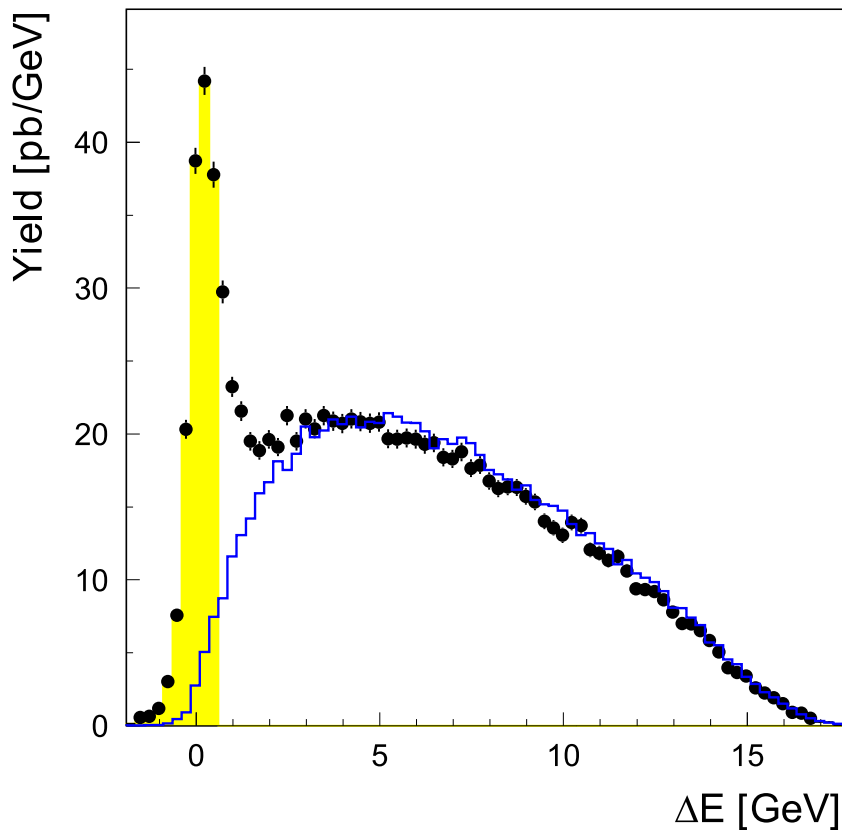
Figure 3.8: Missing energy spectrum for ρ^0-production at Hermes.The ΔE distributions of the measured yield (number of counts within the acceptance divided by the integrated luminosity) (dots) and a Monte Carlo simulation of the non-exclusive background normalized to the same integrated luminosity (histogram). The kinematic cuts and the requirements $0.6 GeV < M_{\pi\pi} < 1.0 GeV$ and $M_{KK} > 1.04 GeV$ were applied. The exclusive region below $\Delta E = 0.6 GeV$ is shaded. This measurement uses only forward spectrometer information.

The Recoil Detector was built to be able to remove a major part of the non-exclusive background. This will allow for cleaner determination of the spin density matrix elements. The combination of the polarized beam with the unpolarized target will especially enable the study of polarization dependent quantities. The improved exclusivity level of the events will also lead to new precise constraints on GPDs.

The ρ^0-meson is also an important channel to study the performance of the Recoil Detector at HERMES, because it gives the cleanest signal via decay channel to two charged pions and at HERMES it is detected with the highest rate of all exclusive processes (about 930 exclusive events per 10^6 DIS-events in the polarized years 2000-sampler).

Presently most of the ρ analysis done at HERMES uses the method of missing energy in order to ensure exclusivity. In Fig 3.8 a clear signal of the exclusive ρ^0 production is seen at missing energy of zero, reconstructed from events with two oppositely charged pions. Conventionally a restrictive cut at a missing energy of $\Delta E = 0.6\ GeV$ is applied, which removes most of the DIS background. The background suppression though the information from the recoil detector will make a more relaxed cut possible, thus increasing the statistics. Double dissociative diffractive background is also present in the missing energy range below $2\ GeV$. A Monte Carlo generation shows that the recoil detector will be very effective in reducing this background due to the well known ρ kinematics, keeping 80% of the exclusive events and the double dissociative background within the cut region may be reduced to less than a few percent.
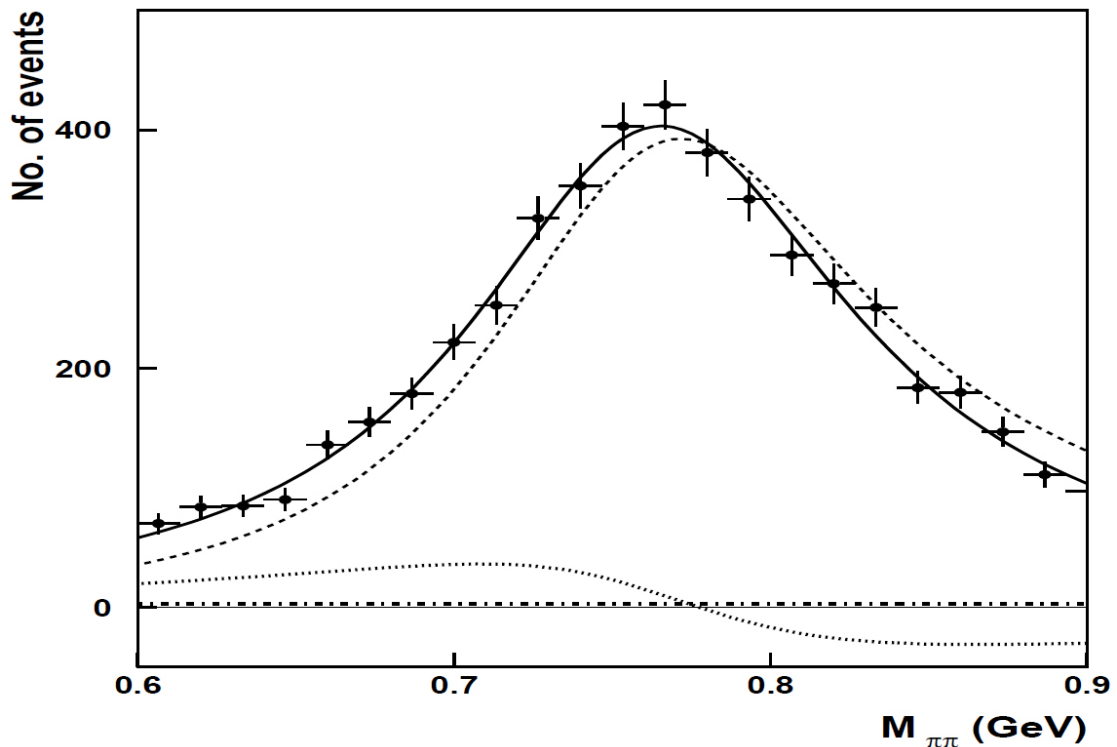
Figure 3.9: Estimation of the non-resonant background. The invariant mass distribution, shown here for exclusive ($\Delta E < 0.6\ GeV$) ρ^0 electroproduction on the deuteron, is fitted with a Breit-Wigner shape using the mass skewing model of Ref. [83] (solid line). The dashed line indicates the Breit-Wigner function, the dash-dotted line represents the non-resonant background, and the dotted line shows the interference term.

The treatment of backgrounds in the case of exclusive ρ^0 meson electroproduction without the Recoil Detector was separated into non-exclusive and non-resonant. From the ΔE spectra we estimate non-exclusive background and from the pion pair invariant mass distribution non-resonant background. The $\pi^+\pi^-$ was fitted with a relativistic p-wave Breit-Wigner function taking into account the skewing of the ρ^0 mass peak using the model of Ref [83] (see Fig 3.9) [84].

3.4   Expected Detector Performance

3.4.1   Kinematic acceptance

The acceptance of the Silicon and the Scintillating Fiber Tracker detector was optimized to match the recoil proton kinematics from BH/DVCS process (shown in fig 3.10). As the Silicon detector is inside the beam vacuum, the lowest momentum that can be detected is given by a threshold due to the aluminium target cell ($75\ \mu m$ thickness), and the kapton foil ($50\ \mu m$ thickness) and to the inner Silicon module ($300\ \mu m$ thickness) mainly. For the requirement of the signal in both Silicon layers this threshold was $135\ MeV/c$, if only a signal in the first layer was required this threshold drops to an average value of $106\ MeV/c$.
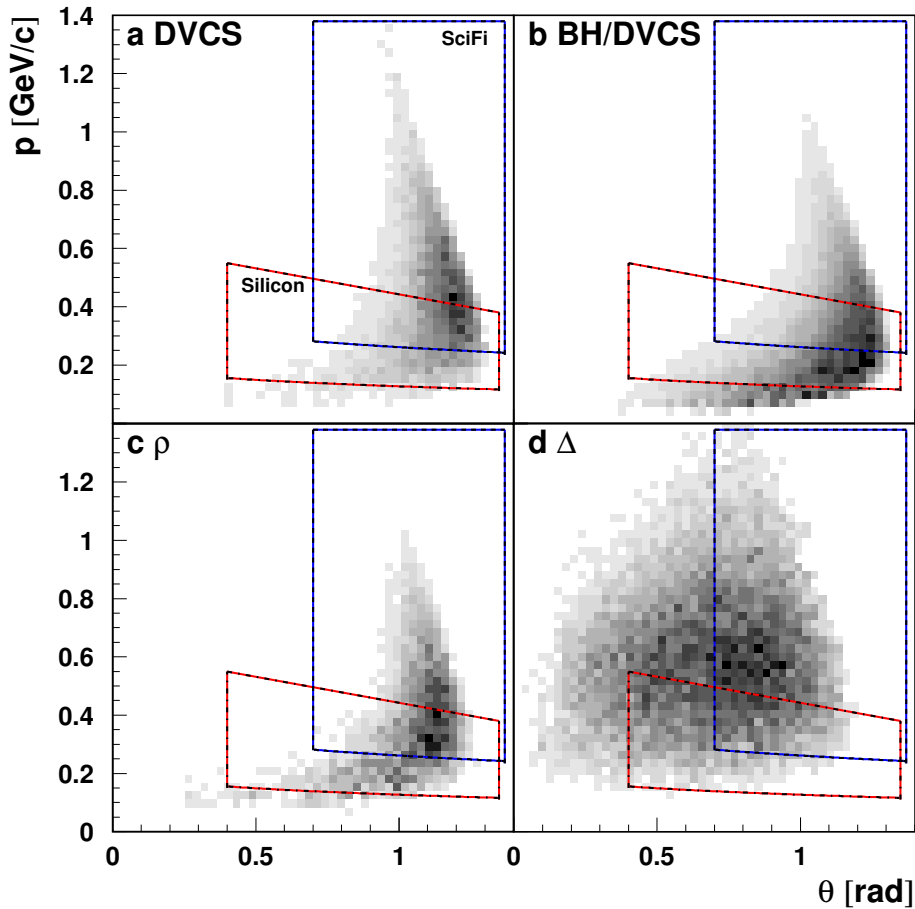
Figure 3.10: Recoil Proton momentum distribution versus polar angle with respect to the beam direction for (a) DVCS only, (b) BH/DVCS, (c) exclusive ρ^0-production, and (d) Δ-decays from Monte Carlo. The lines indicate the kinematic coverage by the Silicon on red and SFT detector in blue [17].

The kinematic distributions for the recoil protons from the different physics processes of interest, based on Monte Carlo before the detector completion, are shown in Fig. 3.10. The boxes indicate the acceptance of the Silicon in red and the SFT detector in blue. There are only small differences between the kinematic distributions for the recoil protons from DVCS and exclusive meson-production. However, the actually measured *BH/DVCS* process yields comparatively more statistics at low momenta. The protons resulting from Δ^+ decays have on average lower angles and higher momenta compared to *BH/DVCS* protons. A large fraction of them therefore can not be seen by the Recoil Detector.

The geometric acceptance can be combined with the detection efficiency, based on the detector thresholds, to form a detection probability. The detection probability for the recoil protons from BH/DVCS events as function of momentum p and polar angle θ are shown in Fig. 3.11. The Silicon detector detects about 70% of the lower momenta recoil protons, while the SFT detector measures about 95% of the higher momenta protons. The acceptance in the azimuthal angle θ is given by the position and size of the second layer of the Silicon detector. Ideally the ϕ acceptance should be 2π, but the necessity of the holding structure for the Silicon detectors reduces it to about $4.8\ rad$ or 78%. For the first layer of the Silicon detector alone this increases to $5.7\ rad$ or 90%. The SFT detector has a ϕ acceptance of 2π. However, due to the material of the Silicon detector frame, the effective acceptance was the same as for the Silicon detector at lower momenta with a transition to 2π at higher momenta.
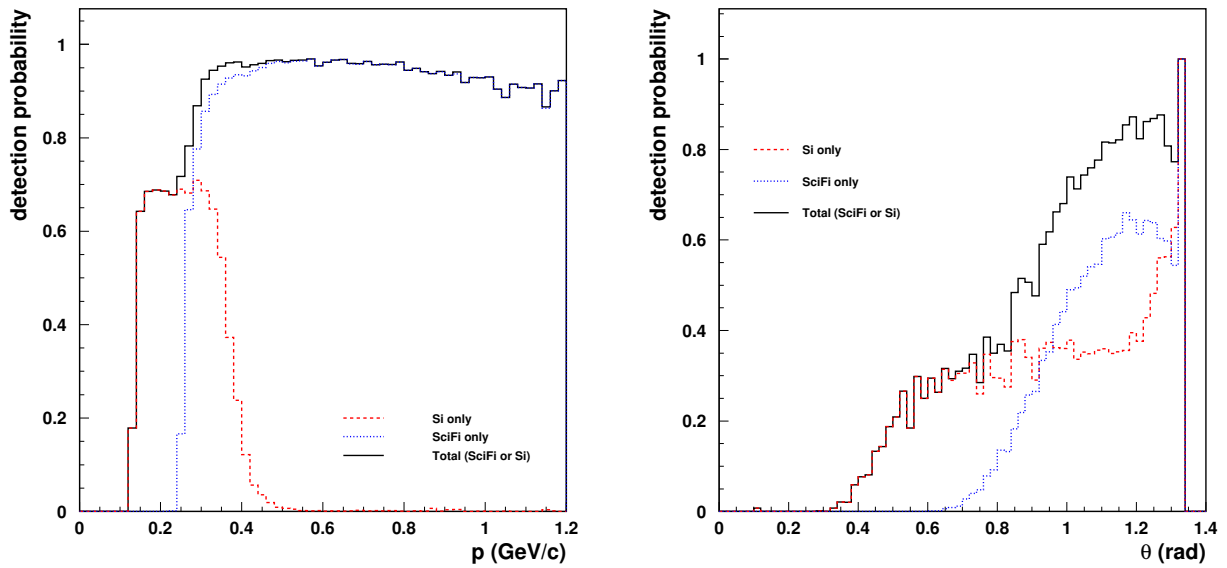
Figure 3.11: Acceptance of the tracking detector in momentum p and in the polar angle θ for the recoil protons from a simulated DVCS sample. The acceptance is shown separately for the Silicon and the SFT detector and for both of them together. Two space point in the Recoil detector are the minimum requirement in this study [17].

In addition to the recoil proton, all other potential reaction products should be detected if possible. This especially refers to pions and photons resulting from Δ-decays. Neutron detection was essentially not possible in this design.

Two-thirds of all Δ^+ resonances decay into a neutral pion and a proton, the neutral pion in turn decays into two photons. In case of π^0 decays the photon detector might detect one of the decay photons in 70% and both decay photons in about 20% of the cases.

3.4.2   Resolution in p, t and θ

Momentum Reconstruction

For the silicon and the SFT detector two different methods are used to measure the momentum of the recoil particles. The method for the Silicon Detector is based on the total energy deposition in both layers of the Silicon detector in combination with the reconstructed track direction. The method for the momentum reconstruction with the SFT detector is based on the deflection of the particle tracks in the magnetic field. The resulting transverse momentum p_t of the particles in combination with the polar angle θ yields all three components of the particle momentum. The precision of the momentum measurement with the Silicon detector is limited by the statistical fluctuations in the energy deposition. For the SFT detector this limit results mostly from the magnitude of the longitudinal magnetic field and from the multiple scattering in the material in front of the detector and in the inner SFT detector.
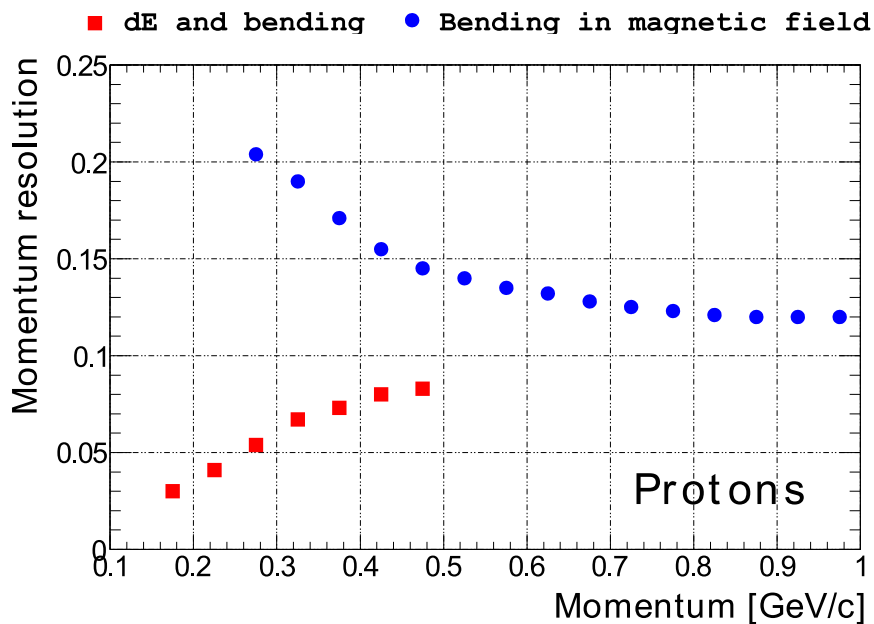

Figure 3.12: Momentum resolution $\Delta p/p$ for the Silicon and the SFT detector [17, 73]. Δp is here defined as the RMS of the distribution p(reconstructed)$-p$(true).

Resolution studies were carried out based on Monte Carlo before the completion of the detector [17]. As shown in Fig. 3.12, the resolution for the proton momentum measured by the Silicon detector increases from 1.5% at momentum below $200 MeV/c$ (stopped protons) to about 9.0% at $500 MeV/c$. For the upper momentum cut-off of the Silicon a detection threshold of $3 MIP$s was assumed, no assumption was done on the detector noise. The resolution provided by the SFT detector for proton below $500 MeV/c$ ranges between approximately 13% and 20%. The increase towards lower momentum for the SFT is caused by multiple scattering. Above $500 MeV/c$ the recoil proton momentum is reconstructed only by the deflection in the magnetic field, with a constant resolution of about 13% for a magnetic field of 1Tesla. This performance reaches the design goal of $< 10\%$ momentum resolution for momentum below $500 MeV/c$.

The momentum resolution delivered by the SFT detector for pions from Δ^+ decay is about 10%. In contrast to the Silicon the SFT detector needs the position of the lepton beam for the momentum reconstruction. The typical beam drift in the HERMES target region is of the order of $1\ mm$. A Monte Carlo simulation to study the effect of the shifted beam showed that this degrades the momentum resolution of the SFT detector by a few percent.

Resolution in t

The recoil particle 4-momentum p_{rec} can be used to determine the value of $-t$ via the relation

$$-t = (p_{rec} - p)^2, \tag{3.15}$$

Since the initial proton is the rest $p = (m_p, 0, 0, 0)$, the accuracy of the determination of $-t$ from the recoil proton depends only on the resolution of the particle momentum, not its direction.
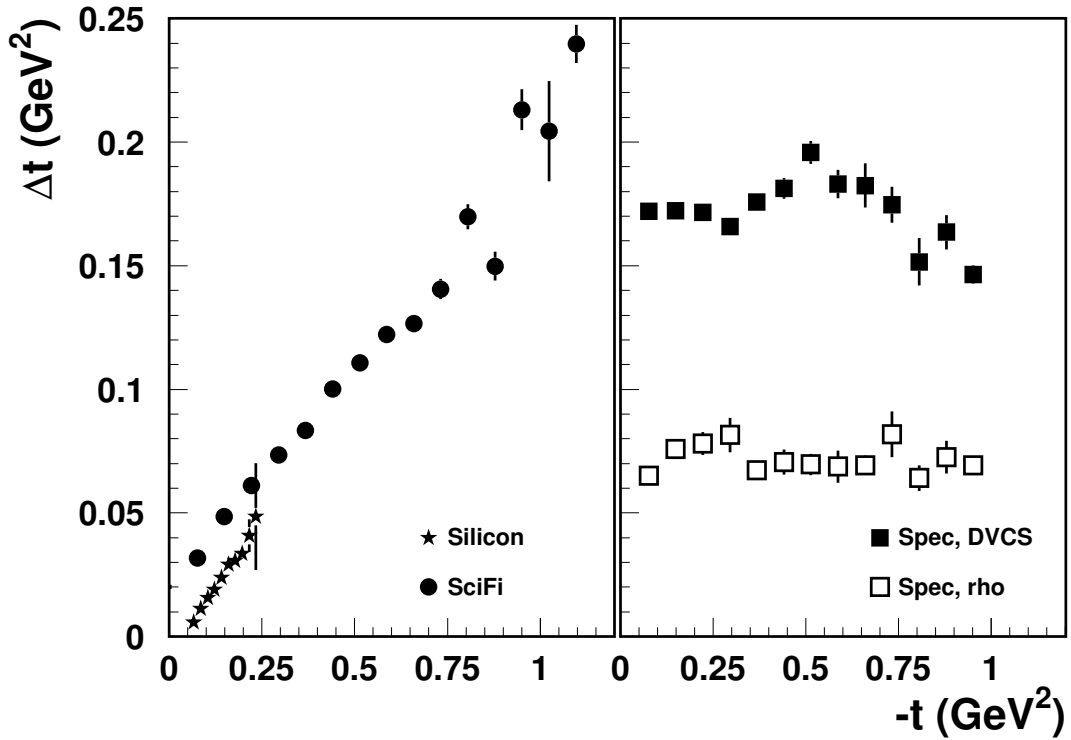
Figure 3.13: Resolution in $-t$ for Silicon and SFT detectors for DVCS (left) and for the forward spectrometer for ρ-production and DVCS (right). Monte Carlo simulation [17, 73].

Hence, for events with low momentum recoil protons, the good momentum resolution of the Silicon detector determines the resolution in t. As shown in Fig 3.13 the right panel shows the t-resolution obtained by the forward spectrometer for BH/DVCS and exclusive ρ^0 production. Compared to this t resolution the Recoil Detector provides an improvement by about an order of magnitude for DVCS events at low values of $-t$. At medium values of $-t$ ($0.25 - 0.5 GeV^2$), where the SFT detector will mainly be used, the resolution in $-t$ is improved by a factor of two for DVCS events and about the same for exclusive ρ^0 production.

Resolution $\Delta\phi$ in the azimuthal angle

The angular resolution provided by the Silicon and the SFT detector for the azimuthal angle ϕ is shown in the two panels of the Fig. 3.14. The result is clearly below the required $0.05rad$ for both detectors, with average RMS values of $0.031rad$ for the Silicon detector and $0.008rad$ for the SFT detector.

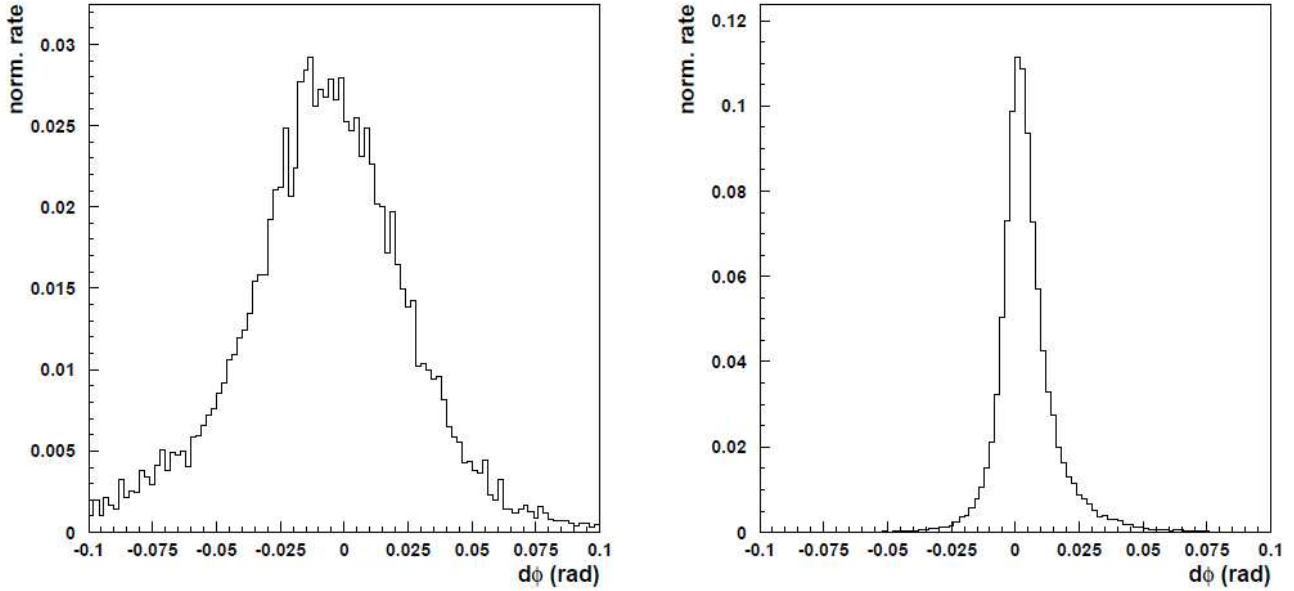Figure 3.14: Resolution in $d\phi$ in the azimuthal angle around the beam, for Silicon (left) and SFT detectors(right). Monte Carlo simulation [17, 73].

3.4.3 Particle Identification

The Recoil detector should be able to distinguish between pions and protons to identify the recoil proton. The relevant momentum range for pion/proton separation is 50 to $800 MeV/c$.

The simplest parameter to use for pion/proton separation is the energy deposition ΔE in the different layers, since the ΔE is different for different particles with the same momentum. For low momentum below $250 MeV/c$ proton produce large signals in the silicon detector and no signal in the SFT detector. Pions in the same momentum range produce a signal in the SFT detector but small signals in the Silicon detector. It can be noticed that $200 MeV/c$ pions in the Silicon detector deposit the same energy lost by protons of $1300 MeV/c$. As a result an almost complete separation of protons and pions can be expected at these momentum.
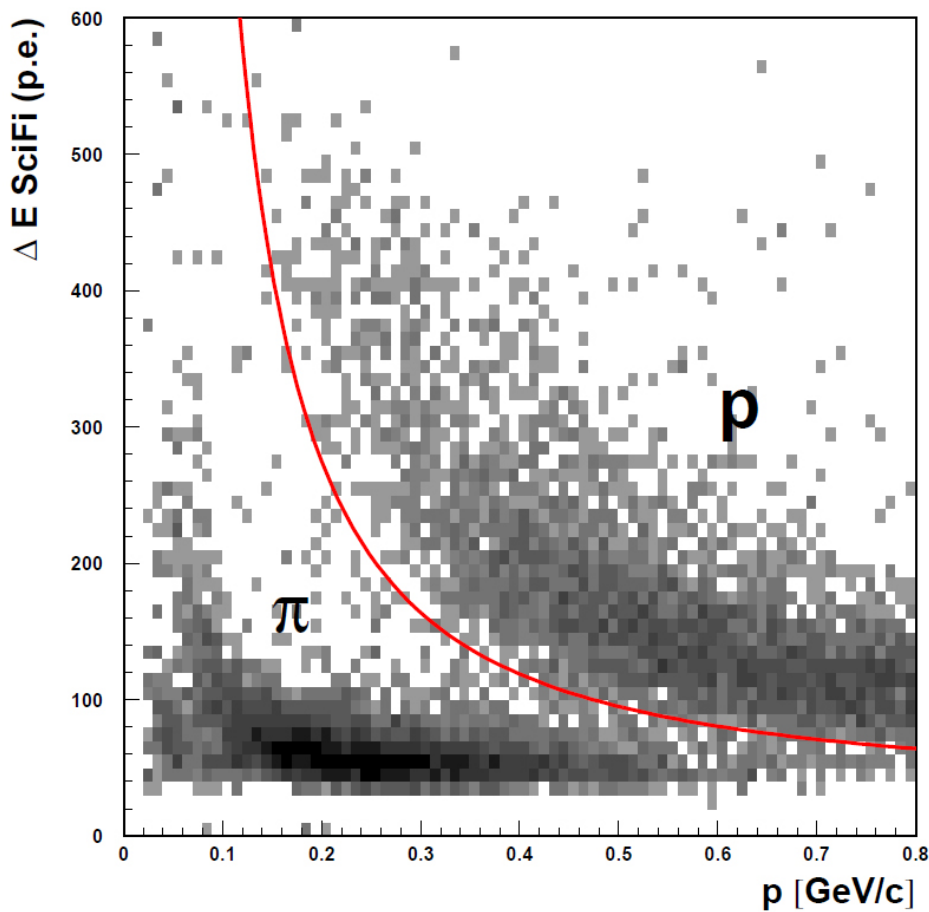
Figure 3.15: Energy deposition versus momentum for pions and protons from Δ^+ decays. The line indicates a possible hyperbolic PID cut. The energy deposition is given in photoelectrons, the momentum measurement is provided by the SFT detector. Monte Carlo simulation [17, 73].

In the range of 250 to $450 MeV/c$, as determined by the SFT detector, a momentum dependent cut on the total energy deposition in the SFT detector provides an adequate particle identification, achieving 90% proton efficiency while rejecting about 98% of the pions, corresponding to an average rejection factor for positive pion of about 50. For momentum above $650 MeV/c$ the pion rejection factor drops below 10. It is expected that the additional information from the photon detector will allow to achieve pion rejection factors of 10 or more up to $800 MeV/c$.

As shown in Fig 3.15 a possible preliminary hyperbolic PID cut, for the final analysis more sophisticated methods for particle identification were used (see ref. [86]).

3.4.4   Overview of expected Detector Performance

Table 3.1 shows an overview of the ideal detector performance and the expected detector performance. Except the low momentum cut-off of the Silicon detector at $135 MeV/c$ all design goals have been met. This value follows from the thickness of the target cell wall, the kapton foil and the first silicon layer. The detector performance is summarized by the reduction of 92% of the background due to the intermediate Δ^+-production [17]. The tracking and PID studies of the Recoil detector are still on going, but first results indicate that the data taken in 2006 and 2007 basically met the expected performance.

PARAMETER	IDEAL PERFORMANCE	EXPECTED PERFORMANCE
p-**acceptance**	$50 - 1400\ MeV/c$	$135 - 450\ MeV/c$ Silicon detector $250 - 1400\ MeV/c$ SFT detector
θ-**acceptance**	$0.1 - 1.35\ rad$	$0.4 - 1.35\ rad$ Silicon detector $0.7 - 1.35\ rad$ SFT detector
ϕ-**acceptance**	$2\ \pi$	4.8 rad Silicon detector $2\ \pi$ SFT detector
p-**resolution**	$< 10\%$ for $p < 500 MeV/c$ $\sim 5\%$ for $p > 500 MeV/c$	$3 - 9\%$ for $p < 500 MeV/c$ 13% for $p > 500 MeV/c$
t-**resolution**	$< 0.07\ GeV^2$	$0.01 - 0.07\ GeV^2$ for $t < 0.3$ $0.07 - 0.2\ GeV^2$ for $0.3 < t < 1.0$
ϕ-**resolution**	$< 0.05\ rad$	$0.031\ rad$ Silicon detector $0.008\ rad$ SFT detector
π/p **PID range**	$50 - 800\ MeV/c$	$135 - 650\ MeV/c$
π^+ **rejection factor**	> 10	> 10 for $p < 650\ MeV/c$
Δ^+ **suppression**	$> 90\%$	92%

Table 3.1: Overview of the ideal and expected detector performance according to Monte Carlo Simulation [17, 73].

3.4.5 Projection for DVCS Measurement at HERMES with the Recoil Detector

The detection of the recoil particles in the measurement of DVCS at HERMES will have two main benefits. The most basic one is the rejection of the events in which a resonance was produced. This can minimize the systematic uncertainty due to the unknown resonance contamination in the sample. Furthermore, the distribution of the otherwise rejected resonant can be studied, and the size of the remaining resonant contamination in the exclusive sample can be assessed.
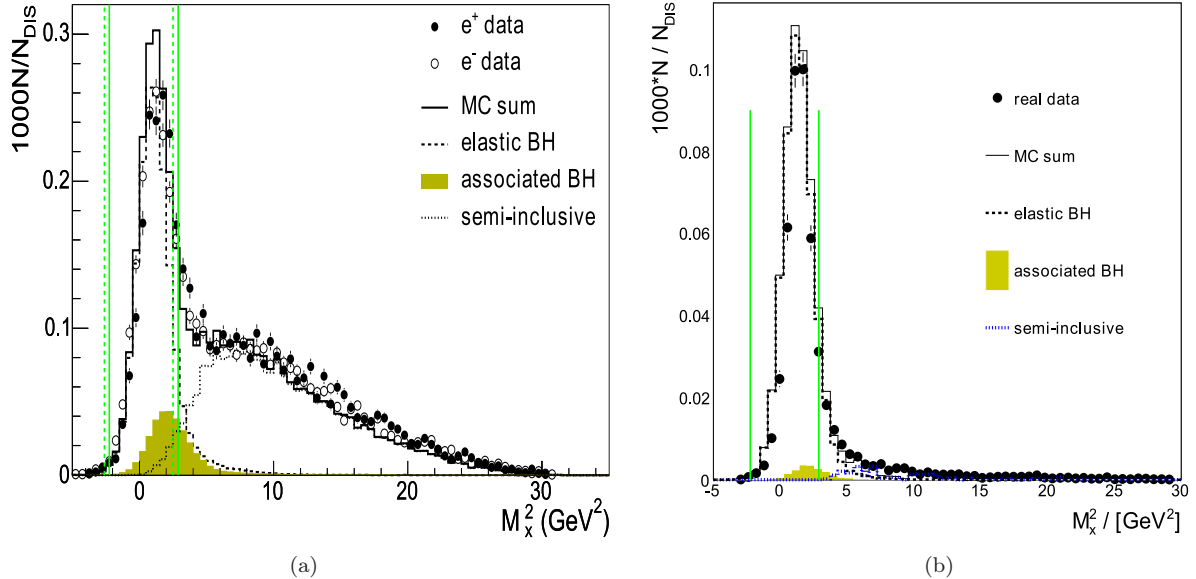

Figure 3.16: The panel (a) shows the missing mass squared distribution from data with positron (filled points) and electron (empty circles) beams and Monte Carlo simulation (solid line). The latter includes the contributions from the elastic BH (dashed line), the associated BH (filled area) and the semi-inclusive (dotted line) processes. The panel (b) shows the comparison between the Monte Carlo simulation (solid line) and the experimental data (filled points). Exactly 1 recoil proton passing the coplanarity cuts was detected by the Recoil Detector. The contribution from the semi-inclusive DIS processes is very little [78, 85, 86].

The other benefit of the recoil detection for DVCS lies in the reconstruction of the kinematics of the recoil particle. Whereas the determination of the variables Q^2 and x_B, or W^2, depends solely on the reconstruction of the scattered lepton, $-t$ depends on the reconstruction of the real photon, if the recoil particle is not detected. As a result, the resolution in $-t$, as reconstructed from the real photon's four-momentum is rather poor, approximately $0.25\ GeV^2$. This variable can alternatively be determined when the four-momentum of the recoiling proton is measured. In this case the resolution in $-t$ depends on the resolution in the proton four-momentum reconstruction. For small values of $-t$ the resolution is expected to improve with the recoil detector by about one order of magnitude.

Chapter 4

The HERMES RECOIL DETECTOR

In order to have a high precision in measurements of exclusive reactions, in 2001 the HERMES collaboration decided to upgrade the HERMES experiment before it's shutdown at end of June 2007. In addition to the HERMES spectrometer, due to the limited acceptance, the detection of recoiling particles by a new detector was required, see Fig. 4.1. The main purpose of 'the Recoil detector', was to investigate different hard exclusive reactions, including the exclusive electroproduction of charged and neutral pions [68], and of vector mesons [69, 70] by the identification of recoiling protons emitted by these exclusive processes which were previously inaccessible due to the limited acceptance of the HERMES experiment [17, 18].
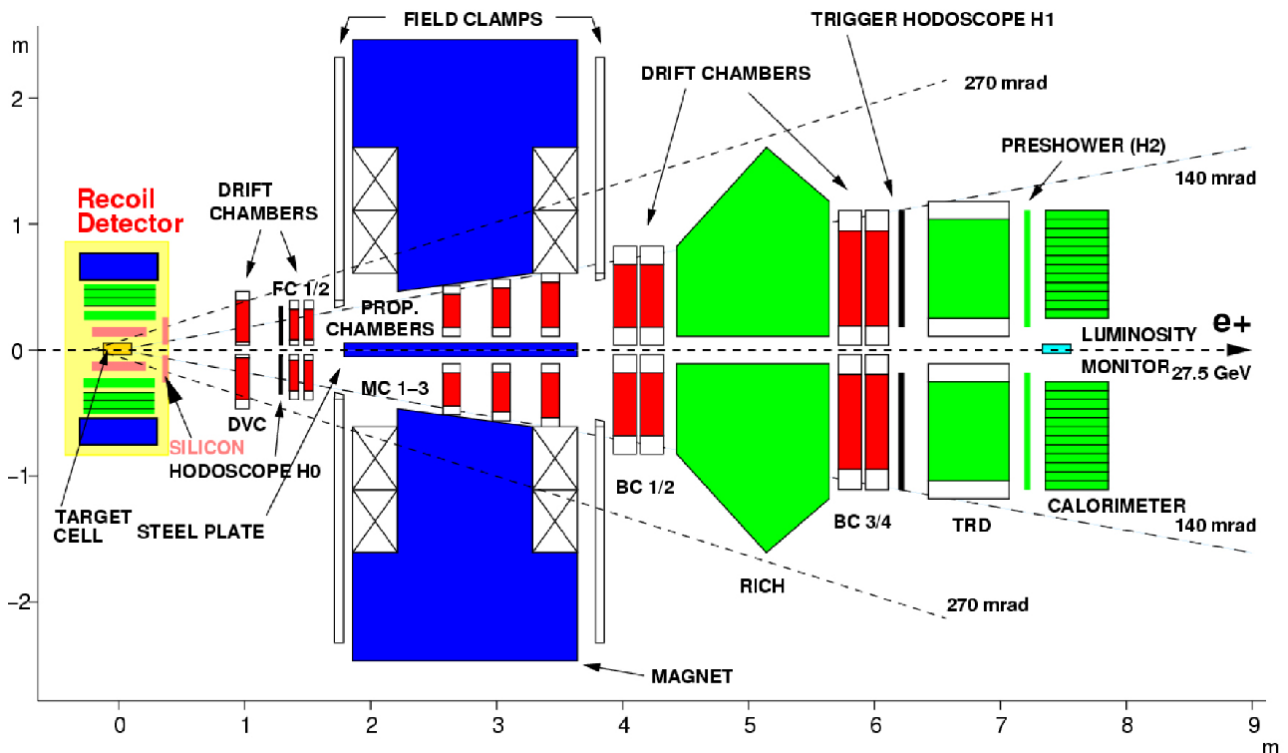
Figure 4.1: Schematic drawing of the HERMES spectrometer with the Recoil Detector surrounding the target cell. The beam enters the spectrometer from the left.

The Recoil Detector (see Fig. 4.2, front view 4.2(a) and back view 4.2(b)) consists of a silicon strip detector, located inside the beam vacuum, a scintillating fibre tracker and a photon detector, around a $150mm$ long target cell made out of a $75\mu m$ thick aluminum tube. The full detector assembly was mounted inside a $1T$

(a)   (b)
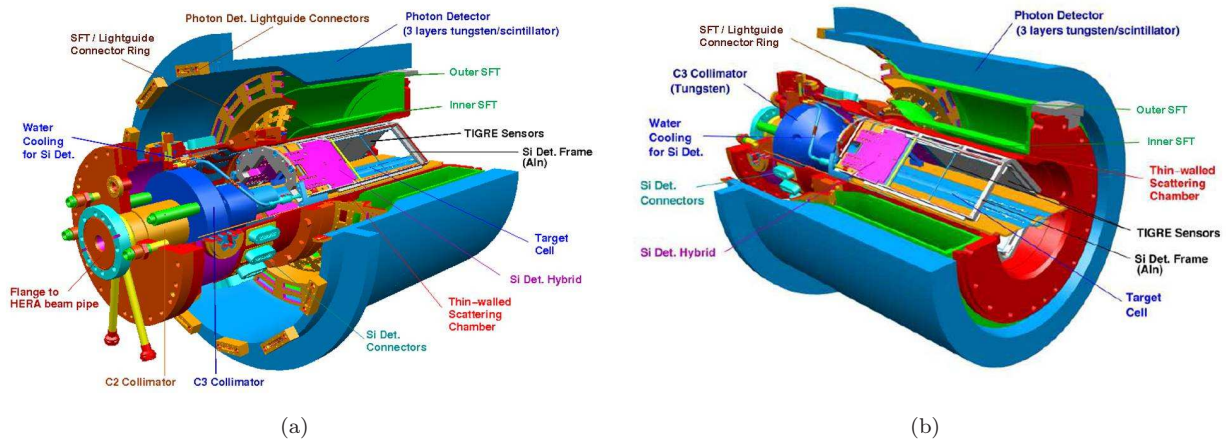
Figure 4.2: Schematic view of the Recoil Detector, front side (a) and back side (b)

super-conducting solenoid and it was able to detect protons and pions with momenta up to $1.40 GeV/c$ and photons in the same angular acceptance. The detector has been operational from February 2006 until June 2007 (see Fig. 4.3). A description of the recoil sub-detectors will be given, going from the inside out.
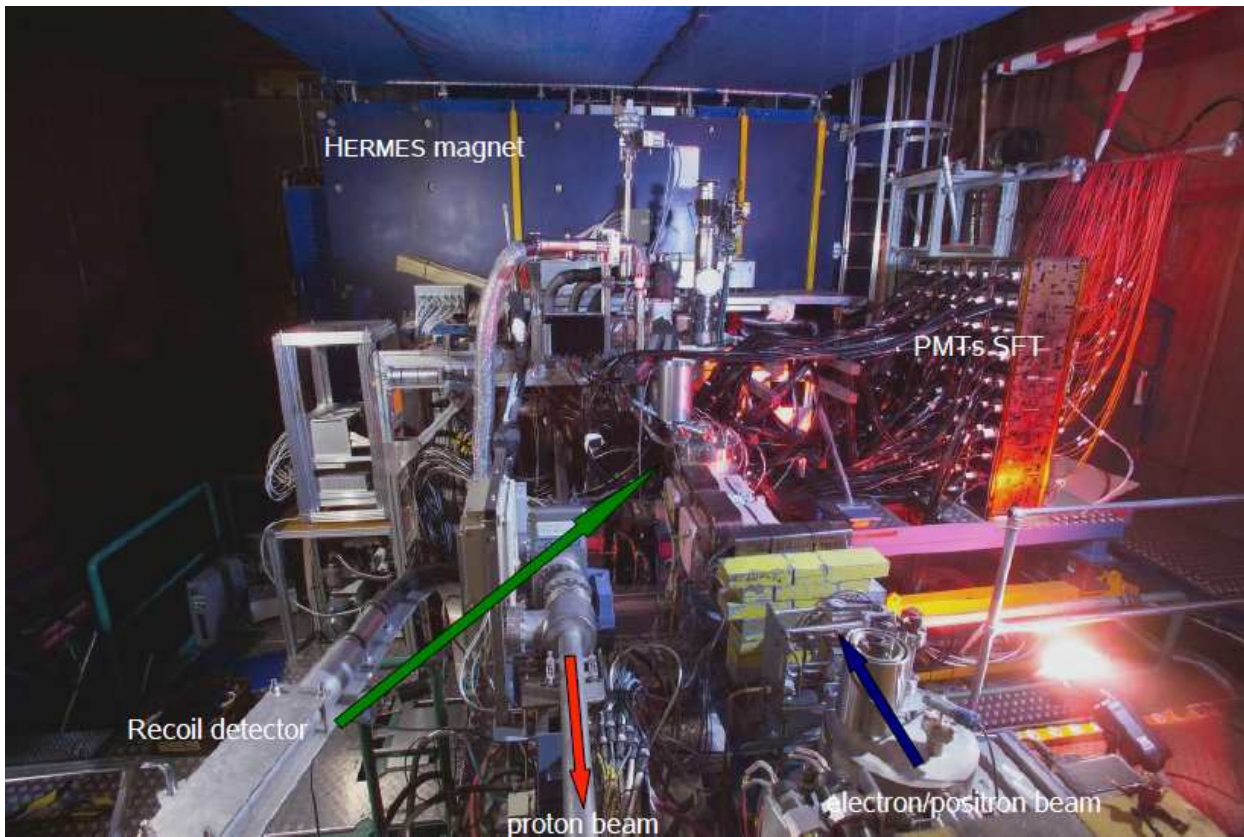
Figure 4.3: Photo of the Recoil Detector after installation where we can see the electron/positron beam pipe, the proton beam pipe passing through the HERMES experiment, the Silicon detector electronic on the left side and the Scintillator fibre PMT's wall with the light guides on the right side of the Recoil Detector.

4.1   Target Cell

The target cell used in the Recoil Detector was very similar to the existing one previously used at HERMES [26]. It was a very refined construction with a shorter active length. The target cell was an aluminium tube with only originally $50\mu m$ wall thickness. This decreasing of the thickness of the wall in the target cell compared to the $75\mu m$ for previous target cell at HERMES was motived by the possibility to lower the low-momentum cut-off of the silicon detector. The target cell had a elliptical cross section, with a major (minor) axis of $2.1(0.91)cm$. The length of the cell was minimized to give the maximum detector acceptance. To maintain the areal density, as the cell length decreases, the flux into the cell is increased. The pumping power that is needed to maintain the vacuum inside the chamber limits the target cell to a length of $15cm$, starting $5cm$ downstream from the center of the usual $40cm$ long target cell at HERMES. The storage cell acts as an internal windowless gas target in the lepton beam. Unpolarized gas was injected through a small capillary located on the lower side of the cell, running along the center of the tube [18].
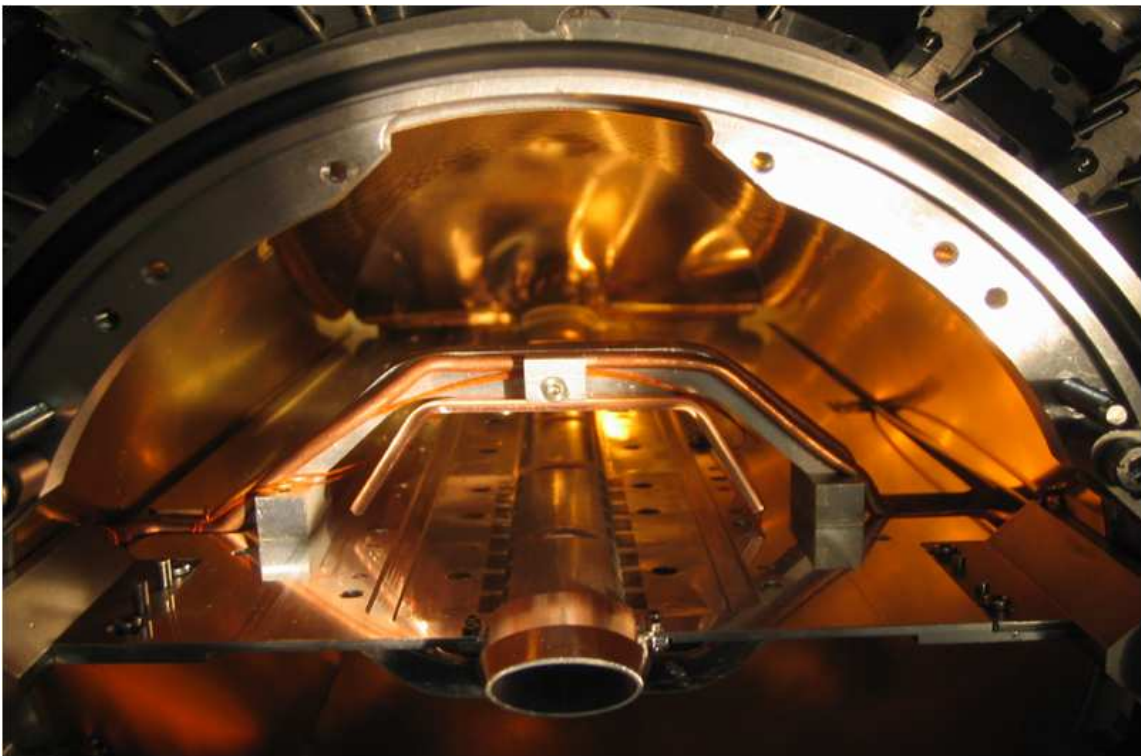
Figure 4.4: Photograph showing the target cell of the Recoil Detector with the new cooling circuit mounted on the target cell as installed during the shutdown of June 2006.

Due to damage in April 2006, caused by synchrotron radiation (SR) from orbit correction bumps, a new cell was rebuilt with additional cooling circuits on it. The new cell was designed and constructed in May and June of 2006. The target cell with a new cooling circuit is shown on Fig. 4.4. This new cooling circuit with a large water flow (of factor two) and close to the heat source was proven to work before installation. It was proved with readings from the experiment that the cell temperature was strongly reduced. Also the thickness was increased to make it more secure ($50\mu m$ Al foil was replaced by $75\mu m$) [71].

Several collimators were installed in front of the Recoil Detector protecting the target cell and the Silicon detector from synchrotron radiation. The scattering chamber covering the active area of the recoil detector and enclosing the vacuum region was $1.2mm$ thick. This was the main contribution of the momentum cut-off of the Scintillating fibre tracker detector.

4.2   Silicon Strip Detector

4.2.1   Detector design

The first sub-detector close to the beam axis was the Silicon Strip Detector (SSD) [72, 73]. Due to the very low energy of the recoil protons it was necessary to minimize the amount of material between the interaction point and the Silicon detector. This was the reason why the Silicon detector was installed in a so inhospitable place for detector and electronics components, inside the HERA ring vacuum in a scattering chamber. This required that all components of the detector and electronics are vacuum compatible. The HERMES experience operating Silicon detector in an ultra high vacuum (the Silicon Test Counter and the Λ-Wheels) was important to have trust in the technology for the recoil Silicon detector. This experience helped us to know how important it is to have a proper shielding against the radio frequency power generated by the HERA beam [18].
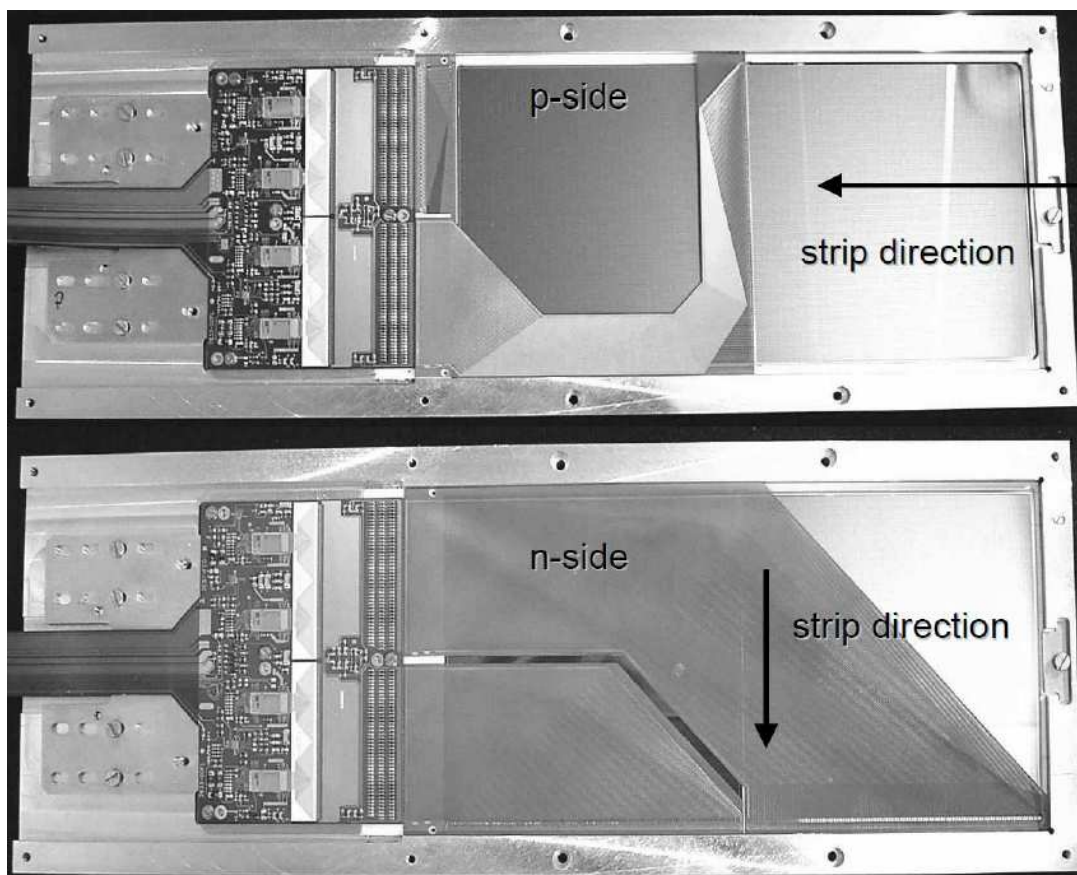
Figure 4.5: Photography showing the Silicon Strip Detector of the Recoil Detector. The p-side on top and n-side on bottom, the strip directions are indicated on the photograph parallel or perpendicular to the beam axes.

Due to financial and time considerations the recoil silicon detector was using an existing technology for the silicon microstrip and the readout chip. The detector consisted of 16 double-sided sensors of the TIGRE design from Micron Semiconductor (see Fig. 4.5) arranged in 8 modules which surrounded the target cell in two layer arranged in a diamond like shape (see Fig. 4.6). The sensors were $99mm \times 99mm$, their thickness was $300\mu m$ and a strip pitch was $758\mu m$ with 128 strips per side. It was the largest square double sided detector available [74], at that time.

Figure 4.6: Left panel: 3-D model of the HERMES recoil silicon detector, where we can see the support structure and the ceramic frame. Right panel: The cross Section of the recoil silicon detector, where we can see the relative positions in respect to the scattering chamber and the target [73].

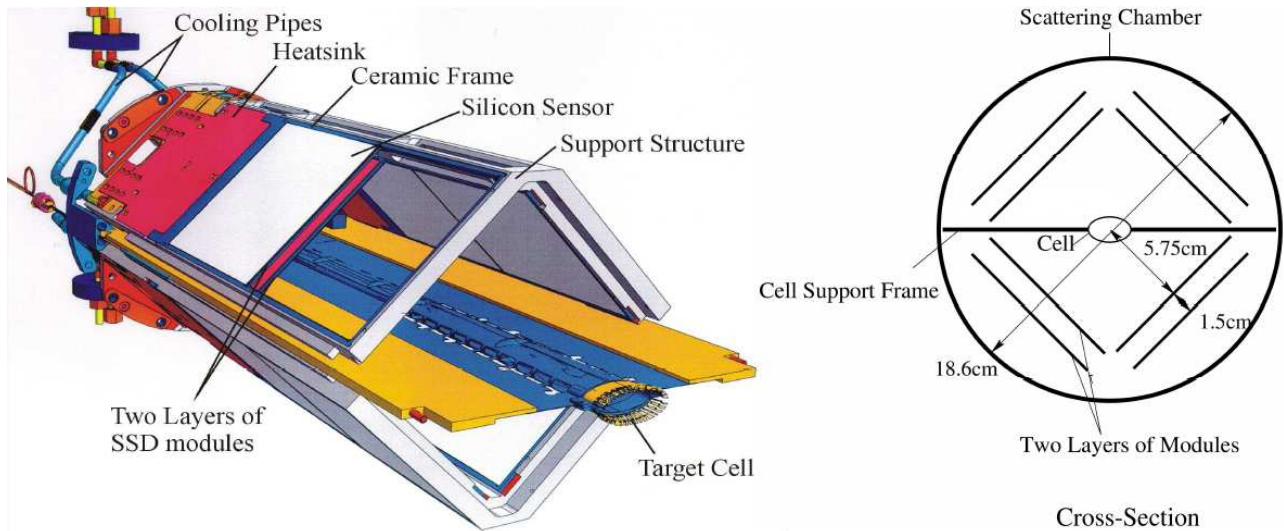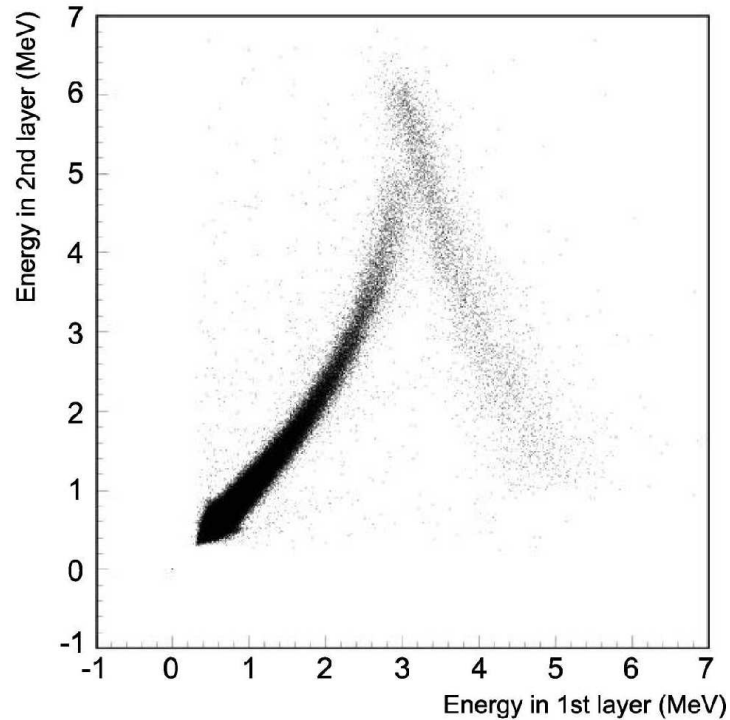Figure 4.7: Deposited energy in both silicon detector layers against each other.

The recoil proton in DVCS or EMP events, where the scattered positron produces a trigger in the HERMES spectrometer fly in phase space with a polar angle $0.1 \leq \theta \leq 1.35 rad$ in full 2π azimuthal acceptance. The length of the target was adjusted so that by placing two Silicon detectors one after the other along the beamline, it nearly covers the full polar angle θ of recoiling proton. This geometry had a 76% azimuthal coverage. The momentum and particle type was determinated from the energy deposited in the Silicon for protons with a momentum between $40 MeV$ and $106 MeV$ that were stopped in the first layer. Protons with momentum between $106 MeV$ and $135 MeV/c$ have just enough energy to punch through the target cell wall and the first layer of the silicon. They were stopped in the second layer. The energy deposit in each layer is shown in Fig. 4.7. Protons with higher momentum were passing both layers.

4.2.2 Read-Out Electronics

The HELIX128 3.0 chip was chosen as the analog readout chip [75]. It was operating at the $10.4MHz$, HERA bunch crossing frequency. The chip consists of 128 channels, each of them containing a charge sensitive preamplifier and a shaper, whose output was sampled into an analog pipeline with 128 memory cells to store the charge until the trigger signal arrived [76].
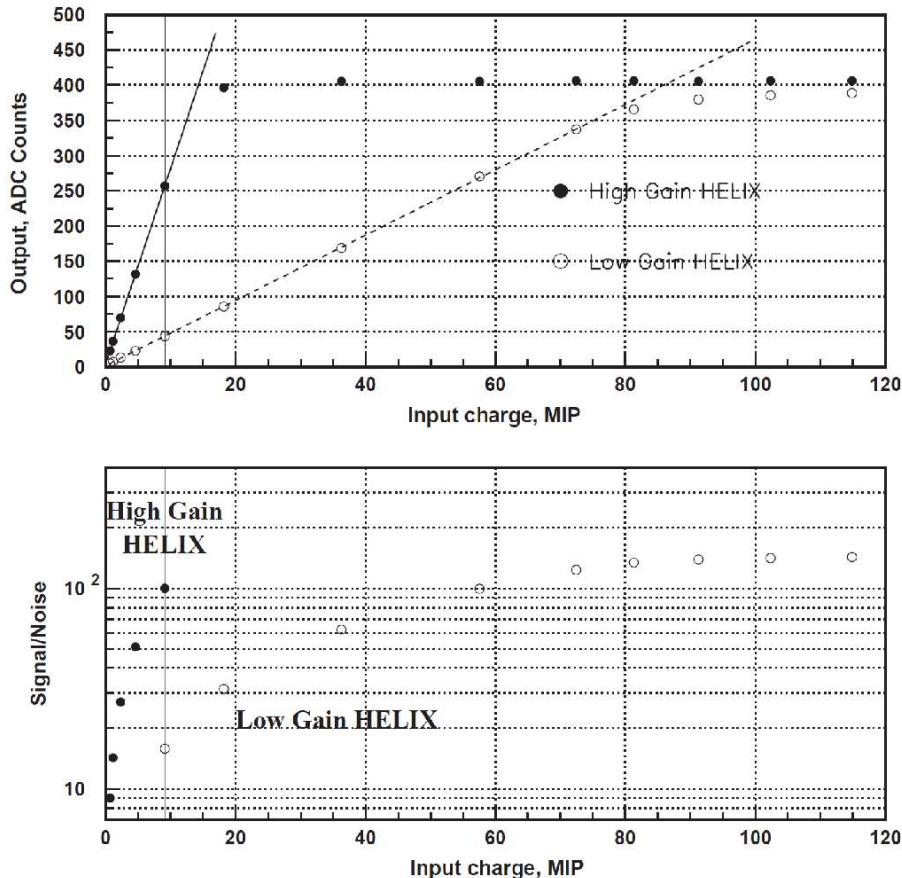
Figure 4.8: Measured response of the readout electronics against the charge injected at the input. Illustration of the increase of the dynamic range of the silicon detector. Every Silicon strip was connected with two readout channels, one high gain channel and one low gain channel through a capacitor.

To cover the larger dynamical range of the expected signal, the TIGRE sensors were connected to the readout electronics via charge divider capacitors. The final value chosen for the capacitance after charge injection tests was $10pF$. With this, the signal was split into high and low gain, which enabled a total dynamical range from $4fC$ up to $270fC$. Each of the 128 strips, per sensor, were connected to one input of two differents HELIX chips. With this, the dynamic range of the analog readout was drastically increased.

4.3 Scintillating Fibre Tracker

The Scintillating Fibre Tracker (SFT) was the second sub-detector of the recoil detector. The SFT detector was located outside of the beam vacuum, in between the scattering chamber and the photon detector in the solenoidal magnet. It contributes to the recoil particle detection with good azimuthal and polar angular resolution, good momentum resolution, charge determination due to the bending in the magnetic field and particle identification to discriminate pions and protons by analyzing the amount of deposited energy. It was designed to cover the full angular acceptance.

4.3.1 Detector design

The SFT was designed to detect and identify charged pions and protons of higher momentum which escape from the scattering chamber, in the range from $0.3 GeV/c$ up to $1.4 GeV/c$. Their momentum was determined by the deflection of the track in the longitudinal magnetic field which also allows charge identification. The radius of curvature ρ in meters of the particle track in the magnetic field is given by

$$\rho = \frac{p_\perp}{0.3 \cdot eB}, \tag{4.1}$$

with $p_\perp (GeV/c)$ being the transverse momentum with respect to the magnetic field $B(T)$ and e being the particle charge. Additionally, the charge of the particle was deduced from the curvature of the track. For example, for a positive particle with a momentum of $500 MeV/c$ in $1T$ magnet, the radius of curvature ρ is about $1.5m$.
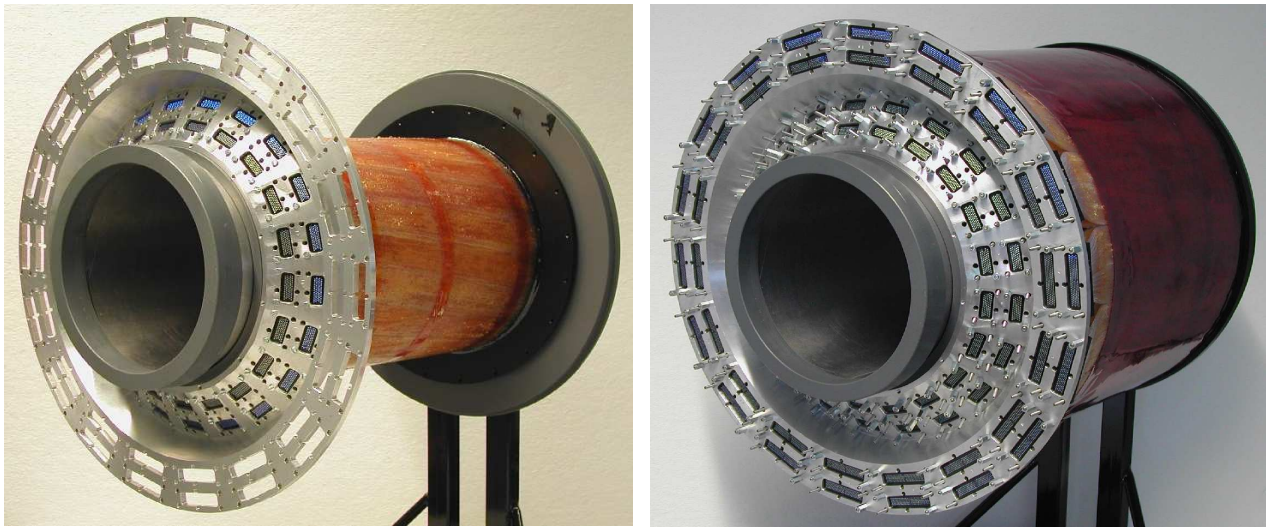
Figure 4.9: Scintillating Fibre Tracker pictures. The left picture shows the SFT with only the inner barrel in place, the right picture shows the completely mounted SFT. Kapton film on the outer barrel serves as a protection from mechanical influence

The SFT consists of two concentric barrels of different diameters with two double layers, as shown in Fig 4.9. For each barrel, the inner double layers were made by scintillating fibres parallel to the beam axis while the outer double layers were made by scintillating fibres stereo tilted with a angle of 10° with respect to the beam axis, as shown in the left of Fig 4.10. The inner(outer) barrel has a diameter of $109mm(183mm)$. Each layer was made of $1mm$ diameter scintillating fibre shifted by half fibre one relative to the other one in the same double layer, as shown on the right of Fig. 4.10).

Figure 4.10: The arrangement of the fibres in the two barrels, the illustration of the tracking concept are shown in the left panel and in the right is shown the detailed geometry structures of the fibres.

The barrels were built as self supporting structures to minimize the material traversed by the particles. Each barrel layer was assembled using pre-shaped modules consisting of 64 fibres for the inner SFT and of 128 fibres arranged in four layers. The Fig. 4.9 shows a front view of t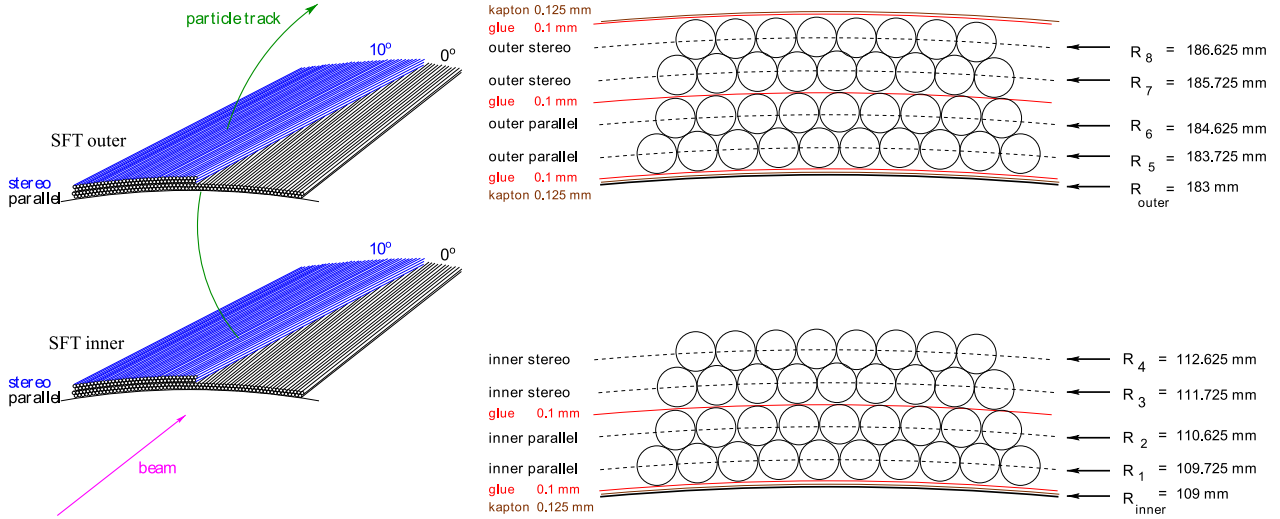he SFT, i.e. the connector plate with all 42 inner and 36 outer (in total 78) connectors. During the construction of the barrels, pairs of fibres were removed from the modules to achieve the correct barrel radius. The inner barrel consists of two layers of 657 parallel scintillating fibres and two layers of 660 stereo scintillating fibres. In total the inner SFT barrel consists of 1314 parallel scintillating fibres and 1320 stereo scintillating fibres.

NUMBER OF FIBRES AND READ-OUT CHANNELS

		FIBRES	READ-OUT
SFI-1		657	657
	INNER PARALLEL		
SFI-2		657	657
SFI-3		660	660
	INNER STEREO		
SFI-4		660	660
SF0-1		1098	
	OUTER PARALLEL		1098
SF0-2		1098	
SF0-3		1090	
	OUTER STEREO		1090
SF0-4		1090	
TOTAL		7010	4822

Table 4.1: Number of fibres and corresponding readout channels per Scintillating fibre layers.

The outer barrel consists of two layers of 1098 parallel scintillating fibres and two layers of 1090 stereo scintillating fibres, in total the outer SFT barrel consists of 2196 parallel scintillating fibres and 2180 stereo scintillating fibres. In the inner barrel every fibre was read out by one read-out channel, in the outer barrel two adjacent fibres, on different layers of the same type (parallel or stereo), were read out by one read-out channel (see Table 4.1). This yields to an azimuthal resolution of around $0.008rad$.

The cluster information was achieved by the combination of hits in each double layer of each barrel. The extraction of the spacepoints was reached by the combination of neighboring clusters of different double layers

of the same barrel. Due to this configuration the SFT provides up to two additional space points. Together with the space point provided by the Silicon detectors the particle track was completely reconstructed.

4.3.2 Multi Cladding Fibres

The scintillating fibres for the SFT detector are from the company KURARAY, model SCSF-78M. The model SCSF-78M is a multicladding fibre with $1mm$ diameter. The fibres were mirrored at the far end to increase the light yield by about 20%, with this mirroring of the far end of the fibres the reduction of the light yield due to the glue applied to the fibres shell during the construction was compensated. This was estimated around 20% (see ref. [87]).
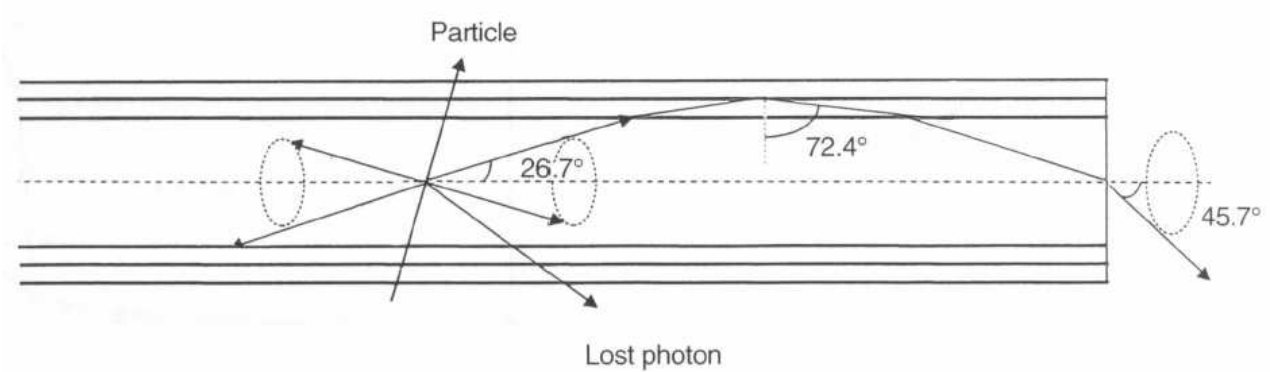

Figure 4.11: Light propagation in a scintillating fibre from the company KURARAY, model SCSF-78M. [88].

Multi cladding fibre (M) has 50% higher light yield than single cladding fibre because of a large trapping efficiency. Clear-PS fibre of this cladding has extremely higher numerical aperture (NA) than conventional Polymethylmethacrylate (PMMA) fibre, and very useful as light guide fibre. Multi cladding fibre has a long attenuation length compared to single cladding fibre. A schematic drawing of multi cladding fibre and the light propagation is shown on Fig 4.11.

MATERIALS

	MATERIAL	REFRACTIVE INDEX	DENSITY $\rho[g/cm^3]$	RADIATION LENGTH $X_o[g/cm^2]$	NUMBERS OF ATOM PER cm^3
Core	Polystyrene (PS)	$n_D = 1.59$	1.05	43.8	$C : 4.9 \cdot 10^{22}$ $H : 4.9 \cdot 10^{22}$
Inner *Cladding*	Polymethylmethacrylate (PMMA)	$n_D = 1.49$	1.19	40.55	$C : 3.6 \cdot 10^{22}$ $H : 5.7 \cdot 10^{22}$ $O : 1.4 \cdot 10^{22}$
Outer *Cladding*	Fluorinated polymer (FP)	$n_D = 1.42$	1.43	40.55	

Table 4.2: Material of the KURARAY SCSF-78M multicladding fibres of 1mm diameter [87, 88].

The fibre core consists of Polystyrene (PS)[1] mixed with scintillation dopants. These dopants determine the scintillating, optical and mechanical properties of the fibres. The cladding of the fibre consists of Polymethyl-

---

[1]$C_6H_5CH{=}CH_2$ [87]

methacrylate (PMMA)[2] for the inner cladding and Fluorinated polymer (FP) for the outer cladding (see Table 4.2). There are no scintillating dopants in the cladding, scintillation can't occur in the cladding. The cladding protects the core of the fibre from mechanical damage thus ensuring perfect surface conditions for the total reflection and it's also prevents light leaking into the neighboring fibres (see Fig 4.12).
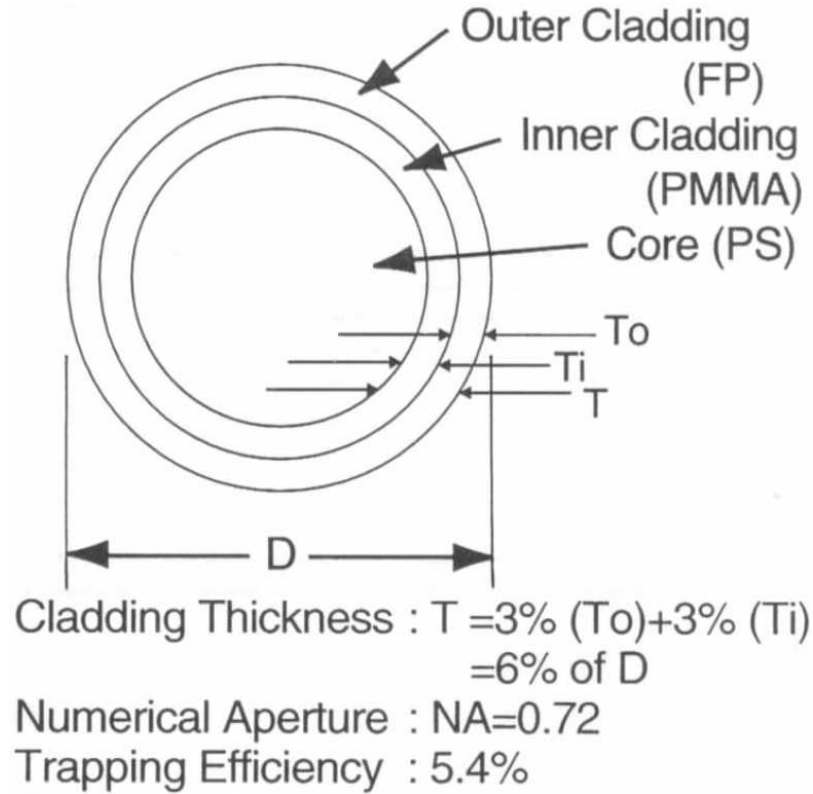

Figure 4.12: Cross section and Cladding Thickness of fibres from KURARAY company model SCSF-78M. [88].

CHARACTERISTIC

PEAK EMISSION	$450\ nm$ blue
ATT. LENGTH	$> 4.0\ m$
DECAY TIME	$2.8\ ns$
CLADDING THICKNESS	$T = 3\ \% \ (T_{outer}) + 3\ \% \ (T_{inner}) = 6\%$ of D
NUMERICAL APERTURE	$NA = 0.72$
TRAPPING EFFICIENCY	$5.4\ \%$
TOLERANCE IN DIAMETER	Cut Fibres ($1{\sim}5\ m$ long) :$|\Delta D/\bar{D}| < 2.0\ \%$ for round fibre.

Table 4.3: Properties of the KURARAY SCSF-78M multicladding fibres of 1mm diameter [88].

The basic characteristics of the KURARAY SCSF-78M multicladding fibres of 1mm diameter are given in Table 4.3. The cladding thickness amounts to 3% of the overall diameter for the inner and another 3% for the outer cladding. The active fibre core has a diameter o $0.94mm$, and the tolerance in diameter is specified by the manufacturer, to be below 2% [88].

---

[2]$C_5H_8O_2$ [87]

4.3.3 Read-out of the SFT

The read-out of the scintillating fibre had several difficulties. First of all the Recoil Detector was surrounded by a superconducting solenoid magnet with a field of $1 Tesla$. The limited space in the target area was very tight due to the pumps for the vacuum system and the cabling of the other detectors of the Recoil detector. A combination of clear fibre acting as light guides and Multianode Photomultiplier Tube was used to accomplish the read-out of the SFT detector.

Light guide (LG)

The SFT fibres were read out via $\sim 4m$ long light guides of Kuraray clear fibres connected to Hamamatsu H7546B 64 channel MAPMTs. Each light guide was a fibre bundle of 64 fibres for the inner barrel and 128 fibres for the outer barrel. They were wrapped in black plastic tape. In most light guides the tape was directly applied to the fibre bundle; in the first design there was a thin layer of plastic foil between the fibres and the black tape.
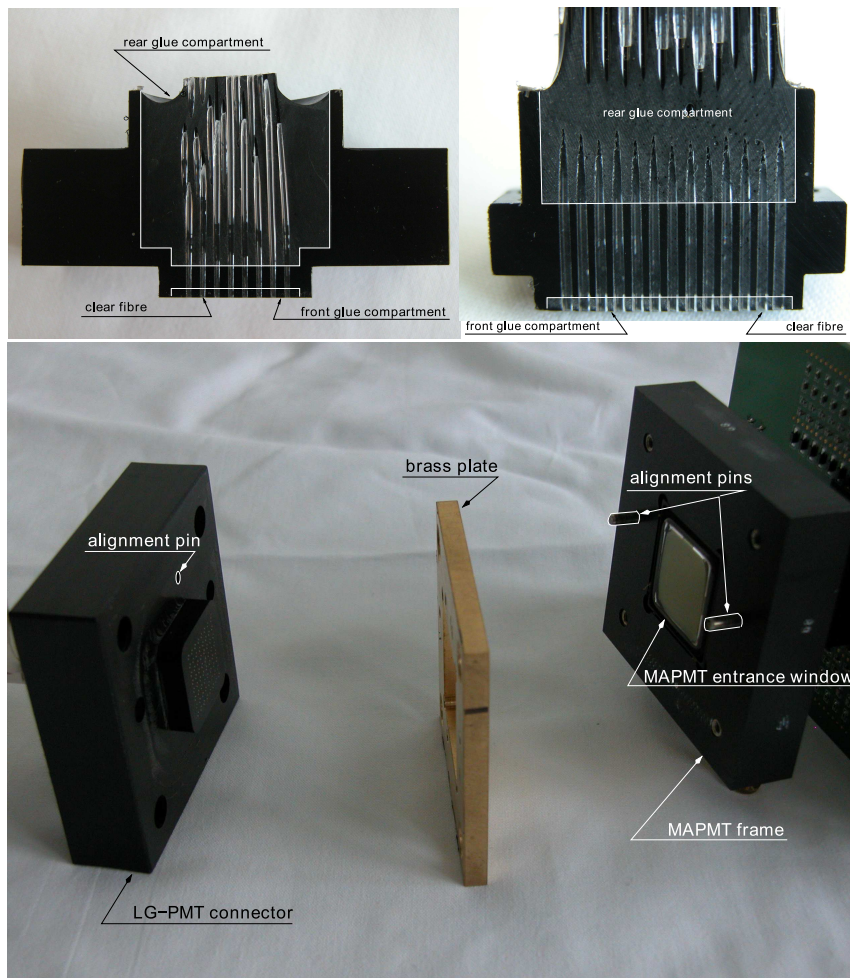

Figure 4.13: Top figures: cross section of the LG connectors for the MAPMTs on the left and the SFT detector on the right side. Both glue compartments are indicated by white lines. Bottom figure: Overview of the LG-MAPMTs connection. Alignment pin positions of the LG and MAPMT frame are indicated. The brass plate in between of the MAPMT and the LG ensures a precise alignment of the LG on the MAPMT cathode.

In order to minimize optical crosstalk on the MAPMTs' cathode, the light Guide fibres were centered on the corresponding pixel. Furthermore, each light guide were centered precisely on the corresponding MAPMT.

All SFT connectors were made of black Poly-Oxy-Methylene (POM), the same material as the MAPMTs' housing. POM offers similar thermal characteristics as the fibre material (PS, PMMA) and can easily be machined with high precision. The black POM is also light-tight and thus suppresses crosstalk inside the connectors. The high precision CNC[3] machine was needed to achieve the connectors' design. The fibres were finally glued to the connectors with a special glue to avoid the corrosion of the cladding and by consequence the degradation of the optical characteristics. A slow curing solvent-free epoxy resin[4] was chosen, which is then mixed with black dye to prevent crosstalk in the connectors and absorb any remaining cladding light. The cured epoxy also allows the polishing of the surfaces shown in Fig 4.13, necessary for achieving high transmission efficiencies.

The connection of the LG on the MAPMT consists of three pieces: a frame (where the MAPMT was glued), a brass plate and the LG connector. The MAPMT frame and the LG connector have a set of two alignment pins each, the position of which was precisely controlled. A brass plate in between of these two pieces was used to align the LG connector to the center of the MAPMTs' cathode, taking into account only the guiding holes of the MAPMTs' cathode offset. The advantage of this technique is to have the possibility to mass produce the LGs and interchange them, because only the guiding holes of the brass plate have to be set according to one individual MAPMT offset. This, in turn, means that for each MAPMT an individual brass plate had to be manufactured which can not be exchanged to any another MAPMT.

Multianode Photomultiplier Tube

The scintillating light was detected with Multianode Photomultiplier Tube, shown in Fig 4.14. This MAPMTs model is the Hamamatsu R5900-00-M64 (Fig 4.14(a)) assembly from the manufacturer in the model Hamamatsu H7546B (Fig 4.14(b)). The anodes of the MAPMTs are arranged in an 8×8 array. In total 78 MAPMTs of 4992 channels are needed to read out the 7010 fibres of the SFT disposed in 4822 channels. The size of each anode pixel is $2 \times 2 mm^2$. Detailed drawings, geometries, distribution, characteristics and main parameter are given in [89].

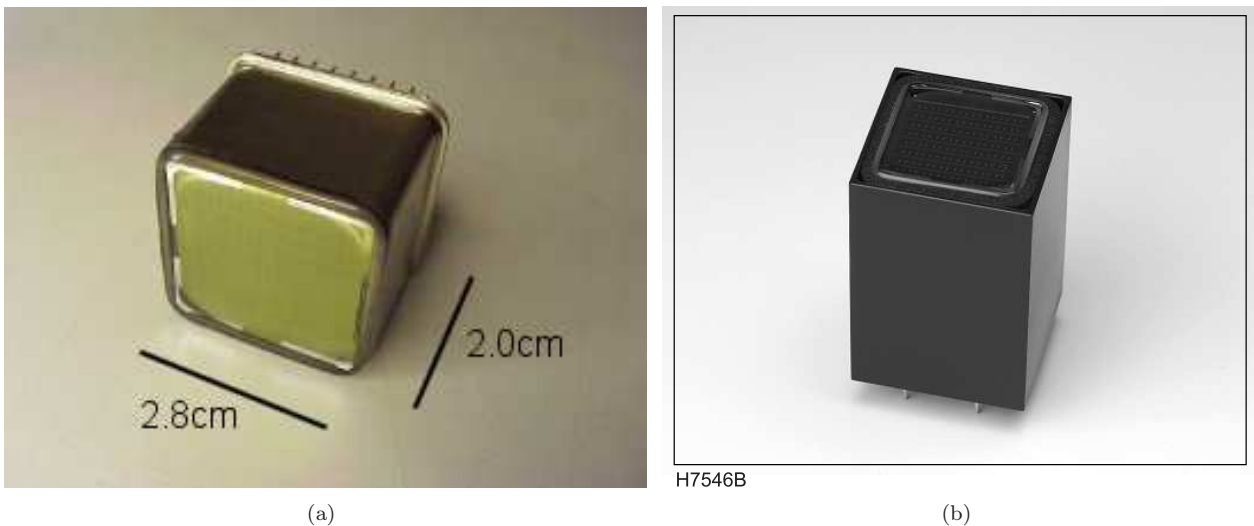| (a) | (b) |

Figure 4.14: Hamamatsu R5900-00-M64 Multianode Photomultiplier Tube from Hamamatsu company model without housing and voltage divider is show on Fig. 4.14(a). The final assembly from the manufacturer of the model Hamamatsu H7546B [89] is show in Fig. 4.14(b).

---

[3]Computerized Numerical Control
[4]Vosschemie Epoxiy BK

Readout electronics

The readout electronics for the SFT detector used one modification of the design of the HADES[5] RICH [90] readout. Therefore the inhouse high density ADC readout had a very low cost per channel. Detailed documentation about the Analog to Digital Converter can be found in [90]. The analog signal from the MAPMTs was processed and digitalized in 64 channel Preprocessing Frontend Modules (PFM). In order to adapt the fast MAPMT signal to the PFM, a Charge Divider Circuit (CDC) was integrated on the Photomultiplier Board. A schema of the CDC is shown in Fig. 4.15.
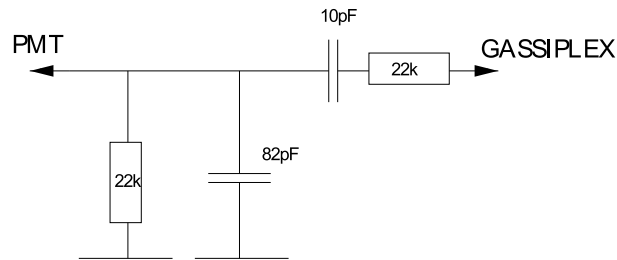

Figure 4.15: Schema of the Charge Divider Circuit (CDC) to adjust resistance of the MAPMT and the GASSIPLEX chips [87, 91]. Interface between MAPMT as signal source and the track and hold unit GASSIPLEX as signal drain.

A schema of the PFM is shown in Fig. 4.16. The main components of the PFM are the four GASSIPLEX chips for the analog signal processing. Each of these are 16 channel analog integrated circuit which use the peaking time of the integrated and shaped signal as a delay, allowing an external trigger to memorize the information in a track-and-hold analog circuit.
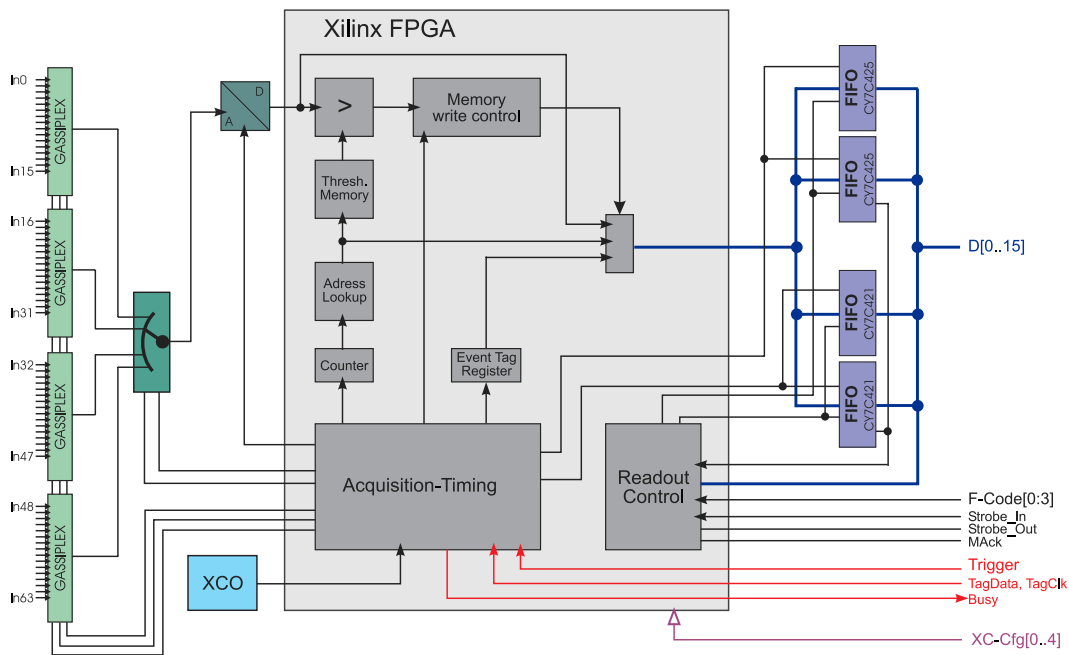

Figure 4.16: Schema of the Preprocessing Frontend Module (PFM) [90]. The green part is responsible for the digitization. The gray part contains the Xilinx FPGA as the local controller and the memory for the thresholds of the sparsification unit. The blue part represents the buffering of the interfacing signal [90, 18, 91].

---

[5]High Acceptance DilEpton Spectrometer

The hardware was based on versatile FPGA chips which consist of a grid of logic gates and can be reprogrammed for different functionality. This provides flexible adjustment of the signal flow and of the control flow of the Data Acquisition (DAQ). The external trigger was delivered to the GASSIPLEX chips of the PFM. After the digitizing of the analog signals, the optional sparsification were performed. The readout of the available data was done by a Readout Controller (RC) via a standard PC or via a Digital Signal Processor (DSP) located in the VME crate controller.

In order to avoid malfunction by weak galvanic connections, the MAPMT was soldered on to the Printed Circuit Board (PCB) as shown in Fig. 4.17. The square soldering bed was surrounded by the resistance adaption.
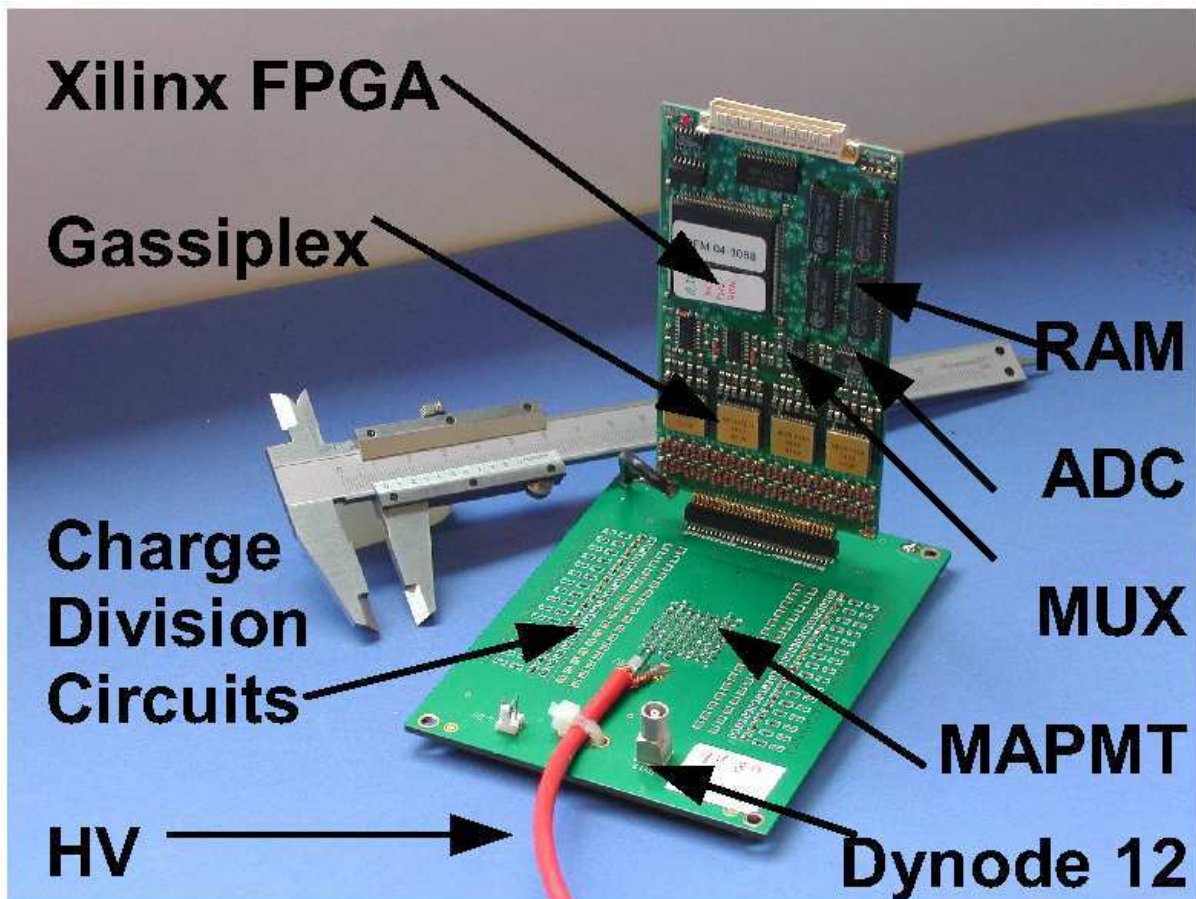

Figure 4.17: Photo of the Printed Circuit Board (PCB) of the CDC and PFM. The PCB hold the soldered MAPMT and the charge division circuits (CDC) the PFM-PCB contains the electronics for the digitization and sparsification [91]

The Gassiplex chips for analog signal processing, which were developed at $CERN$, were the main components of the PFM. Each Gassiplex chip is a 16 channel analog integrated circuit, which has charge sensitive amplifiers, and a selectable filter in order to change the polarity of the analog signal. The integration time of the Gassiplex is around $600ns$, when the HERA bunch cycle time was $96ns$. In order to decide if the signal (which was using negative input signal, and work in a dynamic range up to $500fC$ with a gain of $2.2mV/fC$) corresponds to the right bunch a secondary readout chain was implemented [92].

The readout electronics described above was tested at the University of Gießen. Although designed for long, positively charged pulses, a readout of the short, negative pulse signals was achieved.

4.3.4 The TDC readout of the $12th$ dynode

Due to the SFT detector readout characteristics, the fast scintillator/PMT signals of $10 - 20ns$ length were converted to slow signals with a width of $600ns$ (FWHM). The readout system was not able to distinguish between signals from the HERA bunch which generates the HERMES readout trigger and background signal from adjacent HERA bunches. This can either spoil a true signal due to pile-up with a background event or it can generate ghost hits in one of the SFT detectors. A proper measurement of signal height was crucial for a good particle identification and low number of ghost hits was important for good tracking.

To get rid of the disadvantage of the readout system, it was planned to use the signal from the $12th$ dynode to determine a timing of the signals and to reject all signals from a PMT with a wrong timing. As the $12th$ dynode is common for all 64 channels [89], the relation between ADC and TDC signal was not necessarily unique.
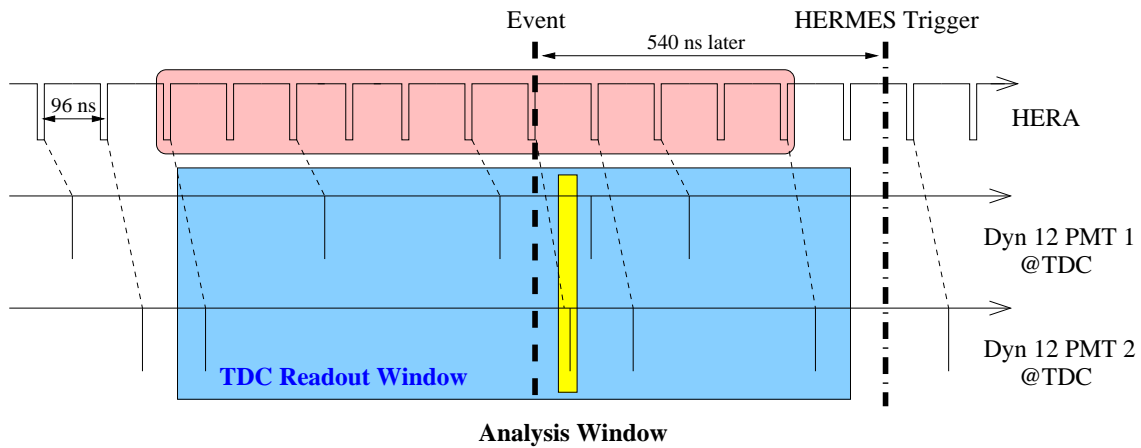

Figure 4.18: The upper graph shows the time structure of the HERA bunches. The shaded area shows the 6 bunches before and 4 bunches after the event. The two time graphs below illustrate two cases with different hit patterns for two PMTs. The lines indicates hits from the dynode 12 at the TDC [92].

The basic principe of the TDC readout is sketched in figure 4.18. The upper graph shows the time structure of the HERA bunches. The shaded area indicates the 6 bunches before and 4 bunches after the event, which have to be taken into consideration. A TDC readout window with these 11 bunches (lower shaded area) will be defined with respect to the HERMES trigger, which arrives $540ns$ later at the target platform.

The two time graphs below illustrate two cases with different hit patterns for two PMTs. The lines indicate hits from the dynode 12 at the TDC. In the first example no hit lies inside the analysis window. All ADC signals from this PMT can be rejected. The measurement of the second example needs a more sophisticated analysis. One ADC channel corresponds to the HERMES event. But, in addition, two ADC signals have a wrong timing. As only one timing is measured for all 64 channels of a PMT, each TDC timing can be correlated to more than one ADC channel.

The setup was consisting of an amplifier, discriminator and TDC. In the first stage the 12th dynode signal was amplified. Tests showed that an amplification of 10 was needed. The 16 Channel Leading-Edge Discriminator LE1600 was packaged in a single-width CAMAC module. It was designed by GSI [93]. The CAEN Mod. $V767$ 128 channel General Purpose Multihit TDC was the feature of the so called "stop trigger matching" mode. In this mode an event consists of a group of hit signals that reach the enabled channels within a time window of programmable width and relative position to the common trigger signal [94]. This single width VME module was located in the SFT VME crate. The TDC was read out together with the readout controller of the MPFMs. The additional NIM and CAMAC crate was located in the rack, which was used for the VME readout, too. The CAMAC crate was controlled by a SIS 5100 Controller.

4.4 Photon Detector

The photon detector's (PD) main objective was to detect photons coming from Δ^+ decay ($\Delta^+ \to p\pi^0 \to p\gamma\gamma$). The PD improves the capability to suppress background by rejecting events in which an intermediate Δ^+ resonance was produced. This was accomplished through the detection of at least one of the photons emitted by the decay of the neutral pion created in the decay of the Δ. These photons were not seen by the Silicon and SFT detector and therefore could be identified as trackless clusters if they hit the photon detector.

The PD was able to complement the tracking of the Recoil Detector, the first layer of the photon detector was contributing to the p/π separation for momentum higher than $600 MeV$. And finally, it was also used to provide a cosmic trigger for the cosmic test and internal alignment of the Recoil sub-detectors.

Figure 4.19: Photograph of the photon-detector. Internal setup of the Photon Detector during production and before mounting the light tide coverage. The green fibres of the wave-length shifters illustrate the three different orientations ($0^0, \pm 45^0$) of the strip segments. The black fibres are used by the gain monitoring system [95].

4.4.1 Detector design

The Photon detector consists of concentric barrels with an inner diameter of $191.75mm$, $51.5mm$ thick, leaving $8.5mm$ of free space for the installation[6]. It has an active length of $288mm$ (acceptance covers the 2π azimuthal angle and the polar angle covers between $0.78 < \theta < 1.90rad$) and consists of six layers, alternating between a tungsten layer, from which incident charged particles produce electromagnetic showers, and scintillator layers, which detect the showers. From inside out, there is $6.3mm$ tungsten, a layer of 60 scintillator strips oriented parallel to the beam axis, a layer of $3.5mm$ of tungsten, a layer of 44 scintillator strips that make an angle of 44.58^0 with the beam direction, and the last layer of $3.5mm$ tungsten and finally there is a layer of 44 scintillator strips that make an angle of -46.55^0 with the beam direction [96].
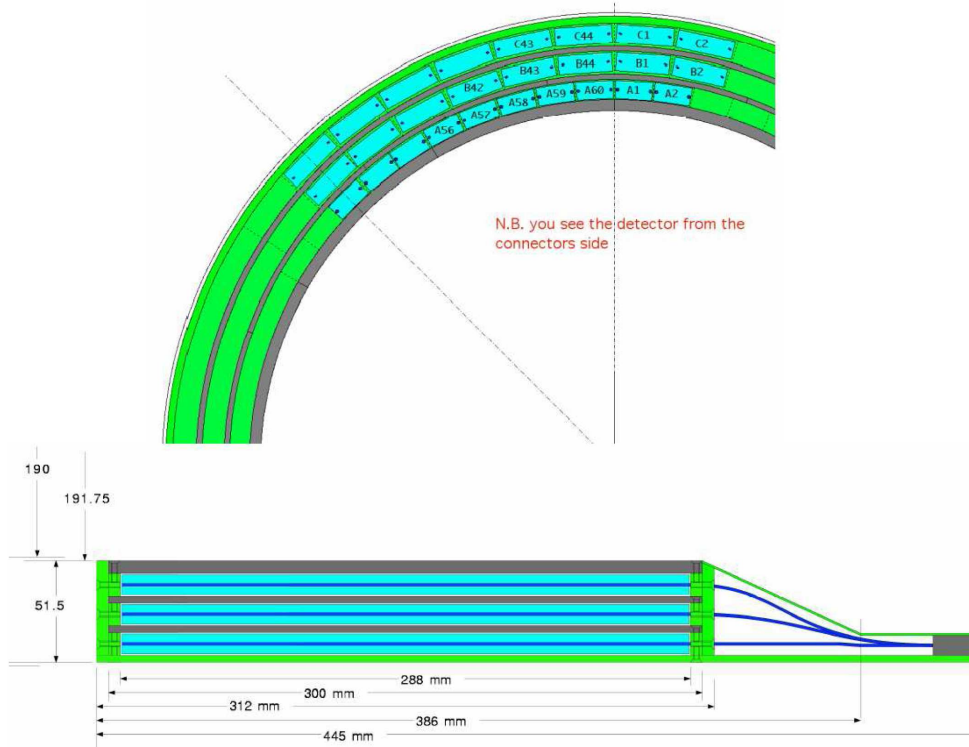

Figure 4.20: Schematics of the photon detector. The upper diagram is shown from the upstream perspective the setup of the layers partially projected on the $x - y$ plane. The lower diagram shows the longitudinal cross-section of the projection on the $x - z$ plane [96].

The inner scintillator layer was called the **A-LAYER**, the middle one the **B-LAYER** and the outer one the **C-LAYER**. All scintillator strips were $110mm$ thick and have the same dimensions $(21, 20) \times 10 \times 288mm^3$ (see Fig 4.20). Layer A was trapezoidal and layers B and C were rectangular. Fig 4.19 illustrates the geometry of the PD. Every scintillator was connected to two wave-length shifters that end in a connector ring on the edge of the detector. These connectors were connected to the wave-length shifters through light guide with multi-anode PMTs (MAPMTs). The multi-anode PMTs were then read-out by charge sensitive ADCs. These was the same types of multi-anode PMTs used by the SFT detector. The light coming out of the wavelength shifter was guided towards the PMTs through light guides of $2m$ length. Every channel from the light guide was separately encapsulated in black plastic to protect them from the outside light and the photons from neighbor channel photons. The light guides were read-out by the same type of MAPMTs as the SFT detector, only 6 HAMAMATSU H7546B PMTs were necessary. The connection of the light guide to the MAPMTs happens through a POLY-OXY-METHYLENE (POM) matrix.

---

[6]The inner radius of the magnet was changed from 24.5 to $25cm$. Before only $1.75mm$ of free space above and below the photon detector was available for mounting, as indicated in Fig. 4.20 [96].

4.5   Superconducting Magnet

In order to reconstruct the momentum by the bending radius of the detected charged particles, a magnet surrounded the recoil detector. The recoil detector magnet was a superconducting solenoid magnet, cooled with liquid helium, with a magnetic field strength of $1Tesla$ longitudinally with the beam direction. Additionally, the magnet protected the recoil detector, especially the Silicon detector from background electrons emitted from Møller Bhabha scattering events by deflecting them.

Figure 4.21: Photograph of the Recoil Detector Superconducting Magnet.

The magnet and its cryostat was built by EFREMOV INSTITUTE, ST. PETERSBURG [98] and commissioned by HERMES collaboration. The Photo is shown in Fig. 4.21.

The magnet was designed as a short superconducting solenoid with Helmholtz coils inside a liquid helium bath. With a current of $166A$ the solenoid provides a $1T$ field with a 20% field homogeneity inside the operating region: a $250mm$ radius cylinder $300mm$ long centered in the target cell. The inductance of the coils was $\sim 10H$ and the stored energy was $144.5kJ$.

4.6 Gain Monitoring System

The Gain Monitoring System (GMS) consist of a light source containing 19 blue LEDs driven by a CAEN C529 LED driver module, utilizing scratched clear fibres guiding the light to the SFT detector and injecting it inhomogeneously into the fibres [97].
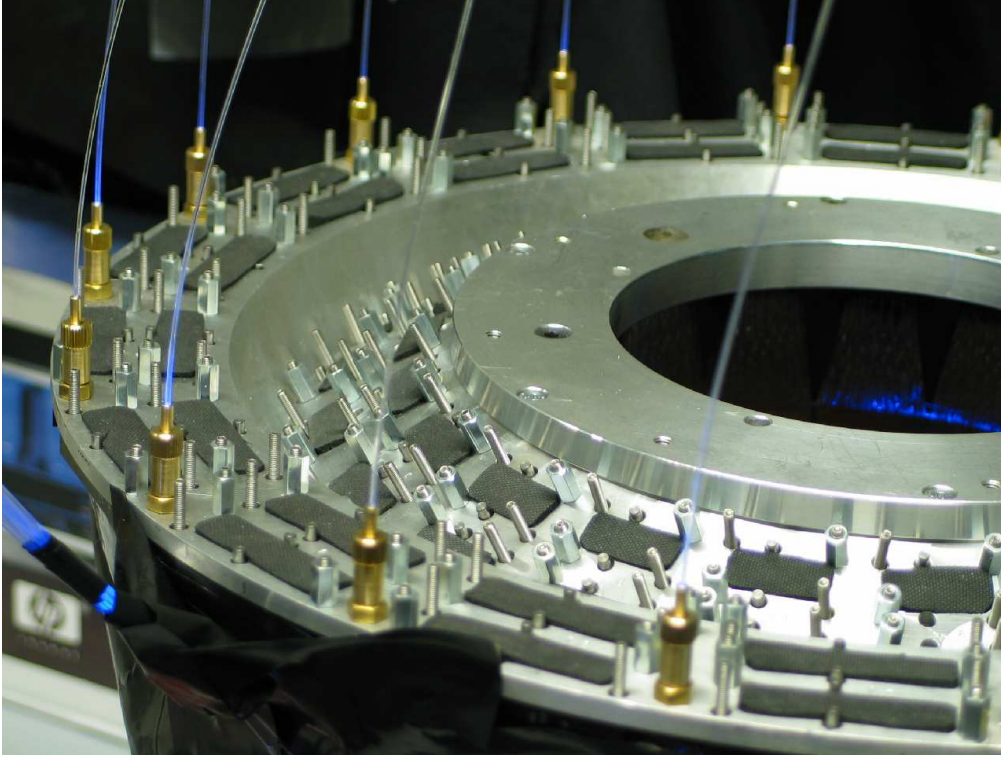

Figure 4.22: Gain monitoring System (GMS) fibres connected to SFT.

The stability of the LEDs was monitored by a PHILIPS PHOTONICS 1911 reference PMT that also reads out the very stable light output from an α-source surrounded by a YAP scintillator crystal. This reference PMT and the α-source were used at the same time by the Photon detector and the SFT detector.
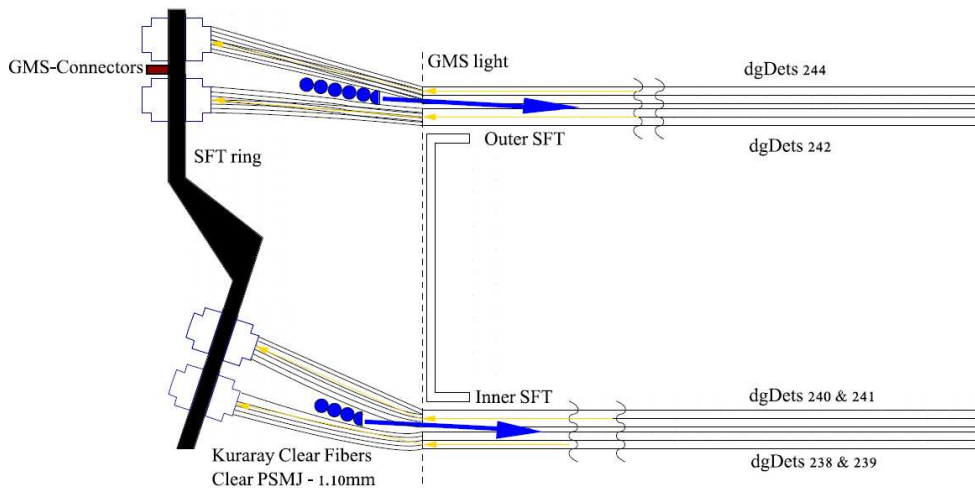

Figure 4.23: Schema of the Gain Monitoring System (GMS) installation position.

The measurements of the GMS-light with the SFT MAPMTs, the reference PMT, and the α-source were taken before each beam injection into HERA, with the same script routine as the pedestal, for the pedestal correction before data acquisition. Due to this constraint it was not possible to use the bunch free zone (where none of the buckets were filled) with an online GMS system without interference of the background generated by the accelerated particles, like in the HERMES spectrometer.
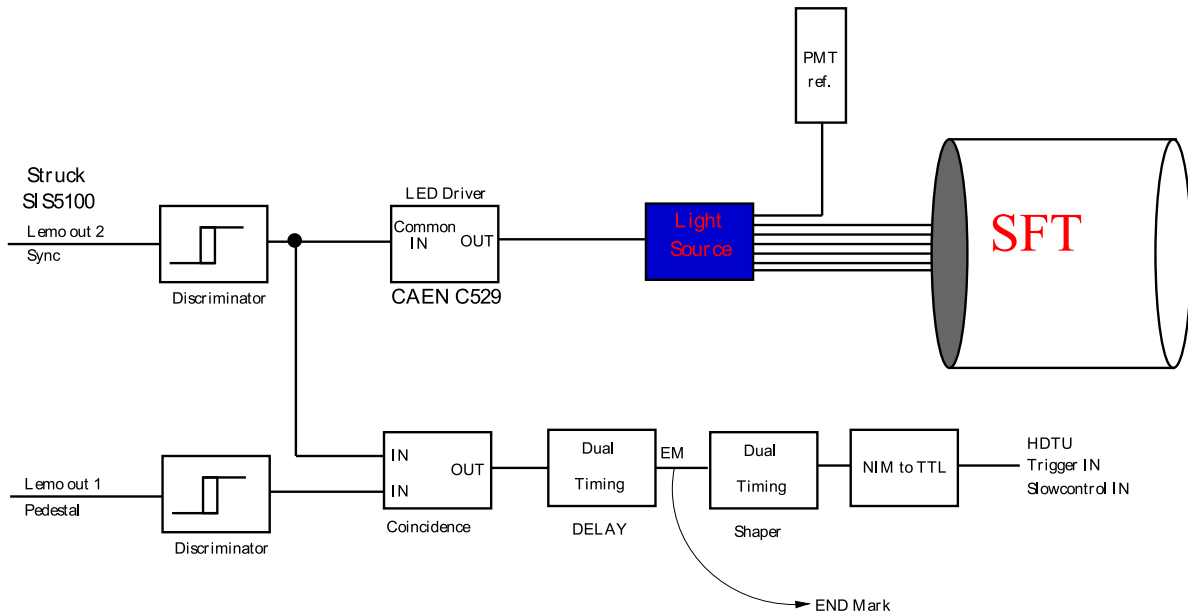

Figure 4.24: Schema of the Gain Monitoring System (GMS) electronic.

The scratched clear fibres guide the light to the SFT and inject it inhomogeneously into the SFT. The installations are shown in Fig. 4.22 and 4.23. There was no direct coupling between the scratched fibres and the SFT modules, due to only a small fraction of re-emitted light entering in the fibres. This method was able to reach several layers of the SFT with the same light source.

CAEN C529 LED driver module used at the *COMMON IN* the synchronize discriminated signal of the struck SIS5100 to puls the light source. The light of the light source at the same time was injected into the SFT detector and the reference PMT. The same discriminated signal going to the LED driver module was inserted into the coincidence module, for triggering (see Fig. 4.24).

4.6.1 Light source

The GMS Light source, shown on Fig. 4.25, should provide light to be transported by fibres to the detector and the reference PMT. For this propose 19 LEDs were used in the light source. They were symmetrically disposed on a concentric surface around the main axis of the light source (see Fig. 4.26). The sphere was fixed with individually adjustable distance rods (part 3) on the mounting plate (part 1).
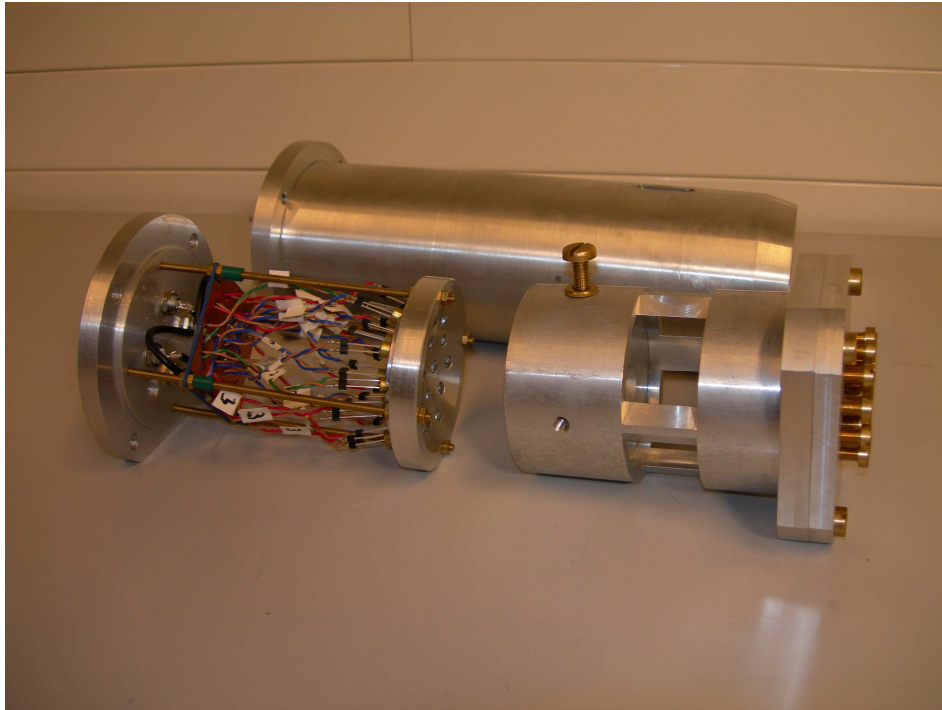

Figure 4.25: Photograph of the Light source for the SFT-GMS. At the middle of the picture are the LED support. The fibres are not installed, they should be fixed on the far right in the cover with the pressure screw.

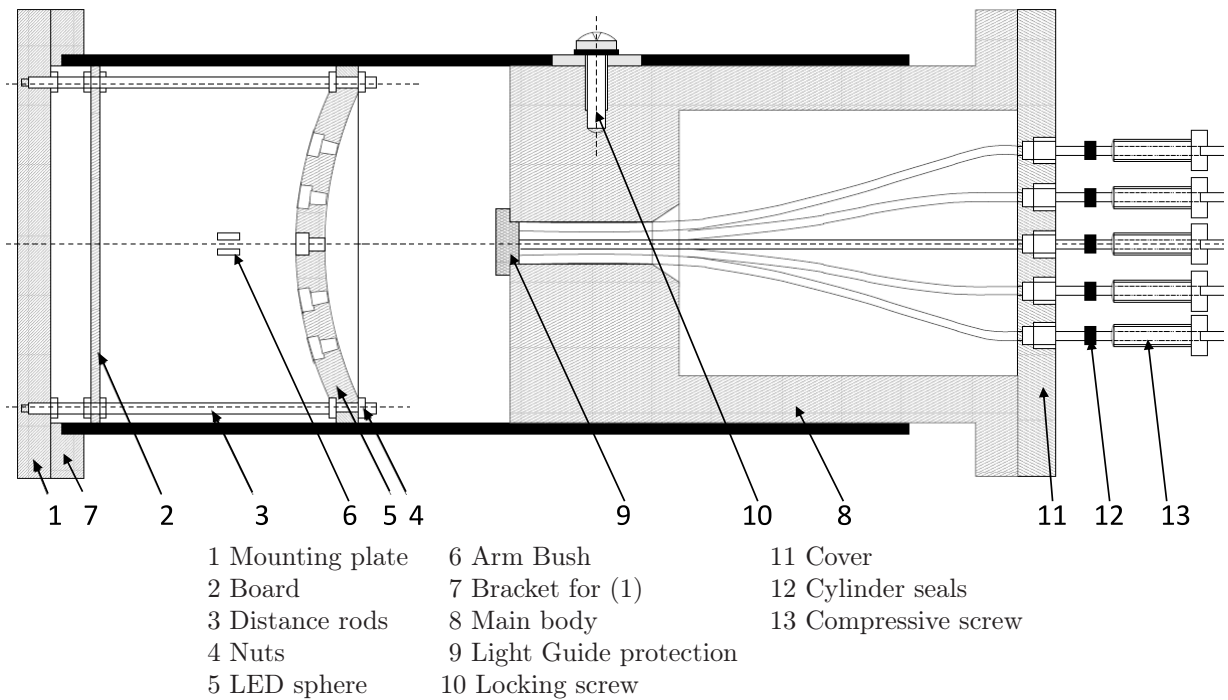| 1 Mounting plate | 6 Arm Bush | 11 Cover |
2 Board	7 Bracket for (1)	12 Cylinder seals
3 Distance rods	8 Main body	13 Compressive screw
4 Nuts	9 Light Guide protection	
5 LED sphere	10 Locking screw	

Figure 4.26: Schema of the Light source for the SFT-GMS.

The angle between each LED was approximately 10.5^o. Ideally the light of the LEDs meets in the focus point, which was at $6cm$ from the sphere's plane. The fibres were placed in the cylinder guide in the middle of the light source. The light guide protection of Plexiglas (part 9) in this process ensures that all fibres lie with their end surfaces at the same level. The fibres were fixed in this position by a compressive screw (part 13) in the cover of the light source (part 11). The light guide protection was removed to avoid unnecessary light losses.
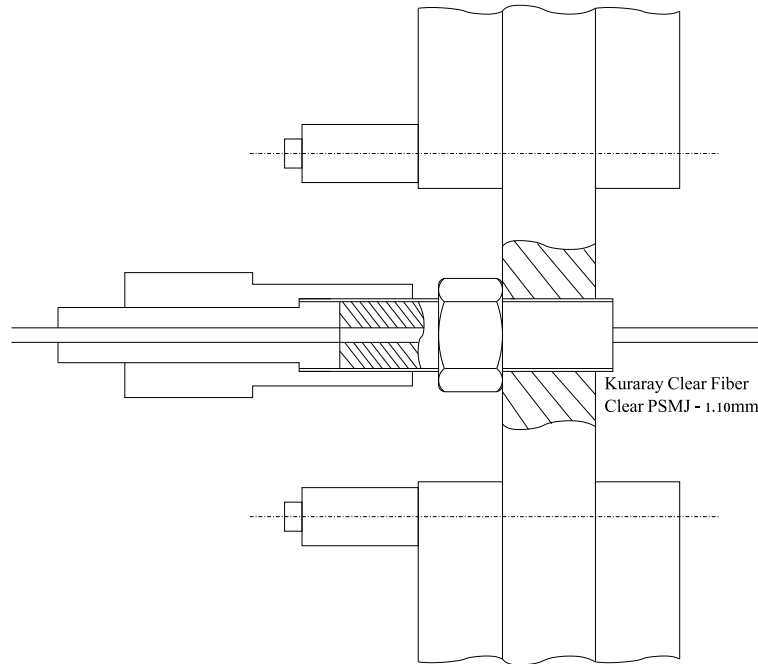

Figure 4.27: Schema of the GMS connectors to the SFT support ring. The GMS system and these connectors were installed on the SFT support ring after the final assembling of the SFT detector and the alignment run at Desy22.

Special connectors were implemented on the GMS fibres to connect the light source to the SFT support ring. The sketch of the connector place on the SFT connector ring is shown on Fig. 4.27, the picture of the GMS light guide connector on the SFT side is shown on Fig. 4.28.
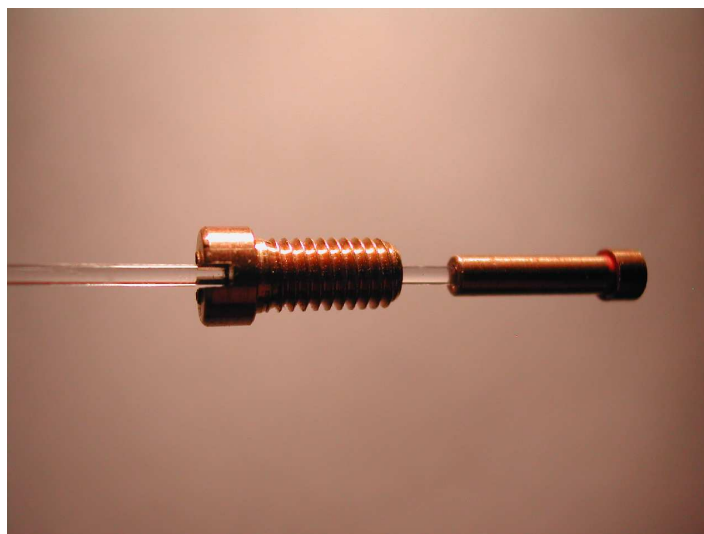

Figure 4.28: Photography of the GMS Light guide connector on the SFT side.

Chapter 5

Scintillating Fiber Tracker performance

5.1 Alignment at Desy22 electron test beam

During the assembly of the SFT the position of the modules within a cylinder was recorded, but not the individual position of the fibers. A precise knowledge of the exact fiber position was mandatory for the reconstruction of the charged particle trajectories. It was proposed to determine the fiber position in an alignment run [100].
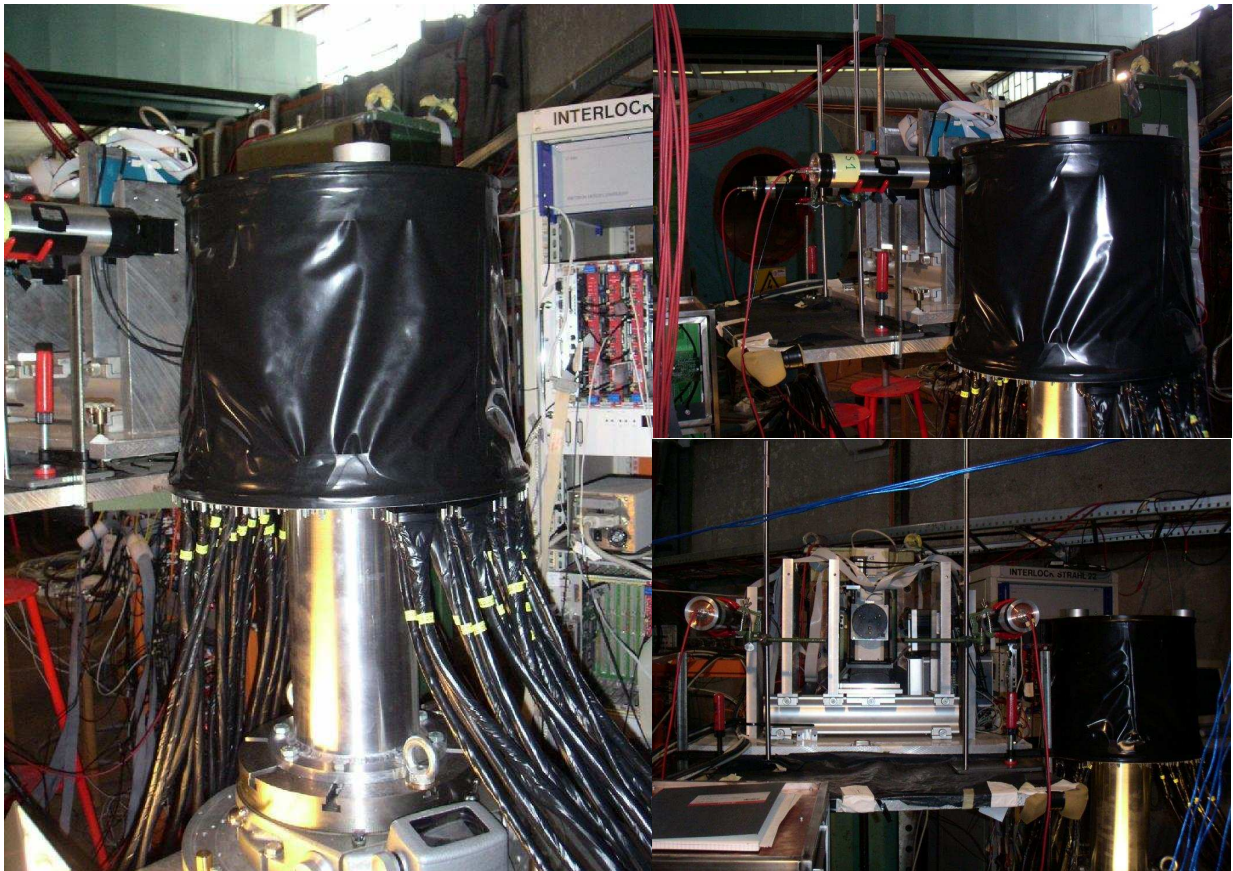

Figure 5.1: Plastic scintillators mounted in front and behind of the Zeus Telescope. Movable table, where the SFT was mounted on an adapting structure to its connector ring, was supported by a precise rotation disc.

The test stand at Desy22 electron test beam facility was equipped with a reference tracking system, called the Zeus Telescope and shown in Pictures 5.1, consists of three silicon detector of $32 \times 32 mm^2$ active area, each of them have two high-resolution single sided strip detectors which provide two space coordinates (x, y). Two plastic scintillators of $0.5mm$ thickness and $40 \times 40 mm^2$ area were mounted in front and behind the telescope, to provide the trigger signal. In front of this devices was a movable table where the SFT was mounted. The SFT cylinder was rotated by 90°, standing on an adapting structure to its connector ring and supported by a precise rotation disc. The setup schematic is shown in Fig. 5.2.
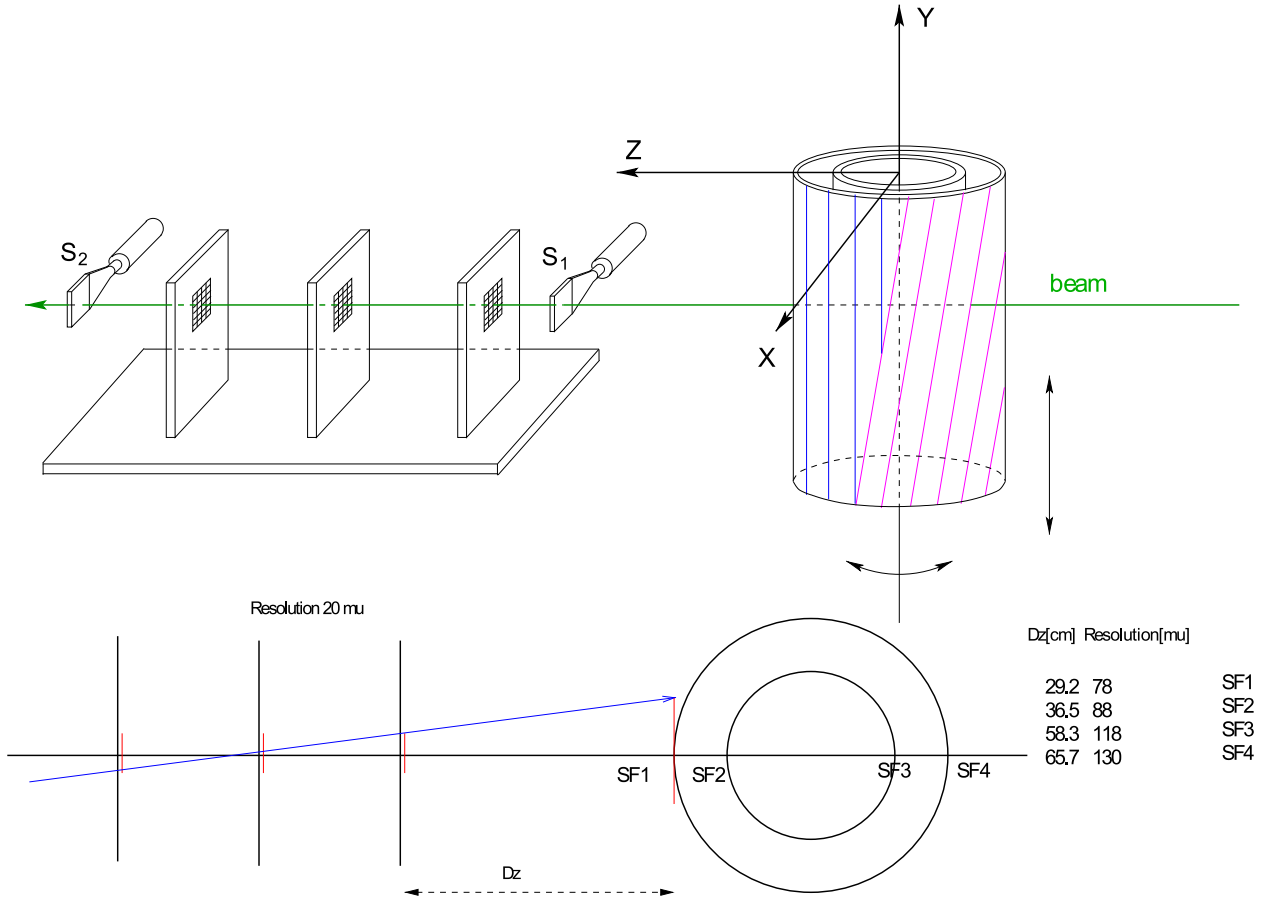

Figure 5.2: Schematic representation of the SFT alignment setup at Desy22. The table on the right side indicates the distance between each plane of the SFT and the Zeus Telescope and the expected coordinate resolution for each position of the SFT detector.

The beam energy was set to $5GeV$, as a compromise between track resolution and beam intensity. The size of the beam window was set by an upstream collimator of $20 \times 20 mm^2$ aperture yielding a slightly large irradiated area at the detector.

For a given angular orientation of the detector 15 runs were taken at different y positions with a step size of $20mm$ to cover the entire fiber length. The vertical scan was repeated at 30 different angular positions with a rotation angle of 6° between them. Runs at two consecutive angles have a large overlap region in the inner SFT, which allows for a cross-check of the 6° rotation angle. The total number of runs used for the alignment was $30 \times 15 = 450$, in addition 150 runs for the calibration and the pedestal measurements were taken.

Tracks were reconstructed with the three stations of the telescope using a procedure developed by ZEUS [101, 102, 103, 104, 105, 106]. Dedicated runs for calibration and alignment of the ZEUS TELESCOPE were taken. The intrinsic resolution of the ZEUS TELESCOPE was determined by comparing for the central station the measured and expected coordinates. With the SFT detector in front a resolution of $20\mu m$ was achieved, without SFT it was slightly better ($\sigma = 19.7 - 19.9\mu m$). At the position of the SFT planes outside the ZEUS TELESCOPE the resolution degrades due to the limited angular resolution. The spacial resolution was estimated on the basis of geometrical considerations between 80 and $130\mu m$, depending on the z position of the SFT planes as summarized in Table 5.1.

SPATIAL RESOLUTION

SFT PLANE	z-POSITION	RESOLUTION
	$[mm]$	$[\mu m]$
SF1	292	78
SF2	365	88
SF3	583	118
SF4	657	130

Table 5.1: Spacial track resolution at the position of the SFT planes. The z distance is given with respect to the first ZEUS TELESCOPE station seen by the beam.

The presence of material from the SFT detector and from a trigger scintillator in front of the ZEUS TELESCOPE induces multiple scattering which potentially broadens the track coordinates at the SFT planes. In order to reduce the impact of the multiple scattering, events were selected with angles in the $z - x$ and $z - y$ planes within a $\pm 5 mrad$ window, as shown in Fig.5.3.
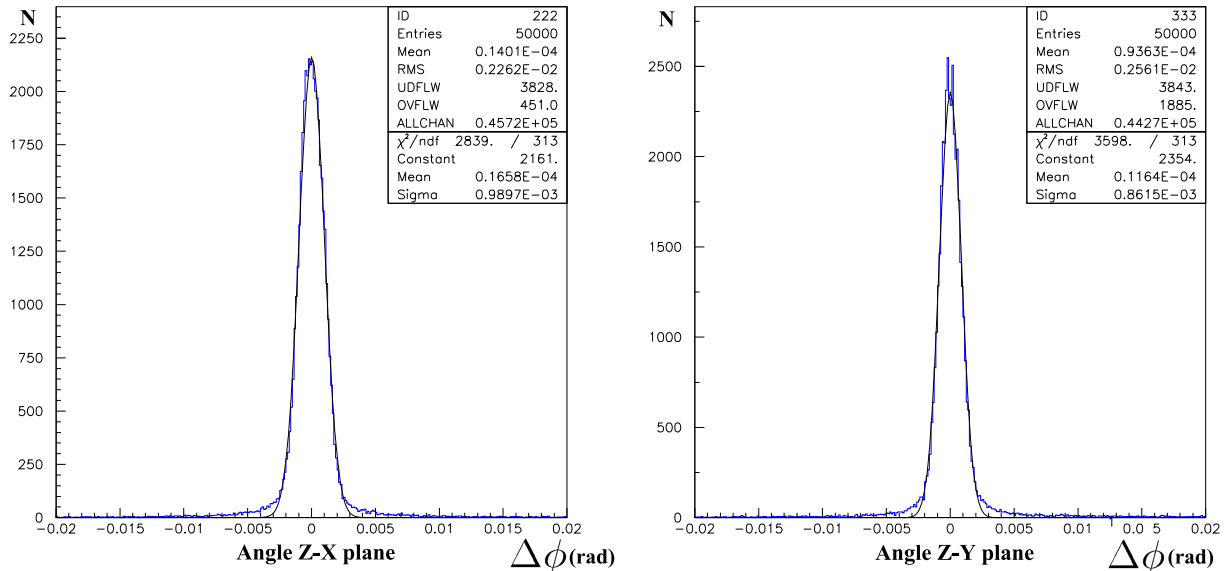

Figure 5.3: Reconstructed track angles in the $z - x$ (left) and the $z - y$ (right) planes in units of rad.

The best resolution for the fibers' center was obtained from the signal amplitude weighted distribution of the telescope-reconstructed x coordinate. A typical distribution of the fiber position is shown in Fig 5.4, where the reconstructed fiber position was compared to the resolution of the telescope. The telescope resolution of about $100\mu m$ is small compared to the fiber diameter of $1mm$. The reconstructed position was fit to a Gaussian distribution to determine the fiber position.
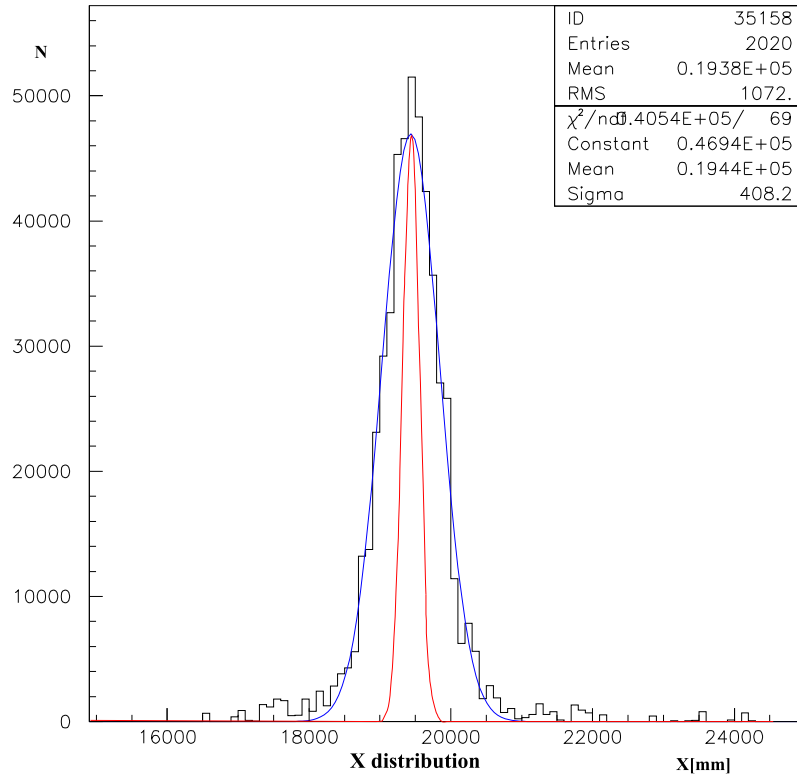
Figure 5.4: Reconstructed fiber position for one channel (histogram) is fit to a Gaussian in order to determine the fiber center. The inner fit curve shows the contribution of the ZEUS TELESCOPE to the resolution.

For a given run about 40 fiber centers were reconstructed over the length of $20mm$ per detector layer. The total length in y of $20mm$ was sub-divided into 4 consecutive sections of $5mm$ length. Taking the 15 runs at the fixed angular position yields in total 56 space points per fiber, two points at each endpoint of the scan (on top and bottom of the detector) were outside of the active area of the fiber.
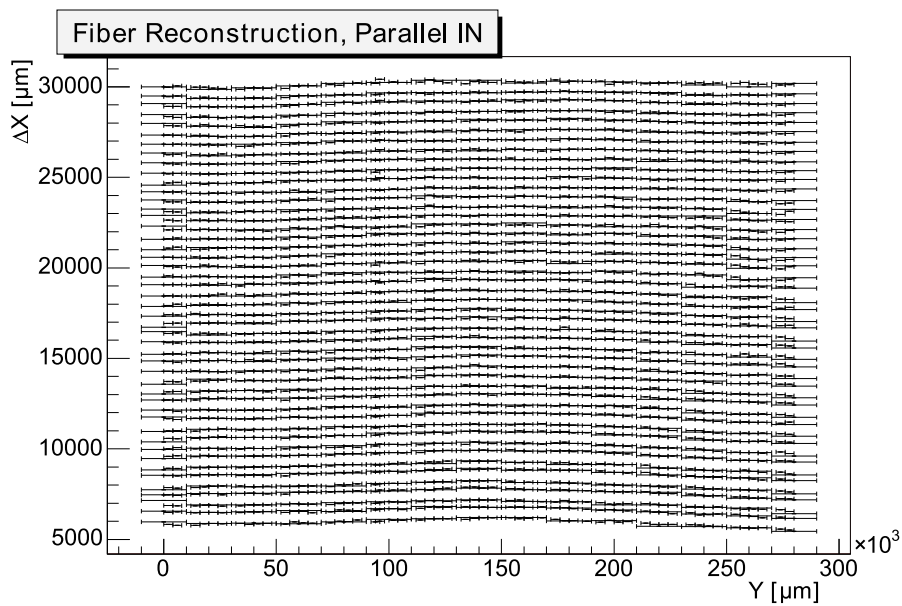

Figure 5.5: Reconstructed parallel fiber positions of the inner SFT detector. Each fiber was measured at 15 different y positions at a fixed angular orientation, in total 56 spaces point for each fiber were fit.

The reconstructed fiber positions, merged for 15 runs, are shown in Fig 5.5. A very modest curvature common to all fibers was observed with the displacement of the fibers in the middle (around $150mm$) of $100\mu m$ with respect to the endpoints. The stability of the fiber reconstruction method was estimated from the residuals of the measured fiber centers to the straight line fit. These residuals are shown in Fig 5.6. A Gaussian fit to the residual distribution yields a sigma of $50\mu m$, with a small systematic shift of the mean.
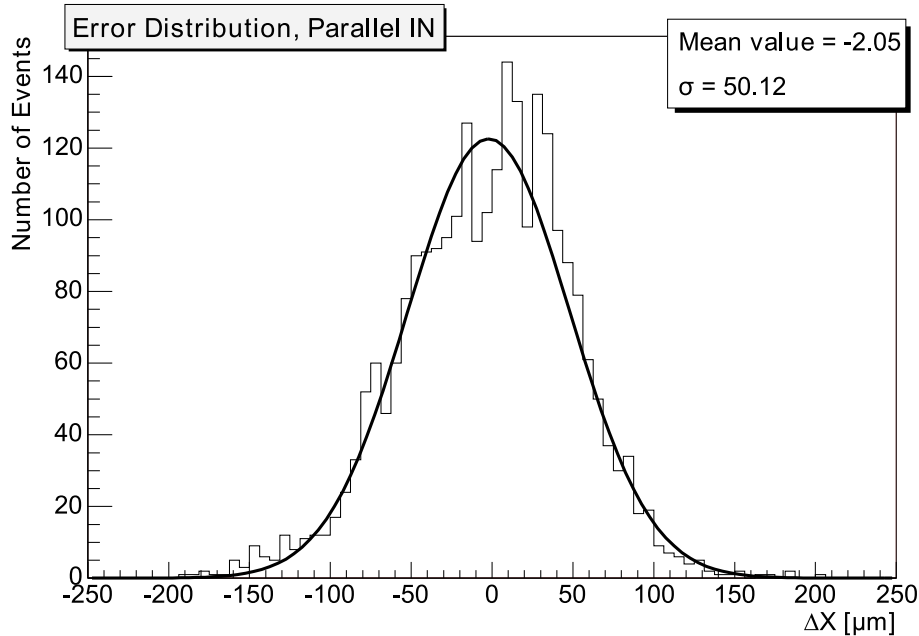

Figure 5.6: The residual of the individual measured fibers positions with respect to an assumed straight line fit through all points.

Another cross-check of the achieved precision was obtained from the overlap between adjacent angles, which covers about $9mm$ in x common to two angular positions. In the first plane of the SFT up to 18 fibers were hence reconstructed in independent runs with an angular rotation of 6° in between.
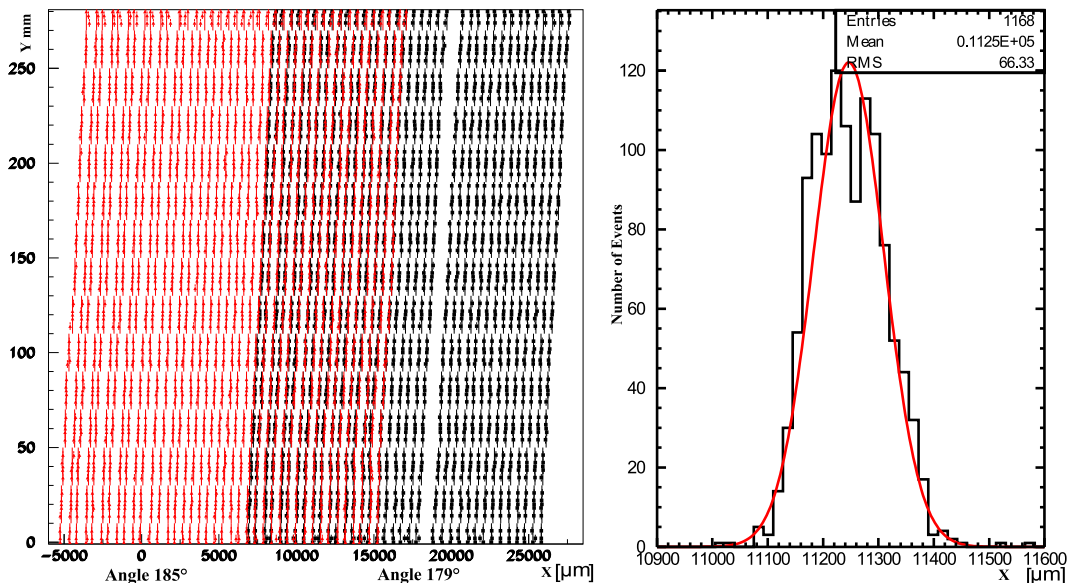

Figure 5.7: Left: Reconstructed fibers from runs at two different positions $\phi_1 = 185^o$ (in red) and $\phi_2 = 179^o$ (in black), the overlap is the central region. Right: Difference in the X position for the fibers in the overlap region between to the two adjacent angle setup ($X_{\phi_2} - X_{\phi_1}$).

The fiber centers for two angles were overlayed in left Fig. 5.7. The fibers reconstructed at these two angles seem to be slightly tilted, a displacement of about $2mm$ was observed for all fibers between top and bottom over the distance of $280mm$. In right Fig 5.7 the difference of $11.25mm$ corresponds to the rotation of 6° (expected value $= 11.44mm$), the RMS of the distribution of $66\mu m$ confirms the precision of this method. After the proving of the method, all fiber positions were parametrized with a polynomials of up to $O(4)$. These parametrizations are shown on Fig.5.8.
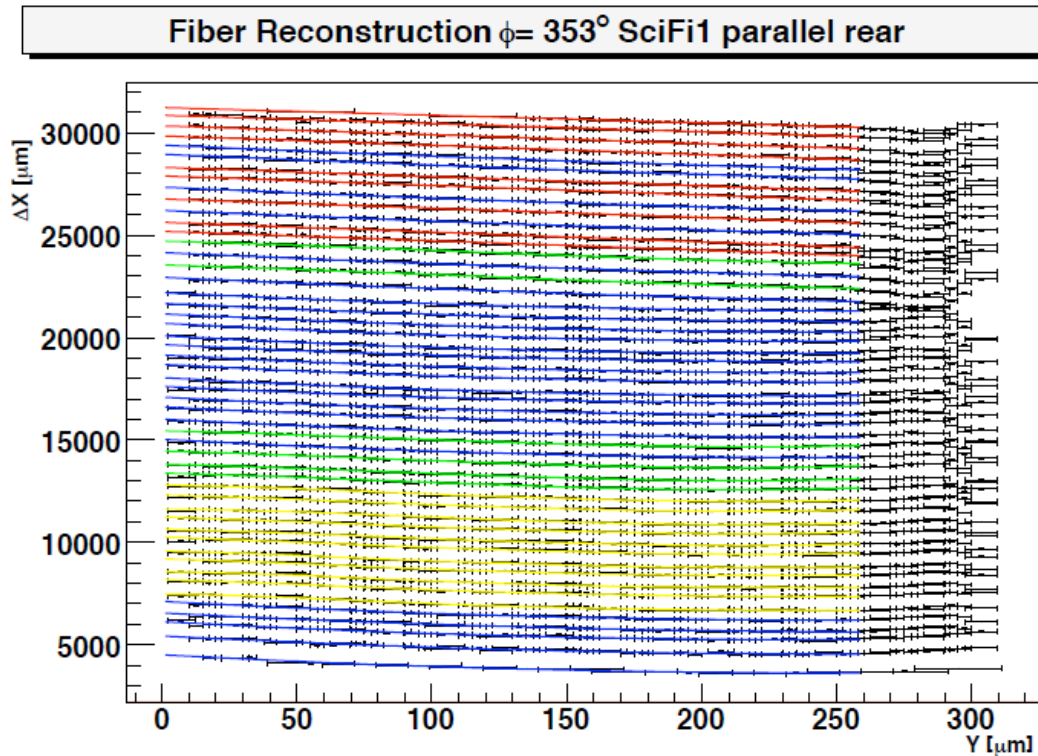

Figure 5.8: Fiber positions of the inner SFT detector fitted with a polynomial of up to $O(4)$. Each color corresponds to a different order of polynomial fit (red $O(1)$, blue $O(2)$, green $O(3)$, yellow $O(4)$).

The space points reconstructed by the ZEUS TELESCOPE were not related to an absolute reference system. Therefore it was important to define reference points on the SFT detector in order to translate the relative one to absolute measurement. The strategy was to define a fiber position which was already measured mechanically at the production step. The endpoint of a few selected *'reference'* fibers have been measured at the assembly stage and their coordinates were related to a visible point on the connector ring. The positions of the reference marks are shown in Table 5.2. The distance in z was measured from the front side of the connector ring.

ALIGNMENT MARKS AND CORRESPONDING FIBERS

SFT		MARK	CONNECTOR	FIBER	DISTANCE [mm]
INNER	Parallel	1	16	38	348.15
	Parallel	2	01	46	347.85
INNER	Stereo	1	15	6 − 8	350.47
	Stereo	2	21	14	349.37
OUTER	Stereo	1	12	118	/
	Stereo	2	18	14	/

Table 5.2: Position of the reference fibers in respect to the reference marks on the connector ring.

5.1.1 Transfer measurement with the FARO-Laser tracker

The reference marks on the connector ring were not visible when the SFT was installed. Due to this reason new reference marks, measured in the old reference system were defined and measured with the FARO-LASER TRACKER. The old marks were named SFT $R01$ and SFT $R02$. Two different locations were chosen for the new marks, the first group on top of the connector ring, between two light guide connector positions, named SFT $K01$, $K10$ and $K16$ and the second group on the top of dummy light guide connectors called SFT $SE01$, $SE02$, $SE03$, $SE04$. These marks are shown in Fig. 5.9.
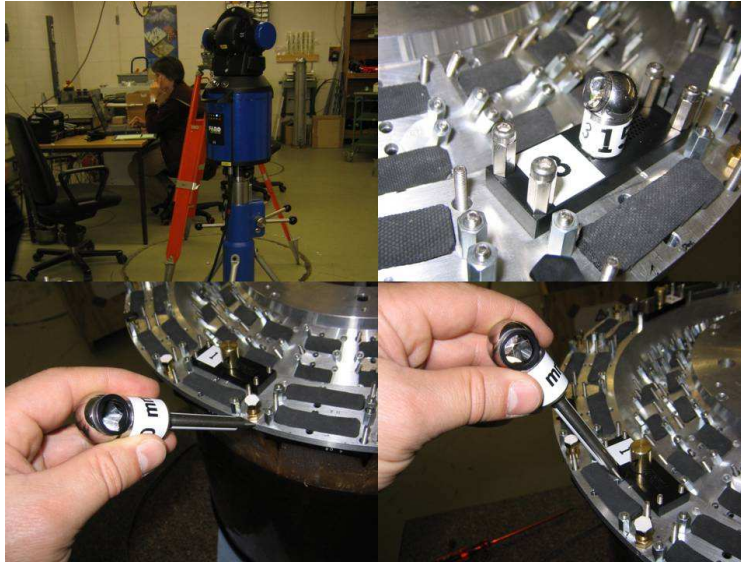

Figure 5.9: Photos of the survey measurement with the FARO-LASER TRACKER (top left). One of the four new marks on the light guide connectors (top right), one of the two old reference marks on the edge of the connector ring (bottom left) and one of the three new marks on the connector ring between two outer light guide connectors (bottom right). It is possible to see the needle and the mirror used to measure in combination with the FARO-LASER TRACKER.

The results of these measurements are shown on Table 5.11 and the 3-D model of the SFT detector reconstructed with the data tracked with the FARO-LASER TRACKER can be seen on Fig. 5.10
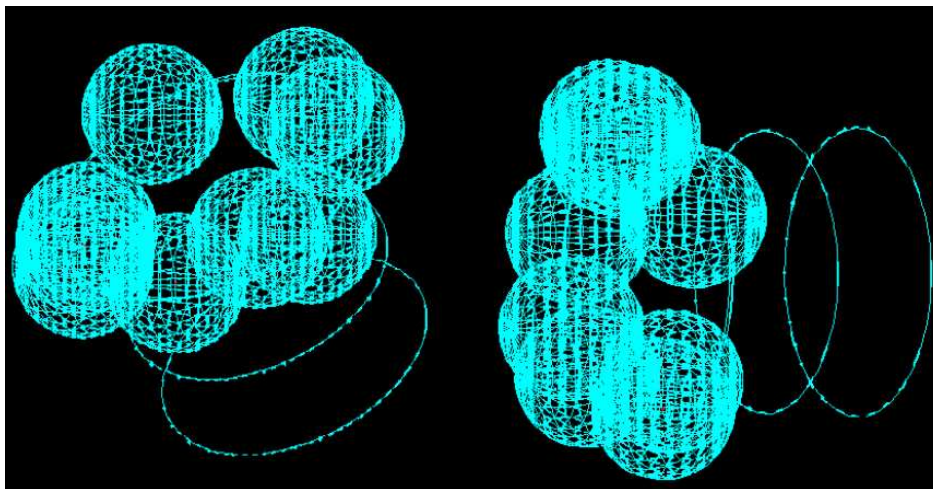
Figure 5.10: Two 3D model of the SFT (left and right) with the FARO-LASER TRACKER measurement. The reference points were measured with the needle, moving the needle around a fixed point it is possible to reconstruct the sphere, the center of each sphere corresponds to one reference point. The circles (representing the circumference of the SFT detector at different levels) were measured with one special needle, not to damage the detector.

HERMES

X1 - Koordinaten für den SFT

19.10.2005

Ergebnisse der Transfermessung mit dem FARO Lasertracker Nr.1

Punkt-Bezeichnung	Y1 [m]	X1 [m]	Z1 [m]	Delta Y1 [mm]	Delta X1 [mm]	Delta Z1 [mm]
SFT_R01	0,19997	960,59612	0,20018			
SFT_R02	0,20103	960,66643	-0,14328			
SFT_K01	0,20181	960,61957	-0,15718			
SFT_K10	0,20129	960,38195	0,15966			
SFT_K16	0,20105	960,69716	0,02478			
SFT_SE01	0,22370	960,61521	-0,14640			
SFT_SE02	0,22378	960,37504	-0,13699			
SFT_SE03	0,22297	960,34265	0,10125			
SFT_SE04	0,22258	960,62684	0,14003			
SFT_SM01	0,22344	960,61518	-0,14636	0,26	0,03	0,04
SFT_SM02	0,22339	960,37496	-0,13708	0,39	0,08	0,09
SFT_SM03	0,22264	960,34269	0,10120	0,33	-0,04	0,05
SFT_SM04	0,22200	960,62682	0,14000	0,58	0,02	0,03
SFT_KREIS_OBEN	0,19875	960,50078	0,00128			
SFT_KREIS_OBEN_NEU	0,20002	960,50081	0,00132			
SFT_KREIS_MITTE	0,00696	960,50044	0,00062			
SFT_KREIS_UNTEN	-0,14212	960,50044	0,00023			

Figure 5.11: Survey measurements with the FARO-LASER TRACKER. Where $SFT R01$ and $SFT R02$ are the old marks, SFT $K01$, $K10$ and $K16$ are the new marks on the connector ring and SFT $SE01$, $SE02$, $SE03$, $SE04$ are the new marks on four different light guide connectors.

5.1.2 Mechanical measurement of the SFT at the survey group

The SFT detector was measured mechanically too, these measurements were done with a special table of measurements with a needle. The measurement setup can be seen in Fig. 5.12

Figure 5.12: Photo of the measurement of the SFT at the Survey Group.

The old reference marks were mechanically measured on the edge of the connector ring of the SFT detector and the new reference marks located in between two outer light guide connectors, see Fig. 5.13 for the new measurement of the reference marks. All these measurements were done with the same reference system in the center of the detector at the same plane as the connector disc.

This method only measured the x, y coordinates of each reference mark. For the old marks these positions were obtained $R01$ ($135.311mm$, $-174.122mm$) and $R02$ ($-203.970.311mm$, $-83.713mm$). For the new reference marks on top of the connector disc measured these numbers $K01$ ($197.873mm$, $0.243mm$), $K10$ ($-198.043mm$, $-0.317mm$) and $K16$ ($-98.879mm$, $-171.561mm$). It was important to measure precisely the new reference marks because these reference marks were only visible after the SFT detector installation. The error of these measurements is really small, it was estimated to be $\pm0.001mm$.
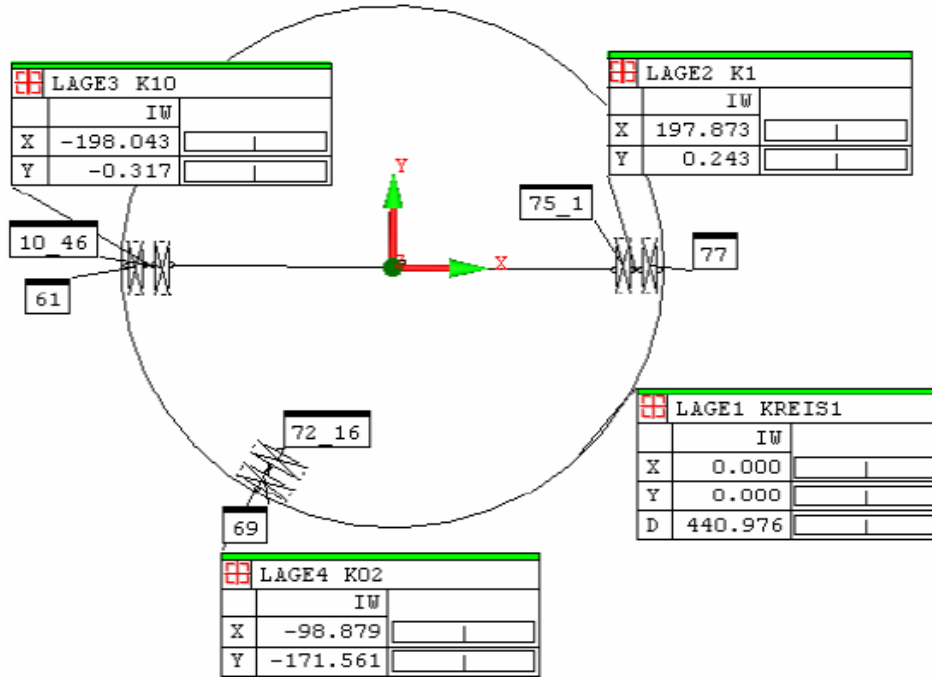
Figure 5.13: Measurement of the three *new* reference marks ($K01$, $K10$ and $K02$) on the connector ring of the SFT at the Survey Group.

The most important measurements from the survey group were the measurement of the radius, the eccentricity and if the two barrels were concentric with respect to the center of the inner barrel of the SFT detector. The results can be see in Fig. 5.14.

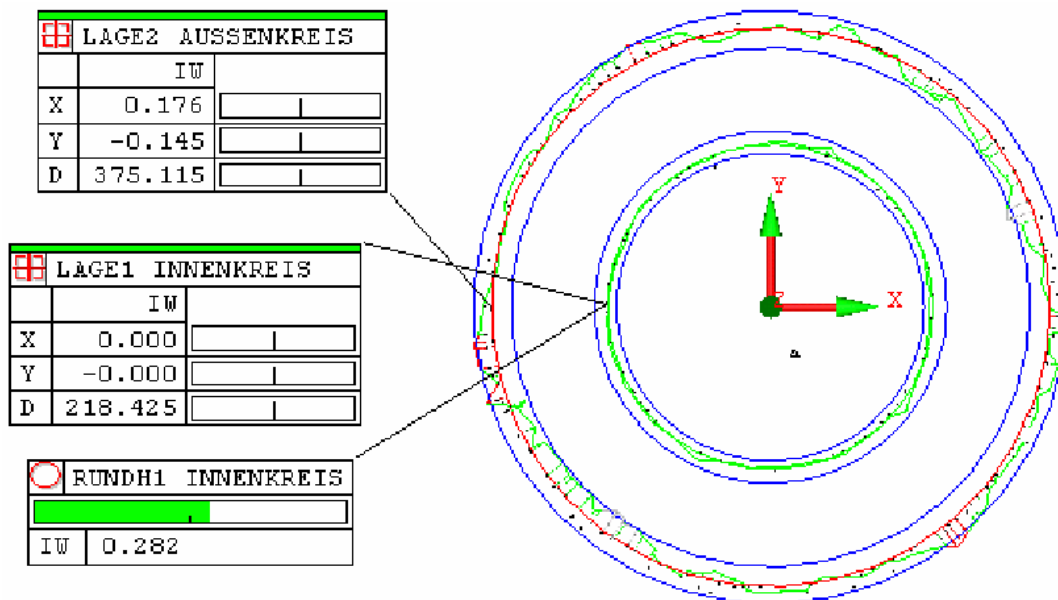Figure 5.14: Measurement of the radius, eccentricity and concentricity of the two barrels of the SFT at the Survey Group.

The two barrels of the SFT are not totally concentric, taking the center of the inner barrel as a reference, the outer barrel is displaced by $0.176mm$ in x and $-0.145mm$ in y. The eccentricity ε of the inner barrel was measured as 0.282. For a perfect circle the eccentricity is zero.

The internal diameter of the inner barrel was measured as $D = 218.425mm$. If we compare this measured value with the designed radius of the inner layer of fibers ($R_{inner} = 109mm$, $D_{inner} = 218mm$) we see that this is slightly bigger then the designed one. The external diameter was measured as $D = 375.115mm$. If we compare this with the theoretical radius of the outer layer adding the glue and the kapton foil $R_{outer} = 187.350mm$ or $D_{outer} = 374.350mm$ we realize this is a little bigger than the designed one. This small difference of the outer SFT detector was problematic during the installation.

5.2   Holding structure

To avoid damage to the light guides, a holding structure was asked to be placed in front of the recoil detector. This holding structure was made at DESY. It was decided to use the light modular profile due to the flexibility and multiple possibility to support the light guides. As a material *Profile F50×200 − L* for the main core of the holding structure and the *Profile F50×50 − L* for the support of the light guides was chosen. The support structure is shown in Fig. 5.15 and 5.16.
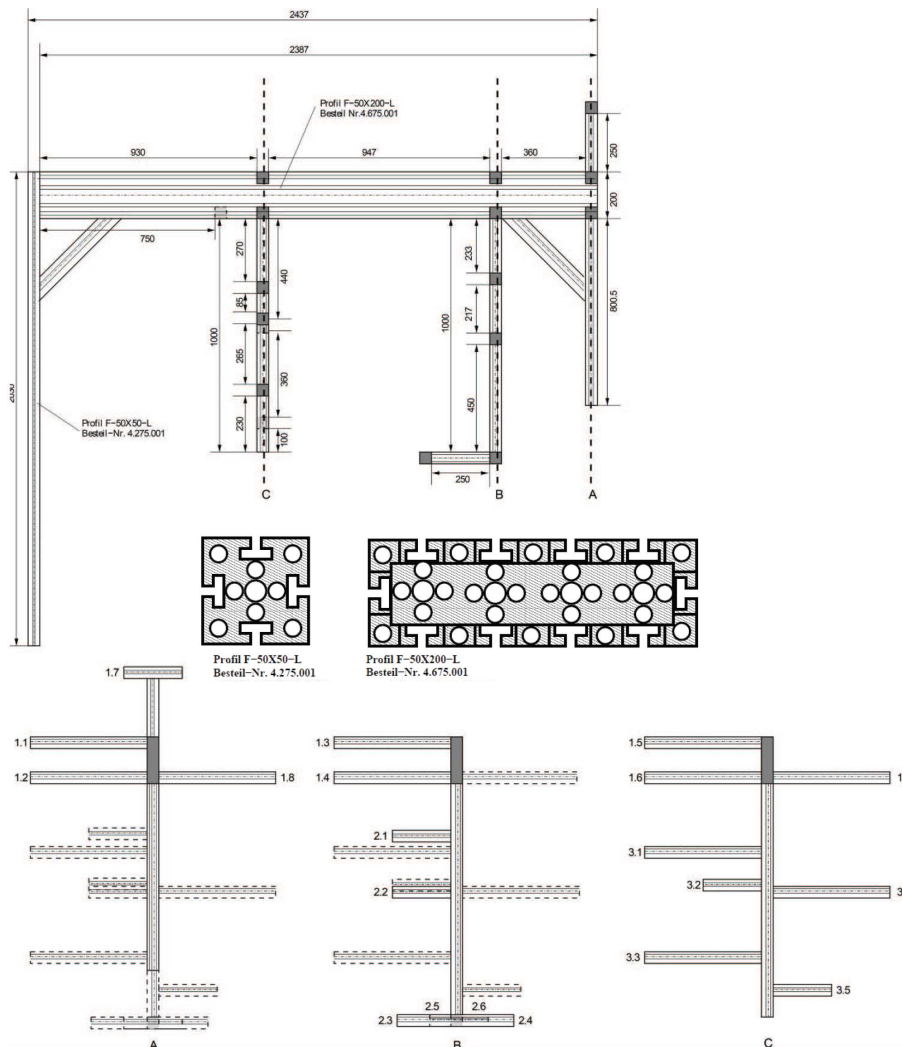

Figure 5.15: Holding structure profile. We can see on this figure on top the front part of the holding structure, in the middle a transverse cut on the *Profile F50×200 − L* and *Profile F50×50 − L* and on the bottom the three arms of the holding structure with several supports each of them. The positions of the supports were chosen to avoid possible damage to the light guides.

Figure 5.16: Photos of the holding structure profile installed in front of the Recoil detector at the East Hall during the cosmic test experiment, with the light guide on top and without the light guide on bottom.

It was necessary to avoid any damage to the light guides or the detector during the installation at the East Hall for the cosmic test experiment. For the first time a full SFT detector was mounted and tested to run, but the installation of the 78 light guides before the cabling of the Silicon detector (but after the Photon detector installation) was more complicated. This was the main motivation to pre-install dummy light guides and the holding structure as a test of all Light guide installations. This test was important to gain a knowledge of which order and which geometry the light guides will take at the final installation. With the help of the Silicon group and the Photon detector group we developed a strategy to have an efficient installation of the recoil detector that is safe for all the components. This strategy was useful when the Silicon detector was needed to be dismounted and repaired.

5.3 Cosmic test run

A few months before the installation in HERMES, the recoil detector was completely assembled. During 2005 the recoil detector was installed in the East Hall close to the HERMES detector (but outside of the interlock area) to check all the sub-detectors together with the electronics and the data acquisition of the Recoil Detector. The fully assembled Recoil detector is shown on Fig. 5.17. During the installation new tools and approaches were tested to avoid unexpected stresses on individual components. The cosmic test run was performed.
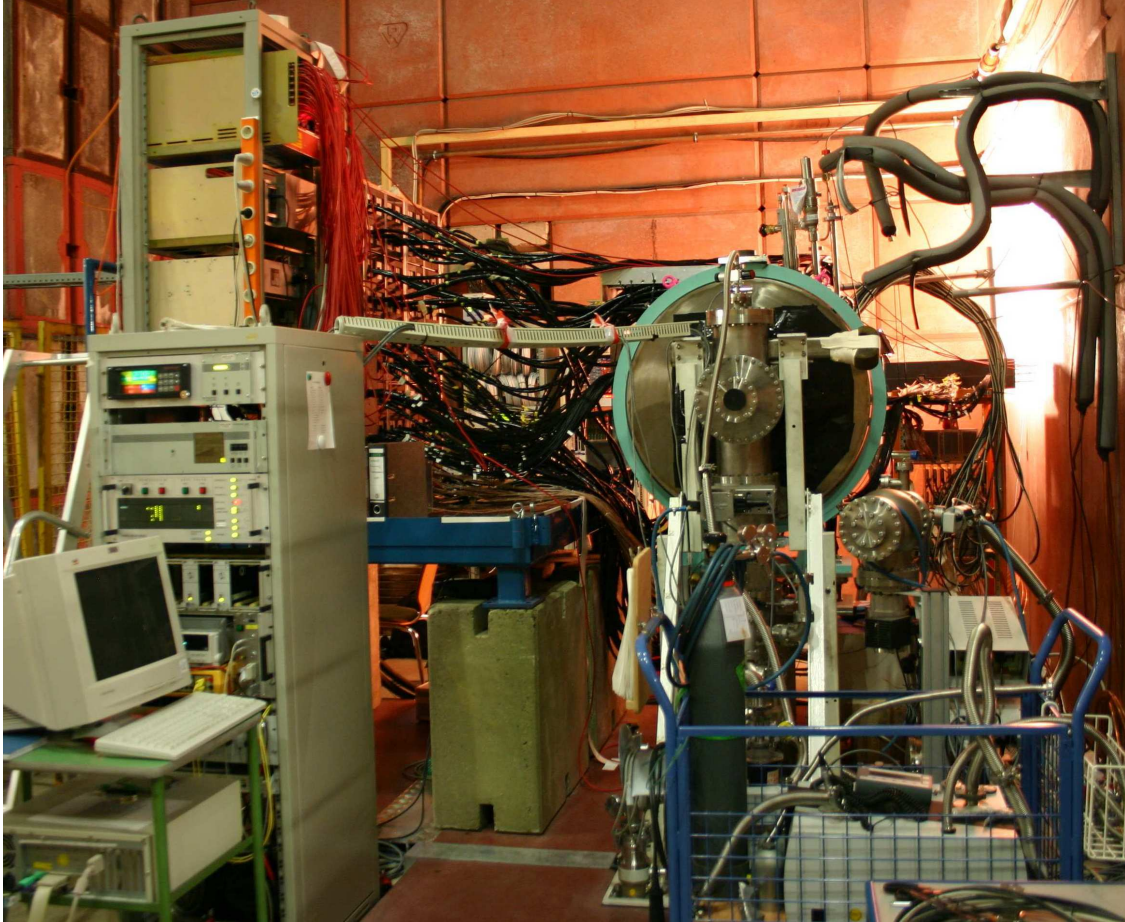

Figure 5.17: Picture of the fully assembled Recoil Detector during the cosmic test run. The Recoil detector is shown with the superconducting magnet in the center, the pump stand (right), the magnet control system (left). We can see on the platform at the left of the picture the rack for the readout electronics, the PMT wall of the SFT and the readout racks of the Silicon and Photon detectors.

The Recoil detector was set up as close as possible to the final experimental conditions. In practice this test was the main check for the recoil detector with a magnetic field and the Silicon detector for the vacuum. The detector was operating continuously in several data taking modes. The readout of the Recoil detector was implemented and prepared to be merged into the HERMES DAQ together with the slow control chain. Some malfunction in the readout was detected during the cosmic test run and some electronics components were completely redesigned, see detailed information in [91].

The setup was ready for cosmic data taking in March 2005. The recoil detector took cosmic data using the cosmic trigger generated by the Photon detector. This cosmic data were used to study the calibration of the Photon detector. This calibration was partially successful because not all scintillator strips of the Photon detector could be calibrated due to the distribution of the cosmic radiation. The alignment procedure was repeated, when the recoil detector was inside HERMES experiment. Some cross check of the internal alignment of the SFT and a verification of the mapping was successfully realized.
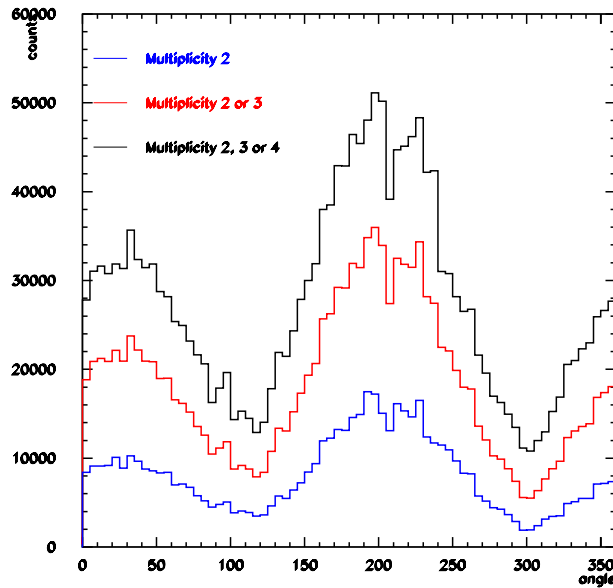
Figure 5.18: Cosmic radiation angular distribution seen by the Recoil detector. Check of the detector response for full azimuthal angle, 30^0 correspond to upward part of the detector.

The cosmic trigger setup was done by the combination of the lower half of the strips of the Photon detector. In Fig. 5.18 the hit distribution for the inner parallel SFT layer is shown. The asymmetry in the number of hits in the SFT versus ϕ was expected like the high numbers of hits on the bottom of the SFT detector due to the trigger geometry setup.
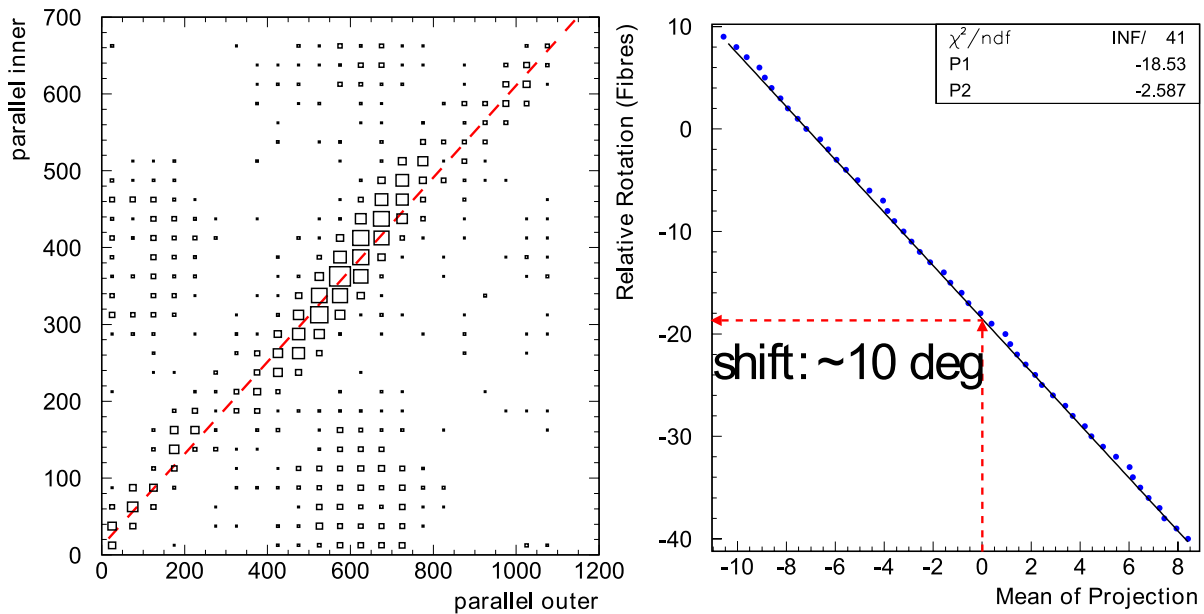

Figure 5.19: Cross check of the internal alignment. On the left side the raw fiber hits on the inner parallel versus the raw fiber hits on the outer parallel SFT. On the right plot the mean value of the projection of these hits by shifting certain number of fibers is shown and confirms the known offset.

Fig. 5.19 show the cross check of the internal aligment of the SFT Detector. The cosmic run produced the first data taken with the full recoil detector setup. At the end of the cosmic test run everything worked as was planned. The cosmic test run was an important and very successful intermediate step to the installation of the Recoil detector.

5.4 Test and repair of the Light Guides

The light guides were installed and reinstalled several times, they were used in the alignment run at DESY22, during the cosmic test experiment in the East Hall and during the cabling test with the new holding structure. Shining some light through the light guide some reduction of the intensity of the light was observed, see Fig. 5.20. Due to this reasons and preparing the SFT detector installation all light guides were tested for transmission efficiency to find damaged fibers.
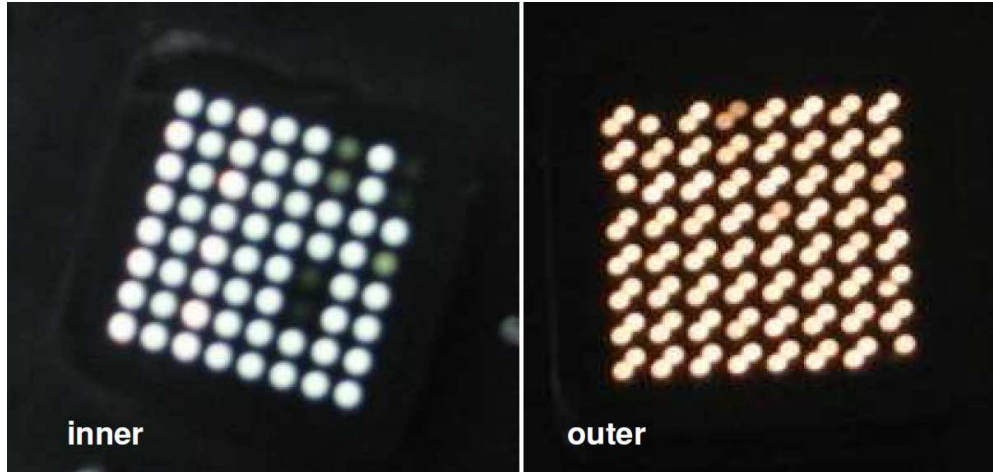
Figure 5.20: Light guide PMT side connector for inner and outer barrel with light shinning through the fibers.

For this purpose the light guides were connected to an LED light source and the readout system. The light guides were tested extended and bent to see the influence in the measurement. The setup in the East Hall is shown in Fig. 5.21.

Figure 5.21: Light guide test setup in the HERA East Hall.

The results of the measurement were plotted as relative transmission efficiency for each PMT channel. There was no significant difference between extended and bent fibers.

The relative transmission efficiency was defined as:

$$\varepsilon_{rel} = \frac{Signal_{Channel}}{Signal_{Maximum}},$$
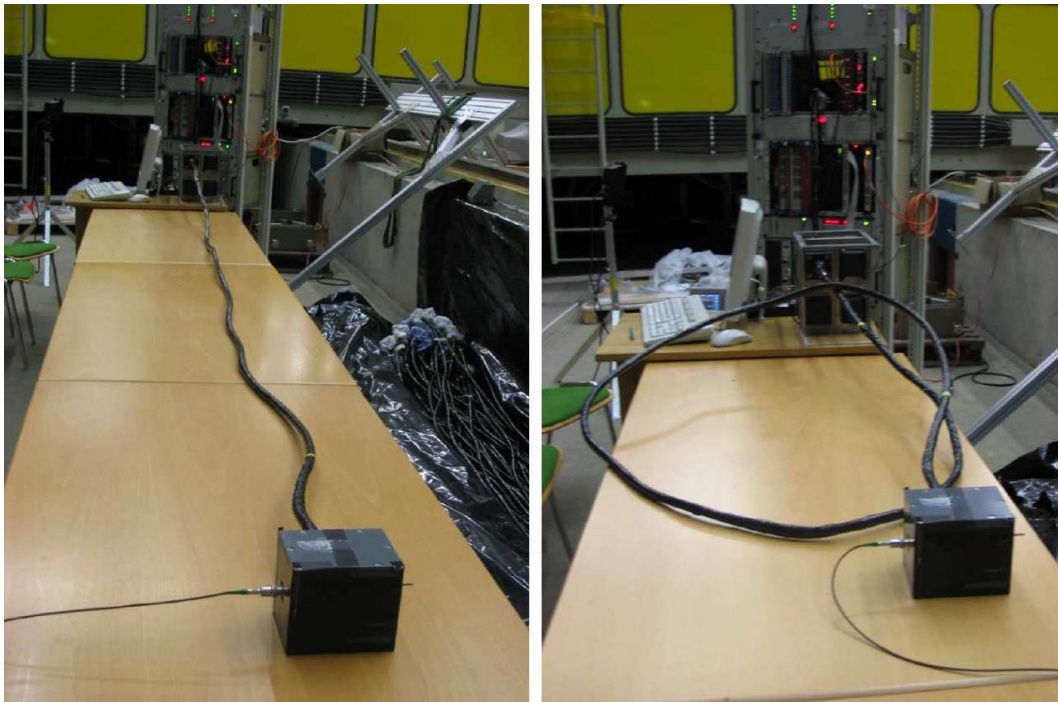
(5.1)

The largest *Signal* of the light guides under investigation (inner/outer) was chosen as normalization factor ($Signal_{Maximum}$) for all channels. Due to the difference between inner and outer layer light guides two different normalization factor was used for different layers.
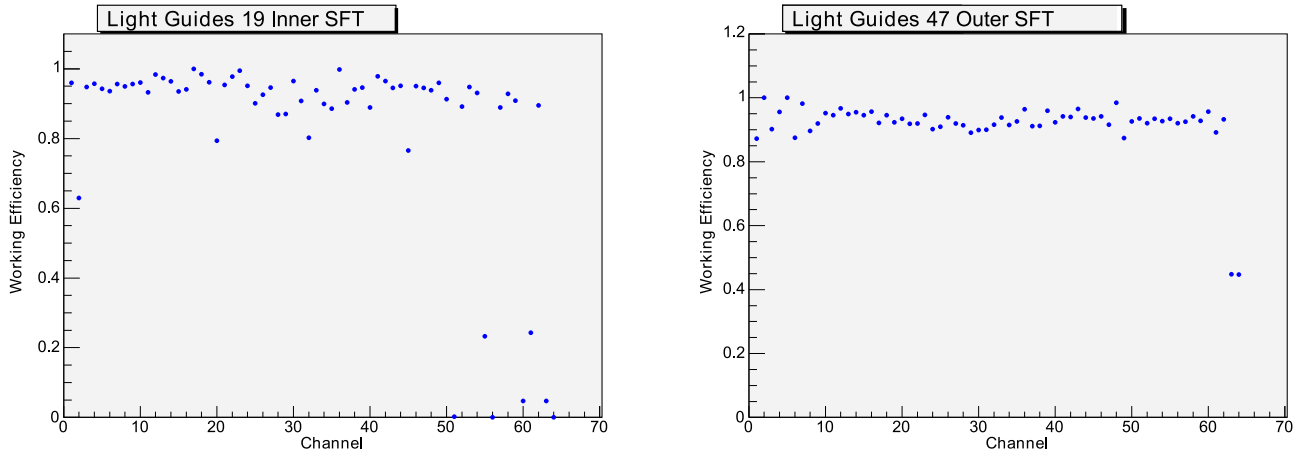

Figure 5.22: Relative transmission efficiency of the light guide per PMT channel. For one inner light guide on the left where a few channels are under 60 % and for one outer light guide where only few are below 80 %, we consider them as damaged.

Due to time consideration the test needed to be done quickly. The light distribution was not guaranteed to be optimally homogeneous. Nevertheless the test found all fibers that had already been marked through visual inspection as probably damaged, but it showed that much larger numbers of fibers showed reduced transmission efficiency, Fig. 5.22 shows the relative transmission efficiency from one inner and one outer layer. Plots for all light guides can be found in the appendix of HERMES-INTERNAL REPORT [107].
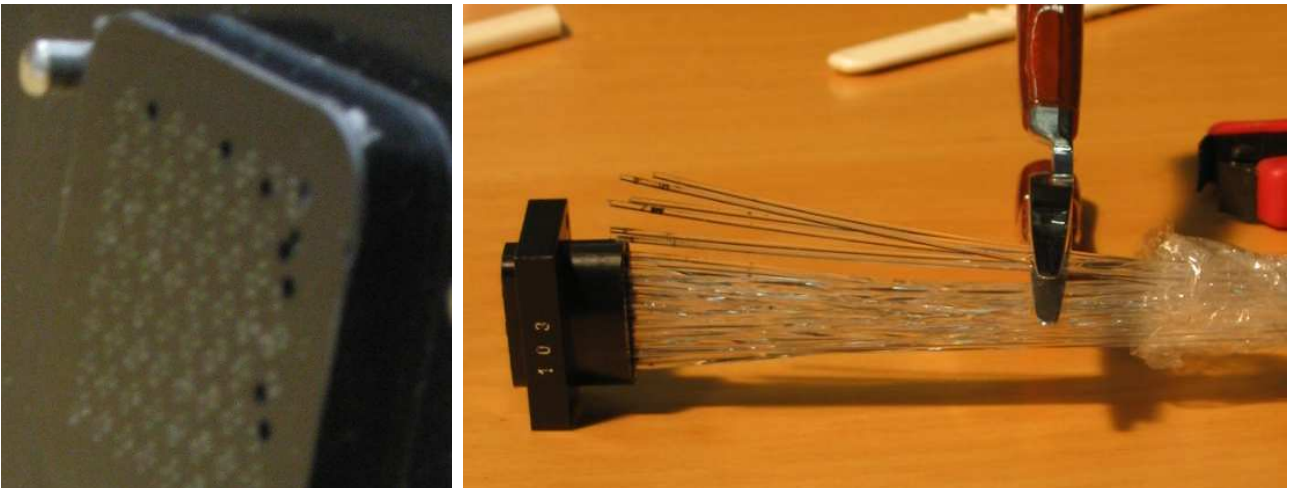
Figure 5.23: Photos of the light guide inspection. Left photo shows the outer light guide PMT-side connector with fibers that have retreated from the surface. The right photo shows the detector side connector for an inner light guide, the black tape was removed and the broken fibers were clearly visible.

Based on the measurement a light guide fiber was labeled as 'damaged' if the relative transmission efficiency was below 60% for transmission in the inner detector. In the outer detector this threshold was 80%, because

two fibers were connected to one PMT channel. The fact that no transmission efficiency in the outer detector was below 40% indicates that in each case only one fiber was damaged.

The tests have shown a certain number of channels with a lower or no signal. The number of affected channels was 167 (or 6.3%) for the inner barrel and 80 (or up to 3.7%) for the outer barrel. The combination of use of spares, repair of the light guides and manufacture of the new light guides allowed the reduction in the number of affected channels to 0.5% in time for the installation.

In the list of affected channels the fibers located at the edge of the detector side connector, in particular channels 61 and 64, were shown up especially frequently. Removing the black tape from one light guide on the detector side showed that the fibers were broken out of the connector, shown on Fig. 5.23. This damage was the result of too much mechanical strain over a period of time while the light guide were installed.

5.4.1 Repair/replacement of the Light guides

Given enough time it was possible to replace completely all the light guides with newly manufactured ones. The new light guides were designed to be less sensitive to damage, in particular an appropriate stress relief for the connectors was included. The black tape was not applied to the fibers directly, but with a layer of foil in between. The black tape covering the light guides was not attached to the fibers anymore, the black tape was replaced in the new light guides by heat shrink tubing.
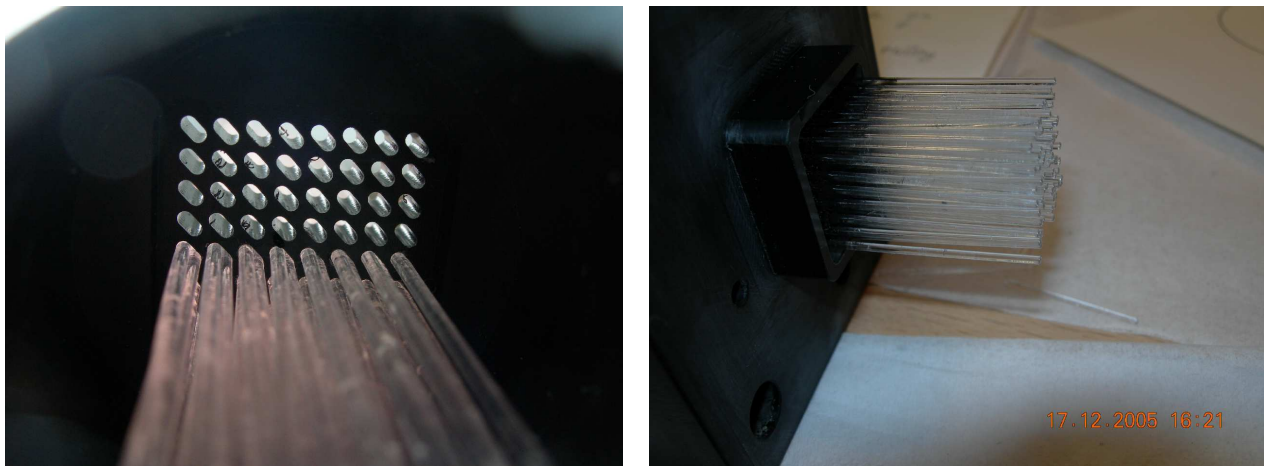

Figure 5.24: Light guide connector on PMT side during the reconstruction at DESY. The left photo shows the inner part of the PMT side connector of the outer light guide during the installation of the light guide. The right photo shows the outer part of the PMT side connector for inner light guides at the time all light guides are installed.

Two further potential sources of damage were identified and were minimized: During installation of the connectors in the connector ring, space was very tight, and it can easily happen that the fingers holding the light guide connector press the fibers together at the edge of the connector. To avoid this, several additional layers of foil close to the connectors were placed to act as a mechanical protection of the outer most fibers of the bundle. Special care was taken installing the connectors. The second potential source of damaging the fibers was the bending of the light guide after the connector was fixed at the connector ring. The light guides should be bent as little and as far away as possible from the connector ring. The position of the light guides was not altered any more after they were connected, as this was one of the most likely ways to damage them. Light guide material for half a set of inner and outer light guides was ordered from KURARAY through DESY. There were 10 spares for inner and 5 for outer light guides at Gießen. In addition there was enough spare material to build one outer or two inner light guides.
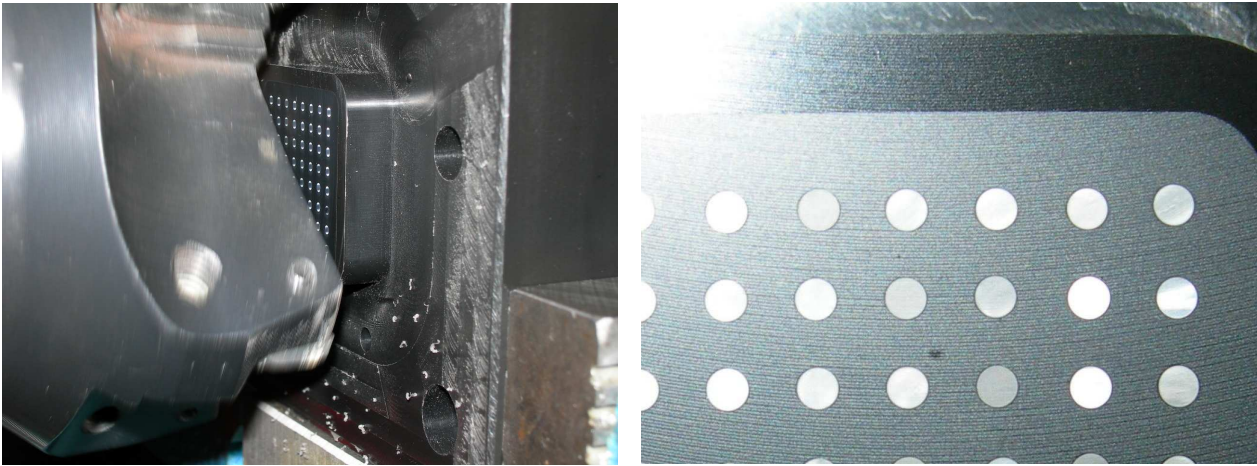
Figure 5.25: Polished Light guide connector at DESY with milling machine. On the left picture one can see the diamond cutting the POM, the hard glue and the fibers at the same time. In the right picture the result of milling operation of the connector light guide at DESY are shown.

Most scintillating fiber modules on the SFT detector have less than 64/128 channels because the first and/or last fibers were removed during construction (62 or 64 for inner modules and 122 for outer modules on average). An appropriate installation of the light guides where damaged light guide channels correspond to removed fibers on the SFT detector allowed us to use this without affecting the operation of the SFT detector.

Figure 5.26: The left picture shows the support where the light guides were glued, the light guide should be glued with the fiber straight at the connector. The right picture shows the storage room in the East Hall. The light guides were stored as straight as possible to avoid damage, before the final installation.

From the 42 inner and 36 outer original light guides only 5 for the inner and 3 for the outer were in acceptable condition to be used. In addition to Gießen spares, we have produced and repaired necessary amount of light guides at DESY. The 10 inner and 5 outer spare light guides stocked at Gießen were used to replace the worst light guides. They needed to build new light guides and repair some existing ones. We have produced 21 inner and 18 outer new light guides in DESY. We have repaired 12 inner and 12 outer light guides. A total of $42 + 2$ inner and $36 + 2$ outer light guides were prepared on time to be installed for the recoil detector. The production of two more light guides asked by the collaboration to have spare light guides during the running time, was also achieved.

5.5 Mapping of the SFT Detector

To have the possibility to reconstruct hits with the SFT detector and reconstruct clusters, it should have a correct mapping. During the assembly of each module within the cylinder, modules were numbered from 1 to 64 for the inner SFT and from 1 to 128 for the outer SFT. The modules composing the inner parallel or stereo were also numbered from 1 to 21 and the outer parallel or stereo from 1 to 18.

Because all modules don't have the same number of fibers, (during construction some were removed from the edge of the modules to fit together) the mapping takes this into account. They were marked on the mapping as fibers 9999. Some fibers on the modules were wrongly connected, inverted or interchanged. All these tiny mistakes were taken into account and corrected in the mapping file. See Fig 5.27 for a schematic view of the mapping.
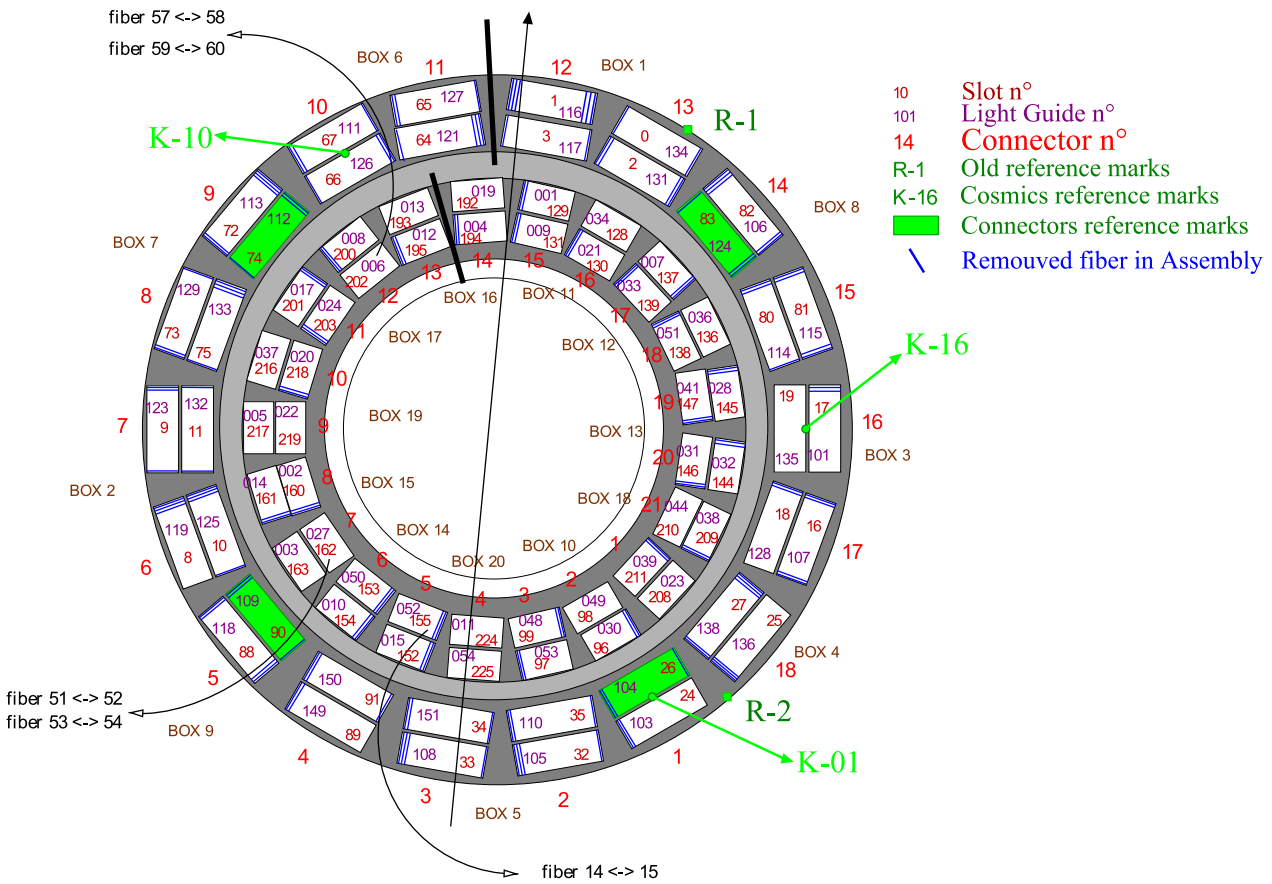

Figure 5.27: Schematic view of the mapping of the modules and fibers of the SFT detector.

The mapping also took account of the electronics and the disposition of the two towers where they were installed, see Fig. 5.28 for details. The electronics on the towers were read by the box of four PMTs, each of them with one MPFM (see Fig 4.17 in chapter 4.3.3). They were used for the readout of the SFT detector, four Readout Controllers (Roc) with five ports each of them.From the *slot* number the Roc, prot and mpfm can easily be found. For each *slot* number there is a unique PMT:

$$slot = roc \times 64 + port \times 8 + mpfm, \tag{5.2}$$

In this way the implementation of the mapping is fixed and only depends on the connection between the SFT detector and the PMTs. This connection depends only on which light guide was connected between the PMTs and the fiber modules. This can be seen in Fig. 5.27 and in Fig. 5.28.
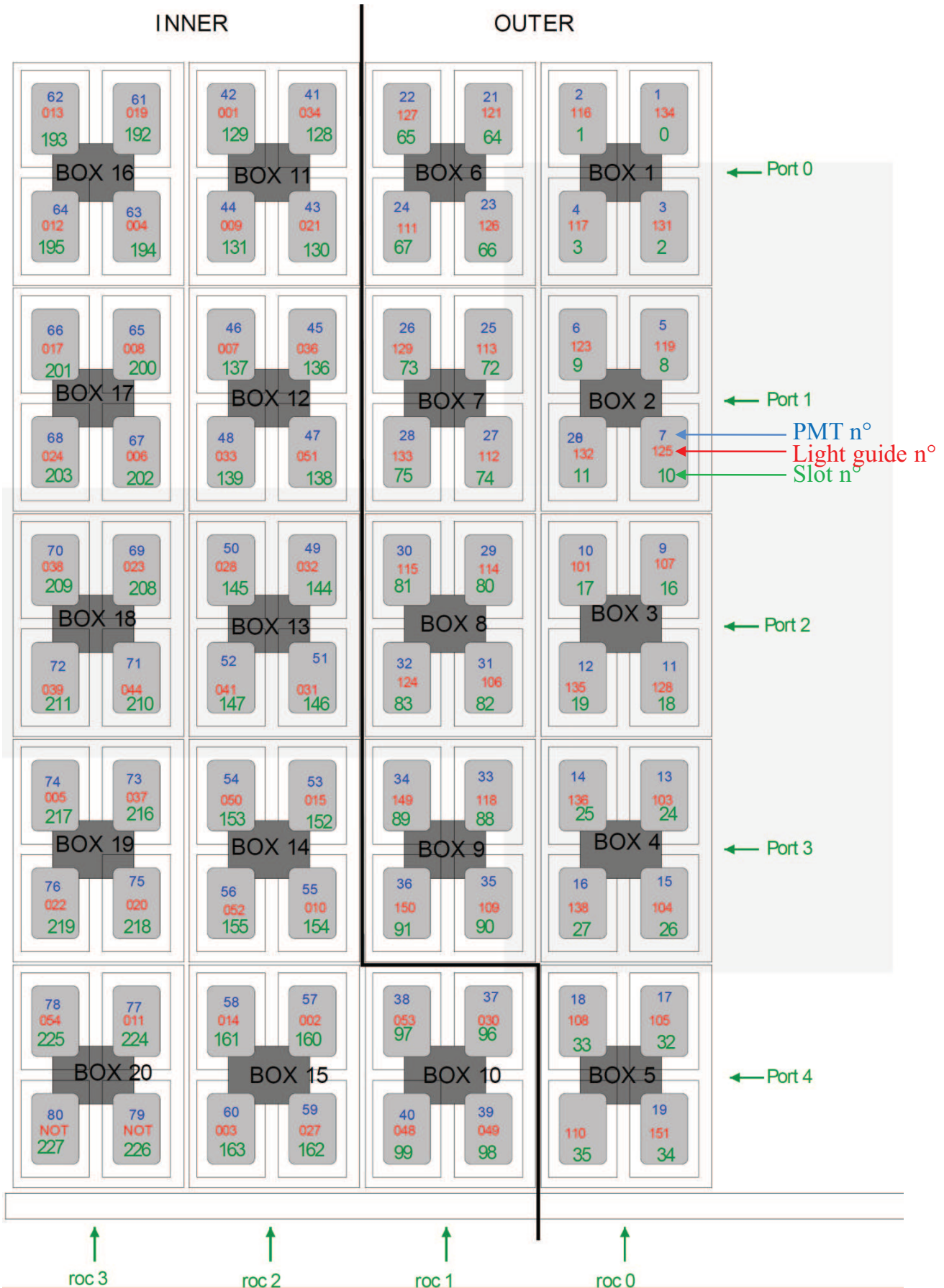
Figure 5.28: Mapping electronics in the two towers of the SFT Detector housed.

5.6 Radiation level monitoring of the SFT detector

Due to the importance of the radiation level on the light guides [108], several tests were done before and during the operation of the recoil detector. First of all these tests were used to determine the signal attenuation due to the radiation damage, and how important the radiation on the recoil Area during the operation will be. For this purpose at the 'hot' points of the HERA-RING at DESY we have installed for a few weeks 16 light guides from the GMS system with *Radiophotoluminescent* (RPL) glass dosimeters. The 'hottest' point at HERA was on the area of the 4 *Kicker* magnets at the e^- injection point, close to the west hall. The position chosen for the light guide and the RPL dosimeter can be seen in Fig. 5.29
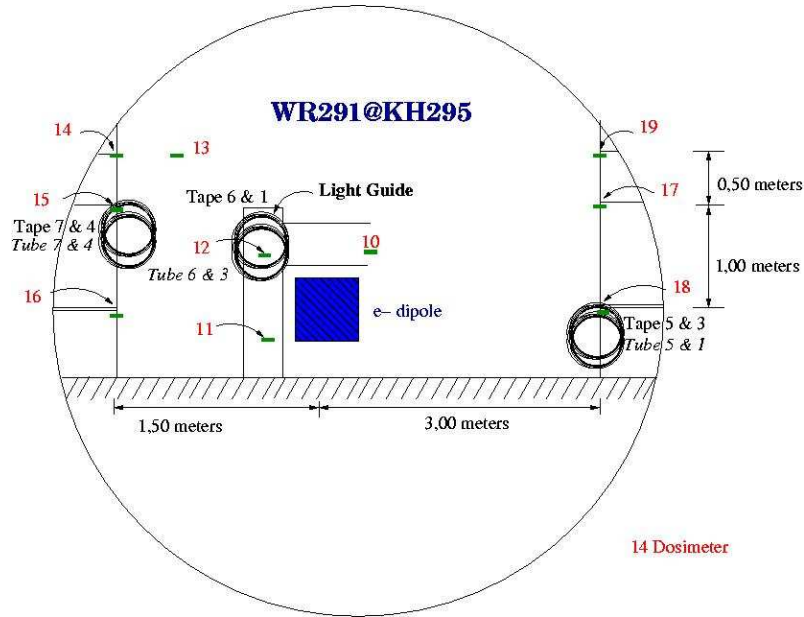

Figure 5.29: Light Guide and RPL dosimeter positions at the area of the 4 *Kicker* magnets at the HERA e^- injection point.
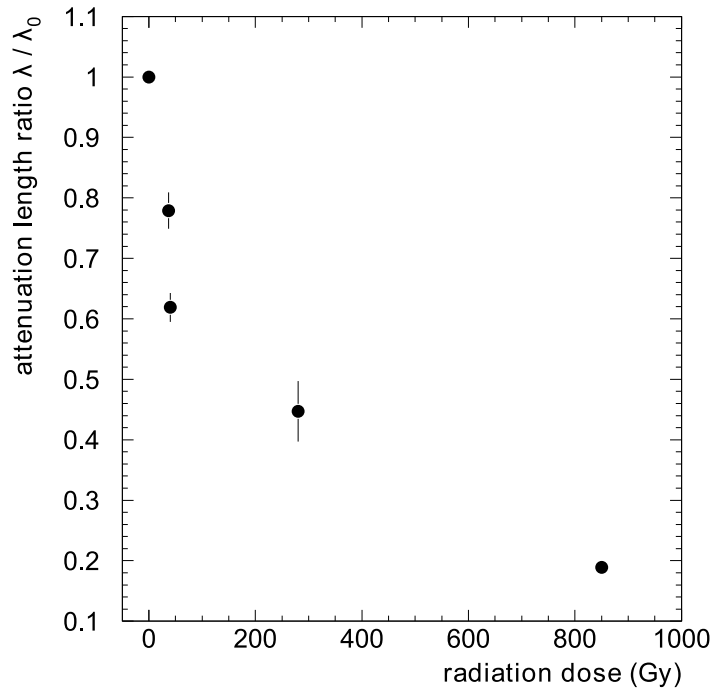

Figure 5.30: The attenuation length ratio as a function of absorbed dose. The attenuation length refers to the ratio before and after irradiation. The results for the individual fibers were averaged over the absorbed dose [99].

The attenuation length ratio as a function of absorbed dose is shown in Fig. 5.30. The attenuation length refers to the ratio before and after irradiation at HERA. The results for the individual fibers were averaged over the absorbed dose [99].

The radiation on the recoil detector area was estimated to be enough to damage the light guide from the SFT detector. Due to this, several RPL dosimeters were installed around the recoil detector and the SFT electronics towers. The positions were chosen to be distributed homogeneously in one plane of the recoil detector, the distribution can be seen in Fig. 5.31.
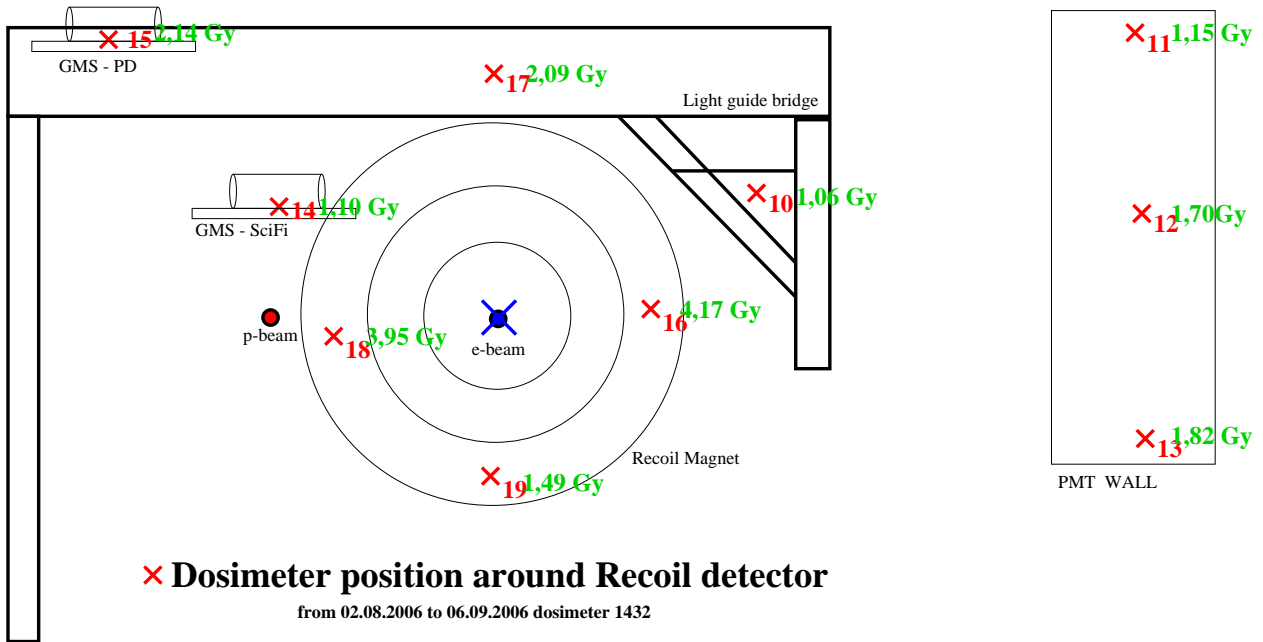

Figure 5.31: RPL dosimeter position surrounding the Recoil Detector and dose collected from 02.08.2006 to 06.09.2006.

The RPL dosimeters were changed every one or two months when it was possible to access the HERMES area. This possibility was only during the maintenance day of HERA, a day chosen by the machine group. The total dose collected by the RPL dosimeters was small and the influence on the light guides attenuation length is negligible, less than 10% when compared to the study [99].

MEASURED DOSE

Dose Position	03.07.06 02.08.06	02.08.06 06.09.06	06.09.06 25.10.06	25.10.06 06.12.06	06.12.06 06.02.07	06.02.07 21.03.07	21.03.07 09.05.07	09.05.07 30.07.07	Total Measured
11	$0.38\ Gy$	$1.15\ Gy$	$0.60\ Gy$	$1.62\ Gy$	$-\ Gy$	$1.9\ Gy$	$6.97\ Gy$	$6.3\ Gy$	$\sim 22\ Gy$
12	$0.63\ Gy$	$1.70\ Gy$	$0.79\ Gy$	$1.90\ Gy$	$2.6\ Gy$	$2.3\ Gy$	$7.03\ Gy$	$7.7\ Gy$	$\sim 25\ Gy$
13	$0.80\ Gy$	$1.82\ Gy$	$0.97\ Gy$	$1.53\ Gy$	$1.9\ Gy$	$2.0\ Gy$	$11.1\ Gy$	$6.0\ Gy$	$\sim 27\ Gy$
14	$0.69\ Gy$	$1.10\ Gy$	$0.66\ Gy$	$0.81\ Gy$	$2.0\ Gy$	$1.3\ Gy$	$14.9\ Gy$	$5.7\ Gy$	$\sim 30\ Gy$
15	$0.27\ Gy$	$2.14\ Gy$	$0.40\ Gy$	$0.63\ Gy$	$1.6\ Gy$	$2.3\ Gy$	$12.9\ Gy$	$2.4\ Gy$	$\sim 24\ Gy$
16	$4.18\ Gy$	$4.17\ Gy$	$5.12\ Gy$	$5.03\ Gy$	$4.2\ Gy$	$6.2\ Gy$	$4.41\ Gy$	$3.0\ Gy$	$\sim 36\ Gy$
17	$3.53\ Gy$	$2.09\ Gy$	$1.33\ Gy$	$2.37\ Gy$	$2.0\ Gy$	$3.7\ Gy$	$4.42\ Gy$	$0.6\ Gy$	$\sim 22\ Gy$
18	$1.49\ Gy$	$3.95\ Gy$	$-\ Gy$	$1.33\ Gy$	$1.4\ Gy$	$2.3\ Gy$	$1.71\ Gy$	$0.6\ Gy$	$\sim 17\ Gy$
19	$1.28\ Gy$	$1.49\ Gy$	$1.32\ Gy$	$2.43\ Gy$	$1.2\ Gy$	$1.4\ Gy$	$1.34\ Gy$	$-\ Gy$	$\sim 15\ Gy$
10	$1.31\ Gy$	$1.06\ Gy$	$1.99\ Gy$	$1.15\ Gy$	$1.2\ Gy$	$1.8\ Gy$	$7.95\ Gy$	$5.9\ Gy$	$\sim 23\ Gy$

Table 5.3: Measured radiation around the Recoil Detector with RPL dosimeter. RPL dose measured by Kay Uwe Hartz from radiation group of DESY.

5.7 GMS stability (Gain Monitoring System)

The Gain monitoring system was used to obtain the relative variation of the gain of the SFT detector and check the response in real time. These measurements were done during the specific procedure after the shutdown of the HERA beam for refilling. This procedure was incorporated in all servicing measurements of the recoil detector.

The result of the GMS was important because it allows us to verify the operability of the SFT detector between each fill. With the GMS it was possible to optimize the High Voltage of the PMTs and calibrate with a single photon electron of the GMS signal some SFT channels (around 330 of all SFT detector) [109]. Shown in Fig. 5.32 is the result of the scanning of the high voltage with the GMS on one particular PMT, it shows the change of the high voltage to be on the top of the plateau in this PMT.
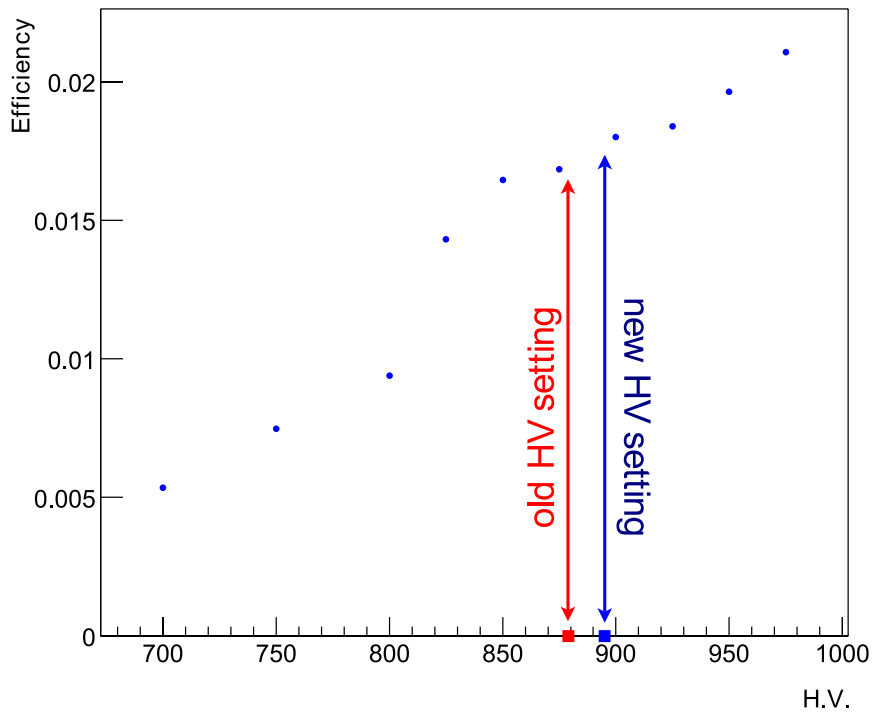

Figure 5.32: Result of the test on the high voltage of the SFT's PMT with help of the GMS. It can be seen on this plot that the high voltage chosen for this particular PMT was changed, after the scan of the high voltage with the GMS.

The GMS light as described in section 4.6.1 arrived to all channels of the SFT. It was possible to know the variation of each channel individually. Each channel on the SFT detector was fit with one Gaussian and two Poison distribution corresponding to the pedestal and the first and second photon electron (p.e) peak.

The low intensity of the light source and the cladding of the fibers let us get one or two p.e. peak per channel. GMS measurements were fitted with Gaussian and two Poisson distributions, corresponding to the pedestal and the first and second p.e peak. The fit for one channel is shown in Fig. 5.33. The GMS measurements were fitted before pedestal subtraction and sparsification, the SFT detector readout electronics yield negative pulse signal (see subsection 4.3.3), therefore the pedestal are on the right of the signal.
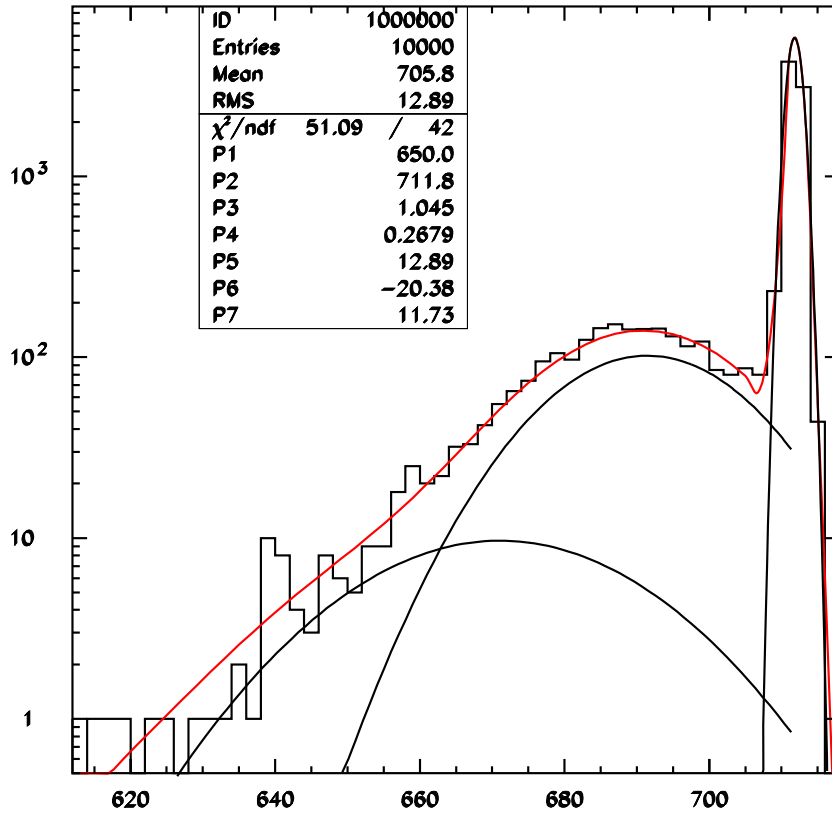
Figure 5.33: GMS measurement for one channel fitted with Gaussian and two Poisson distributions, corresponding to the pedestal and the first and second p.e. peak

It was decided to analyze online the GMS results for the PMTs when all channels were combined. This is shown in Fig. 5.34 left for one individual channel and on the right of the same figure is shown the combination of all channels in one.

Figure 5.34: GMS measurement for one channel on left and for the same PMT for all channels combined.

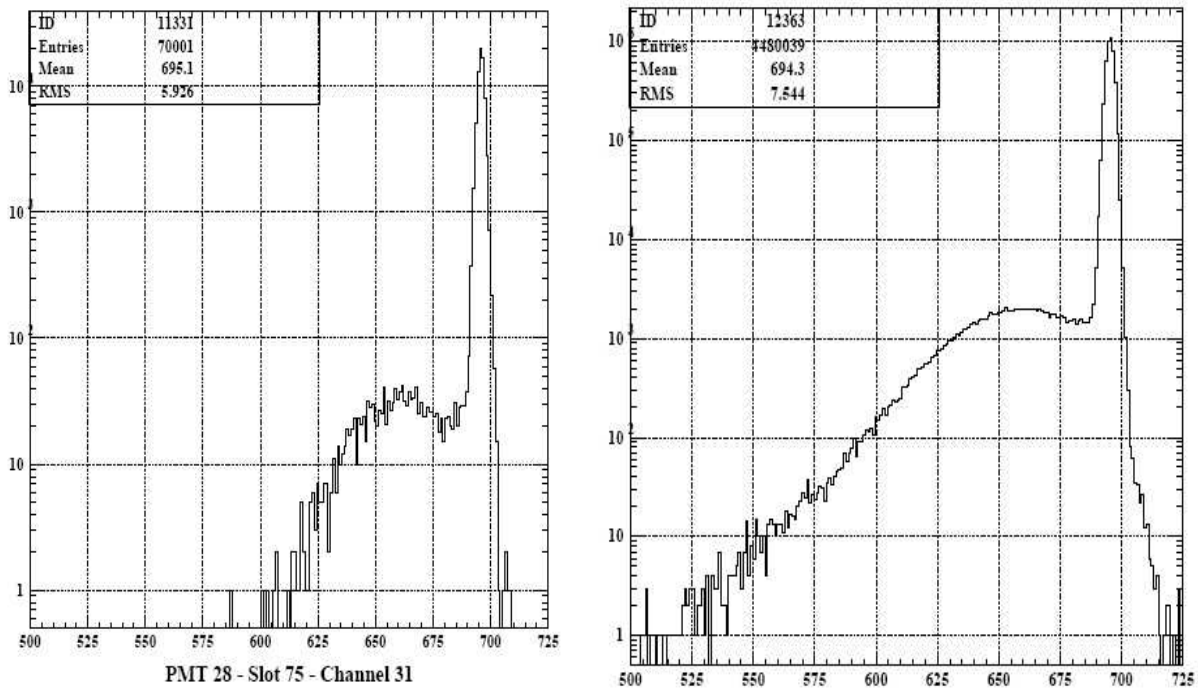The light from the light source was injected at the same time also at the reference PMT, located above the holding structure inside the HERA tunnel. Then the response was compared with very stable light output from the α-source. Because the GMS light source can fluctuate, this comparison on the PMT reference was important to have the possibility to understand the possible variation of the GMS signal on the SFT detector.
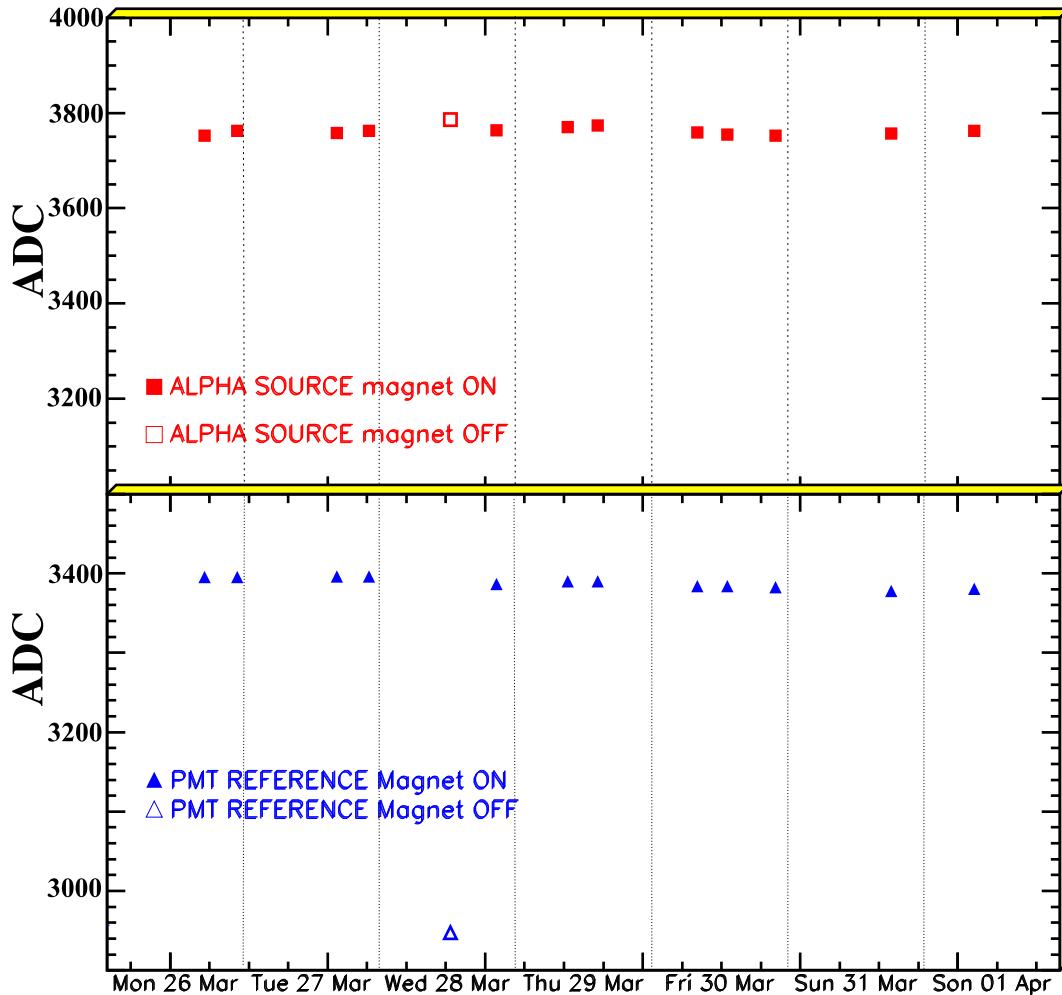

Figure 5.35: PMT reference and α-source of the GMS system of the recoil detector, operation stability for one week.

The reference PMT was monitored with one very stable light output from α-source. This measurement was used to verify the stability of the PMT reference and the light source. In Fig. 5.35 is shown the stability of the α-source (red) and the PMT reference (blue) with the magnet *on* or *off* (close/open symbols). The PMT reference was stable except when the recoil magnet was *off*, the decrease of the signal of the light source and not on the α-source indicate the influence of the recoil magnet on the light source and not on the PMT reference.

This variation of the gain was done for each PMT individually. A huge variation on the GMS light was not observed during the operation of the SFT detector. In Fig 5.36 is shown for all PMT of the first ROC of the SFT the fit variation of the sparcified GMS signal during one week. These types of plots were shown during the weekly onsite meetings at DESY.
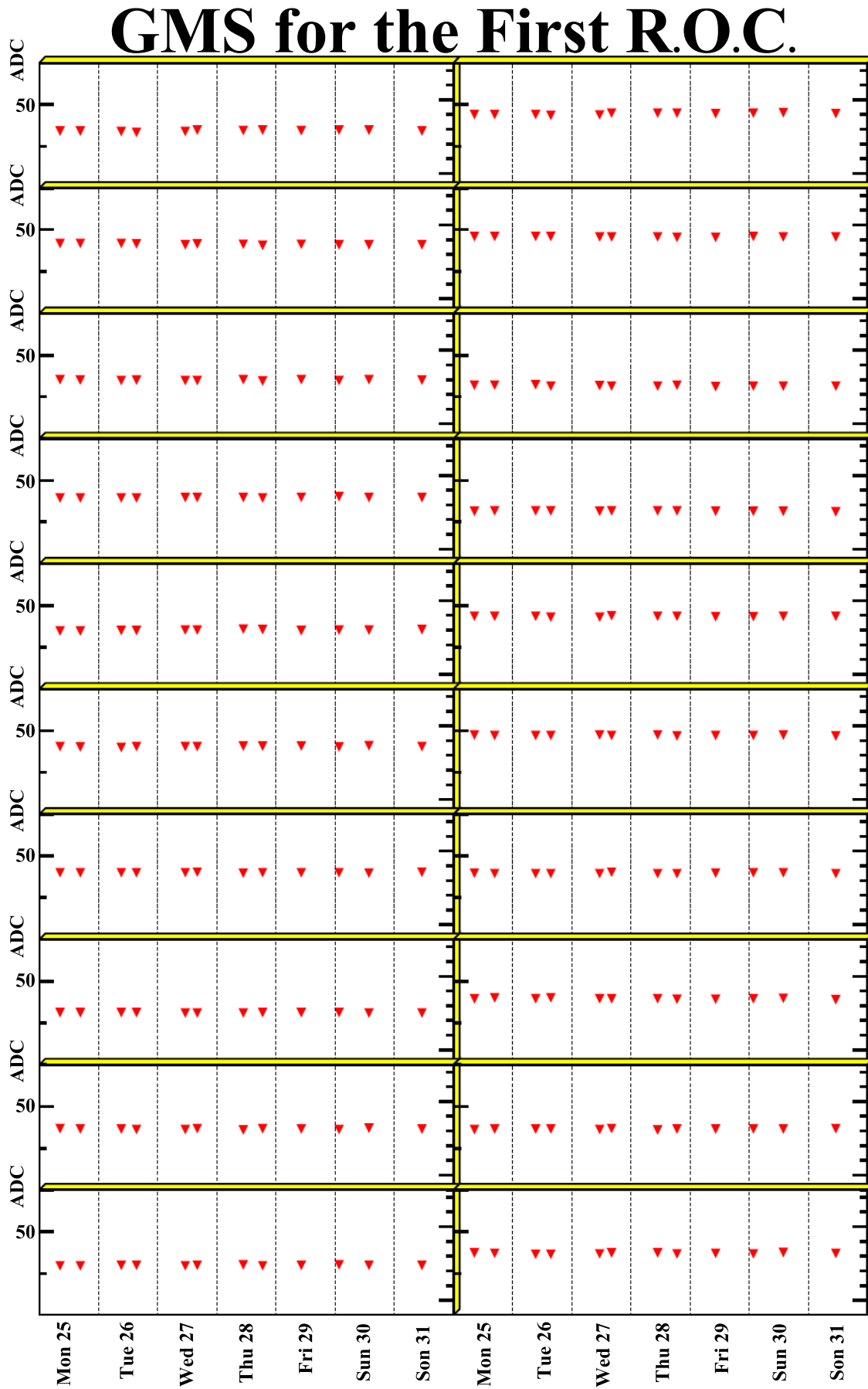
GMS for the First R.O.C.

Figure 5.36: Weekly stability of the GMS for the SFT PMTs, shown only for the first ROC.

5.8 Pedestal stability

During measurement, when we record data with threshold sparsification, it is highly important to control the electronic noise. This is the case of amplitude measurement, the pedestal measurement and control [91]. The pedestal drifting can affect all measurements of the detector. It has been mainly cut off during the online data taking by threshold sparsification on the data, and further subtracted in the stage of offline decoding [86].
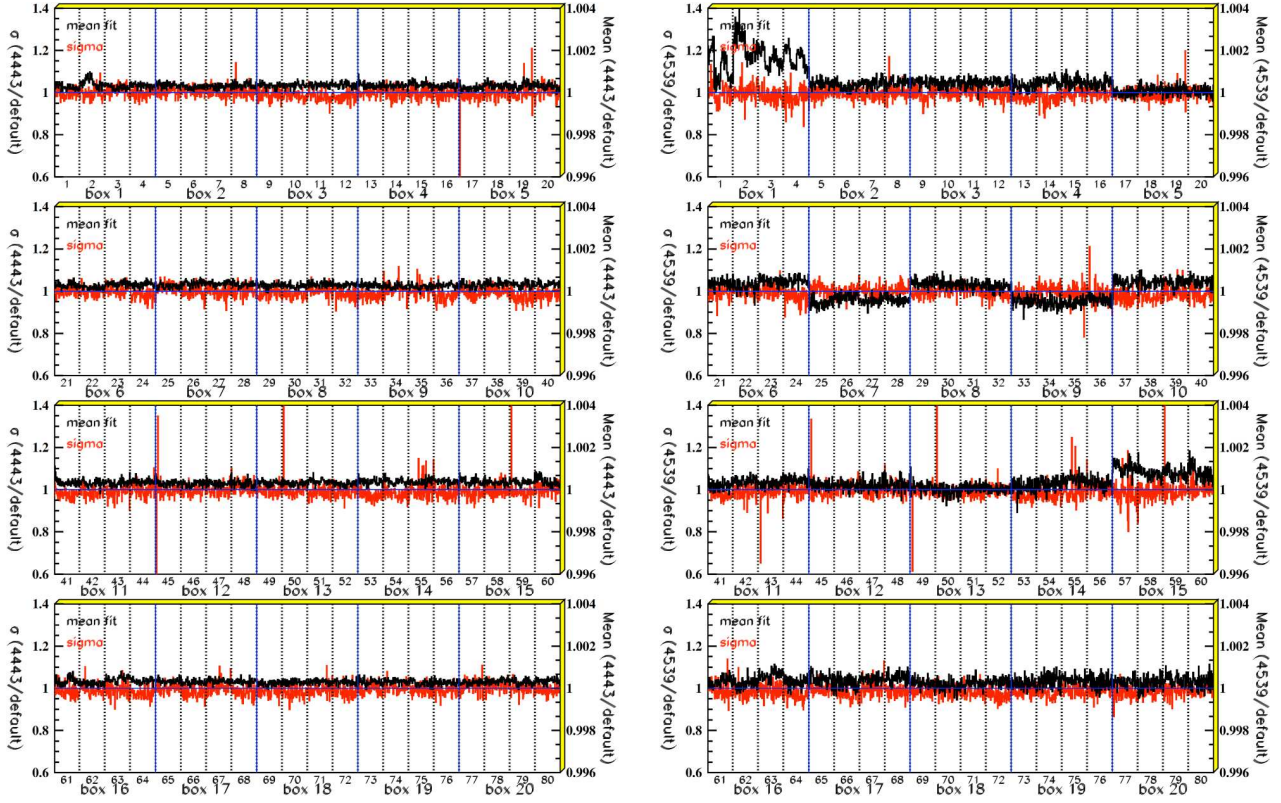

Figure 5.37: The Pedestals of all channels of the SFT detector were compared with the reference pedestals, these reference pedestals or default values of the pedestals are used to calculate the threshold of the sparsification. In the left plot the ratio between the new pedestal and the default. The new pedestal in this case does not change compared to the reference one. In the right upper plot it can be seen the pedestal drift on the *box 1*, these drifts were estimated of 2 or 3 ADC channels. After this shift on the pedestals, the new pedestals were used for the calculation of the threshold sparsification.

The stability of the SFT pedestal was verified during the procedures involved in servicing measurements of the recoil detector. The reference pedestal was used to the threshold sparsification and to compare the pedestal value taken during the servicing measurement of the recoil detector. The ratio between the new pedestal and the default is shown in Fig. 5.37, where the ratio indicates a drift on the new pedestal, like the example on the right side in Fig. 5.37, the new pedestals were used in calculation of the sparsification threshold.

5.9 Multiplicity of the SFT detector

Other plots shown at the weekly onsite meetings at Desy, used to verify the proper operation of the SFT detector, were the multiplicity plots. These plots were used to understand the effect of the noise level on the data. The possible source of the noise in the recoil detector was electrical noise (due to machine operation), Møller scattering, on target electrons, synchrotron radiation, scattering on collimator and proton showers coming from the proton beam. In order to measure all this noise, the timing structure of Hera bunches was used. Certain measurements were done in bunch free times, when there was no e-bunch passing though Hermes, (more details can be found at [86]). The pedestal drifting shown in section 5.8 also can affect the determination of the noise occupancy of the SFT.

The hit multiplicity in the wrong TDC windows indicates the noise level expected per DIS events in the SFT detector. Shown in Fig. 5.38, the hit multiplicity recorded before the correct TDC window corresponds to trigger 21 in the left plot and the hit multiplicity after the correct TDC window in the right plot. In both plots the hit multiplicity for each layer on the SFT detector are shown, in the top for the inner SFT and in the bottom, for the outer SFT detector. In the plots before the correct TDC windows the hit multiplicity is relatively low compared to the hit after the correct TDC window.
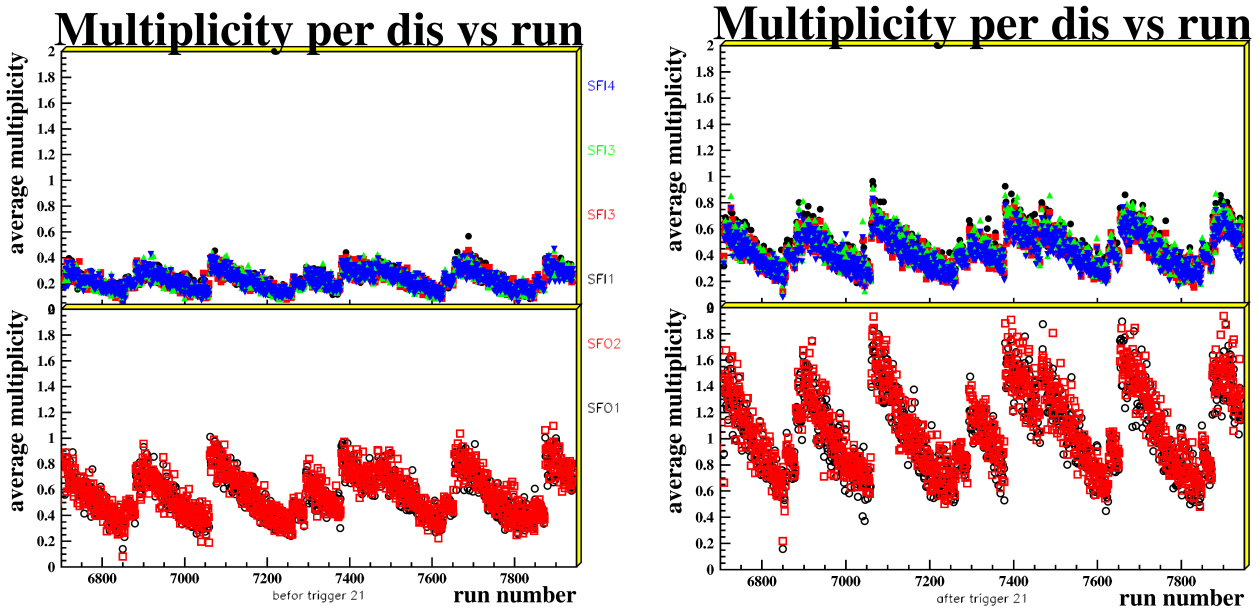
Figure 5.38: Hit multiplicity per DIS event in the wrong TDC window. Before the correct TDC windows in the left Figure and after the correct TDC windows in the right Figure. Trigger 21 is the main trigger, this trigger was optimized to select events with DIS electrons.

The hit multiplicity plots also show the beam current behaviour in time, where we can see Hera fills. There are more hits when the beam current is high. This observation show that the noise coming from the beam (Møller scattering, synchrotron radiation, scattering on collimator and proton showers) is relatively small.

The hit multiplicity in the correct TDC window is shown in Fig. 5.39. In the correct TDC window the hit multiplicity is around 4 hits per layer. The hit multiplicity in the correct TDC window is clearly stable and does not depend on the level of the beam intensity. The noise seen in the wrong TDC windows is small compared to the detector response at the correct TDC window.
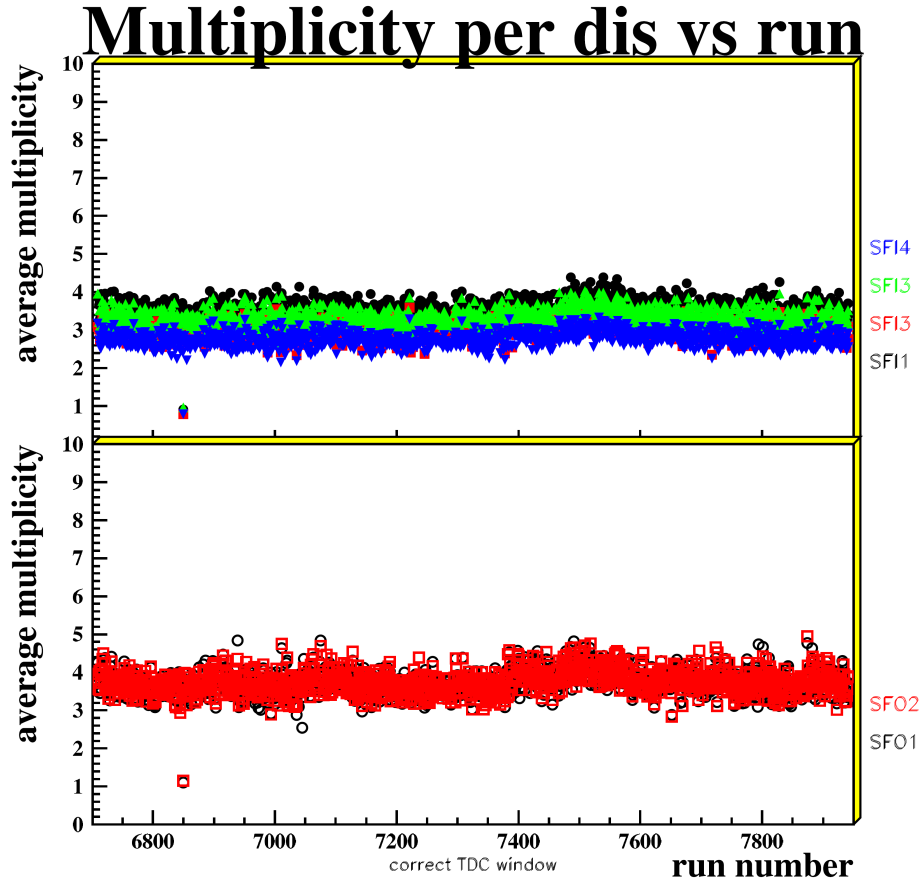

Figure 5.39: Hit multiplicity per DIS event in the correct TDC window. In the correct TDC window the hit occupancy on each layer is around 4 hits.

Chapter 6

Scintillating Fiber Tracker Efficiency

The SFT detector efficiency is the probability of detecting a track if it has taken place. The detector efficiency is a function of the variables that describe the event, momentum, ϕ or θ. For every measurement dealing with cross-section, one has to correct for the detection efficiency.

The detection efficiency ε of our complex SFT detector was measured with the final data sample. To measure the efficiency of the detector, one needs a sample of events for which the detection does not depend on that detector. If in n out of N events the detector produces a signal, then

$$\varepsilon = \frac{n}{N} \tag{6.1}$$

The efficiency of the SFT detector was calculated for each plan, parallel and stereo, inner and outer SFT, and for space points.

6.1   Tracks Selection

The track on the Recoil detector are reconstructed from all the space points measurement on the Silicon detector and the SFT detector. For the study on the efficiency this procedure was modified with a new flags (or option) to the *eXtra Tracking Code* or XTC. The new flags implemented, give us the possibility to use all hits above a thresholds and remove from the tracking reconstruction method the layer of study.

The new flag are:

 - - sft-thresholds n –Thresholds for the SFT detector in ADC units.

 - - removelayer *layer_no*

With a possible values for *layer_no*:

 1 : Inner Triggers

 2 : Outer Triggers

 3 : Inner SFT

 4 : Outer SFT

 5 : Upper frame TIGERs

 6 : Lower frame TIGERs

 7 : All TIGERs (Remove Si)

 8 : All SFT layers

Due to the high number of ghost tracks, the requirement on the selection of the good tracks for this studie is necessary. This requirements were:

- Tracks with 3 Space point + 1 Space point on the Photon detector

  Inner Silicon

  Energy deposited in $S[1-2]I[1-4] > 100\ keV$ 'Space point'

  Outer silicon

  Energy deposited in $S[1-2]O[1-4] > 100\ keV$ 'Space point'

  Cut in the inner SFT

  Energy deposited on 'Parallel Cluster' $> 0\ p.e.$

  Energy deposited on 'Stereo Cluster ' $> 0\ p.e.$

  Ratio between Energy deposited in layers: $0.1 <$ (Energy on parallel/Energy on stereo) < 10

  Photon Detector cut

  $-0.2\ rad < \varphi$ Calculated $- \varphi$ Space point$< 0.2\ rad$

  Energy of Space point $>\ 1 MeV$

- PID

  Inner SFT Detector cut

  $pid1 + pid2 + pid5 + pid6 > 0$ and momentum track positive for Protons
  $pid1 + pid2 + pid5 + pid6 < 0$ for Pions

  Outer SFT Detector cut

  $pid1 + pid2 + pid3 + pid4 > 0$ and momentum track positive for Protons
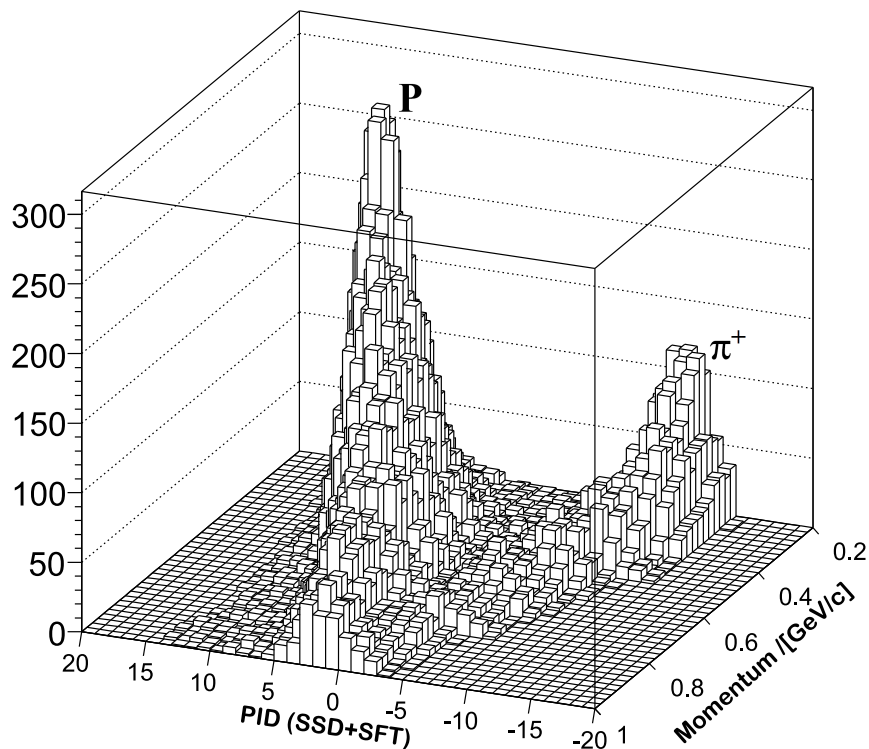 $pid1 + pid2 + pid3 + pid4 < 0$ for Pions

Figure 6.1: The three dimensional distribution of PID versus the reconstructed momenta, from [86].

The particle identification (PID) show on Fig. 6.1 is performed by using the conditional probability method. The PID is done by combining all the information from the three sub-detectors. The Silicon detector provides two PID values, $pid1$ and $pid2$, from the inner and outer detector. The SFT have four PID values, $pid3$, $pid4$, $pid5$ and $pid6$, instead of two as of the Silicon detectors. The four PID values are separately from inner parallel layer, inner stereo layer, outer parallel layer and outer stereo layer. The reason to separate the SFT PID in sub-layer level is to reduce the systematic uncertainties, which mainly come from the calibration uncertainties of the different PMTs. Comprehensive description of the Recoil detector PID can be found in [86].

6.2 Track parameters and hit positions

The reconstructed track parameters (P, θ, ϕ) and the measurement of the beam position, which was taken as the track vertex, the intersection point between the track and the layer of the SFT detector can be calculated. Using the following assumptions:

- constant magnetic field $\overrightarrow{B} = (0, 0, B_z)$;

- negligible multiple scattering;

- no other interactions;

With this assumptions, the track moves along a helix which is defined by five parameters:

$$\{QD_0, \ \phi_0, \ Q/R, z_0, \ cot\theta\} \tag{6.2}$$

Q is the charge; D_0 is the distance of closest approach of the helix to the origin in the xy plane; ϕ_0 is the angle between the transverse momentum vector and the x axis at the point of closest approach; R is the radius of curvature; θ is the angle between the momentum vector and the z axis at the point of closest approach [110]; see Fig. 6.2 and 6.3 for the description of track trajectory in rz and $r\phi$ planes.
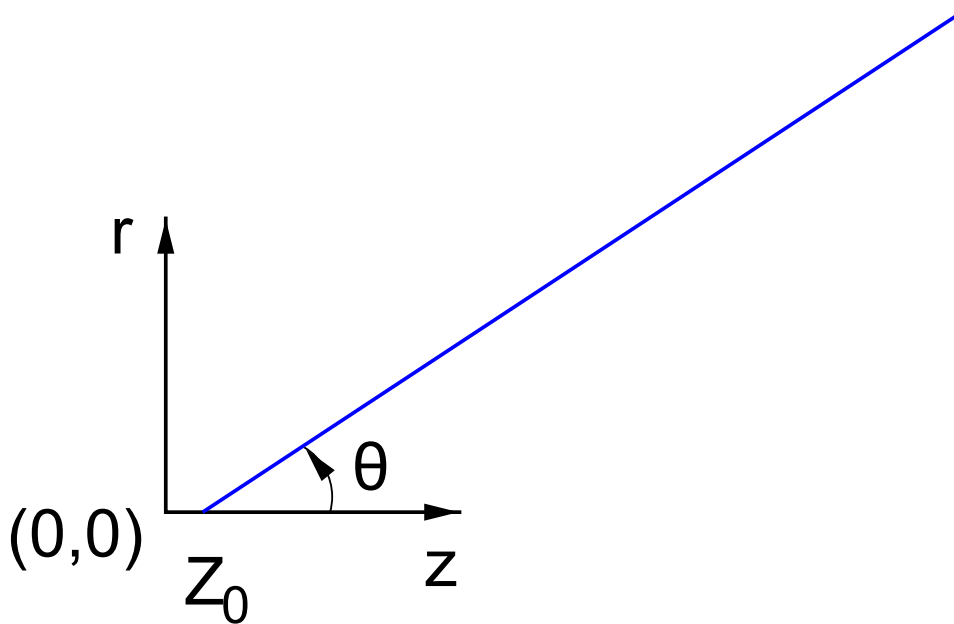

Figure 6.2: Track trajectory in the rz plane.
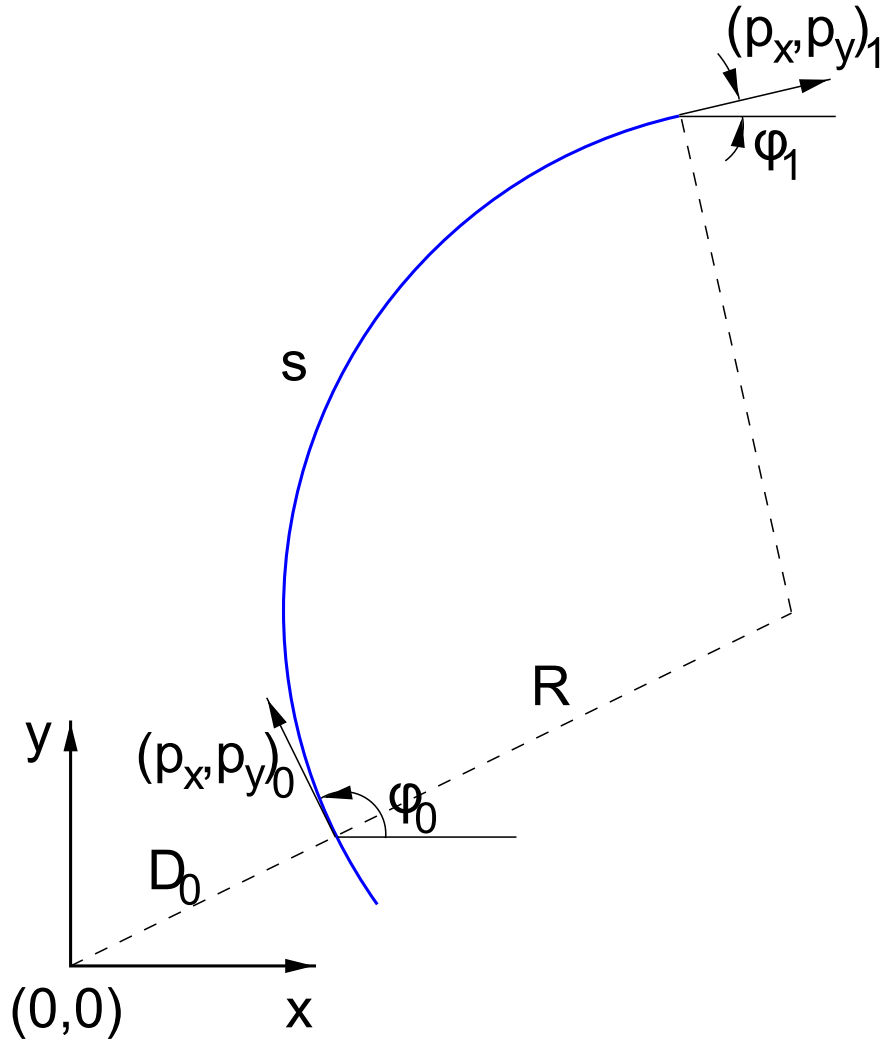
Figure 6.3: Track trajectory in the $r\phi$ plane.

The point of the closest approach is given by:

$$
\begin{aligned}
x_0 &= QD_0 sin\phi_0 \\
y_0 &= -QD_0 cos\phi_0 \\
z_0 &
\end{aligned}
\tag{6.3}
$$

Where the distance of closest approach of the helix D_0 is given by:

$$
D_0 = \sqrt{x_0{}^2 + y_0{}^2}
\tag{6.4}
$$

Any point along the path of the helix can be expressed in terms of the path length s which is a function of ϕ, the tangent angle at a point along the track.

$$
s(\phi) = -QR(\phi - \phi_0)
\tag{6.5}
$$

The radius of curvature R is related to the track's momentum and the magnetic field, for R in meters, B in Tesla and p_T in GeV:

$$
R = \frac{p_T}{0.3B}
\tag{6.6}
$$

V vertex
O xy origin
D point of closest approach
C centre of curvature

Figure 6.4: Calculation of track parameters.

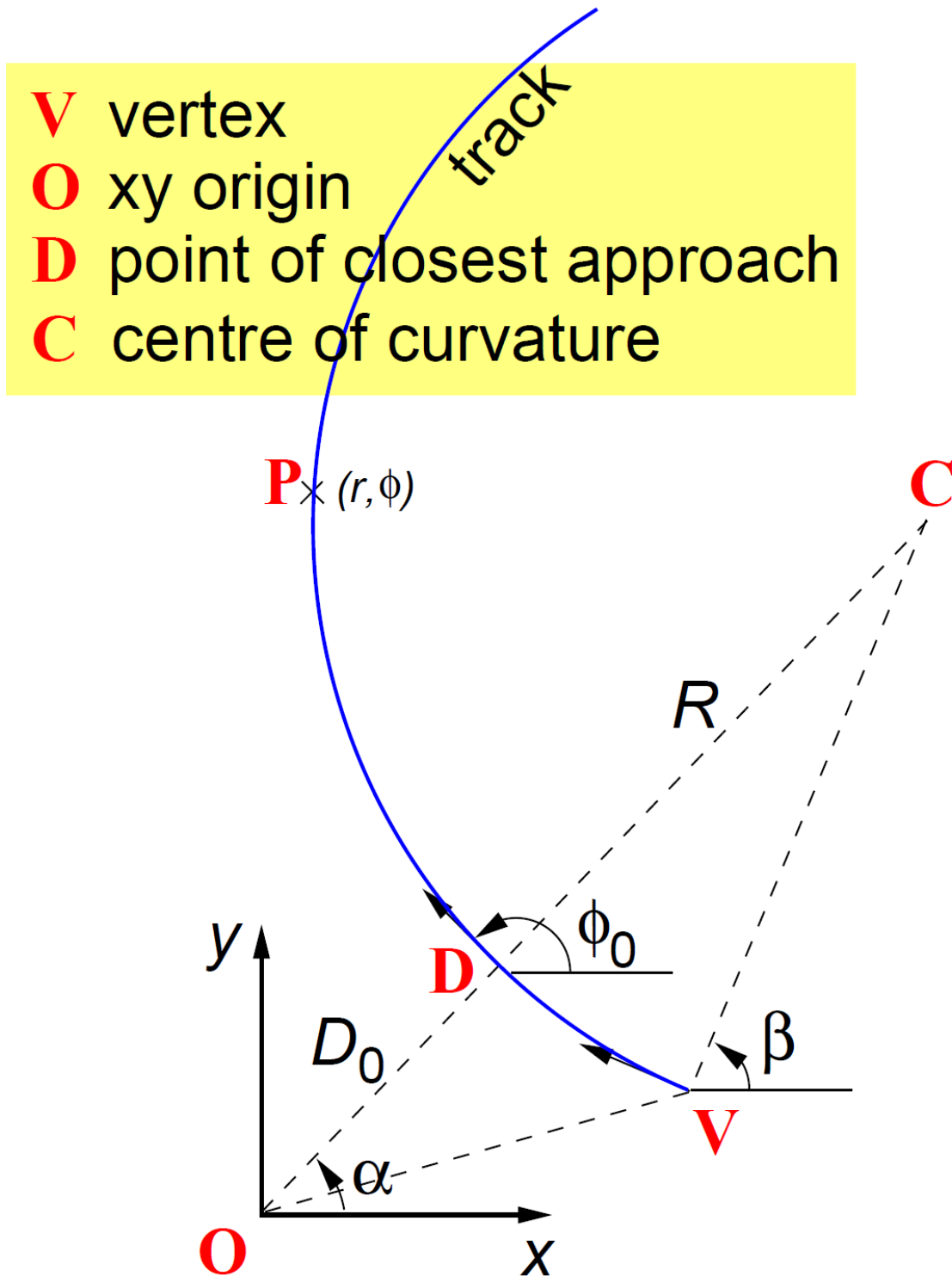In the plane (R, ϕ), the position of the particle following a helical trajectory can be described in term of the circle parameters ϕ_0, D_0 and R.

Referring to Fig. 6.4, a given point P on the arc has polar coordinates (r, ϕ). This point forms a triangle $\widehat{OPC}$ with sides of length $|\overrightarrow{OP}| = |\overrightarrow{PC}| = r$ and $|\overrightarrow{OC}| = D_0 + R$ and the angle $(\phi - \alpha)$ at the origin.

$$cos(\phi - \alpha) = cos(\phi - \phi_0 + Q\pi/2)$$
$$= Qsin(\phi - \phi_0) \tag{6.7}$$

The sides and angle of the triangle are related by the 'cosine' rule:

$$R^2 - (R + D_0)^2 - r^2 = -2r(R + D_0)cos(\phi - \alpha) \tag{6.8}$$

Which yields $\phi(r)$ dependence like:

$$\phi(r) = \phi_0 - Q \times sin^{-1}\left(\frac{D_0{}^2 + r^2 + 2RD_0}{2r(R + D_0)}\right) \tag{6.9}$$

When it is valid to approximate that $D_0 = 0$ this simplifies to:

$$\phi(r) = \phi_0 - Q \times sin^{-1}(r/2R) \tag{6.10}$$

If $(\phi - \phi_0)$ is small such that $sin(\Delta\phi) \approx \Delta\phi$, and if $r << 2R$ then $sin^{-1}(r/2R) \approx r/2R$; then the track is approximately linear:

$$\phi(r) = \phi_0 - \left(\frac{Q}{2R}\right) \times r \tag{6.11}$$
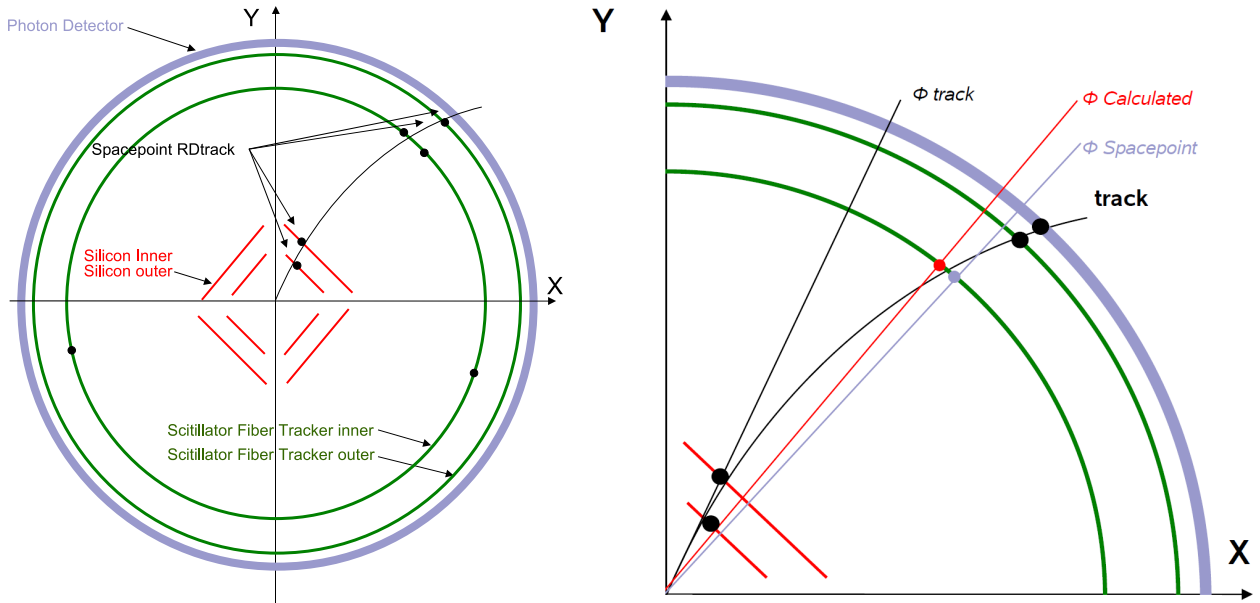
Figure 6.5: Track path through the recoil detector. On the left side shown the track with the corresponding space points on the different subdetectors, on the right side we explain the angles ϕ of the track on the vertex, the ϕ of each space point and the ϕ calculed with eq. 6.9.

The track parameters were used to calculate the angle ϕ in the layer under study with the eq. 6.9, this ϕ angle is different as the ϕ of the track on the vertex or the ϕ of the space point, as we can see on Fig. 6.5. Ideally the ϕ calculated should be equal as ϕ space point. Also we can calculate the cartesian variables $\{x,y,z\}$ where, the

track trajectories calculated pass through the layer of the SFT detector. All this variables should be ideally identical as the space point variables.
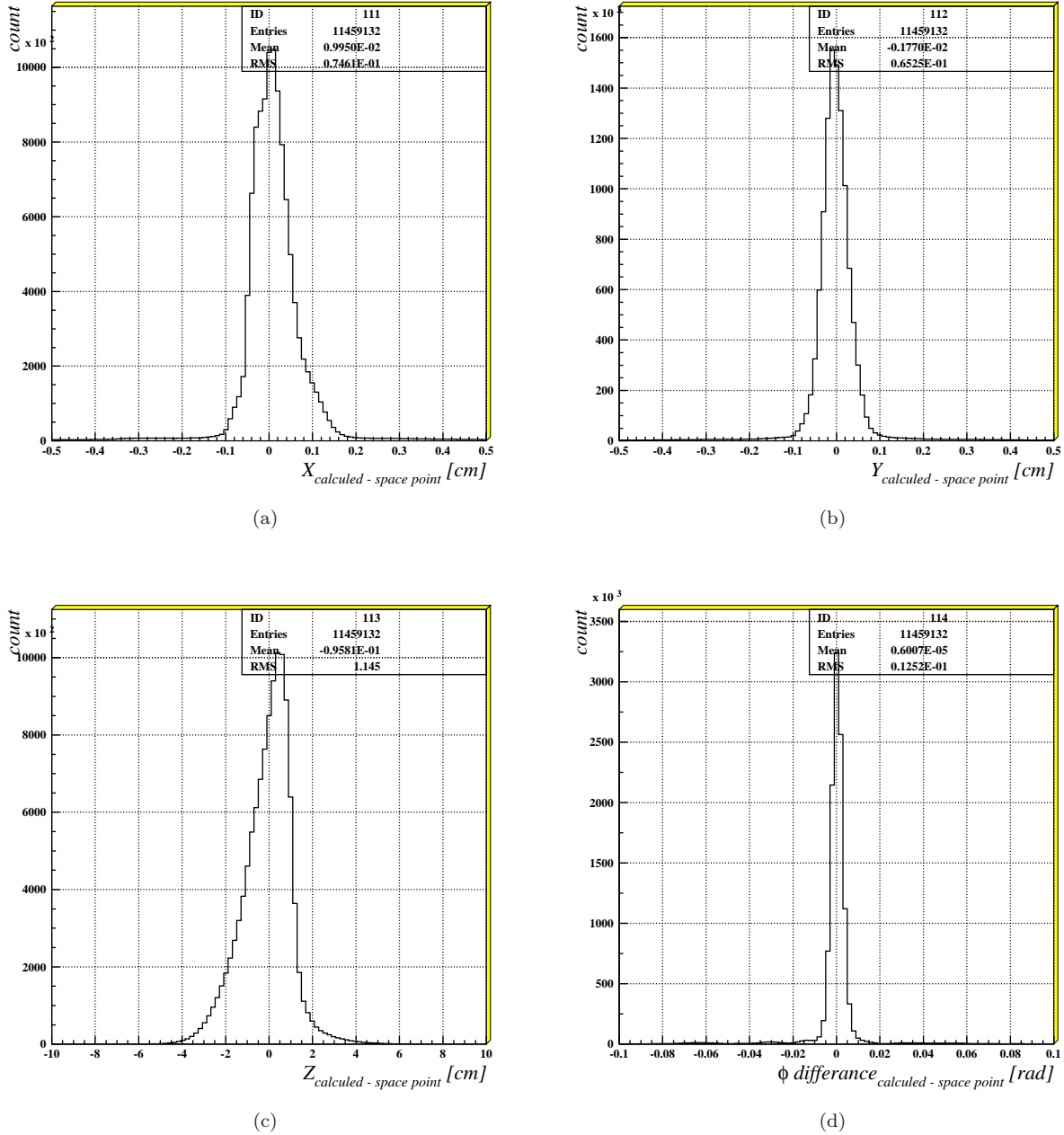
Figure 6.6: Track parameter difference for SFT inner detector.(a) X coordinate, (b) Y coordinate, (c) Z coordinate and (d) ϕ.

The difference between the variable X, Y, Z, ϕ calculated and the space points are shown on the Fig. 6.6. This difference are shown for the inner SFT detector and for protons tracks. In the outer SFT detector and for pions tracks this differences are slightly broad. It is possible to see clearly for X and Y the difference between the variable calculed and from the space point is less than $\pm 0.2 cm$. Due to the resolution of the Z vertex on the forward spectrometer the track parameter resolution is large as it was expected the difference is $\pm 2 cm$. The variable ϕ, the best due to the design of the SFT detector, have a resolution nearly of one fiber.[1]

---

[1]The ϕ angle for one fiber on the inner layer of the SFT is $0.0095 rad$.

Figure 6.7: ϕ difference for Inner SFT Protons for Parallel Clusters in (a) and Stereo Clusters in (b)
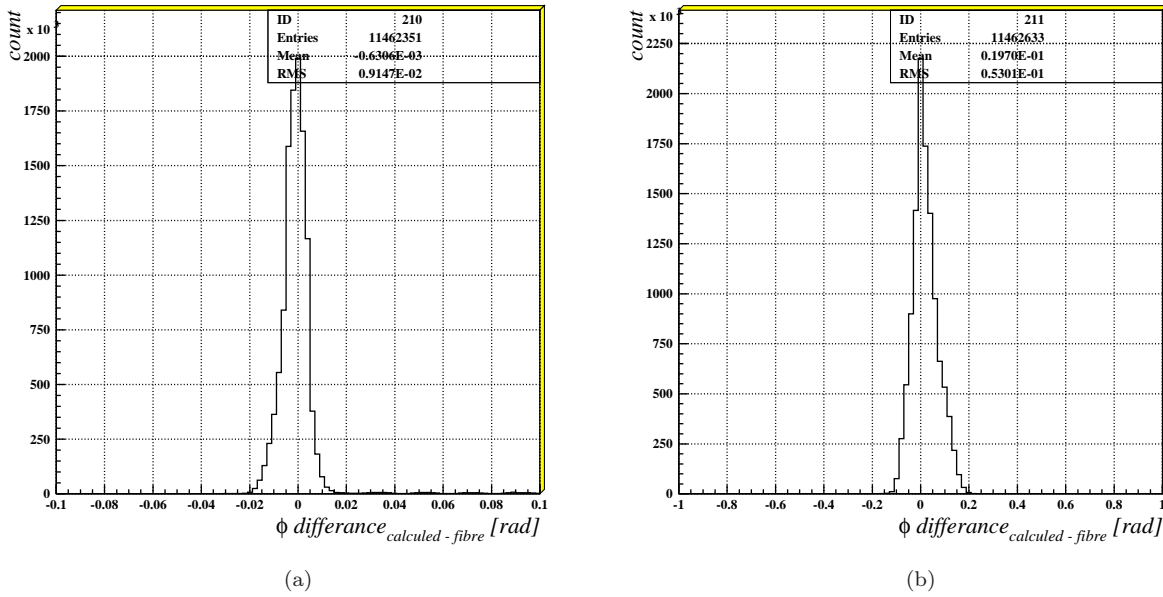
For proton tracks the RMS of ϕ angle difference for space point in the inner SFT is around $0.0125 rad$, as we can see on the Fig. 6.6(d); for the parallel fiber on the inner SFT at cluster level this value goes down (see Fig. 6.7(a)) and is high for the stereo fibers (see Fig. 6.7(b)). The efficiency was chosen to be monitored versus this variable ϕ, the statistics was not enough to have a ϕ range comparable small as one fiber. Due to this, we chose a small as possible the ϕ range, we divide the $2\pi\ rad$ on 100 divisions, each of this division are equivalent to have 6 fibers together on each division.

6.3 Efficiency of the SFT detector

In this section we will present the efficiency for the SFT detector for protons and pions for the space points and the clusters. We will expose the stability of the efficiency per quadrant and compared the efficiency for protons with the efficiency for pions. At the end of the section the outer SFT detector efficiency will be presented as well.

6.3.1 Inner SFT efficiency

The efficiency is calculated by counting the number of tracks that are passing through a section of the detector and the number of them that are detected there. Respectively N_{all} and N_{det}.

$$\varepsilon^i = \frac{N_{det}{}^i}{N_{all}{}^i}, \tag{6.12}$$

where i is the "Fiber bins index", index corresponding to the number of divisions we made from our cylindrical detector to accumulate enough statistics in each division ($1 < i < 100$).

In Fig. 6.8 we can see the ϕ distribution of the tracks passing though the detector (black). The space point or cluster events when hits are detected in the SFT (red). The difference between the ϕ calculated from the track parameters and the real track parameters is due to the track parameters are defined on the vertex and not on the intersection with the detector. We should use this tracks parameter on eq. 6.9 to calculate the ϕ of the SFT detector to be able to compare the number of tracks passing through a section of the detector and the detected number of them.
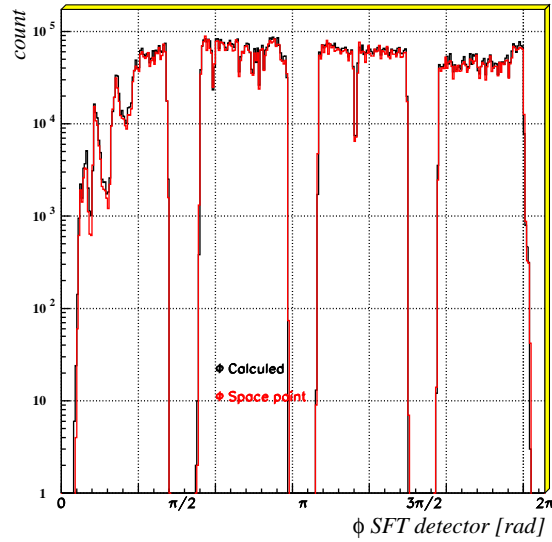
(a) ϕ distribution for SFT inner Protons Space points
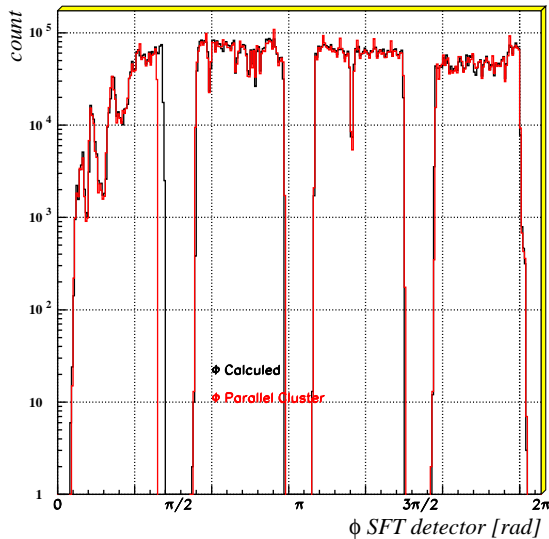
(b) ϕ distribution for SFT inner Protons Parallel Clusters
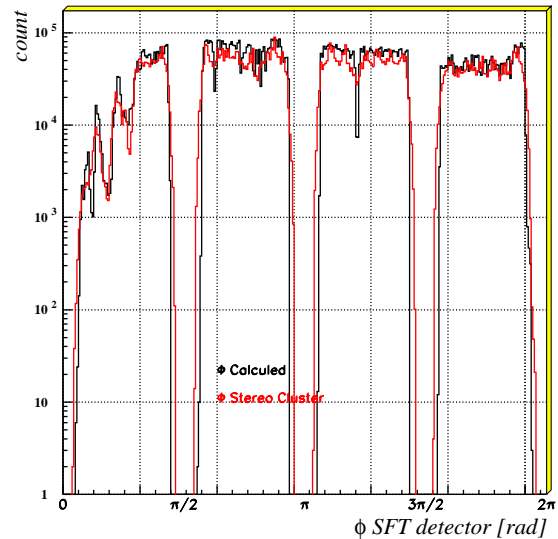
(c) ϕ distribution for SFT inner Protons Stereo Clusters

Figure 6.8: ϕ distribution for Inner SFT Space point for Protons (a), Parallel Clusters (b) and Stereo Cluster (c). The ϕ distribution of the tracks passing though the detector (black) and the space point or cluster when hits detected (red).

The difference between the ϕ calculated from the track and the ϕ of the space points or clusters should not be bigger than $\pm 0.1 \ rad$ event if the RMS of this difference is small for space point and parallel cluster (around $\pm 0.01 \ rad$ see Fig. 6.6(d) and 6.7(a)). We use this large difference value due the possible misalignment or

geometrical difference on the detector and also due to the possible errors on the calibration of the Recoil detector. This can give use big difference between where is expected track (due to the calculation) and where are the hits ρ on the detector. In this case a possible good track can yield efficiency on this part of the detector.
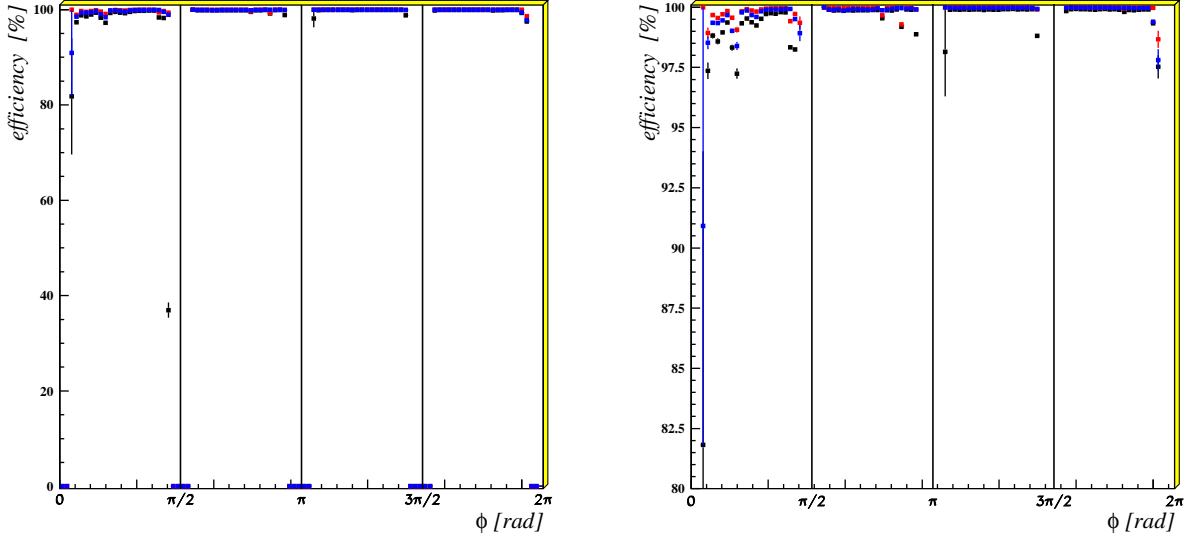
(a) Efficiency versus ϕ for inner SFT for Space Point Protons   (b) Efficiency versus ϕ for inner SFT for Space Point Protons (zoomed)

Figure 6.9: Efficiency versus ϕ for Inner SFT Protons for Space point (black), parallel Cluster (red) and stereo cluster (blue).

Using the eq.6.12 on the data shown on Fig. 6.8 it was possible to calculate the efficiency of the inner SFT detector for proton tracks versus ϕ angle. The efficiency result is shown on Fig. 6.9. It is possible to see the efficiency on the inner SFT detector is higher than 99.5% for all quadrants. Only on the first quadrant of the detector (between 0 and 2π)[2] it is possible to observe a small decrease of the efficiency on the detector. On this quadrant one of the side of one layer of Silicon module has bad coordinate resolution. This can explain the inefficiency on the first quadrant.

On the Fig. 6.9(a) it can be seen that the efficiency goes to 0% where is out of the acceptance of the Silicon detector (at 0, $\pi/2$, π and $3\pi/2$). This inefficiency of the detector is not real, it is due to the method how we calculated the efficiency, we chose only tracks (see section 6.1) with space point on both layers of the Silicon detector and in the other layer of the SFT. On the Fig. 6.9(b) the zoom let us see the difference in the efficiency between the space point on black, parallel Cluster in red and stereo Cluster in blue. On the first half of the first quadrant of the SFT detector the fluctuation on the efficiency is more visible, even if the efficiency error ($\Delta\varepsilon$) is relatively small. The statistical error on the efficiency is calculated as:

$$\Delta\varepsilon = \frac{\sqrt{N_{all}/(N_{all}-1)}}{N_{all}{}^2} \cdot \sqrt{(N_{no\_det}{}^2 \cdot N_{det}) + (N_{no\_det} \cdot N_{det}{}^2)} \tag{6.13}$$

where N_{det} is the number the efficient tracks, N_{no_det} is the number the inefficient tracks and N_{all} is the number total of tracks ($N_{all} = N_{det} + N_{no\_det}$).

---

[2]The first quadrant on the silicon detector were named arbitrarily between $3\pi/2$ and 2π on the HERMES coordinate system, and the first fibers on the SFT were on the top at $\pi/2$.

The efficiency of the Inner SFT can be used to check the stability of the detector. Fig. 6.10 shows the efficiency of the inner SFT detector for proton tracks versus run number per quadrant. The efficiency is shown for a space point in black, parallel cluster in red and stereo cluster in blue. Each point combined 1000 run of the recoil detector. The efficiency stability is shown for 2007. In all periods the fluctuation on the stability of the SFT was from quadrant to quadrant less than 0.5%. On the first quadrant it was large but not as big as 1.0%.
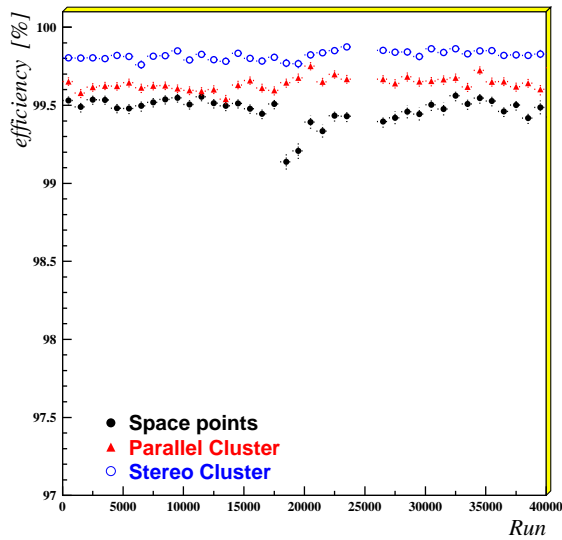
(a) Proton efficiency for FIRST QUADRANT versus run.
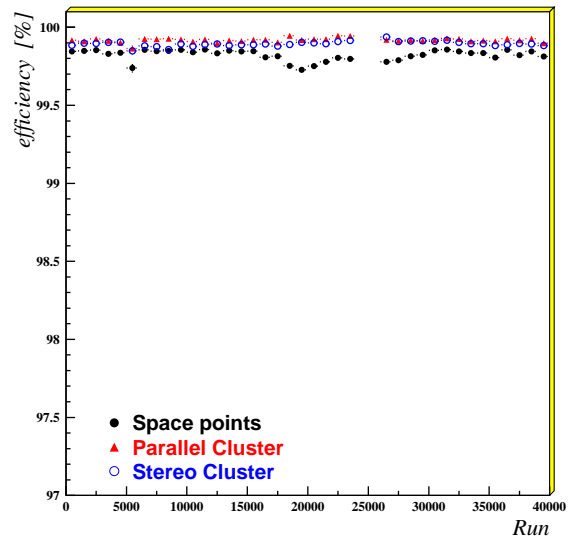
(b) Proton efficiency for SECOND QUADRANT versus run.
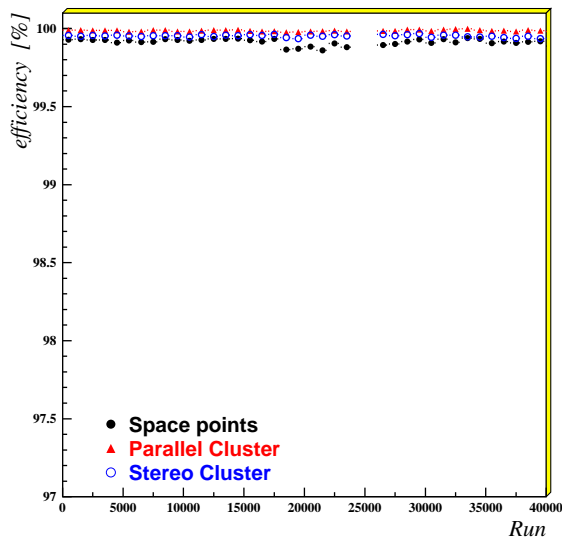
(c) Proton efficiency for THIRD QUADRANT versus run.
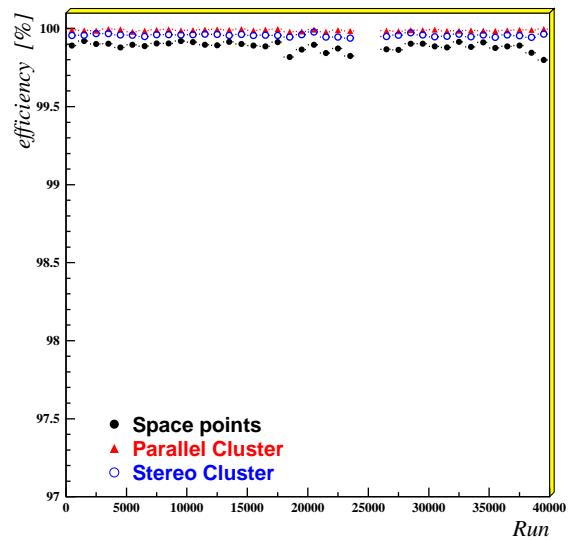
(d) Proton efficiency for FOURTH QUADRANT versus run.

Figure 6.10: Proton tracks efficiency for the inner SFT versus run per quadrant. The efficiency is shown for a space point in black on the figures, parallel cluster in red and stereo cluster in blue. Each point combined 1000 run of the HERMES detector. The efficiency stability is shown for 2007 period of data taking.

The same studie was done for pion tracks, on the inner SFT detector. The results are shown in Fig. 6.11 clearly indicate a decrease on the efficiency for positive pions (π^+) on the SFT detector, compared to protons.

(a) Efficiency versus ϕ for inner SFT Pions (π^+)   (b) Efficiency versus ϕ for inner SFT Pions (π^+) zoomed
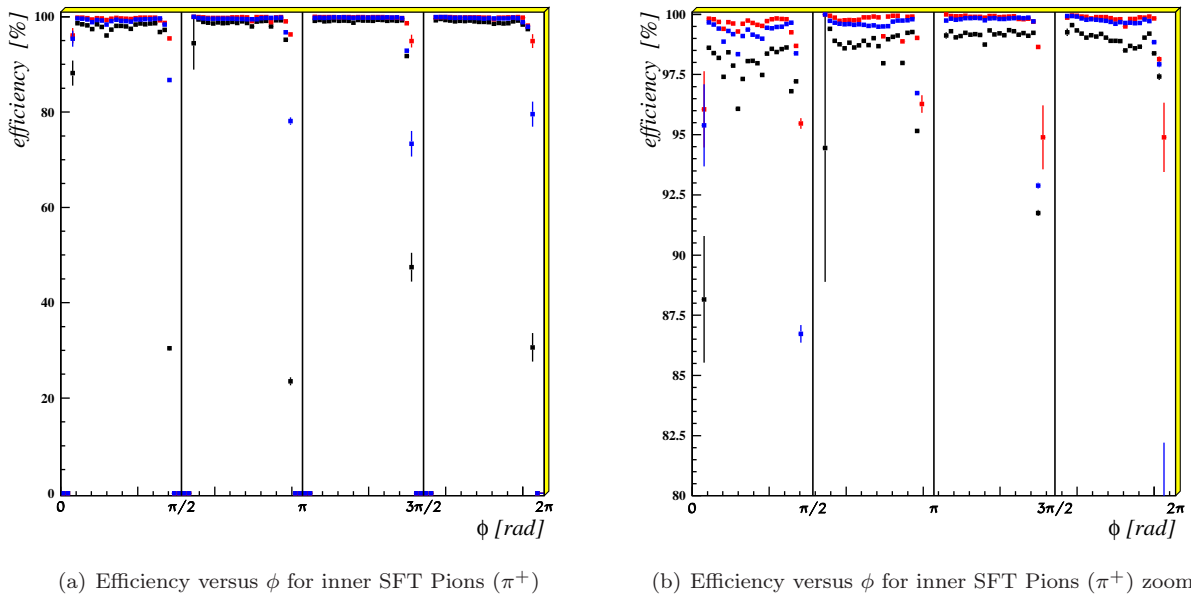
Figure 6.11: Efficiency versus ϕ for Inner SFT Space points (black), parallel Clusters (red) and stereo clusters (blue), for Pions.

The efficiency comparison between the proton tracks and the pion tracks shown for clusters on the inner SFT detector (see Fig. 6.12) are small.

(a)   (b)
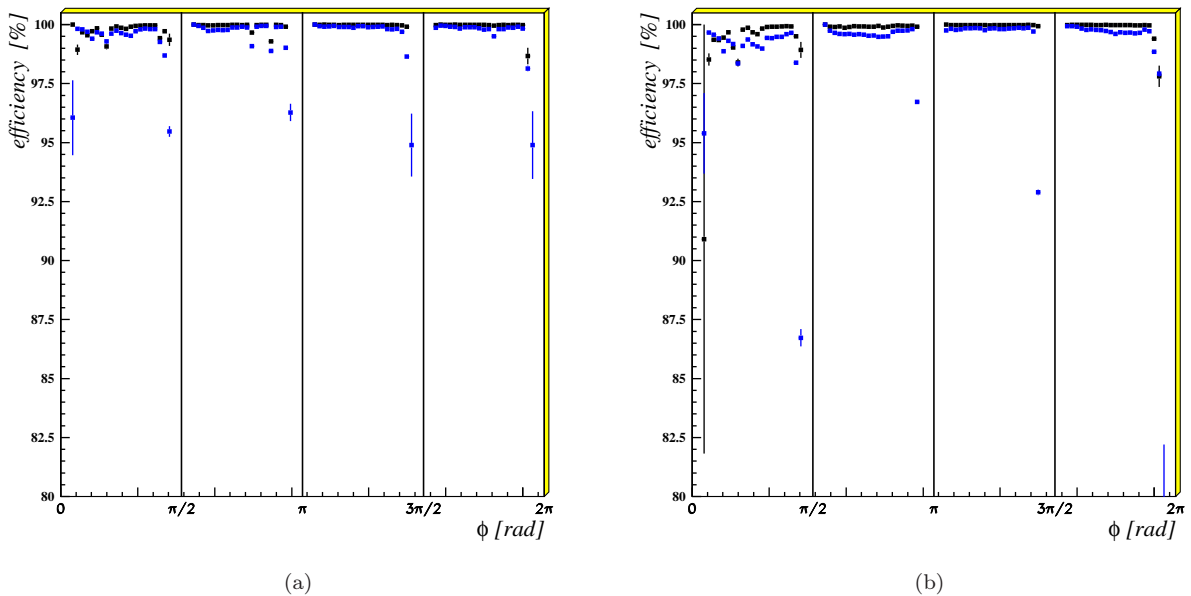
Figure 6.12: Efficiency versus ϕ for Inner SFT, parallel (a) and stereo (b) for Protons (black) and Pions (blue).

6.3.2 Outer SFT efficiency

The efficiency calculation for the outer SFT was challenging us due to several reasons. One of the reasons was the possible scattering of the tracks in the first layer. The possibility for not correctly calculate path of the tracks trough the outer SFT give us a large uncertainty on the ϕ position as it is shown on left side of Fig. 6.13. The other and not expected reason for the difficulty on this calculation was a elevated number of ghost hits on the first quadrant of the outer SFT, between 0 to $\pi/2$ on HERMES coordinate system. This was producing a huge efficiency variation on this quadrant, this can be seen on the right side of Fig. 6.13.
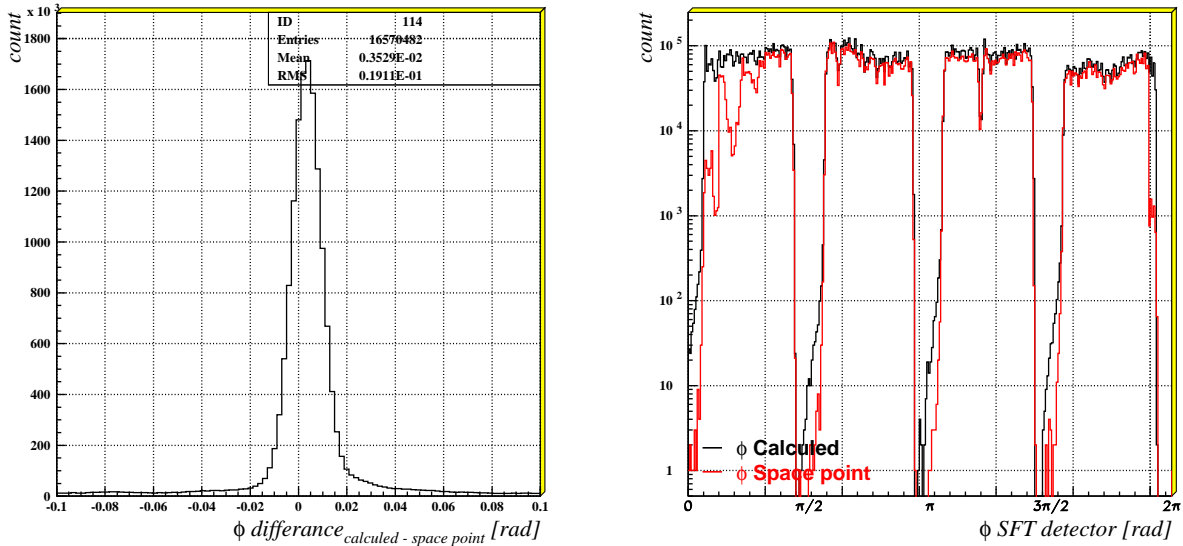
Figure 6.13: ϕ distribution for SFT outer Protons Space Points

The same method which was used for the inner SFT, used to extract the efficiency of the outer SFT. As it can be seen on Fig. 6.14 the result for the outer SFT was a bit lower as it was obtained for the inner SFT.
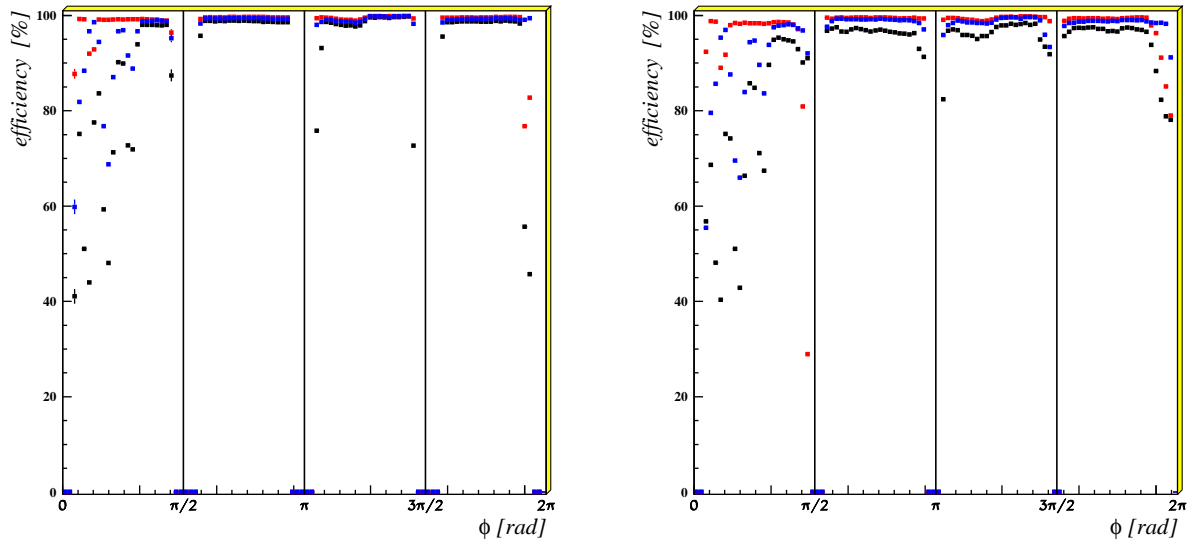
(a) Efficiency versus ϕ for SFT outer Space Point for Protons.   (b) Efficiency versus ϕ for SFT outer Space Point for Pions.

Figure 6.14: Efficiency versus ϕ for the outer SFT for Proton (left) and Pion (right) tracks for Space point (black), parallel Cluster (red) and stereo cluster (blue).

On the Fig. 6.14(a) we can see the efficiency of the outer SFT for proton tracks versus ϕ for Space point in black, parallel Cluster in red and stereo cluster in blue. In the beginning of first quadrant shows a below 50% efficiency for the space points. It is important to emphasize that the decrease off efficiency in this quadrant is due in most part to the stereo layer and only tiny portion of the parallel layer. The other quadrants of the outer SFT shows a similar efficiency as the inner SFT for proton tracks.

On Fig. 6.14(b) we can see the efficiency for the pion tracks on the outer SFT. The efficiency for this tracks is slightly low as it is for the inner SFT, we can see the same effect on the first quadrant as for proton tracks and also we can see on this first quadrant the efficiency of the space point decrease due also to the stereo layer and not so much due to the parallel.
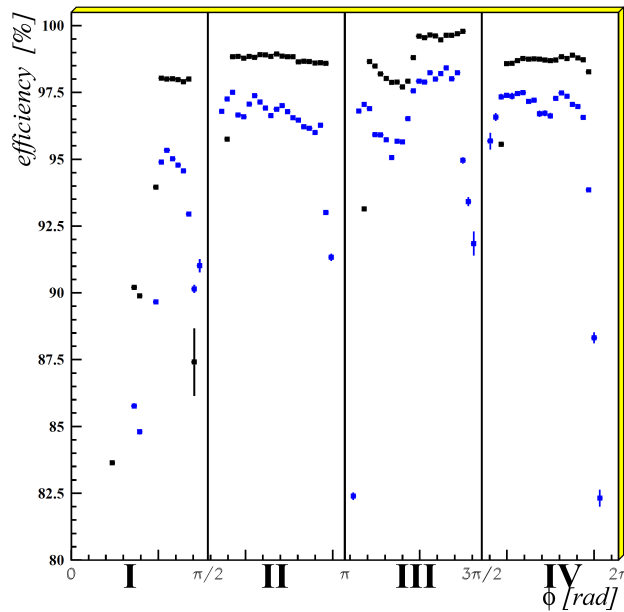
Figure 6.15: Compared Efficiency versus ϕ for Outer SFT for Protons in black and Pion in blue.

The efficiency of space point for proton and pion tracks are shown on Fig. 6.15. We can see clearly the efficiency of the protons is higher than the efficiency for pions (π^+).

More interesting on this Fig. 6.15 is shown the structures on the each quadrant of the outer SFT. This structures were under investigation and the only explanation about them was the electronics design and the light guide disposition. For the outer SFT the parallel and the stereo layer were connected to the same *PMT BOX* and only two or three of them are covering one quarter. On third quadrant (between π and $3\pi/2$) it can be clearly seen this structure. The other structure is located inside the PMT himself, using four *Gassiplex* in each Preprocessing Frontend Module, see section 4.3.3. Also this structure is visible with a small effect on the efficiency. On second quadrant (between $\pi/2$ and π) it is possible to distinguish on the first half of the quadrant the *Gassiplex* chip structure.

A extended studies on the determination of SFT detector efficiency versus fibers in function of particle type and momentum was done by X. Lu and more detail can be read on his diploma thesis [111].

Chapter 7

Analysis of ρ^0

In this chapter we describe the data set used and the analysis procedure of the diffractive-exclusive production of ρ^0 meson. The selection requirements imposed on the data in order to obtain exclusive ρ^0 production data are also described. The study is done on diffractive slope b extraction (related to the transverse size of the struck nucleon and meson) as a function of Q^2 for the ρ^0, with and without the recoil detector measurement. The results are compared and conclusion are made.

The reaction in study one can describe as:

$$ep \rightarrow e'\gamma^*p' \rightarrow e'\rho^0 p' \rightarrow e'\pi^+\pi^- p'. \tag{7.1}$$

where $e(e')$ is incoming (scattered) electron, $p(p')$ is target (recoil) proton, γ^* is the virtual photon and $\pi^+\pi^-$ are the decay products of the ρ^0 meson.

7.1 Data quality selection.

The data were collected during 2007 using positron beam with a unpolarized Hydrogen gas target. One important aspect of the event selection is the data quality of the data sample with respect to the detector performance. The HERMES spectrometer and the RECOIL DETECTOR consists of several subdetector systems which all have to be fully operational to assure a reliable data analysis. As soon as a single component is not operational properly or perform unstable in time, part of the recorded data sample has to be discarded Generally the shift crew is responsible for identifying the problems during each fill and recording fill-level and run-level data quality information in the experiment logbook. Information from the logbook of the data taking was used to exclude runs with a suspicious data quality or runs taken for different specific studies from the selection. On the burst level, data quality criteria were applied by using burst lists. These lists are based on the information stored in μDST productions and are made available for each data production by the HERMES data quality group [112]. Burst lists contain information about the status of the HERA beam, the target, the DAQ, the data reconstruction and the spectrometer components for each individual burst. Because different analyses may not require full functionality of detector components, like ours, where we discard *Data Quality* bits for *RICH* from selection because we assume that all hadrons are Pions. A final data selection must be applied at burst level where slow control information is available.

7.2   Event Selection.

After the application of the data quality criteria on the Forward Spectrometer and the Recoil detector clean and stable data samples are obtained. As the HERMES spectrometer detects a large variety of different processes, additional cuts have to be imposed to select the type of events one wants to study and remove those events which are not interested and from the 'background'. In general the selection criteria are chosen to reduce the contamination due to the background.

The ρ^0 vector meson has a short lifetime which is characteristic for a particle which decay via the strong interaction (decay immediately after formation). The decay width of the ρ^0 is 149.4 ± 1.0 MeV [113]. One can estimate via the relation $\tau = \hbar/\Gamma$ the life time of the ρ^0 to be $\tau_{\rho^0} = 4.4 \times 10^{-24} s$. The distance before decaying can be approximated by $c\tau$ with c being the speed of the light, which gives $c\tau_\rho^0 = 1.3 fm$, which is roughly the scale of the nucleon size.
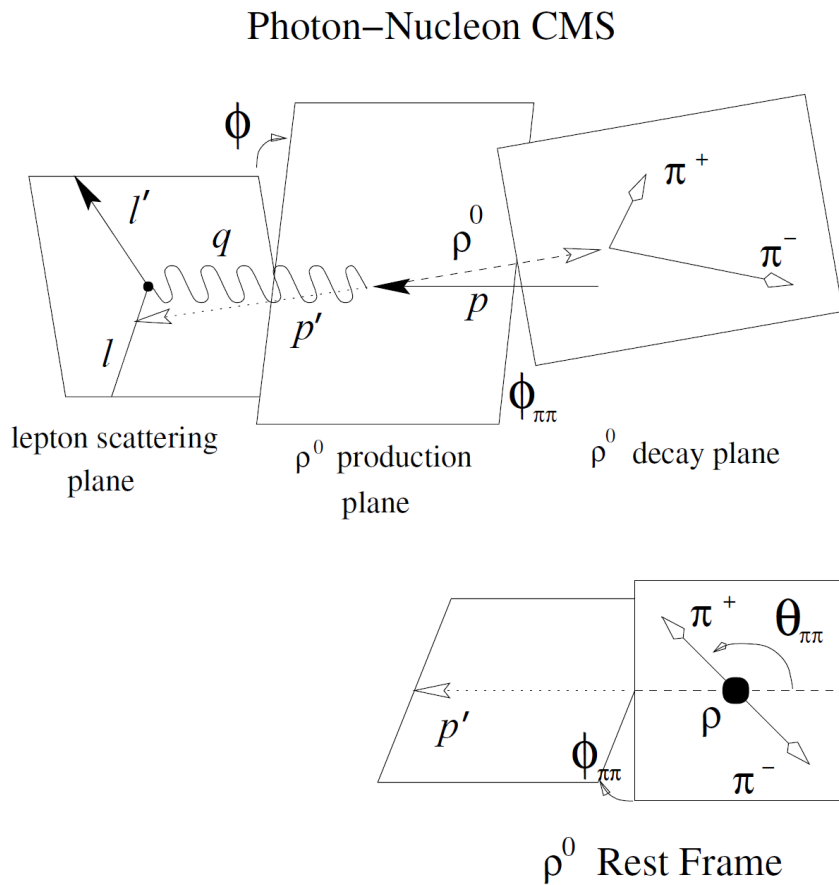
Figure 7.1: Definition of ρ^0 production with different stages in the process $\gamma^* N \to \rho^0 N' \to \pi^+\pi^- N'$. Here Φ is the angle between the ρ^0 production plane and the lepton scattering plane in the "hadronic" center-of-mass system of virtual photon and target nucleon. The Θ and ϕ variables are respectively the polar and the azimuthal angles of the π^+ in the vector meson rest fram.

From all recorded events we have selected those ones which contain at least one scattered electron, two hadrons in main spectrometer and a recoil track, that later we could identify as Proton. This subsample was our "final" dataset to be analyzed. Fig. 7.1 show the kinematic variables of the reaction in study.

7.2.1 Geometry of tracks.

In order to be sure that the detected lepton on the forward spectrometer originated from the lepton beam scattered inside the target cell, several requirement were imposed.

The Geometrical acceptance of the HERMES spectrometer and a cut on the vertex position were imposed. Furthermore it was required that the $z-$component of the vertex position was within the dimensions of the target cell for tracks on the Forward Spectrometer and on the Recoil Detector. The difference of vertex position between Forward spectrometer and Recoil Detector tracks was asked to be lower than $|\Delta Z| < 2\ cm$, to make sure that both tracks were from the same vertex. The resulting ΔZ distribution is shown in Fig. 7.2.

ID	1502
Entries	439626
Mean	-0.4421E-01
RMS	2.049
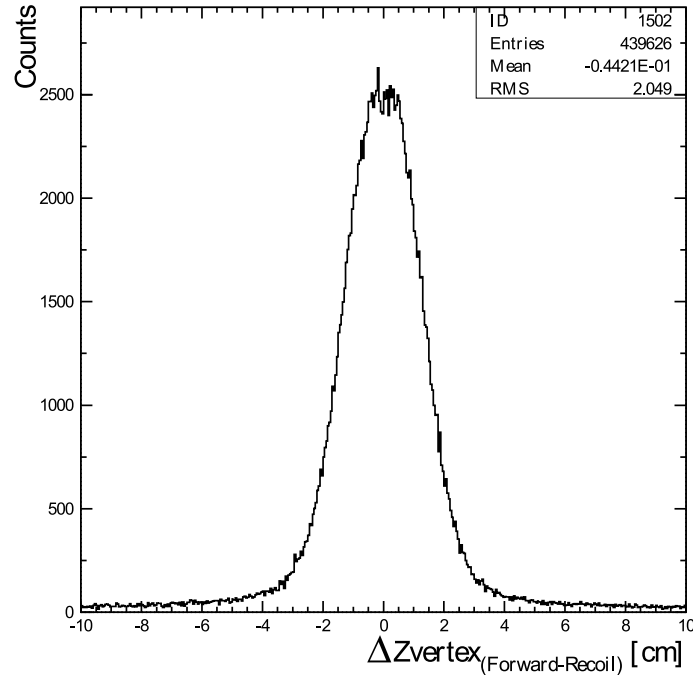
Figure 7.2: ΔZ Vertex distribution of ρ^0 events.

These requirements select tracks that pass through the forward spectrometer and originate from the target cell. Furthermore it was required to reject tracks which might be affected by the edge effects of the spectrometer, using a set of geometrical requirements, referred to as *fiducial volume cuts*. An overview of the applied geometric requirements is given in table 7.1.

GEOMETRICAL CUTS

POSITION IN THE CALORIMETER	$|x_{calo}| < 175\ cm$
	$30\ cm < y_{calo} < 108\ cm$
REAR FIELD CLAMP	$|x| < 100\ cm$
	$|y| < 54\ cm$

TARGET REGION

Z VERTEX POSITION FORWARD SPECTROMETER	$5\ cm < Z_{Vertex\ Forward\ Spectrometer} < 20\ cm$
Z VERTEX POSITION RECOIL DETECTOR	$5\ cm < Z_{Vertex\ Recoil\ Detector} < 20\ cm$
Δ Z	$-2\ cm < \Delta Z < 2\ cm$

Table 7.1: The geometrical cuts applied on the lepton, proton and both pion tracks.

7.3   Selection of exclusive ρ^0 events without Recoil Detector.

On the identified lepton track, which pass the geometrical criteria, additional cuts were imposed. Kinematic requirements were imposed on these events in order to select exclusive ρ^0 production events and to exclude events coming from other processes. An overview of the applied requirements are listed and described in table 7.2

Kinematical cuts

Cuts	Description
$p_{\pi^+} \cdot p_{\pi^-} \; < \; 0$	Selects hadrons with opposite charge.
$\|p_e\| \; > \; 3.5 \; GeV/c$	Improves lepton identification and calo-trigger condition.
$W^2 \; > \; 7.0 \; GeV^2$	Removes baryon resonances.
$y \; < \; 0.85$	Cuts down need for radiative corrections from lepton.
$m_{kk} \; > \; 1.04 \; GeV$	Cuts small amount of ϕ production at low invariant mass to improve fit quality.
$0.6 \; GeV \; < \; m_{\pi\pi} \; < \; 1.0 \; GeV$	ρ^0 mass window
	Reduces background levels.
$-t' \; < \; 0.4 \; GeV^2$	Reduces small amount of background and selects forward scattering kinematics, diffractivness of the process.
$-1.0 \; GeV \; < \; \Delta E \; < \; 0.6 \; GeV$	Decreases background effects and selects exclusive events without the recoil detector information.

Table 7.2: Kinematic requirements for the selection of exclusive ρ^0 production events.

Since we are interested in exclusive vector meson production we rejected events containing additional tracks. Events were selected with exactly three tracks, where the lepton was identified by requiring $PID3 + PID5 \; > \; 1$, and the two hadrons were identified by requiring $PID3 + PID5 \; < \; 1$ (see section 2.7.4).
In order to select exclusively produced ρ^0 mesons, one assumes that the detected hadrons are actually pions and the true resonant ρ^0 production events should appear as a peak in the two-pion invariant mass distribution

$$M_{\pi\pi} \; = \; \sqrt{(p_{\pi^+} + p_{\pi^-})^2}, \tag{7.2}$$

where (p_{π^+} and p_{π^-}) are the four-momenta of the decay pions. The invariant mass $M_{\pi\pi}$ of two hadron system was determinated under the assumption that both hadrons are pions.

The value of $M_{\pi\pi}$ for resonant $\pi^+\pi^-$ pairs is expected to be distributed around the ρ^0 mass. The two pion invariant mass distribution is depicted in Fig. 7.3. The ρ^0 events show up clearly in the wide bump around the expected mass value. The narrow peak in the lower mass region correspond to K_S^0 mesons production which have a mass of $497.614 \pm 0.024 MeV$ and also decay into $\pi^+\pi^-$ with a branching ratio of $(69.20 \pm 0.05)\%$ [113].

For the selection of the resonant $\pi^+\pi^-$ pairs the events were filtered out in a first step by imposing a mass window $0.6 \; GeV \; < \; m_{\pi\pi} \; < \; 1.0 \; GeV$ on the event sample. As can be seen on the plot, not all of the events selected within the mass window did correspond to the exclusive ρ^0 production. This sample is diluted with background events of hadron pairs produced in various processes. Since the non-exclusive events can be misidentified as exclusive ρ^0 events, other restrictions are required for background suppression.
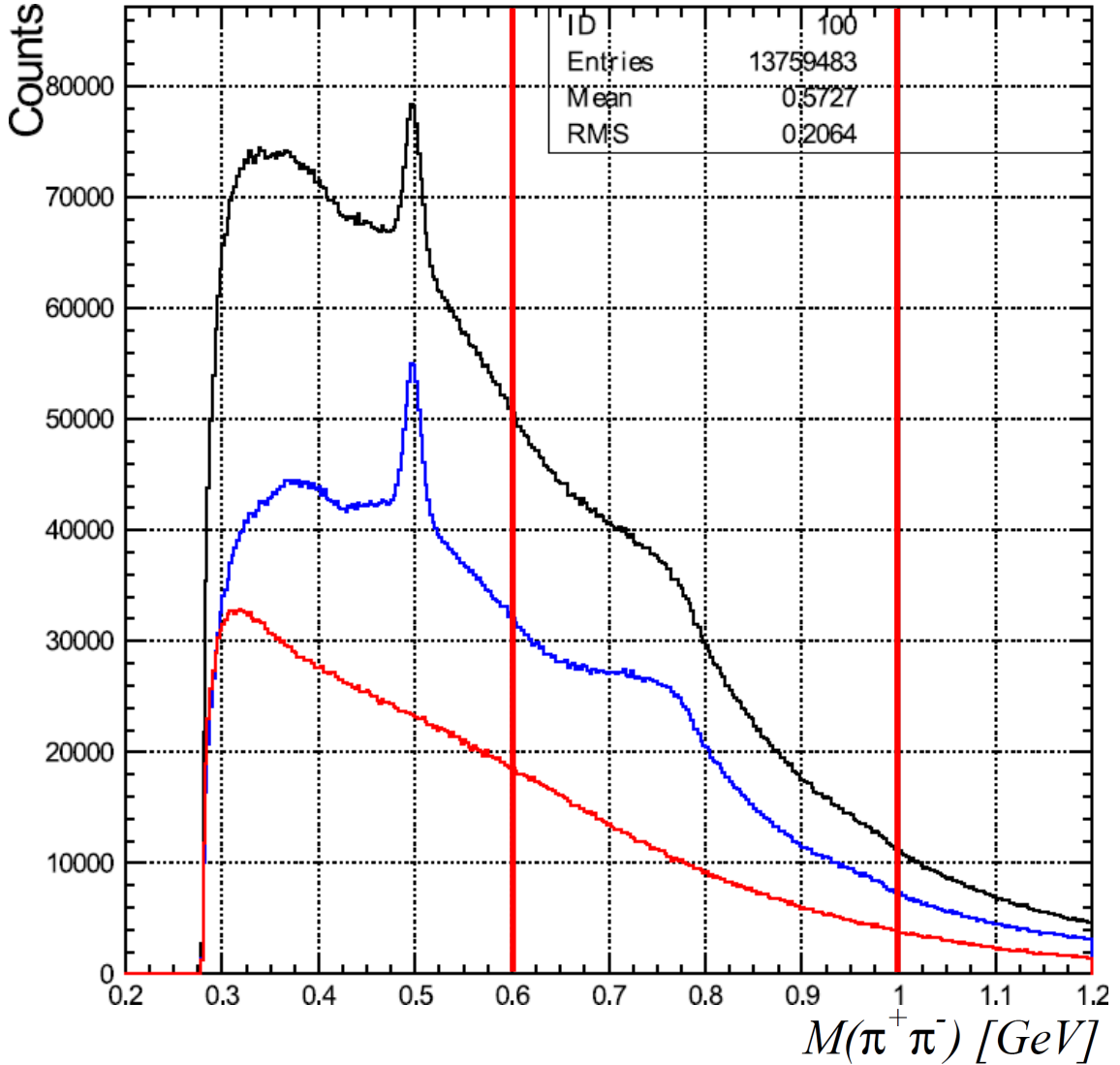
Figure 7.3: The reconstructed invariant mass distribution $M_{\pi\pi}$ on the Forward Spectrometer assuming that both hadrons are π, after imposing the requirements to the kinematic variables W^2, Q^2 and y of the scattered lepton. The vertical lines indicate the $M_{\pi\pi}$ range for the ρ^0 selection used in the analysis. The black histogram is $M_{\pi\pi}$ for two hadrons selection on the forward spectrometer. The blue is when this two hadrons have opposite charge and the red is when they have the same charge, representing the background events of hadron pairs produced in various non-exclusive processes.

The "exclusivity" of the ρ^0 measurement without the recoil detector is characterized by the variable

$$\Delta E = \frac{M_x{}^2 - M^2}{2M} \stackrel{lab}{=} \nu - E_V + \frac{t}{2M}, \tag{7.3}$$

where $M_x = \sqrt{(k - k' + p - v)^2}$ is the reconstructed invariant mass of the undetected recoiling proton, $E_V = E_{\pi^+} + E_{\pi^-} = \nu + t/(2M)$ is the energy of the exclusively produced ρ^0 meson, $(E_{\pi^+} + E_{\pi^-})$ is the sum of the energies of the two detected pions in the laboratory system, ν is the photon energy and $t/(2M)$ is the kinetic energy of the recoiling proton. Without detection of the recoiling proton, for exclusive ρ^0 electroproduction $M_x = M$ and $\Delta E = 0$, for the perfect measurement.

To restrict the sample to exclusive production in the forward region a cut on ΔE was used. Fig 7.4 shows the ΔE distribution of the sample with ρ^0 mass window. The narrow peak at $\Delta E \approx 0$ indicates the exclusive event candidates, while the majority of the events is non-exclusive and is the wide structure at higher ΔE. Exclusive candidates were selected, without recoil detector information, using $-1.0 GeV < \Delta E < 0.6 GeV$.

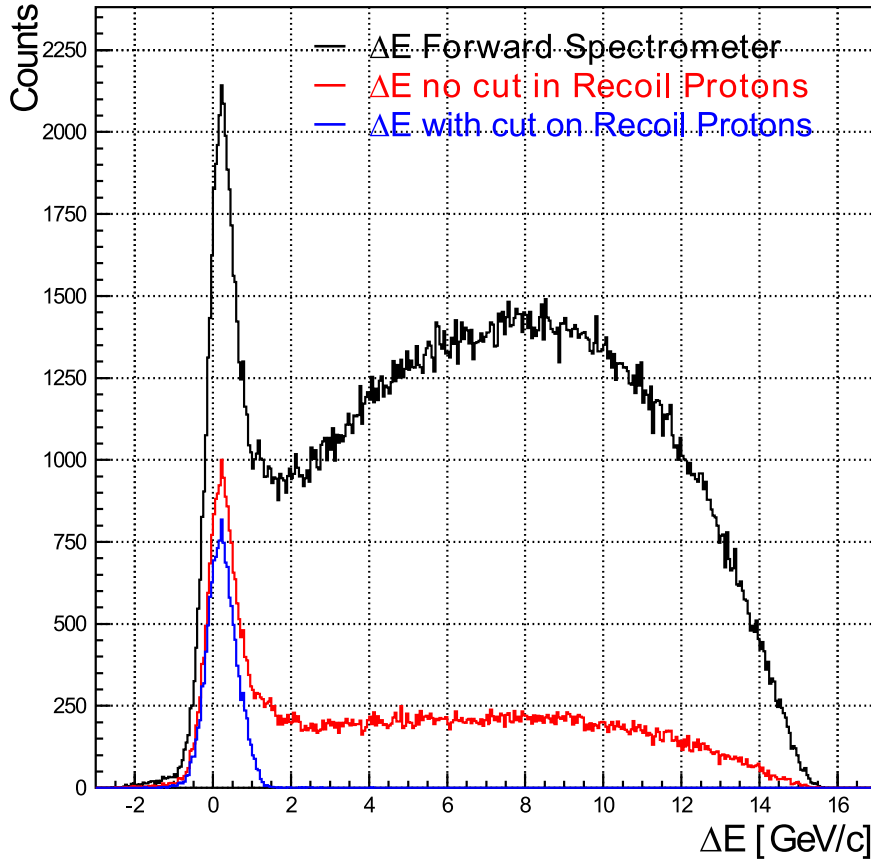Figure 7.4: ΔE distribution of the event sample within the ρ^0 mass window. The narrow peak at $\Delta E \approx 0$ corresponds to the exclusive events. The black histogram corresponds to the event sample without recoil information, the red corresponds to the sample when we require a proton track in the recoil detector, and the blue is the result of the use of further requirements on the kinematic of the proton track in the recoil detector mainly $\Delta\phi$.

7.4   Selection of exclusive ρ^0 events with Recoil Detector

Recoil Detector information was used to clean the sample for exclusive process by asking for a recoil proton track. To further clean up of the background from the physics processes and the possible ghost particles reconstructed from the Recoil Detector, useful cuts need to be used.

Further requirement on the kinematic of the proton track on the recoil detector improve the selection of the exclusive sample of the unpolarized hydrogen data 07c2 production. A kinematic cut on $\Delta\phi$ was introduced which is the difference between the reconstructed ϕ with the information on the Forward Spectrometer and the ϕ of the proton track measured on the Recoil Detector, and in the same way an Δp which is the difference between the momentum p of the recoiling proton reconstructed with the information from the Forward Spectrometer and the momentum p of this proton track measured in the Recoil Detector. Due to the fact that the reconstructed azimuthal angle has a very good resolution and the momentum reconstruction reaches the design goal (see Fig 3.12 and Fig 3.14 in Section 3.4.2) [17, 73], this two cuts were proposed as $|\Delta\phi| < 0.1 \ rad$ and $|\Delta P| < 1.00 \ GeV/c$. A combination of this two variables are used in DVCS analysis with the Recoil detector and were named ω and R [78, 86].

Fig. 7.5 shows the distribution of the variables used for cuts, left $\Delta\phi$ and right Δp. As shown in Fig 7.4 the selection of exclusive ρ^0 with the Recoil Detector improves the requirement on the kinematic if the recoil proton tracks are used.
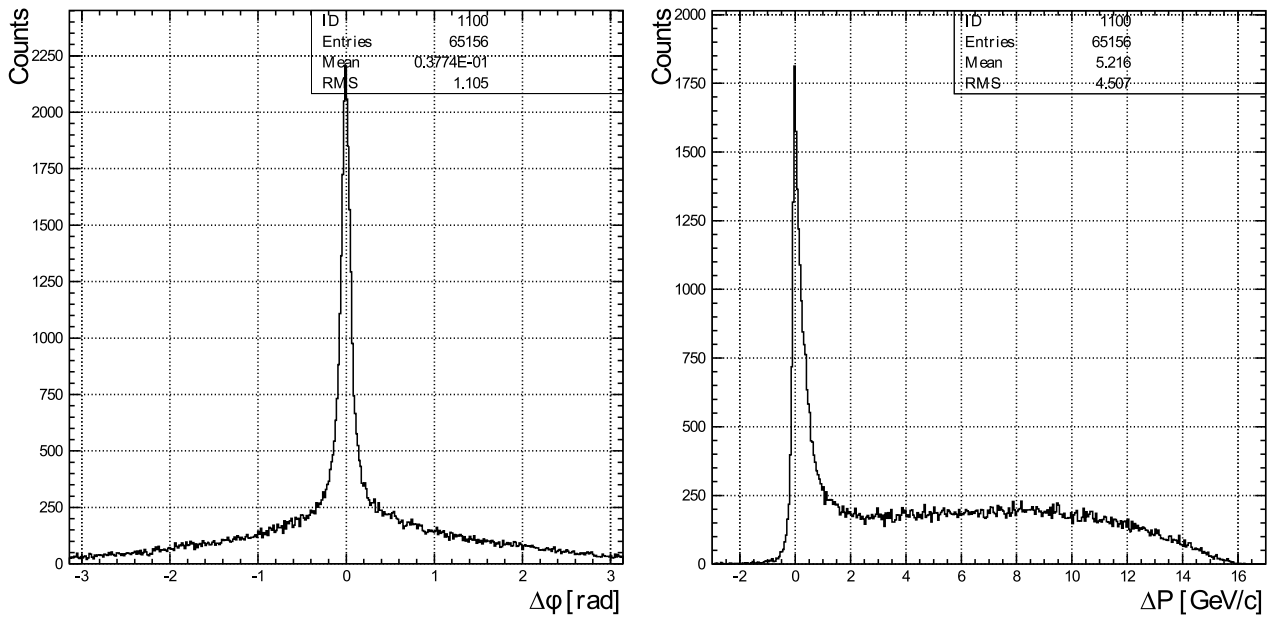

Figure 7.5: Δp and $\Delta\phi$ distribution of the recoil protons. These two variables were used to reduce the background, the cut were set around the peak as 0.1 rad for the difference between the azimuthal angle reconstructed from the observed and as 1.00 GeV/c for the difference between the momenta.

The Fig. 7.6 shows the effect of the step by step cuts on the ΔE distribution. The left side shows the effect for different Δp cuts on the ΔE distribution. This Δp cut was compared with a direct cut on ΔE similar to the cut used without the Recoil Detector information. More important is the cut on $\Delta\phi$ due to the resolution on the azimuthal angle ϕ. In the right side is shown the effect of this cut on the ΔE distribution.
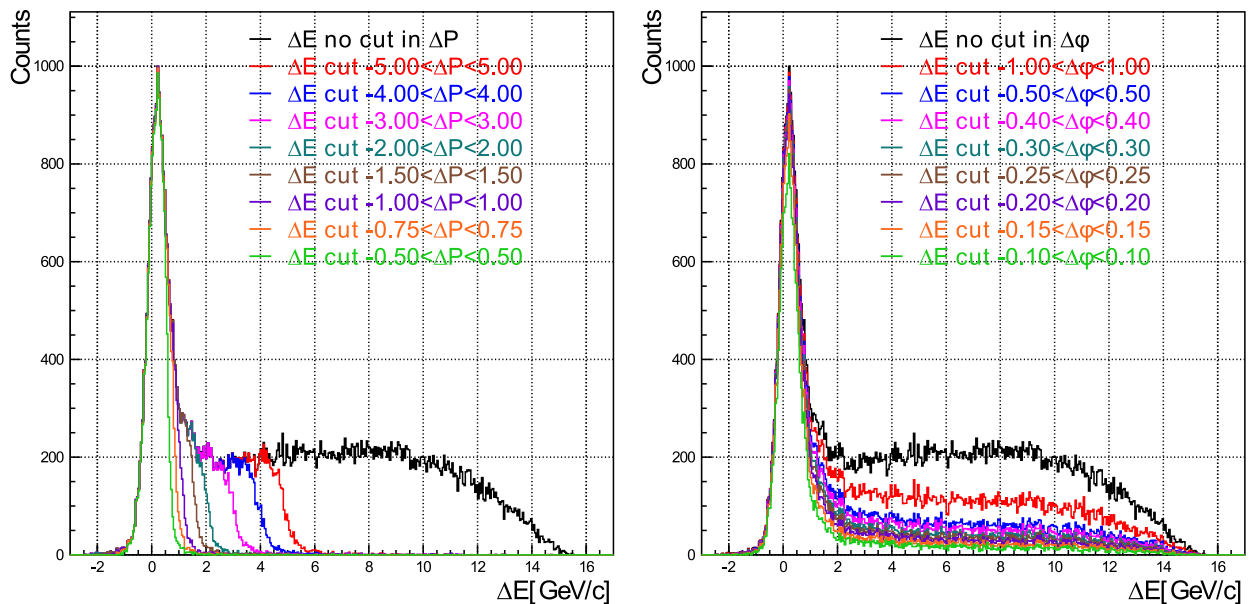

Figure 7.6: ΔP and $\Delta\phi$ cut effects on ΔE distribution of the selected events. In the left for different cut on Δp, the high entries of ΔE histogram are removed first. In the right side is shown the effect of the $\Delta\phi$ cut on the ΔE distribution.

The two kinematical cuts used in this analysis were the difference between the azimuthal angle reconstructed from the observed and the difference between the momentum. We show the effect of this cuts on the ΔE distribution step by step in Fig. 7.6. The following cuts were chosen: $|\Delta\phi| < 0.1rad$ and $|\Delta p| < 1.00GeV$. A *Monte Carlo* study should be done to adjust the cuts to the optimal values.
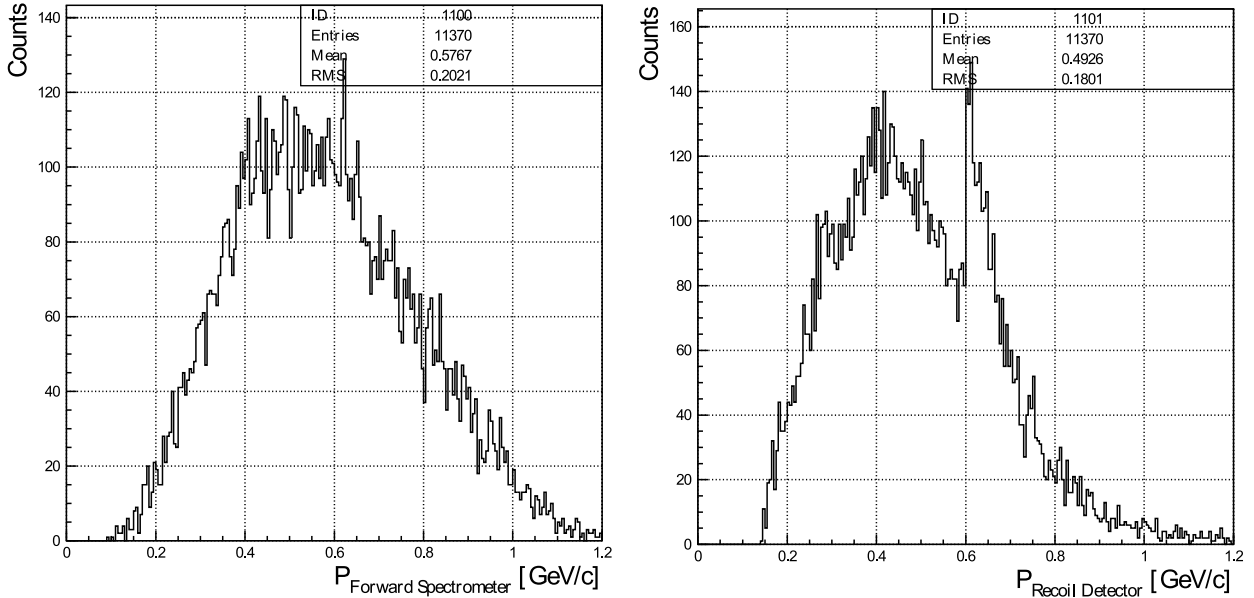
Figure 7.7: Left: Proton momentum as reconstructed from Forward Spectrometer information. Right: Proton momentum as measured in the Recoil Detector.

The Fig. 7.7 left shows the proton momentum as reconstructed from the Forward spectrometer information. Right shows the momentum measured with the Recoil Detector of proton tracks. These plots are done for our data sample with the kinematical cuts $\Delta\phi$ and ΔE.

Figure 7.8: The proton momentum, p as measured in the recoil detector versus p reconstructed from Forward Spectrometer information. This plots are done for our data sample with the kinematical cuts $\Delta\phi$ and ΔE. The left show the averaged values, the right plot shows the 2-D distribution.

The momentum distribution measured in the Recoil Detector has a discontinuity at $0.6 GeV/c$ due to the use of two different methods to the measure the momentum p of the tracks. The momentum of the recoil proton track below $0.6 GeV/c$ are measured by energy deposition method (see Fig. 4.7 in Section 4.2) in the Silicon recoil detector, for higher momentum the measurement is determinated from the track radius in the longitudinal magnetic field (see Fig. 3.12 in Section 3.4.2).

Fig. 7.8 shows the momentum profile of proton tracks measured on the Recoil detector. The profile represent the deviation betw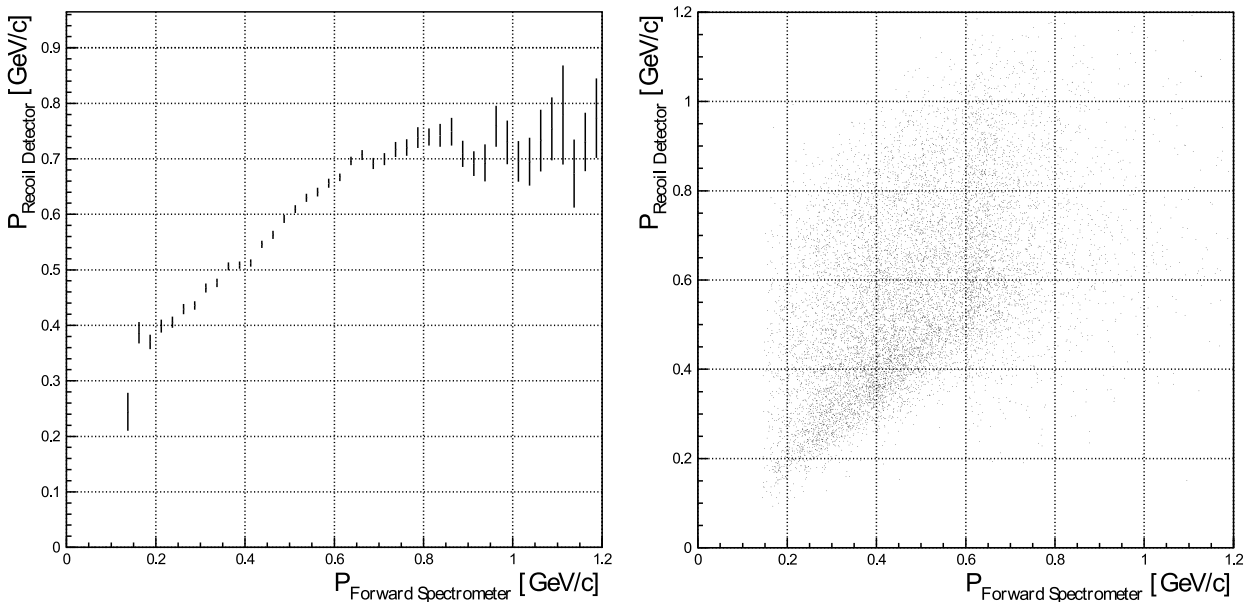een the momentum reconstructed from the Forward Spectrometer and the momentum measured from the Recol Detector. The right plot shows the momentum p of the recoil proton measured with the recoil detector versus the value obtained from the information of the Forward Spectrometer.
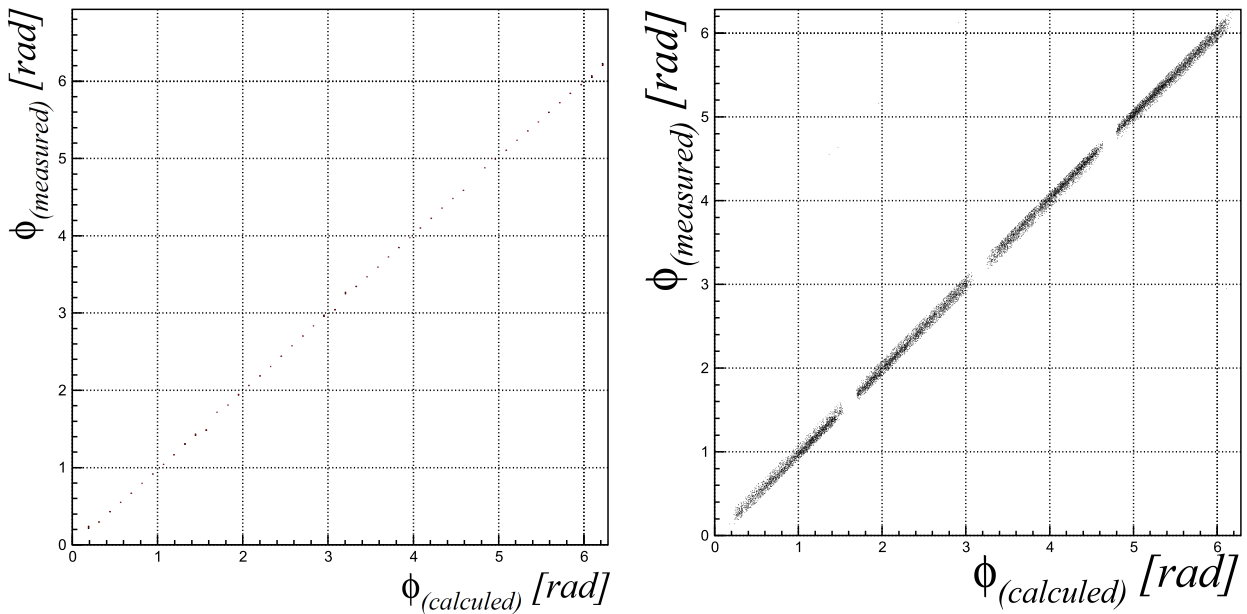
Figure 7.9: The Azimuthal proton angle, ϕ measured in the recoil detector versus ϕ reconstructed from the forward Spectrometer. The left side shows the angle valus, the right part shows the 2-D distribution.

Fig. 7.9 shows the Azimuthal angle profile for the ϕ measured versus the ϕ reconstructed of the recoil protons. The left side shows the azimuthal angle profile of the recoil proton, the profile represent the equivalence between the azimuthal angle reconstructed with the Forward Spectrometer and the azimuthal angle measured with the Recoil Detector. The right plot show the ϕ measured versus ϕ reconstructed of the recoil protons. The Silicon detector ϕ acceptance, is the reason for gaps.

7.5 ρ^0 meson mass reconstruction.

In the analyses with the Forward Spectrometer only, the ρ^0 candidates were reconstructed through unidentified hadron pairs and imposing the exclusive cuts on ΔE. Beside the exclusive ρ^0 events, the sample contains a contribution from exclusive w and $\rho^\pm$ mesons and also a contribution from non-resonant background. The contribution from exclusive w and $\rho^\pm$ mesons is less than 1%. [80, 81, 82].

Fig. 7.10 (top) represents the ρ^0 meson mass reconstruction without Recoil Detector Information. The distributions of the invariant mass $M_{2\pi}$ without Recoil Detector information is shown for data in the region $\Delta E < 0.6 GeV$ and $-t' < 0.4 GeV^2$. Although the number of exclusive ρ^0 events increases by raising the ΔE requirement, also the background contamination increases from 11% to 17% for $\Delta E < 0.6 GeV$ to $1 GeV$. The integral of the background fit is 7510.66 and for the signal fit at the same interval is 25061.1. The background is on this case playing an important role on the *Sum* of the fits.

Fig. 7.10 (bottom) represents the distribution of the invariant mass $M_{2\pi}$ reconstruction with Recoil Detector information for data region without the exclusive cut on ΔE. Cuts on the proton tracks from the Recoil Detector are applied to improve the selection of exclusive events. Using the Recoil Detector information the integral of the background fit is 1924.63 and for the signal fit at the same interval is 11550.8. The background is clearlly suppressed in the analysis with the Recoil Detector.

The red curve is the polynomial function background. The blue curve is the *Breit-Wigner Shape* distributions of the invariant mass $M_{2\pi}$. The sum of the two functions is used to describe the total spectra, the parameters of the fits are shown in the Fig 7.10. The background signal is integrated for the interval between 0.6 to $1.0 GeV$. The background to signal ratio for the analysis with Recoil Detector is 0.17, in comparison to 0.30 for the analysis without the Recoil Detector. The lower background with the Recoil Detector shows the improvement of the selection of exclusive events and the suppression of the background contamination.

Without the Recoil Detector, the cleanest possible sample for exclusive processes has a background contamination from *semi-inclusive, non-resonant, single-* and *double-diffractive* processes. A MONTE CARLO simulation for ρ^0 was used to estimate the different background contaminations. It has been evaluated that at HERMES on average 18% of the exclusive events fall outside the imposed ΔE window [69].

Entries	41571
Mean	0.7582
RMS	0.1586
χ^2 / ndf	747.8 / 394
p0	-74.52 ± 3.18
p1	316.7 ± 12.2
p2	-209.1 ± 8.2
p3	69.53 ± 1.06
Width	0.1193 ± 0.0020
Peak	0.7668 ± 0.0006

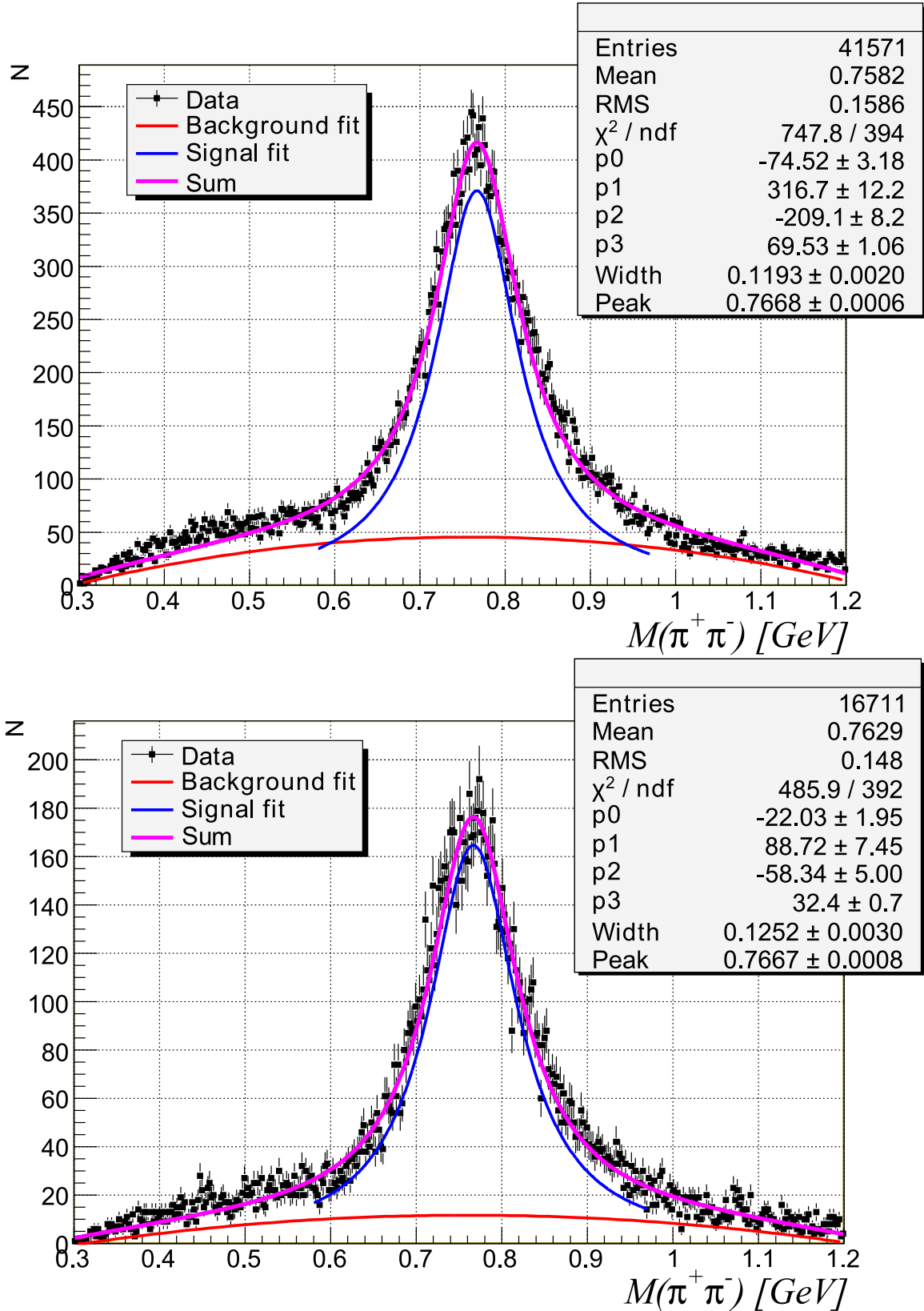| Entries	16711
Mean	0.7629
RMS	0.148
χ^2 / ndf	485.9 / 392
p0	-22.03 ± 1.95
p1	88.72 ± 7.45
p2	-58.34 ± 5.00
p3	32.4 ± 0.7
Width	0.1252 ± 0.0030
Peak	0.7667 ± 0.0008

Figure 7.10: ρ^0 meson mass reconstruction without (top) and with (bottom) the Recoil Detector. The distribution of the invariant mass $M_{2\pi}$ reconstruction with Forward Spectrometer (top) is for data in the region $\Delta E < 0.6 GeV$. The distribution of the invariant mass $M_{2\pi}$ reconstruction with Recoil Detector information (bottom) is for all data region without the cut on ΔE, cuts on the kinematic of the proton tracks from the Recoil Detector are applied to improve the selection of exclusive events. The red curve represents a polynomial fit on the background, the blue curve is the *Breit-Wigner Shape* and the pink curve is the sum of two.

7.6　Diffractive Slope parameter b extraction from data

Since the slope parameter b is a measure of the transverse size of the ρ^0 vector meson ($b \approx \frac{1}{3}(\langle r_{\rho^o}^2 \rangle + \langle r_p^2 \rangle)$), where $\langle r_p^2 \rangle$ is a measure of the transverse size of the proton [114, 115, 116]). In certain theorical models, $b(Q^2)$ is related to the $-t'$ dependence of GDPs [117]. The $b(Q^2)$ dependence and the change of the $-t'$ slope as a function of Q^2 is explained by higher-twist contributions in here [118].
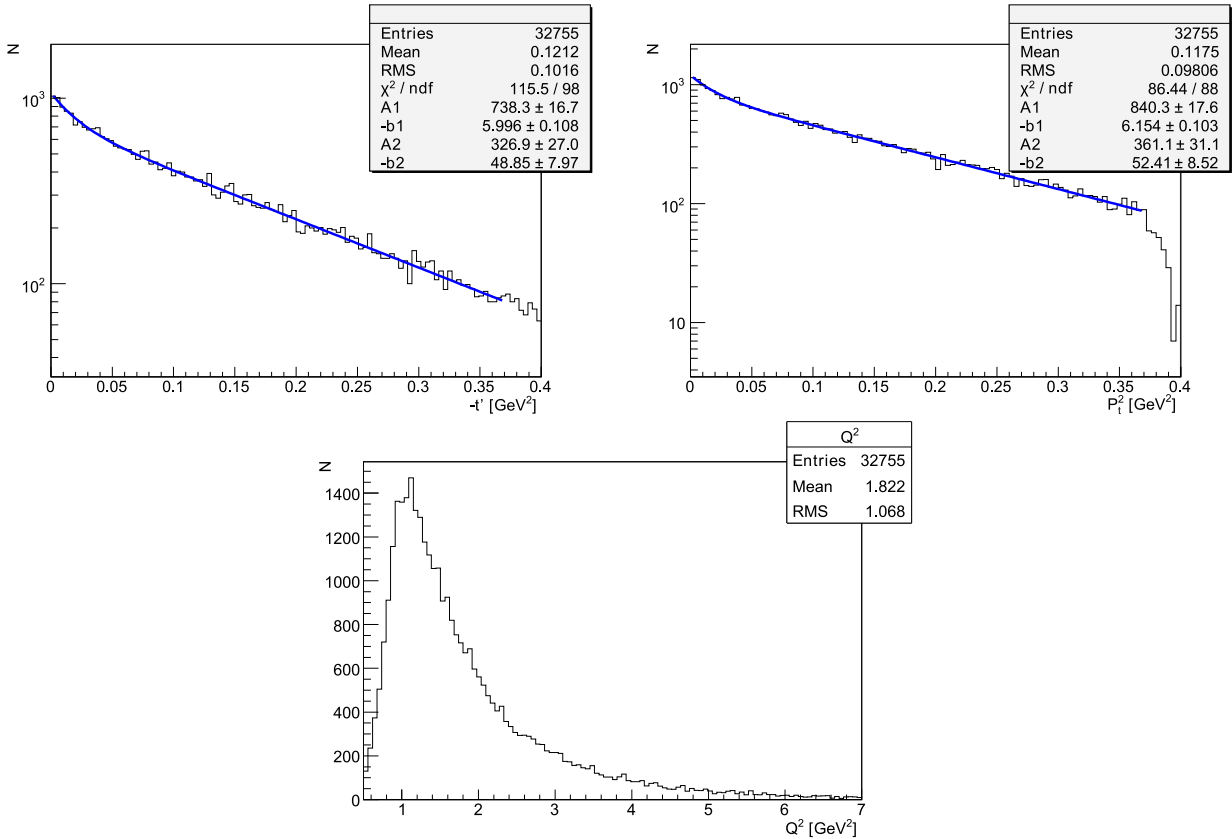

Figure 7.11: Measured $-t'$, p_t^2 and Q^2 distributions from ρ^0 diffractive exclusive production for the analysis without Recoil Detector information. Both the $-t'$ and p_t^2 are in logarithmic scale. The blue line is the fit result of the sum of the two exponential function ($A_1 e^{-b_1(-t')} + A_2 e^{-b_2(-t')}$) representing the signal and the gas contamination. Negligible contribution of background from non exclusive ρ^0 production.

In the first step the slope parameter b has been extracted using the Forward Spectrometer without the Recoil Detector information. This analysis give us the way to estimate the background contamination in real data without the Recoil Detector in comparison with the analysis where the Recoil Detector information is used. The slope b has been extracted using the variables $-t'$ and p_t^2. In both cases b is extracted by performing a one dimensional binned fit in the shape of an exponential ($Ae^{-b(-t')}$ and $Ae^{-b(p_t^2)}$) distribution.

Fig. 7.11 and Fig. 7.12 show the distributions of, $-t'$, p_t^2 and Q^2 for data without and with Recoil Detector information and without cut on Q^2. Since reaction identification is not perfect without the Recoil Detector, a small amount of background has to be accounted for.

For the analysis without the Recoil detector but with the exclusive cut on ΔE, the fit curves are a one dimensional binned fit in the shape of the sum of two exponential function ($A_1 e^{-b_1(-t')} + A_2 e^{-b_2(-t')}$) representing the signal and the gas contamination. The first parameter $b1$ represent the slope parameter b

for hydrogen and the second parameter $b2$ ($\approx$50) seems to be [119] a nitrogen contamination in the hydrogen sample.

For the analysis with the Recoil Detector the fit function used is the one exponential ($A_1 e^{-b_1(-t')}$), because of estimated negligible amount of non exclusive background. The hydrogen data can be described by a single exponential, while for compound targets one need a double exponential, to fit both the coherent and the incoherent contribution. One coming from incoherent scattering when scattering happens on nucleons inside nucleus, and one corresponding to scattering where the nucleus remains intact. [120, 121]
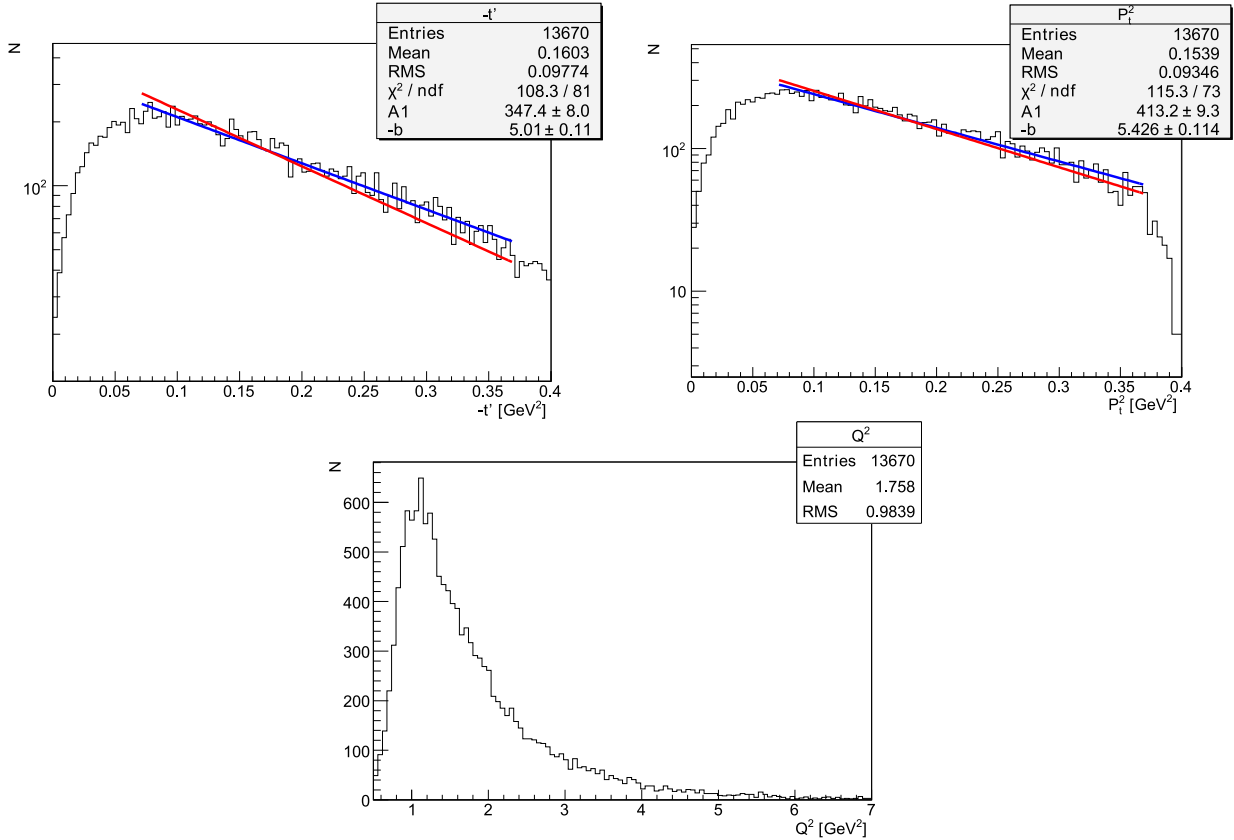

Figure 7.12: The distribution of $-t'$, p_t^2 and Q^2, for analysis with the Recoil detector and no cut on Q^2. Both the $-t'$ and p_t^2 are in logarithmic scale. The blue curve are the fit signal and the red is the representation of the $b1$ slop analysis without the Recoil Detector. We restrict fit region in $-t'$ from $0.07\ GeV^2$ till $0.37\ GeV^2$ because of the Recoil Detector acceptance and not be affected by the gas contamination.

At low $-t'$ the data with and without the Recoil detector are different due to the big acceptance effect of the Recoil detector and the possible gas contamination on the Hydrogen sample. The analysis without the recoil detector used three exponential to fit, the last exponential is the background shape. It can be seen that the fit with recoil Detector do not describe the data at low $-t'$, the fit was restricted to a $-t'$ region where influence by the acceptance effect of the Recoil Detector is minimal. This effect should be investigated via *Monte Carlo* studies. Due to the limited acceptance of the Recoil Detector, it is evident that a correction is needed.
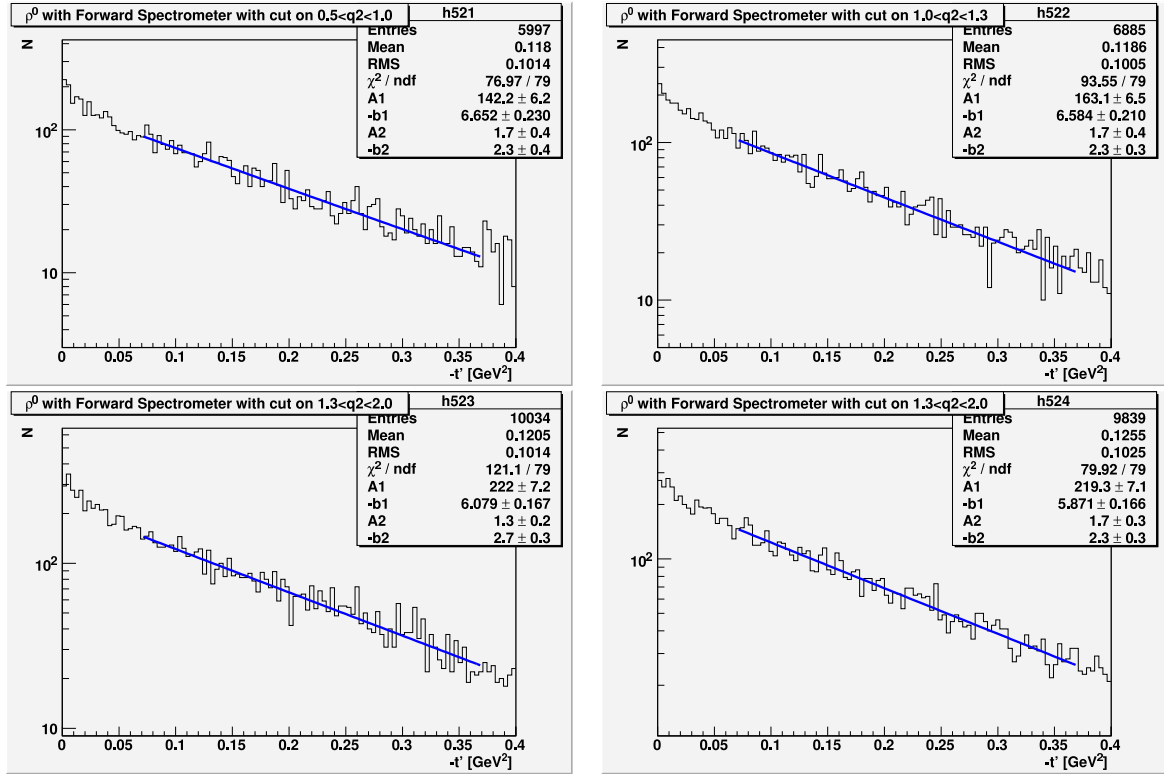
Figure 7.13: The $-t'$ dependence in various Q^2 bins for the analysis without the Recoil Detector information. The distribution of the $-t'$ for analysis with the Forward Spectrometer on different Q^2 regions fitted for the same region of $-t'$ from $[0.07 - 0.37]$, to minimize acceptance effects.
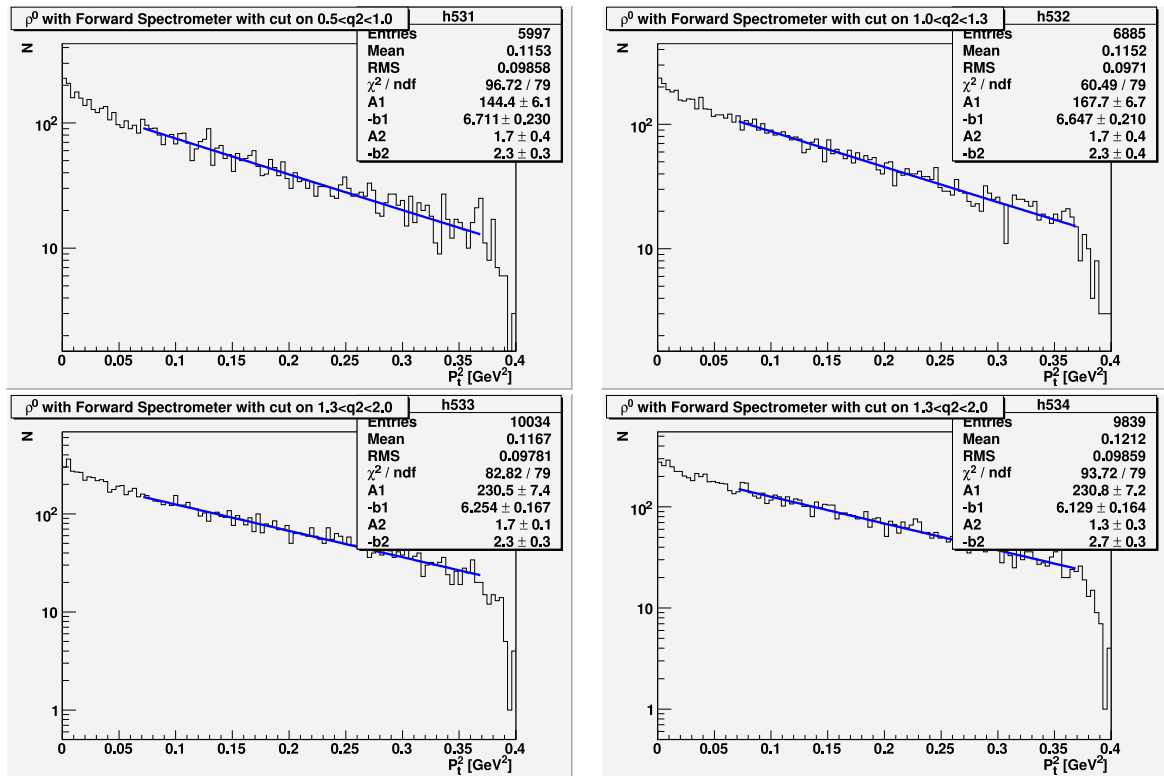
Figure 7.14: The p_t^2 dependence in various Q^2 bins for the analysis without the Recoil detector information. The distribution of the p_t^2 for analysis with the Forward Spectrometer on different Q^2 regions fitted for the same p_t^2 range from $[0.07 - 0.37]$.
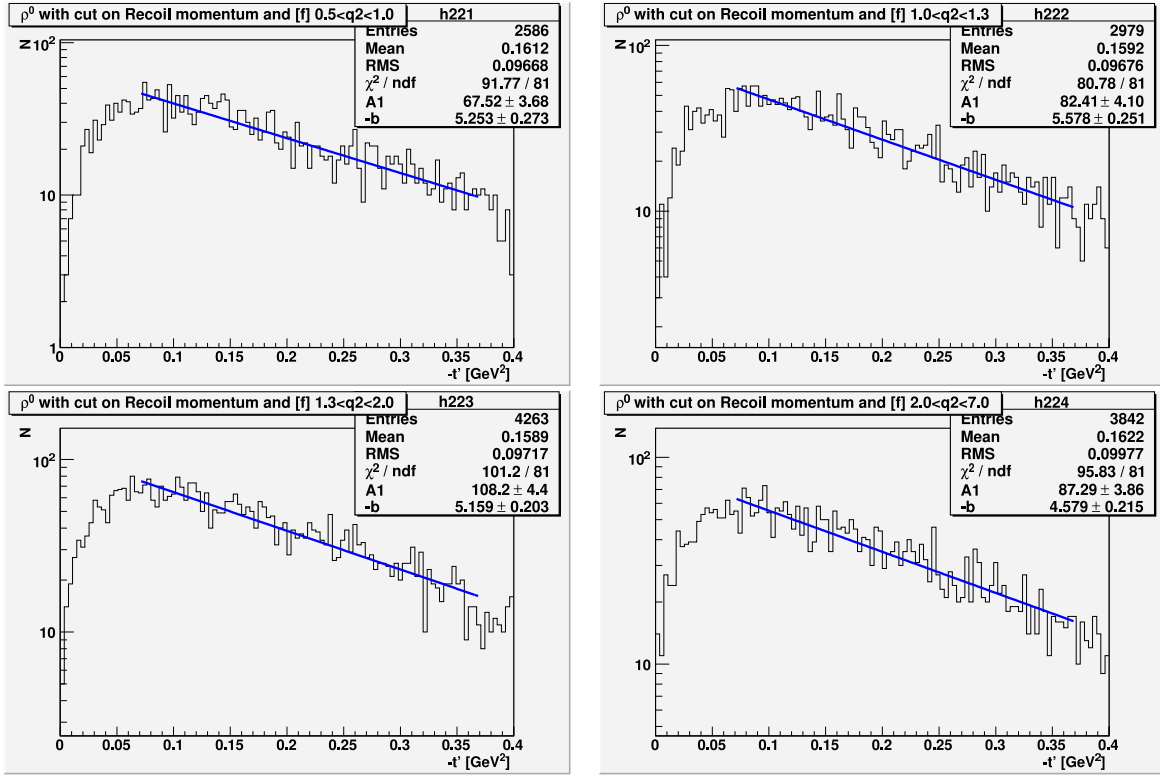
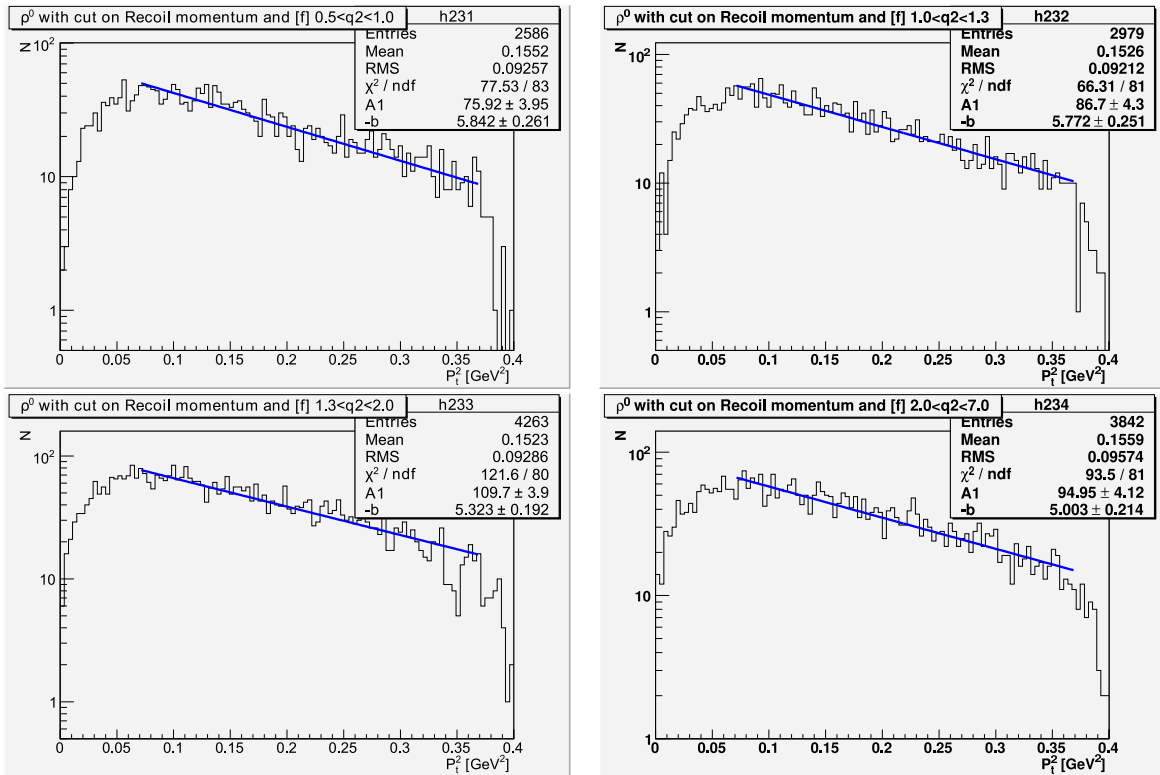Figure 7.15: The same as Fig. 7.13, but with Recoil Detector information included.

Figure 7.16: The same as Fig. 7.14, but with Recoil Detector information included.

The bin in Q^2 should provide equivalent statistics in each region and should be comparable to the bins previously used in HERMES. Thus the bins used in this study are $0.5-1.0 GeV^2$, $1.0-1.3 GeV^2$, $1.3-2.0 GeV^2$ and $2.0-7.0 GeV^2$.

Figure 7.17: Measured Q^2 dependence of the diffactive slope parameter in exclusive ρ^0 production with and without the Recoil Detector for a hydrogen target.

All the values of b extracted from the different Q^2 bins for $-t'$ and p_t^2 can be seen in Fig. 7.13 and Fig. 7.14 for the analysis without the Recoil Detector information. Each Q^2 bins was fitted with a double exponential function to extract the b slope and the background. The background slope was varied in limits, according to the slopes we got for the non exclusive region.

The values of b extracted in the analysis with the Recoil Detector from different Q^2 bins for $-t'$ and p_t^2 can be seen in Fig. 7.15 and Fig. 7.16. Each Q^2 bin was fitted with a one exponential function.

The $-t'$ and p_t^2 distribution on different Q^2 region were fitted for the same region on $-t'$ and p_t^2 from $0.07\ GeV^2$ to $0.37\ GeV^2$ for the analysis with the Recoil Detector and from $0.05\ GeV^2$ to $0.37\ GeV^2$ for the analysis without the Recoil Detector. We choose to start the fit not at low values of $-t'$ and p_t^2 due to the acceptance of the Recoil Detector and the possible gas contamination [122, 123].

Fig. 7.17 shows the diffractive slope parameter b as a function of Q^2 for analysis with (in black) and without (in red) the Recoil Detector. The b for $-t'$ and p_t^2 the figures show similar behavior for b on this variables for the different Q^2 bins (see third panel). On the figure each Q^2 bin is represented by the *weighted mean* value of the data. The extraction of the b slope for different Q^2 without the Recoil Detector could be influenced by the background. A *Monte Carlo* study should be done to check this hypothesis, with the Recoil Detector the extracted b slope is systematically low. Main effect: Loss of acceptance at low $-t'$.
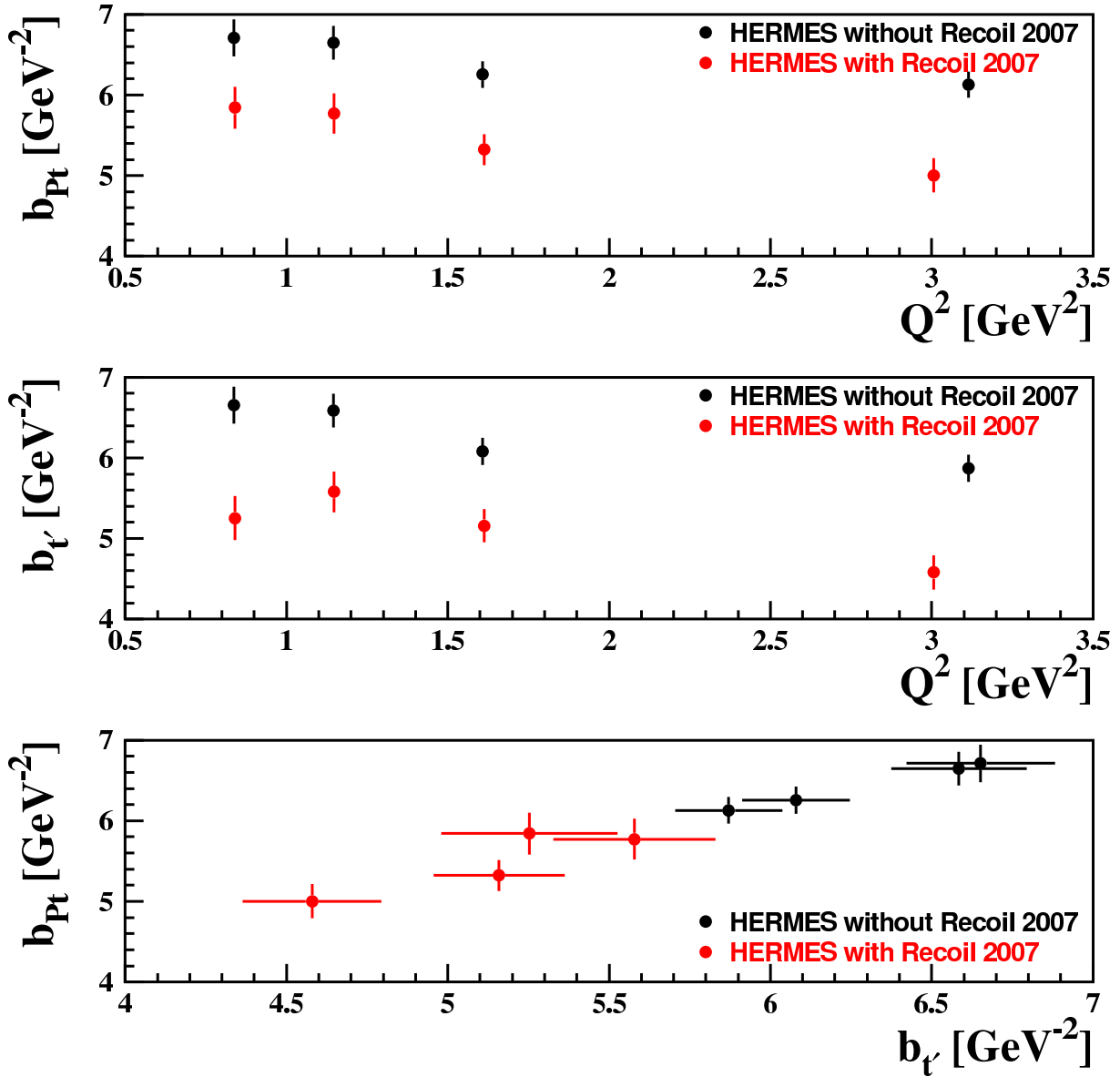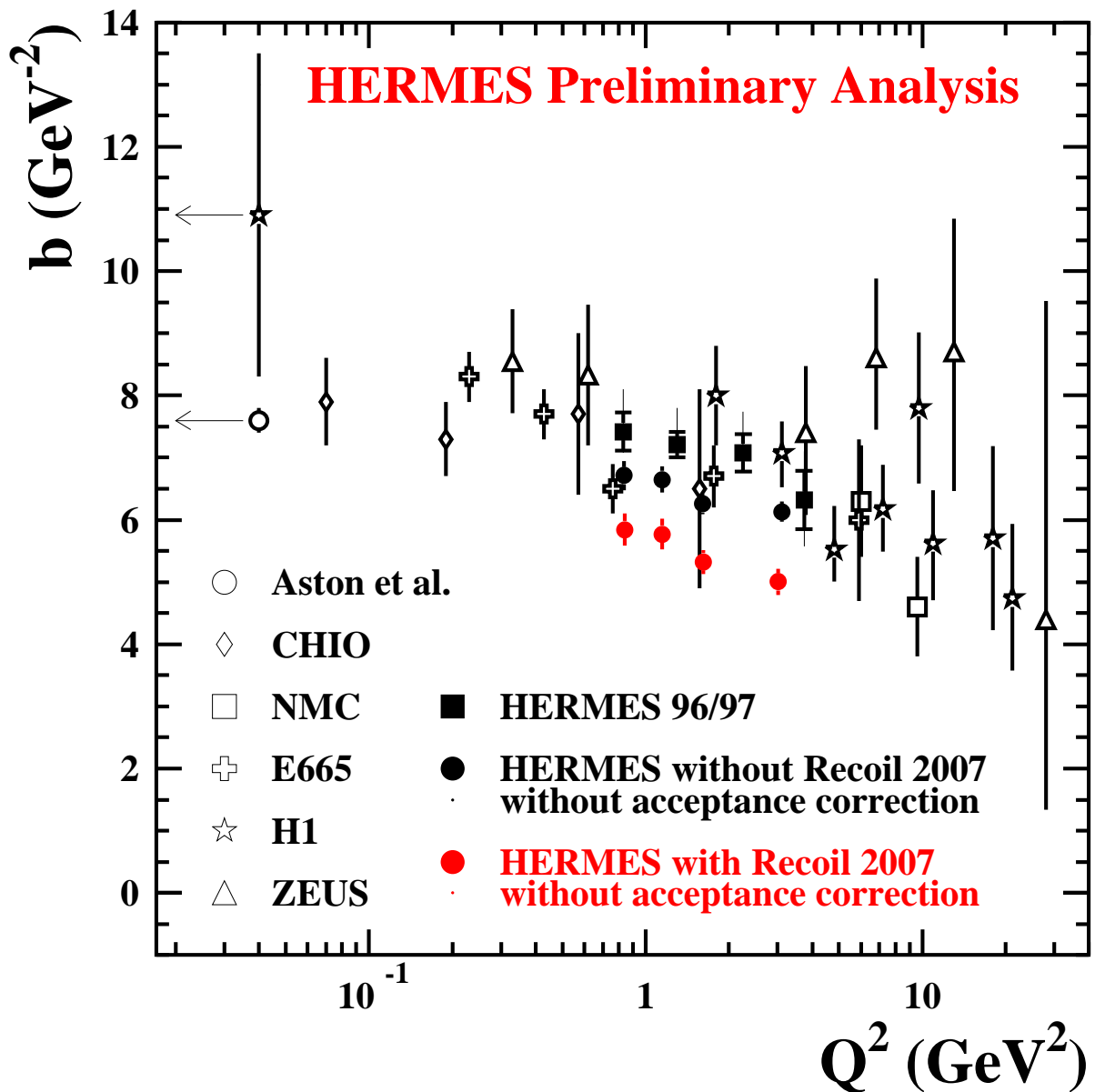

Figure 7.18: The measuremed Q^2 dependence of the diffractive slope parameter in exclusive ρ^0 production without recoil detector for hydrogen target (data 96/97) and with the Recoil Detector for hydrogen target (data 2007). The data are compared to electroproduction results from CHIO, E665, NMC, H1, ZEUS and real photoproduction results from H1 and Aston *et al* [80]. Points are low, probably because of the acceptance effect of the Recoil Detector.

The dependence on the momentum transfer t' of the cross section for ρ^0 production could be well described by an exponential $e^{-b|t'|}$ characterized by a diffractive slope parameter b. The diffractive slope parameter for the ρ^0 production with and without Recoil Detector was found to be compatible. The ρ^0 slope parameter exhibited a decreasing behavior with Q^2, which can be interpreted as a shrinkage of the vector meson radius with Q^2.

In Fig. 7.18 the obtained slope values for data from 96/97 of HERMES for hydrogen target compared to data from other experiments. The b slope values of the data from 2007 for hydrogen target with recoil Detector information obtained show systematically low values. These new data points and the results of previous measurement clearly indicate a common decrease of the slope parameter with Q^2.

Conclusions

The Hermes experiment used a 27.6 GeV lepton beam from the Hera storage ring to scatter off an internal gas target for the investigation of the spin structure of the nucleon. The contribution of the quark spin to the nucleon spin is measured to be around 30%. Measurements of the gluon spin indicated a very small contribution to the spin of the nucleon. The remaining contributions from the orbital angular momentum of the quarks and the gluons remain to be unknown.

An approach based on General Parton Distributions (GPDs), is the most promising way to access the size of the contribution of the total angular momentum of the quarks and the gluons. It can be experimentally accessed via hard exclusive reactions. Furthermore the GPDs can be measured selectively by requesting a certain final state. ρ^0 meson production is unique in the sense that it enables the access to distributions of the quarks and of the gluons.

Hermes did various measurements of hard exclusive reactions using the main spectrometer and missing mass technics, but the measurements were affected by non-exclusive background. In order to improve the cleanness and the resolution of the kinematic variables, the Collaboration decided to upgrade the Hermes forward spectrometer with the Recoil Detector. This new part of Hermes consists of three subdetectors: a silicon strip detector inside the vacuum, a scintillating fiber tracker and the photon detector. All three detectors were located inside a solenoidal magnet which provided a 1T longitudinal magnetic field.This detector was an ideal novel tool to combine energy and position measurements for charged particles in momentum range of 0.1 to 1.4 GeV/c. The Recoil Detector was fully commissioned and operating. Data was taken continuously until the Hera shutdown in July of 2007.

The Recoil Detector improves the selection of exclusive events by a direct measurement of the momentum and track of the recoiling particle as well as by rejecting non-exclusive background. In addition it also improve the resolution especially in the low momentum region. Taking advantage of the high luminosity runs from Hera in 2006 and 2007, a large amount of data has been taken with unpolarized proton and deuteron targets, using the Recoil Detector.

The work presented in this thesis mainly consists of the building, installing and commissioning the Scintillating Fiber Tracker and the analysis of the data produced with the Recoil detector. The Recoil detector was installed in January 2006. This thesis describes the installation of the Scintillating Fiber Tracker with all the multiple checks made by our group to understand the functioning of the Scintillating Fiber Tracker.

It explains the mapping of the light guides, PMTs and electronics components. It describes the monitoring of radiation level at the area of the Recoil Detector, servicing measurement, the Gain monitoring system to verify the operability of the detector and the pedestal stability to sparsify the data. We describe the calculation of the efficiency of the Scintillating Fiber Tracker for different type of particles, in detail.

The alignment test run at DESY Area 22 where the exact positions of each fibers with a resolution of 50 μm was measured is also described. The eccentricity and concentricity of the Scintillating Fiber Tracker is estimated. The Recoil Detector assembly in the HERMES experiment hall in order to take cosmic data, is described along with the instalation of the holding structure.

The efficiency of Scintillating fiber tracker was measured and determined precisely for protons and for pions. The efficiency of the inner Scintillating fiber tracker was determined to be higher than 99.5% for the protons and stable during the full period of data tacking with variation less than 0.5%. For the first quadrant of the outer layer of the Scintillating fiber tracker a decrease of the efficiency was observed.

The analysis of the diffractive-exclusive production of ρ^0 mesons is described, using the set of unpolarized Hydrogen target data from 2007. The selection requirements imposed on the data in order to obtain exclusive ρ^0 production are explained in detail. The study of the diffractive slope parameter b, related to the transverse size of the struck nucleon and meson, as a function of Q^2, with and without the recoil detector measurement, was done.

This analysis give us the way to estimate the background contamination in HERMES data without the Recoil Detector by comparing it with the analysis where the Recoil Detector information was used. The diffractive slope b was extracted using the variables $-t'$ and p_t^2. The extraction of the diffractive slope b for different Q^2 without the Recoil Detector is possibly influenced by the background *Monte Carlo* studies need to check this hypothesis. With the Recoil Detector the extracted diffractive slope b shows systematically lower values. This phenomenon also needs *Monte Carlo* studies to check how the Recoil Detector influences the acceptance, especially in the low $-t'$ region. The data clearly indicate a common decrease of the slope parameter with Q^2, which is another hint for existence of shrinkage of the vector meson radius.

To conclude this exploratory study of the diffractive slope b for different Q^2 on exclusive production of ρ^0 meson shows a decreasing behavior of b with Q^2, which can be interpreted as a shrinkage of the vector meson radius. It gives us a good basis for further studies in elastic electroproduction of vector mesons at the onset of color transparency effects. The final measurement of the $b(Q^2)$ dependence will require additional *Monte Carlo* studies of the HERMES Collaboration and can finally be used to tune *GPD models*.

Bibliography

[1] M. Gell-Mann, "A Schematic Model Of Baryons And Mesons," Phys. Lett. **8** (1964) 214.

[2] G. Zweig, "An SU(3) Model For Strong Interaction Symmetry And Its Breaking," CERN-TH-401, 1964.

[3] D. H. Perkins, "Introduction to high energy physics," *Reading 1972, 353p.*

[4] D. J. Griffiths, "Introduction to elementary particles," *Weinheim, USA: WILEY-VCH (2008) 454p.*

[5] J. Ashman *et al.* [European Muon Collaboration], "A measurement of the spin asymmetry and determination of the structure function g(1) in deep inelastic muon proton scattering," Phys. Lett. B **206** (1988) 364.

[6] K. Abe *et al.* [E143 collaboration], "Measurements of the proton and deuteron spin structure functions g1 and g2," Phys. Rev. D **58** (1998) 112003, hep-ph/9802357.

[7] D. Mueller, D. Robaschik, B. Geyer, F. M. Dittes and J. Horejsi, "Wave functions, evolution equations and evolution kernels from light-ray operators of QCD," Fortsch. Phys. **42** (1994) 101, hep-ph/9812448.

[8] X. D. Ji, "Deeply-virtual Compton scattering," Phys. Rev. D **55** (1997) 7114, hep-ph/9609381.

[9] [HERMES Collaboration], "HERMES technical design report," DESY-PRC-93-06.

[10] M. Düren, "The Hermes Experiment: From The Design To The First Results," Habilitation Thesis, Friedrich Alexander Univertität Erlangen-Nürenberg (1995).

[11] M. Düren, "Hermes: A New Experiment To Clarify The Spin Puzzle. (In German)," Phys. Bl. **52** (1996) 243.

[12] K. Ackerstaff *et al.* [HERMES Collaboration], "Measurement of the neutron spin structure function g1(n) with a polarized He-3 internal target," Phys. Lett. B **404** (1997) 383, hep-ex/9703005.

[13] A. Airapetian *et al.* [HERMES Collaboration], "Measurement of the proton spin structure function g1(p) with a pure hydrogen target," Phys. Lett. B **442** (1998) 484, hep-ex/9807015.

[14] K. Ackerstaff *et al.* [HERMES Collaboration], "Flavor decomposition of the polarized quark distributions in the nucleon from inclusive and semi-inclusive deep-inelastic scattering," Phys. Lett. B **464** (1999) 123, hep-ex/9906035.

[15] A. Airapetian *et al.* [HERMES Collaboration], "Precise determination of the spin structure function g(1) of the proton, deuteron and neutron," Phys. Rev. D **75** (2007) 012007, hep-ex/0609039.

[16] A. G. S. Osborne, "Exclusive rho0 meson cross section ratios on deuterium and hydrogen targets," DESY-THESIS-2006-024.

[17] R. Kaiser [HERMES Collaboration], "A large acceptance recoil detector for HERMES," DESY-HERMES-01-17.

[18] R. Kaiser *et al.* [HERMES Collaboration], "The HERMES Recoil Detector, Technical Design Report" HERMES-Internal $02 - 003$ (2002).

[19] "Hera - Proton Electron Colliding Beam Project At Desy," CERN Cour. **20** (1980) 99.

[20] M. Dohlus, G. H. Hoffstaetter, M. Lomperski and R. Wanzenberg, "Report from the HERA taskforce on luminosity optimization: Theory and first luminosity scans," DESY-HERA-03-01.

[21] A. A. Sokolov and I. M. Ternov, "On Polarization and spin effects in the theory of synchrotron radiation," Sov. Phys. Dokl. **8** (1964) 1203.

[22] D. P. Barber *et al.*, "High spin polarization at the HERA Electron Storage Ring," Nucl. Instrum. Meth. A **338** (1994) 166.

[23] D. P. Barber *et al.*, "The HERA polarimeter and the first observation of electron spin polarization at HERA," Nucl. Instrum. Meth. A **329** (1993) 79.

[24] M. Beckmann *et al.*, "The longitudinal polarimeter at HERA," Nucl. Instrum. Meth. A **479**, 334 (2002), physics/0009047.

[25] K. Ackerstaff *et al.* [HERMES Collaboration], "The HERMES spectrometer," Nucl. Instrum. Meth. A **417** (1998) 230, hep-ex/9806008.

[26] A. Airapetian *et al.* [HERMES Collaboration], "The HERMES polarized hydrogen and deuterium gas target in the HERA electron storage ring," Nucl. Instrum. Meth. A **540** (2005) 68, physics/0408137.

[27] C. Baumgarten *et al.*, "The storage cell of the polarized H/D internal gas target of the HERMES experiment at HERA," Nucl. Instrum. Meth. A **496** (2003) 277.

[28] A. Nass *et al.*, "The HERMES polarized atomic beam source," Nucl. Instrum. Meth. A **505** (2003) 633.

[29] C. Baumgarten *et al.*, "Measurements of atomic recombination in the HERMES polarized hydrogen and deuterium storage cell target," Nucl. Instrum. Meth. A **496** (2003) 263.

[30] C. Baumgarten *et al.* [HERMES Target Group], "An atomic beam polarimeter to measure the nuclear polarization in the HERMES gaseous polarized hydrogen and deuterium target," Nucl. Instrum. Meth. A **482** (2002) 606.

[31] J. Stewart, G. Court, J. Morton, H. Tallini, W. Haeberli, T. Wise and K. Zapfe-Duren, "Aspects of the design of the polarized H/D internal gas target storage cell for the HERMES experiment at HERA," *Prepared for 5th International Workshop on Polarized Beams and Polarized Gas Targets, Cologne, Germany, 6-9 Jun 1995.*

[32] W. R. Leo, "Techniques for nuclear and particle physics experiments: A how to approach," *Berlin, Germany: Springer (1987) 368 p.*

[33] M. G. van Beuzekom, E. Garutti, D. Heesbeen, J. J. M. Steijger and J. Visser, "First experience with the HERMES silicon detector," Nucl. Instrum. Meth. A **461** (2001) 247.

[34] J. J. M. Steijger, "The lambda wheels, a silicon vertex detector for HERMES," Nucl. Instrum. Meth. A **453** (2000) 98.

[35] J. T. Brack *et al.*, "The HERMES forward tracking chambers: Construction, operation, and aging effects," Nucl. Instrum. Meth. A **469**, 47 (2001).

[36] S. Bernreuther *et al.*, "The HERMES back drift chambers," Nucl. Instrum. Meth. A **416** (1998) 45, hep-ex/9803005.

[37] S. Bernreuther *et al.*, "Design and performance of the large HERMES drift chambers," Nucl. Instrum. Meth. A **367** (1995) 96.

[38] A. Andreev *et al.*, "Multiwire Proportional Chambers In The Hermes Experiment," Nucl. Instrum. Meth. A **465** (2001) 482.

[39] T. A. Shibata *et al.*, "A high precision laser alignment monitoring system for HERMES tracking detectors," Nucl. Instrum. Meth. A **411** (1998) 75.

[40] Z. Ye, E. C. Aschenauer, "Misalignment Effect on the Beam-Spin and Beam-Charge Asymmetries in DVCS," HERMES-Internal $05 - 038$ (2005).

[41] W. Wander, "Reconstruction of High Energy Scattering Events in the HERMES Experiment," DESY-THESIS-1996-023.

[42] R. Kaiser *et al.*, (for the HERMES PID Group), "Particle Identification at HERMES," HERMES-Internal $97 - 025$ (1997).

[43] H. Avakian *et al.*, "Performance of the electromagnetic calorimeter of the HERMES experiment," Nucl. Instrum. Meth. A **417**, 69 (1998), hep-ex/9810004.

[44] E. C. Aschenauer and K. Van der Kerckhove [HERMES Collaboration], "The photon detector of the HERMES dual-radiator RICH," Nucl. Instrum. Meth. A **433** (1999) 168.

[45] N. Akopov *et al.*, "The HERMES dual-radiator ring imaging Cerenkov detector," Nucl. Instrum. Meth. A **479**, 511 (2002), physics/0104033.

[46] H. E. Jackson, "The Hermes Dual-Radiator Rich Detector," Nucl. Instrum. Meth. A **502**, 36 (2003).

[47] A. T. Maas, "Particle identification with RICH detectors: Algorithms and their optimization. A case study on the experiments CERES and HERMES," DESY-THESIS-2000-051.

[48] E. Aschenauer *et al.*, "Optical characterization of n = 1.03 silica aerogel used as radiator in the RICH of HERMES," Nucl. Instrum. Meth. A **440** (2000) 338.

[49] K. Negodaeva, DESY Zeuthen "The PID efficiency of the HERMES RICH detector for the IRT method," HERMES-Internal $00 - 028$ (2000).

[50] Y. Miyachi [HERMES Collaboration], "The HERMES RICH Aerogel Radiator," Nucl. Instrum. Meth. A **502** (2003) 222.

[51] L. F. Zhang, "Ring imaging Cerenkov counter with aerogel radiator for HERMES," DESY-HERMES-99-64.

[52] P. Carter [HERMES Collaboration], "The aerogel radiator of the HERMES RICH," Nucl. Instrum. Meth. A **433** (1999) 392.

[53] B. Hommez, "Hadron Identification With The Hermes Rich," Nucl. Instrum. Meth. A **502** (2003) 294.

[54] R. Kaiser [HERMES Collaboration], "Particle identification with the HERMES RICH detector," Czech. J. Phys. **50S1** (2000) 341.

[55] M. Tytgat [HERMES Collaboration], "Particle identification with the HERMES RICH," Nucl. Instrum. Meth. A **433** (1999) 286.

[56] X. Artru, G. B. Yodh and G. Mennessier, "Practical Theory Of The Multilayered Transition Radiation Detector," Phys. Rev. D **12**, 1289 (1975).

[57] D. M. Thiessen, "The gas system for the HERMES transition radiation detector," DESY-HERMES-96-28.

[58] U. Elschenbroich, "Analysis of Luminosity Monitor Data for Different Years," HERMES-Internal 02 − 013 (2002).

[59] T. Benisch *et al.*, "The luminosity monitor of the HERMES experiment at DESY," Nucl. Instrum. Meth. A **471** (2001) 314.

[60] H. Tanaka, "Laser-based gain monitoring system for HERMES experiment," DESY-HERMES-02-39.

[61] G. Schnell, "Longitudinal polarization of the Lambda in deep inelastic scattering of polarized positrons from nucleons," DESY-HERMES-99-37.

[62] F. Meißner, G. Kyle, S. Pate, A. Schwind and A. Brüll, "Photoproduction Trigger for Hermes," DESY-HERMES-96-026.

[63] X. D. Ji, "Gauge invariant decomposition of nucleon spin," Phys. Rev. Lett. **78** (1997) 610, hep-ph/9603249.

[64] A. V. Belitsky and D. Mueller, "Nucleon hologram with exclusive leptoproduction," Nucl. Phys. A **711** (2002) 118, hep-ph/0206306.

[65] M. Diehl, "Generalized parton distributions," Phys. Rept. **388** (2003) 41, hep-ph/0307382.

[66] A. V. Radyushkin, "Nonforward parton distributions," Phys. Rev. D **56** (1997) 5524, hep-ph/9704207.

[67] X. D. Ji, "Off-forward parton distributions," J. Phys. G **24** (1998) 1181, hep-ph/9807358.

[68] A. Airapetian *et al.* [HERMES Collaboration], "Single-spin azimuthal asymmetries in electroproduction of neutral pions in semi-inclusive deep-inelastic scattering," Phys. Rev. D **64** (2001) 097101, hep-ex/0104005.

[69] A. Airapetian *et al.* [HERMES Collaboration], "Exclusive leptoproduction of rho0 mesons from hydrogen at intermediate virtual photon energies," Eur. Phys. J. C **17** (2000) 389, hep-ex/0004023.

[70] A. Airapetian *et al.* [HERMES Collaboration], "Double spin asymmetry in the cross section for exclusive rho0 production in lepton proton scattering," Phys. Lett. B **513** (2001) 301, hep-ex/0102037.

[71] I. Lehmann *et al.*, [HERMES Collaboration], "Heating Studies on the HERMES Target Cell," HERMES-Internal 06 − 080 (2006).

[72] N. C. Pickert, "Commissioning of the recoil silicon detector for the HERMES experiment," DESY-THESIS-2008-005.

[73] I. Vilardi, "Detection of low momentum protons with the new HERMES recoil detector," DESY-THESIS-2008-033.

[74] J. Stewart, "The HERMES recoil silicon detector," Nucl. Instrum. Meth. A **511** (2003) 271.

[75] M. Kopytin *et al.*, "Decision on the readout chip for the new Hermes Silicon Recoil Detector," HERMES-Internal $02 - 020$ (2002).

[76] L. Santamaria, "Study on the crosstalk sources of the Hermes Recoil Silicon Recoil Detector at DESY," SUMMER STUDENT PROGRAM 2004 DESY-ZEUTHEN.

[77] M. Diehl, T. Gousset, B. Pire and J. P. Ralston, "Testing the handbag contribution to exclusive virtual Compton scattering," Phys. Lett. B **411** (1997) 193, hep-ph/9706344.

[78] B. Krauss, "Deeply virtual Compton scattering and the HERMES recoil-detector," DESY-THESIS-2005-008.

[79] M. Klostein,"Exclusive rho0 meson electroproduction at HERMES," DESY-HERMES-98-46.

[80] M. Tytgat, "Diffractive production of rho0 and omega vector mesons at HERMES," DESY-THESIS-2001-018.

[81] A. A. Rostomyan, "Exclusive Rho(0) Production At Hermes," DESY-THESIS-2008-042.

[82] J. Dreschler, "Transverse target-spin asymmetry in exclusive electroproduction of rho(0) mesons," DESY-THESIS-2008-031.

[83] P. Soeding, "On the Apparent Shift of the rho Meson Mass in Photoproduction," Phys. Lett. B **19** (1966) 702.

[84] A. Airapetian *et al.* [HERMES Collaboration], "Double-spin asymmetries in the cross section of rho0 and Phi production at intermediate energies," Eur. Phys. J. C **29** (2003) 171, hep-ex/0302012.

[85] Z. Ye, "Transverse target-spin asymmetry associated with deeply virtual Compton scattering on the proton and a resulting model-dependent constraint on the total angular momentum of quarks in the nucleon," DESY-THESIS-2007-005.

[86] W. Yu, "Beam-Helicity Azimuthal Asymmetry measured with the Recoil Detector in Exclusive Electroproduction of Real photons at HERMES," DESY-THESIS-2009-018.

[87] M. Hoek, "Design and construction of a scintillating fibre tracker for measuring hard exclusive reactions at HERMES," DESY-THESIS-2006-027.

[88] Kuraray co.,LTD., "Catalogue," Methacrylic Resin Division.

[89] Hamamatsu Photonics k.k. Electron Tube Center, "Multianode Photomultiplier Tube Assembly H7546B." http://www.hamamatsu.com

[90] A. Kastenmuller *et al.*, "Fast detector readout for the HADES-RICH," Nucl. Instrum. Meth. A **433** (1999) 438.

[91] T. Keri, "Detection of exclusive reactions in the HERMES Recoil Fiber Tracker," DESY-THESIS-2008-021.

[92] M. Hartig, "The TDC readout of the 12th dynode for the SciFi PMTs" HERMES-Internal $04 - 066$, (2004).

[93] GSI, *LE 1600 / LE 1620, CAMAC 16 Channel Leading-Edge Discriminator*, http://www-aix.gsi.de/ gfe_o/elec_tt/LE1600/LE1600-a.html

[94] CAEN, *Technical Information Manual, Mod V767 128 channel General Purpose Multihit TDC.*

[95] Y. van Haarlem, "The HERMES recoil photon-detector and nuclear p(t)-broadening at HERMES," DESY-THESIS-2007-033.

[96] A. Borysenko, G.P. Capitani, M. Tytgat, Y. Van Harrlem, "Status of the Recoil Photon Detector," HERMES-Internal, (2002).

[97] R. Kaiser for the HERMES Recoil Group "Status of the Hermes Recoil Detector" HERMES-Internal $04 - 034$, (2004).

[98] M. Statera, "Superconducting magnetic systems for high energy polarized physics," DESY-THESIS-2006-069.

[99] J. Streit-Lehmann, Diplomarbeit "Entwincklung und Bau einer Lichtquelle für das Gain Monitoring System eines Hermes-Detektors aus szintillierenden Fasern," II.Physikalisches Institut Justus Liebig Universität Gießen (2006).

[100] R.F. Pérez-Benito and H.Y.F.J. Stenzel, "Alignment of the SciFi Detector at the DESY22 electron testbeam," HERMES-Internal $05 - 063$ (2005).

[101] I. M. Gregor et al., "Test-beam Results of the First Prototype for the Hermes Silicon Recoil Detector," HERMES-Internal $2002 - 050$ (2002).

[102] M. Moritz, "Measurement of the high Q**2 neutral current DIS cross section at HERA," DESY-THESIS-2002-009.

[103] M. Milite, "The internal structure of charmed jets in photoproduction at HERA and tests of the ZEUS microvertex silicon sensors," DESY-THESIS-2001-050.

[104] J. Martens, "Simulations and quality control of the silicon strip detectors of the ZEUS microvertex detector, (In German)," DESY-THESIS-1999-044.

[105] D. Dannheim, "The silicon strip detectors of the ZEUS microvertex detector," DESY-THESIS-1999-027.

[106] M. Moll, "Tempering experiments on radiation damaged silicon detectors. (In German)," DESY-THESIS-1999-040.

[107] R. Kaiser for the HERMES Recoil Group "Status of the SFT and its Light Guides" HERMES-Internal Report $05 - 040$, (2005).

[108] S. Margulies, M. Chung, A. Bross, C. Kim and A. Pla-Dalmau, "Effects of irradiation on Kuraray multiclad fibers," *Prepared for Workshop on Scintillating Fiber Detectors (SCIFI 93), Notre Dame, IN, 24-28 Oct 1993.*

[109] W. Yu, *Analysis Meeting, DESY, 27 April 2007.*

[110] S. Gearge, *Calculation of track parameters and positions, 3 december 1997.*

[111] X. Lu, "The HERMES recoil detector: Particle identification and determination of detector efficiency of the scintillating fiber tracker," DESY-THESIS-2009-043.

[112] HERMES Data Quality website, http://www-hermes.desy.de/groups/daqlgrp/

[113] Particle Data Group, C.Amsler et al., Physics Letters **B667**, 1 (2008).

[114] B. Povh and J. Hufner, "Geometric interpretation of hadron proton total cross-sections and a determination of hadronic radii," Phys. Rev. Lett. **58** (1987) 1612.

[115] B. Povh and J. Hufner, "Systematics Of Strong Interaction Radii For Hadrons," Phys. Lett. B **245**, 653 (1990).

[116] B. Z. Kopeliovich, J. Nemchik and I. Schmidt, "Color transparency at low energies: Predictions for JLAB," Phys. Rev. C **76** (2007) 015205, hep-ph/0702272.

[117] K. Goeke, M. V. Polyakov and M. Vanderhaeghen, "Hard Exclusive Reactions and the Structure of Hadrons," Prog. Part. Nucl. Phys. **47**, 401 (2001), hep-ph/0106012.

[118] L. Frankfurt, W. Koepf and M. Strikman, "Hard diffractive electroproduction of vector mesons in QCD," Phys. Rev. D **54** (1996) 3194, hep-ph/9509311.

[119] K. Ackerstaff *et al.* [HERMES Collaboration], "Observation of a coherence length effect in exclusive rho0 electroproduction," Phys. Rev. Lett. **82** (1999) 3025, hep-ex/9811011.

[120] A. Airapetian *et al.* [HERMES Collaboration], "Exclusive ρ^0 electroproduction on transversely polarized protons," Phys. Lett. B **679** (2009) 100, 0906.5160 [hep-ex].

[121] A. Airapetian *et al.* [HERMES Collaboration], "Spin Density Matrix Elements in Exclusive ρ^0 Electroproduction on 1H and 2H Targets at 27.5 GeV Beam Energy," Eur. Phys. J. C **62** (2009) 659, 0901.0701 [hep-ex].

[122] A. Mussgiller on behalf of HERMES Recoil Group "Silicon Calibration Status, heavy Stuff" Technical Recoil Meeting presentation, Wednesday, April 16, 2008.

[123] J. Bowles on behalf of HERMES Recoil Group "Target Gas Contamination Studies for HERMES"

Acknowledgements

It would not have been possible to write this Ph.D. thesis without the help of many members of HERMES collaboration. I would like, first of all, to express my sincerest gratitude to my supervisor Prof. Dr. Michael Düren who gave me the opportunity to work at HERMES and have supported my work. Special thanks to Elke-Caroline Aschenauer who have tacked huge responsibility on the management of the Recoil Detector listening and supervising on each moment my work at DESY. Also I want to thanks James Stewart for their great point of view, opinion and support during my time in Hamburg.

Many thanks to the former members of the Gießen group, Bjoern Seitz, Matthias Hoek and Markus Ehrenfried for the support and fruitful discussions on the Scintillating Fiber Tracker design. To George Serbanut, Matthias Hartig, Shaojun Lu, Lukas Rubáček and Julia Streit for the innumerable discussions concerning the Sintillator Fiber Tracker. To Hasko Stenzel who coordinated the Alignment at DESY22 test beam and help me with the data of the SFT alignment. I am specially grateful to Tibor Keri with whom I learn how to overcome the difficult time of the installation and help me to understand more about electronic and DAQ of our detector. To Weilin Yu to support me and my change of mood during our time working together in Hamburg and for all help on the understanding of the analysis. I want thanks specially Avetik Airapetian for the task of teaching me about the ρ^0 analysis at HERMES and his help during the latter part of my Ph.D.

I would like to thank all colleagues in the HERMES collaboration in Hamburg. I am especially thankful to Andreas Mussgiller and Sergey Yashenko, who help me a lot in understanding the Recoil Detector and who did an amazing development work (alignment, tracking and analysis software) until was possible to use the data from the Recoil detector. Thanks to the *Gent* group and specially to Yves Van Haarlem, Michael Tytgat and Charlotte Van Huse for all explanation and nice discussions about the photon detector. Thanks to the *Glasgow* group for the nice week spend on this beautiful (sunny) city, specially to Andrew Osborne, Dan Protopopescu, Jennifer Bowles, Jonathan Burns, David Mahon, Gordon Hill and Inti Lehman. Also many thanks to Ralf Kaiser for the help and support during the light guide reparation. Thanks to the *Erlangen* group specially to Nils Pickert, Dietmar Zeiler and Friedrich Stinzing. I want to thanks Alexander Kisselev for the exceptional support on the decoding of the Recoil Detector, to Vitaly Shutov for the assistance on the DAQ and to Vladimir Vikhrov for the unique aid on the instalation of the SFT detector. For the help on the run of the cosmics ray test and for the installation of the detector I want to thanks Ingrid-Maria Gregor, Volker Prahl and Yorck Holler. Also I should thanks the technician and apprentice from Giessen, Zeuthen and Frascati during the five week of the light guide repair at DESY for the exceptional work accomplish.

I want to thanks from the HERMES collaboration particularlly the offside meeting management, Caroline Riedl, Larry Felawka and Benetikt Zihlman for the nice thursday afternoon. It was a real pleasure to know and work with all of the members of the HERMES collaboration, particuly with Hayg Guler, Dominik Gabbert, Achim Hillenbrand, Markus Diefenthaler, Rebecca Lamb, Francesca Giordano, Ricardo Fabbrie, Ignazio Vi-